Doctoral Thesis

On the modeling of multi-phase reactive flows: Thermo-chemical conversion in the raceway zone of blast furnaces

carried out for the purpose of obtaining the degree of

Doctor technicae (Dr. techn.)

submitted at TU Wien, Faculty of Mechanical and Industrial Engineering
by

Markus Bösenhofer

Matr.Nr.: 1425249

under the supervision of

Ao.Univ.Prof. Dipl.-Ing. Dr.techn. Michael Harasek

and

Univ.Prof. Dipl.-Ing. Dr.techn. Anton Friedl

at the
Institute of Chemical, Environmental and Bioscience Engineering
E166

reviewed by

Univ.-Prof. Dipl.-Ing. Dr.techn
Robert Scharler

Institute of Thermal Engineering
Technische Universität Graz
Plüddemanngasse 104/IV
8010 Graz, Austria

Univ.-Prof. Dipl.-Ing. Dr.techn.
Johannes Schenk

Chair of Ferrous Metallurgy
Montanuniversität Leoben
Franz-Josef-Straße 18
8700 Leoben, Austria

Vienna, September 2020

Markus Bösenhofer

Affidavit

I declare in lieu of oath, that I wrote this thesis and performed the associated research myself, using only literature cited in this volume. If text passages from sources are used literally, they are marked as such.
I confirm that this work is original and has not been submitted elsewhere for any examination, nor is it currently under consideration for a thesis elsewhere.

Vienna, 10th September 2020

_____
Markus Bösenhofer

We are all agreed that your theory is crazy. The question that divides us is whether it is crazy enough to have a chance of being correct.
- Niels Bohr (⋆1885, †1962)

To my parents, whose continuous support enabled me...

Kurzfassung

Eine effiziente und ressourcenschonende Industrie ist die Voraussetzung für eine nachhaltige Gesellschaft. Es bedarf unermesslicher Forschungs- und Entwicklungsanstrengungen, um diesem emissionsarmen, auf Recycling basierendem Wirtschaftssystem näher zu kommen. Ein solches System, wäre ein wichtiger Baustein zur Sicherung des Überlebens der menschlichen Spezies auf der Erde. Momentane Entwicklungs- und Optimierungsanstrengungen basieren hauptsächlich auf ökonomischen Überlegungen. Ohne sorgfältig überlegte und mutige politische Entscheidungen, wird das reine Streben nach wirtschaftlicher Effizienz auf lange Sicht nicht ausreichen um einen gesunden Planeten an die nächsten Generationen weiter zu geben.

Ausgehend von Experiment-getriebener Forschung mit Unterstützung von händischen Berechnungen, entwickelte sich die Forschung in den letzten Jahren zu einem integrierten Prozess, welcher Experimente und Modellierung verbindet. Dank der immer höheren Rechenleistungen, werden in der Forschung immer komplexere Berechnungen, Modellierungen oder Simulationen bis hin zu virtuellen Experimenten durchgeführt. Diese Experimente verwenden sorgfältig validierte Modelle, um die zugrunde liegenden Physik eines realen Problems zu untersuchen. Zu Beginn wurden nur kleine, akademische Probleme modelliert, während heutzutage räumlich aufgelöste Berechnungen von industriellen Prozessen in der Entwicklung und Optimierung immer wichtiger werden.

Die numerische Strömungsmechanik (*CFD*) hat unter Beweis gestellt, dass sie ein wichtiges Werkzeug für die Unterstützung bei der Erforschung und Entwicklung von industriellen Prozessen ist. Die Simulation von großtechnischen Prozessen beruht zum Teil auf Modellen, da es derzeit selbst auf den größten Großrechnern noch nicht möglich ist, alle notwendigen Größen- und Zeitskalen aufzulösen. Im Endeffekt benötigen aber alle Modelle Eingabeparameter, welche üblicherweise durch Experimente bestimmt werden. Deshalb können selbst die besten Modelle keine physikalisch richtigen Ergebnisse liefern, wenn die Eingabeparameter von falschen oder unpassenden Experimenten stammen.

Der Hochofenprozess, die wesentliche Roheisenproduktionsmethode, wird seit Jahrhunderten kontinuierlich verbessert. Momentan wird versucht, die Effizienz des Hochofens durch Einblasen von Kohlenstoff- bzw. Energieträgern, sogenannte Alternative Reducing Agents (ARAs) in die Wirbelzone zu steigern. Das direkte Messen des thermo-chemischen Umwandlungsprozesses von ARAs ist technisch sehr aufwendig. Zusätzlich können Versuchsläufe am Hochofen schwerwiegende Betriebsstörungen auslösen. Die CFD Modellierung des ARA Injektionsprozesses ermöglicht es, potentielle neue, nachhaltige ARAs durch virtuelle Experimente zu bewerten. Dazu wird ein umfassendes Simulationsmodell benötigt, welches Mehrphasenströmungen sowie homo- und hete-rogene thermo-chemische Umwandlungsprozesse beherrschen muss. Die Qualität der chemischen Mechanismen und die verwendeten Kinetikparameter bestimmen die Vertrauenswürdigkeit der Simulationsergebnisse. Folglich müssen themo-chemische Umwandlungsraten neuer ARAs vor den Simulationen experimentell bestimmt werden.

Diese Arbeit beschreibt einen geeigneten Ablauf (Versuchsaufbau, Kinetikbestimmung) zur Bestimmung von thermo-chemischen Umsatzkinetiken von ARAs zu ermitteln. Dazu werden zuerst Referenzbedingungen der Wirbelzone definiert und nachfolgend vorhandene Versuchsaufbauten evaluiert. Ein digitaler Zwilling eines ausgewählten Versuchsaufbaus – Sandias Pressurized Entrained Flow Reactor ($PEFR$) – wird erstellt und, um detaillierte Informationen über die Bedingungen in der Reaktionszone zu erhalten, eine Versuchsreihe modelliert. Zusätzlich wird ein geeignetes Simulationsmodell für die ARA Umsetzung im open-source CFD Code OpenFOAM® entwickelt.

Zusammenfassend kann gesagt werden, dass vorhandene Versuchsaufbauten die benötigten Aufheizraten, welche nötig wären um die Bedingungen in der Wirbelzone zu simulieren, bei erhöhten Drücken nicht erreichen. Zusätzlich weisen die tatsächlichen Bedingungen signifikante räumliche Schwankungen auf und weichen stark vom Sollwert ab. Dies gilt insbesondere für die Temperatur. Da die meisten Methoden zur Bestimmung von kinetischen Parametern von räumlichen Variationen abhängen, ist detailliertes Wissen über diese von enormer Bedeutung. Der Umwandlungsprozess von ARAs hängt auch stark von der Gasphasenchemie ab, weshalb die umfassende Modellierung von chemischen Reaktionen in der Gasphase wichtig für die virtuellen Experimente ist. Im Hochofen verändert sich die Gasphasenchemie von mischungslimitiert in der Nähe der Windformen zu chemischlimitiert im Koksbett. Modelle für die Turbulenz-Chemie Interaktion, welche beide Verbrennungsregime abdecken, sind der Schlüssel zu verbesserten Simu-lationsergebnissen. Der Einfluss der reaktiven Koksphase auf die thermo-chemische Umwandlung von ARAs bedarf noch weiterer Untersuchungen.

Abstract

An efficient and resource-conserving industry is a prerequisite for a sustainable society. Tremendous research and development efforts are required to progress towards this low-emission, recycling-based economy which is necessary to ensure the survival of the human species on earth. Current industry developments and optimization are primarily for economic reasons. However, without deliberate and bold political decisions, the endeavor for economic efficiency alone will not be sufficient in the long term to pass over a healthy planet earth on to future generations.

Research and development has changed considerably in recent decades, from purely experiment-driven (with some calculations by hand) towards an integrated process combining experiments and modeling. Meanwhile, ever-increasing computational power enables using increasingly complex calculations, models, or simulations in contemporary research. This includes the establishment of virtual experiments, which use thoroughly validated models to reveal the underlying physics of a real-world problem. While modeling was first applied to small, academic problems, the spatially resolved modeling of industrial processes is now becoming progressively more important in development and optimization.

Computation Fluid Dynamics (*CFD*) has proven to be a vital tool for supporting the ongoing research and development of industrial processes. The simulation of industrial-scale processes relies on models, since resolving all size and time scales is still impossible even with today's high-performance computation centers. Ultimately, all models require input parameters, which are usually obtained from experiments. Therefore, even the most sophisticated model fails to provide physically-correct results if the input parameters come from faulty or inappropriate experiments.

The blast furnace process, which is the major pig iron production route, has been under continuous optimization for centuries. The current optimization measures focus on replacing coke by injecting carbon and energy carriers – Alternative Reducing Agents (ARAs) – into the raceway zone of the blast furnace. Directly measuring the thermo-chemical ARA conversion process is challenging and experimental trails at blast furnaces can cause severe operational problems.

Using CFD to model the ARA injection process enables virtual experiments to evaluate potential sustainable ARAs. A comprehensive modeling framework is required for these simulations, which needs to master multi-phase flow and homo- and heterogeneous thermo-chemical conversion processes. The quality of chemical kinetic conversion mechanisms and the employed kinetic parameters determine the reliability of the simulation results. Thus, thermo-chemical conversion rates for new ARAs must be determined experimentally prior to the virtual experiments.

The current work presented aims to identify a suitable work-flow (experimental setup, extraction procedure) to determine the thermo-chemical conversion kinetic of ARAs. To accomplish this, a screening of existing experimental equipment is carried out based on previously-defined reference raceway conditions. Furthermore, a digital twin of a selected experimental setup – Sandia's Pressurized Entrained Flow Reactor (*PEFR*) – is established and a set of experiments is modeled to obtain detailed information about the conversion conditions in the reactive zone. Furthermore, an accompanying modeling framework for the ARA conversion was developed based on the open-source CFD toolbox, OpenFOAM®. The emphasis of the implemented framework is its applicability to thermo-chemical conversion modeling.

Summarizing these activities indicates that currently available experimental equipment fails to achieve the required heating rates under elevated pressure to reproduce raceway conditions. Furthermore, the actual conditions in the reaction zone are subject to significant spatial variations and substantial deviations from the set point. This is particularly true for temperature. Extracting reliable kinetic parameters depends on a detailed knowledge of the spatial variations, since most extraction/fitting approaches are sensitive to them. The ARA conversion process is strongly affected by gas phase chemistry; thus, comprehensively modeling homogeneous chemistry is important for the virtual experiments. Gas phase chemistry changes from mixing dominated in the vicinity of the tuyeres to chemistry dominated towards the dense coke bed. Turbulence-chemistry interaction models capable of both combustion regimes are the key for improved modeling results. The influence of the reactive coke phase on the thermo-chemical conversion of the ARAs needs further investigation.

Acknowledgements

Contents

List of Appended Publications

Journal Publications

Journal Paper I

Suitability of pulverised coal testing facilities for blast furnace applications,
Markus Bösenhofer, Eva-Maria Wartha, Christian Jordan, Christoph Feilmayr, Hugo Stocker, Franz Hauzenberger, Johannes Rieger, Stefan Tjaden, Arleen Walk and Michael Harasek,
Ironmaking & Steelmaking **2020**, 47(5), pp. 574-585,

Journal Paper II

Computational fluid dynamics analysis of char conversion in Sandia's pressurized entrained flow reactor,
Markus Bösenhofer, Ethan Hecht, Christopher R. Shaddix, Bernhard König, Johannes Rieger and Michael Harasek,
Review of Scientific Instruments **2020**, 91, 074103,

Journal Paper III

The Eddy Dissipation Concept—Analysis of Different Fine Structure Treatments for Classical Combustion,
Markus Bösenhofer, Eva-Maria Wartha, Christian Jordan and Michael Harasek,
Energies **2018**, 11, 1902,

Journal Paper IV

Characteristic Chemical Time Scales for Reactive Flow Modeling,
Eva-Maria Wartha, Markus Bösenhofer and Michael Harasek,
Combustion Science and Technology **2020**, in press,

Reviewed Conference Publications

Reviewed Conference Paper I

Pulverized Coal Conversion in Blast Furnaces – Analysis of Involved Scales,
<u>Markus Bösenhofer</u>, Eva-Maria Wartha, Christian Jordan, Franz Hauzenberger, Christoph Feilmayr, Hugo Stocker, Johannes Rieger, Bernhard König and Michael Harasek

Reviewed Conference Paper II

The Relevance of Reaction Mechanisms in the CFD Modelling of Blast Furnaces,
<u>Markus Bösenhofer</u>, Michael Harasek, Christian Jordan, Christoph Feilmayr and Franz Hauzenberger,

Reviewed Conference Paper III

Characterization of gas phase reaction regime in the raceway zone,
<u>Markus Bösenhofer</u>, Eva-Maria Wartha, Christian Jordan, Michael Harasek, Christoph Feilmayr and Franz Hauzenberger,

Reviewed Conference Paper IV

A raceway model based on open-source software,
<u>Markus Bösenhofer</u>, Eva-Maria Wartha, Christian Jordan, Michael Harasek, Christoph Feilmayr, Franz Hauzenberger and Bernhard König,

Author's Contributions

Journal Publications

Journal Paper I

Markus Bösenhofer carried out the comparison and evaluation of the available PCI test rigs based on available literature. Furthermore, Markus Bösenhofer prepared and conducted the conceptual comparison of the different test rigs based on mechanistic models. In addition, Markus Bösenhofer planned and wrote the scientific paper.

Journal Paper II

Markus Bösenhofer created the three-dimensional CFD model of the investigated reactor and conducted all simulations. In addition, Markus Bösenhofer implemented the conversion model used for evaluating the char conversion experiments. Markus Bösenhofer also evaluated the simulation data and wrote the scientific paper.

Journal Paper III

Markus Bösenhofer performed the theoretical analysis, implemented all simulation models, and carried out the flame simulations. In addition, Markus Bösenhofer planned and carried out the theoretical evaluation using a simple test problem. Furthermore, Markus Bösenhofer did the data evaluation and wrote the scientific paper.

Journal Paper IV

Markus Bösenhofer implemented the simulation models used in this publication. Furthermore, Markus Bösenhofer carried out and interpreted the simplified test cases. In addition, Markus Bösenhofer planned the scientific publication, wrote significant parts of it, and contributed to portions of the theoretical discussion.

Reviewed Conference Publications

Reviewed Conference Paper I

Markus Bösenhofer created the proposed evaluation method for the solid-fuel conversion and developed its proof of concept. In addition, Markus Bösenhofer performed the data evaluation and interpretation. Moreover, Markus Bösenhofer planned and wrote the scientific paper.

Reviewed Conference Paper II

Markus Bösenhofer performed the literature review on available kinetic parameters and updated the existing global reaction mechanism for blast furnace conditions. Moreover, Markus Bösenhofer evaluated and validated both the original and updated mechanisms using experimental data from literature. In addition, Markus Bösenhofer performed the mechanism comparison for raceway conditions, planned, and wrote the scientific paper.

Reviewed Conference Paper III

Markus Bösenhofer implemented the computational models used for the simulations and carried out the simulations. Furthermore, Markus Bösenhofer performed the data evaluation and discussed the results in context with theory. In addition, Markus Bösenhofer planned and wrote the scientific paper.

Reviewed Conference Paper IV

Markus Bösenhofer implemented the computational models used for the simulations and carried out the simulations. Moreover, Markus Bösenhofer performed the model validation and carried out the whole data evaluation presented in this scientific paper. Furthermore, Markus Bösenhofer planned and wrote the scientific paper.

Other Scientific Publications of Relevance

Additional Publication I - Conference Paper

Multiphase Reactive Systems – Analysis Of Involved Time Scales,
<u>Markus Bösenhofer</u>, Eva-Maria Wartha, Christian Jordan, Bernhard König and Michael Harasek
Proceedings: 9th European Combustion Meeting (ECM) **2019**, 6 pages.

Additional Publication II - Conference Paper

Mesh Partitioning of Reactive Flow Simulations – Speed-up and Other Side Effects,
Eva-Maria Wartha, <u>Markus Bösenhofer</u>, Christian Jordan and Michael Harasek
Proceedings: 9th European Combustion Meeting (ECM) **2019**, 6 pages.

Additional Publication III - Reviewed Conference Paper

Computational Improvements for the Eddy Dissipation Concept by Operator Splitting and Tabulation,
Eva-Maria Wartha, <u>Markus Bösenhofer</u> and Michael Harasek
Proceedings: 28th European Symposium on Computer Aided Process Engineering **2018**, pp. 1687–1692, DOI:10.1016/B978-0-444-64235-6.50294-1.

Additional Publication IV - Conference Paper

Pulverized coal injection (PCI) test facilities and methods – Overview and recommendations,
<u>Markus Bösenhofer</u>, Christian Jordan, Michael Harasek, Christoph Feilmayr, Franz Hauzenberger, Arleen Walk and Stefan Tjaden
AISTech - Iron and Steel Technology Conference Proceedings **2018**, pp. 287-295.

Additional Publication V - Conference Paper

A Flame D modeling study employing Eddy Dissipation Concept modifications,
<u>Markus Bösenhofer</u>, Christian Jordan and Michael Harasek
Proceedings: 8th European Combustion Meeting (ECM) **2017**, 6 pages.

Additional Publication VI - Reviewed Journal Paper

Properties of Biomass and Biomass Waste Fuels for Fluidized Bed Conversion,
Markus Bösenhofer and Franz Winter,
Holistic Approach Environment **2017**, 7(2), pp. 103–111, DOI: 10.33765/thate.

Additional Publication VII - Reviewed Conference Paper

Investigation of Alternative Reducing Agent Conversion in the Raceway Cavity of Blast Furnaces by Numerical Simulation,
Michael Harasek, Christian Maier, Christian Jordan, Markus Bösenhofer and Christoph Feilmayr,
AISTech - Iron and Steel Technology Conference Proceedings **2016**, pp. 353–365.

Additional Publication VIII - Conference Paper

The Role of Fluidized Bed Technology for Waste to Energy, Its Current Status and Potential - An Austrian Perspective,
Markus Bösenhofer, Amon Purgar and Franz Winter
Proceedings: 22nd International Conference on Fluidized Bed Conversion **2015**, 7 pages.

Additional Publication XI - Conference Paper

Fluidized bed conversion of biomass and biomass waste in Austria,
Markus Bösenhofer and Franz Winter
Proceedings: 23rd European Biomass Conference & Exhibition (EUBCE 2015) **2015**, 5 pages.

Additional Publication X - Conference Paper

A parametric study on the sulfur species distribution within the cylinder of diesel engines,
Markus Bösenhofer and Franz Winter
Proceedings: 7th European Combustion Meeting (ECM) **2015**, 6 pages.

Chapter 1

Introduction

1.1 Motivation

The efficient utilization of raw materials is a prerequisite for a sustainable civilization. Efficiency enhancements can minimize potentially-harmful pollutants and resource exploitation, which are key priorities in developing a sustainable economy for humans [1, 2]. Thus, developing and optimizing new and existing processes for transforming and supplying energy and primary materials is a necessary component of the transition from the current economic system to a sustainable one. The iron and steel-making industry, as a major contributor to the world's energy and raw material consumption, also must also bear this burden [3–8].

Developing new and optimized equipment, alternative processes, and experimental work can consume considerable amounts of primary materials and energy. However, virtual prototyping can significantly reduce the environmental impact of product development and optimization processes. In the last two decades, Computation Fluid Dynamics (*CFD*) has developed from its academic application to a reliable engineering tool [9–11]. Its application ranges from simple flow field optimization to complex reactive multi-phase flows for biomass boiler [12, 13] or blast furnace optimization [14–16]. The validity of CFD results is highly sensitive to employed models for, e.g., turbulence, chemistry, or phase coupling [17–19]. Therefore, carefully selecting and validating the employed models for the specific process conditions under investigation is a key task for virtual prototyping in CFD. Doing so ensures, physically-correct simulation results. Simulation models can also be applied to obtain insights about processes where measurements are otherwise difficult, e.g, the raceway zone of blast furnaces or any other system involving high temperatures, elevated pressures, and limited optical access. In academia, CFD is often used to gain deeper insights into experiments and extract additional knowledge. The spatially-resolved information

about velocity, temperature, pressure, or species concentrations provide valuable information about the actual processes involved in the experimental apparatus, while the sensitivity analysis of process parameters discloses the underlying physics.

The blast furnace process is one of these complex reactive multi-phase flows modeled with CFD [20–24]. This counter-current process produces pig iron from iron ores via gaseous intermediates. Figure 1.1 illustrates the blast furnace iron making process. Burden and metallurgical coke are fed in layers from above, while hot blast is introduced through tuyeres at the bottom of the furnace. The hot blast oxidizes the available coke, which releases heat, carbon dioxide, and water vapor, and forms a cavity – the raceway – in the vicinity of the tuyeres. Carbon dioxide and water vapor are then reduced to carbon monoxide and hydrogen when entering the coke bed and fuming towards the top of the furnace. The downward-moving iron ores are reduced by the rising gas mixture, which consists mainly of nitrogen, carbon monoxide, and hydrogen. The resulting nitrogen-, carbon dioxide-, and water vapor-rich gas is discharged at the blast furnace top. The arising solid iron declines towards the tuyeres and starts to melt due to the high temperatures. Liquid iron accumulates below the tuyeres covered by a slag layer formed by the ingredients. The slag layer prevents re-oxidation of the liquid iron and is discharged with the pig iron from the blast furnace via tap holes.

The European Union (*EU*) classifies the high-quality coke coals required for metallurgical coke as a scarce and strategic resource [28–30]. Injecting Alternative Reducing Agents (ARAs) into the raceway zone of blast furnaces proved to reduce coke consumption and total carbon dioxide emissions [3–7, 7, 8, 31, 32]. To ensure a high coke replacement ratios of ARAs, thermo-chemical conversion must be completed in the oxygen-rich zone near the tuyeres. Otherwise, the pulverized particles may leave the blast furnace unreacted, which causes a low coke replacement ratio [6, 8, 31, 33–35]. Detailed knowledge of the thermo-chemical conversion processes is necessary to optimize the degree of ARA utilization. Pulverized Coal Injection (*PCI*) is probably the most common example for ARA utilization. Other, bio-based ARAs have also been investigated in available literature. However, various significantly different challenges have not been solved yet [7, 34, 36–39]. CFD modeling can be used to study the thermo-chemical conversion processes connected to different ARAs and provide useful information for their industrial application. The quality of these predictions depends on accurate knowledge about the thermo-chemical conversion kinetic of the investigated ARA. Figure 1.2 illustrates the ARA injection process into the raceway zone. Thermo-chemical conversion starts with a drying (neglected in Figure 1.2) and devolatilization phase, in which the solid releases small hydrocarbons and tars – volatiles.
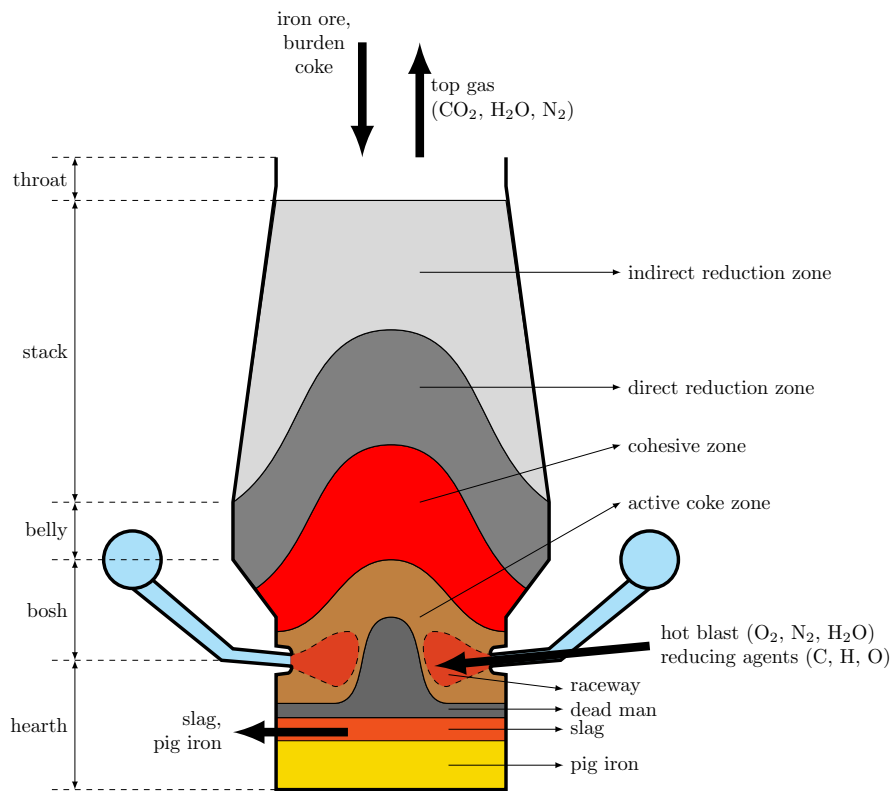
Fig. 1.1: Schematic illustration of the iron making process in the blast furnace; adapted from [25–27].

The released gaseous compounds are oxidized by the hot blast in the vicinity of the ARA surface. At the end of the devolatilization process, the remaining solid, carbon-rich matrix reacts with the hot blast's oxygen, releasing heat, carbon monoxide, and water vapor. Carbon monoxide is further oxidized to carbon dioxide in the gas phase. The solid matrix is also gasified by carbon dioxide and water vapor. These processes characterize the three ARA conversion steps [40, 41]:

- devolatilization zone,

- oxidation zone, and

- solution-loss reaction zone.

During an ideal injection process, ARAs consume the entire oxygen introduced by the hot blast and protect the coke from being oxidized. The subsequent carbon gasification reactions, which are moderate compared to oxidation, consume injection residues and portions of the metallurgical coke to produce carbon monoxide and hydrogen. The relocation of the intense oxidation reactions from the coke to the ARA is the key concern for reducing the coke consumption of blast furnaces.

High replacement ratios provide environmental and economic benefits, since low-quality coal or other carbon carriers are consumed instead of metallurgical coke [41].
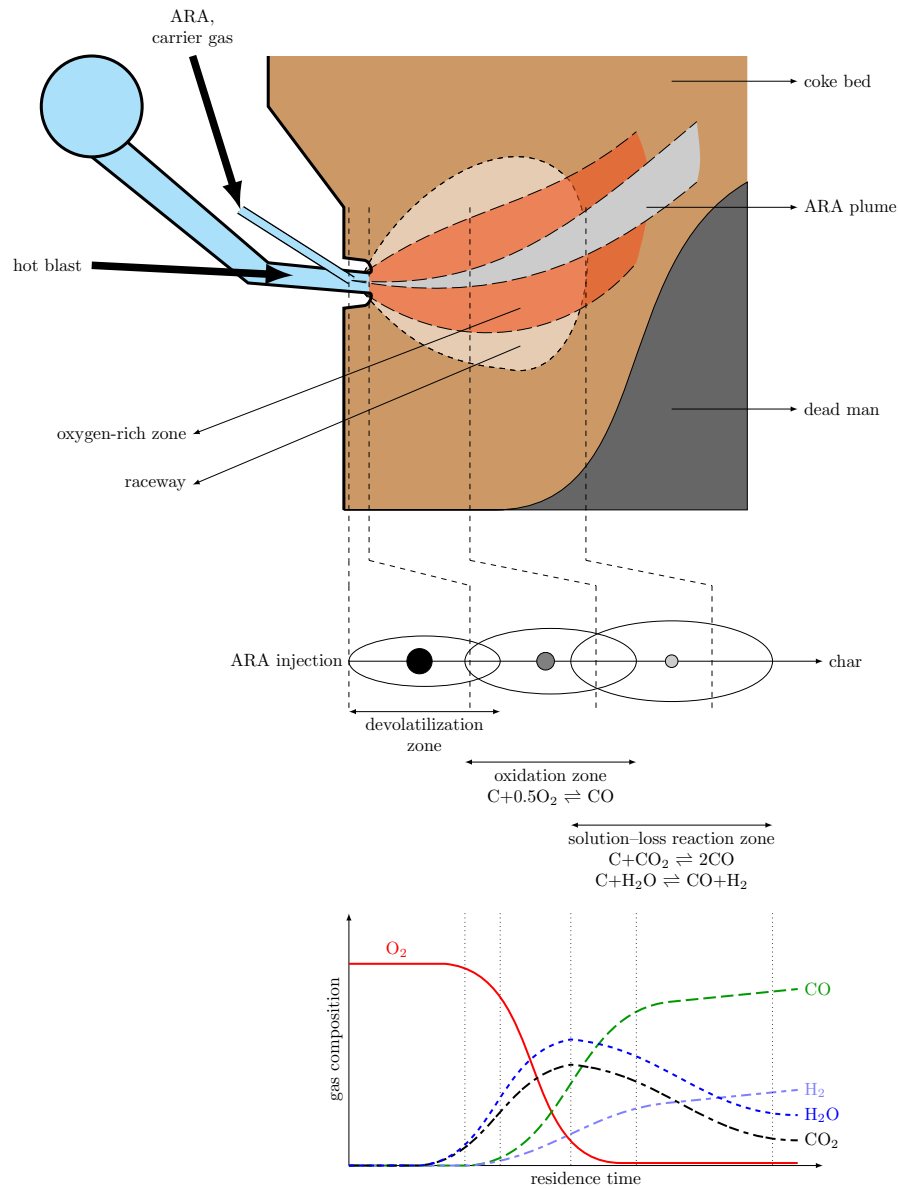
Fig. 1.2: Schematic illustration of the Alternative Reducing Agent (ARA) injection process into the raceway zone of blast furnaces; adapted from [40, 41].

Identifying suitable ARAs can be done by applying CFD analysis to the injection process. However, kinetic parameters for the simulations rely on experimental data obtained from lab-scale reactors. These experiments have to reproduce temperature, pressure, and species concentration ranges of interest. Typical kinetic fitting methods assume uniform temperature and species concentration distributions, as well as plug flow due to the lack of spatially- resolved measurements. Moreover, suitable kinetic parameters for multiple gas and gas-solid reactions are required for

reliable predictions, since heterogeneous reactions significantly depend on the homogeneous gas phase reactions.

1.2 Review State-of-the-Art Blast Furnace Modeling

Investigating complex multi-physics processes via CFD provides additional insights and enables digital optimization. Various blast furnace models can be classified by their purpose and scope, as demonstrated in previous literature. Beside full furnace models, detailed models of specific furnace regions, e.g., raceway zone or shaft, exist [20–24]. The model scope ranges from a pure multi-phase flow that studies the flow characteristics of coke and burden [20, 21, 25, 26, 42–69] to reactive multi-phase flow models that consider the thermo-chemical conversion of carbon carriers and/or iron ore [14–16, 20, 22, 27, 70–110]. Models investigating gas-solid flow phenomena primarily use the Discrete Element Method (*DEM*) or Computation Fluid Dynamics-Discrete Element Method (*CFD-DEM*) approaches. By contrast, reactive multi-phase models typically use the Euler-Euler (*E-E*) approach for the bulk phases (blast, coke, burden, liquid iron, and/or slag) and the Euler-Lagrange (*E-L*) approach to model liquid or solid ARA injection [14, 77, 81, 83, 84, 92, 93]. The blast furnace models found in the literature are divided into three categories: Gas-solid flow models, detailed zone models, and full furnace models. A short review of the different categories is given below.

Gas-Solid Flow Models   Gas-solid flow models of full scale blast furnaces often use a continuous phase assumption, employing the E-E approach, since the numerical effort for discrete particle simulations is excessively costly [25, 26, 45]. These models use the Kinetic Theory of Granular Flow (*KTGF*) [111–113] or the granular pressure model [114] to model the rheology of continuous solid phases. Recent literature has proposed gas-solid flow models for the full blast furnace using DEM based approaches for the solid phases [44, 46–49, 68, 69]. The DEM-based models sometimes use down-scaled blast furnace geometries due to the high numerical effort that arises from discretely modeling individual particles, while the continuum-based models can handle real-scale geometries. The main objective of the full scale blast furnace models is to investigate solid flow patterns inside the furnace, e.g., dead man formation or coke and burden distribution.

Special gas-solid flow models exist to investigate the raceway formation [43, 50–53, 55, 63–66] and the furnace shaft [56–62]. Models for the latter focus on the solid burden distribution and fluid permeation of the cohesive zone and the direct and indirect reduction zone of the blast

furnace. The majority of these shaft models employ the CFD-DEM approach. The raceway formation models study the influences of the hot blast rate, tuyere diameter, or hot blast injection angle to identify optimal operation conditions. Most of the raceway formation models use the E-E approach. The models proposed by Hilton and Cleary [50], Miao et al. [52], Rabadan Santana et al. [63], and Feng et al. [66] use the CFD-DEM approach. Modeling the raceway shape and size in detail is essential, because of its role in the the operation efficiency of blast furnaces, e.g., the thermo-chemical conversion of ARAs.

Detailed Zone Models Detailed zone models focus on a specific blast furnace zone. These models achieve a high level of detail because of their focus on a small region of the furnace. Besides the multi-phase flow, they also consider comprehensive thermo-chemical conversion of the involved raw materials (phases). Detailed zone models exist for the shaft [27, 67, 80, 87–89, 91] and the raceway zone [14–16, 74–77, 82–84, 88, 92–105, 107, 108].

The detailed shaft models focus on predicting the cohesive zone [27, 80, 87, 88, 91]. Modeling the burden distribution and the iron ore reduction in detail is important for achieving a reasonable prediction of the cohesive zone. CFD-DEM [88, 91] and E-E [27, 80, 87] shaft models have been presented in literature. Despite different modeling approaches, these models all take a single fluid (blast) and a single solid (coke and iron ores) phase into account. Coke and iron ores are distinguished by their properties in the solid phase. Most of the shaft models neglect liquid iron and slag phases. One possible explanation is the increased numerical effort and the additional modeling difficulties caused by additional phases and their interaction.

The detailed raceway zone models focus on the thermo-chemical conversion of ARAs and the metallurgical coke. Their aim is to optimize the ARA injection process to achieve high coke replacement ratios. Some models are capable of simultaneously modeling the raceway formation and ARA conversion [14, 83, 95], while others focus on the ARA conversion and assume a static raceway size and shape [16, 77, 92, 96, 101, 102]. Most raceway models use an E-E Two-Fluid Model (*TFM*) approach, which assumes the blast (gas) and coke (solid) phase as a continuum. ARA phases are typically modeled as Lagrangian phases. The models presented by Peters et al. [88] and Cui et al. [95] use a DEM approach for the solid phase. Moreover, the Peters et al. model incorporates a Multi-Fluid Model (*MFM*) approach to model the blast, liquid iron, and slag phases in addition to the discrete coke/burden phase.

Full Blast Furnace Models   Full scale blast furnace models use the MFM approach to describe the flow and interaction of the major phases, e.g., gas, coke/burden, liquid, fines [42, 70–75, 79, 81, 82, 86, 106, 109, 110]. Full scale models based on the DEM are rare in literature, but the models developed by Hou et al. [106] and Peters et al. [88] can be considered as full scale CFD-DEM models. Because of the numerical effort required for the complex MFMs, the pure Eulerian models rely on coarse, two-dimensional computational grids of real scale geometries. The model developed by Zhou et al. [85] couples detailed sub-models for the different furnace regions through an iterative procedure, thereby splitting the numerical effort and enabling detailed blast furnace investigations [85]. This kind of model can study blast furnace efficiency and operational changes caused by feedstock variation.

To summarize, the short model review first shows how models at different levels of detail have been presented in the literature. Recent models [14, 22, 24, 82, 85, 88, 110] can predict the key features of modern blast furnaces, e.g., the detailed thermo-chemical conversion of ARAs, properties of the cohesive zone, and the detailed interaction of gas-solid flows. CFD-DEM approaches are appearing more frequently in blast furnace modeling, while MFMs are very common due to their favorable numerical properties. Most of these models share a dependence on commercial software tools or proprietary, closed-source codes.

The detailed raceway zone model developed in this work is based on the model proposed by Maier et al. [102, 103, 104]. They developed a raceway model based on a dual-grid approach in ANSYS® Fluent® v6. The dual-grid approach solves the conservation equations for the blast and coke phase on a separate computational grid. Phase fraction effects are incorporated by using the Fluent® porous media model, with the second phase being a vacuum to avoid non-physical effects. Phase fractions must be predefined in the dual-grid model. User-defined functions introduce the phase coupling terms between the blast and coke phase equations. Steady-state results are obtained using the Semi-Implicit Method for Pressure Linked Equations (*SIMPLE*) algorithm, which solves each grid region sequentially. This simple approach differs from E-E models and only allows steady-state simulations. Detailed information about the dual-grid model can be found elsewhere [102–104, 115].

1.3 Objectives

Kinetic data for the thermo-chemical conversion of coke, ARA, iron ore reduction, and gas phase processes are all critical to reasonably predicting blast furnace processes. In addition to temperature, pressure, and gas composition, kinetic data for heterogeneous reactions depends on micro- and macroscopic solid properties [116–118]. Kinetic parameters from the literature, which usually have limited areas of application, are typically employed in CFD simulations [119]. Studying the ARA conversion process in the raceway zone requires a reasonable rate description of the thermo-chemical conversion processes occurring at the corresponding conditions. Consequently, the ambient conditions within the raceway zone must be reproduced by the experimental setup used for determining the conversion rates of ARAs. Table 1.1 summarizes representative blast furnace conversion conditions.

Literature on kinetic parameters for these conditions is sparse [119]. Furthermore, it is unclear if currently-used test equipment can reproduce blast furnace conditions and is suitable for identifying gas-solid kinetic parameters for raceway zone simulations. Therefore, the first objective of this thesis is to investigate the reliability of experimentally-determined gas-solid kinetic parameters. This includes identifying suitable test equipment for blast furnace conditions and assessing the reliability of the extracted kinetic parameters. The underlying assumptions for identifying kinetic parameters, e.g., idealized temperature, species, and velocity profiles, are investigated by detailed CFD modeling.

Tab. 1.1: Generic conversion conditions for Alternative Reducing Agent (ARA) in the raceway zone of blast furnaces [36]**Journal Paper I**.

temperature range	heating rates	pressure	hot blast velocity	particle velocity	flow type	residence time
1200 - 2500 °C	10^4 - 10^6 K/s	2 - 5 bar	≈200 m/s	≈20 m/s	turbulent	20 - 30 ms

The second objective is to develop a suitable, generic modeling framework for simulating industrial-scale applications. The generic framework needs to incorporate multiple Eulerian and Lagrangian phases as well as the thermo-chemical conversion of gaseous and solid raw materials. Unlike the model developed by [102–104, 115], the new modeling framework is based on the open-source CFD framework, OpenFOAM® [120]. Additionally, the dual-grid approach will be replaced by a generic E-E MFM model approach to facilitate future model extensions. The main purpose of the model re-implementation is to model homogeneous and heterogeneous combustion

and conversion processes. The new model framework will be thoroughly validated to ensure physically correct results and trends.

The following research questions will be answered in this thesis:

- Which experimental equipment is suitable to measure reaction kinetics under blast furnace conditions?

- Which kinetic extraction approaches give reliable results under blast furnace conditions?

- What are suitable methods for the CFD modeling of multi-phase reactive systems that incorporate homogeneous and heterogeneous reactions?

- What does a generic modeling framework for reactive multi-phase flows look like?

These research questions are partially answered in the attached publications. The remainder will be answered in this thesis. An extensive theory part (chapter 2) explains the complexity of the modeling work, and follows the executive summary of the attached publications (section 1.4) Next, the thesis demonstrates a Race Way Model (*RWM*) description and validation (chapter 3). Finally, chapter 4 summarizes and discusses the findings, while the conclusions and outlook are described in chapter 5.

1.4 Paper Summary

The enclosed scientific papers can be linked to either of the two objectives outlined in the previous section. **Journal Paper I**, **Journal Paper II**, and **Reviewed Conference Paper I** connect to the first objective: the reliable identification of kinetic parameters in solid fuel conversion. **Journal Paper III**, **Journal Paper IV**, **Reviewed Conference Paper II**, **Reviewed Conference Paper III**, and **Reviewed Conference Paper IV** complement the modeling framework for multi-phase reactive flows.

1.4.1 Journal Paper Summary

1.4.1.1 Journal Paper I

This work provides a review of existing lab-scale equipment for determining coal conversion rates. It summarizes typical ranges in the operation conditions and links them to typical conversion conditions in the raceway zone of blast furnaces. The influence of the different operation parameters, e.g., temperature, pressure, or relative velocity, on the conversion rates is discussed, followed by an evaluation of their influence on coal conversion rates. The review showed that none of the currently-used test reactors agree with generic blast furnace conditions, except for some specially designed drop-tube or flow reactors. Finally, critical process parameters to ensure blast furnace conditions were discussed and identified based on the mechanistic coal conversion models.

1.4.1.2 Journal Paper II

In this paper, Sandia's Pressurized Entrained Flow Reactor (*PEFR*) is modeled to investigate the properties of the reaction zone. The work includes a three-dimensional CFD simulation of the reactor used for two different experiments. Steady-state temperature, velocity, and species concentrations are compared to the typically-presumed plug flow and uniform temperature and concentration profiles. The results indicate species and temperature stratification in radial direction within the vicinity of the coal injection point. The flow field reveals a vortex ring next to the injection point due to the arrangement of the co-flow and installations. Tracking tracer particles along the steady-state velocity distribution yields a residence time that deviates from the residence time for the plug flow assumption. The non-uniform temperature distribution also shows a significant effect on the solid burnout. Detailed knowledge of the reaction zone is

necessary to obtain reliable kinetic parameters, since an error of approximately 10% is introduced by the kinetic parameters, assuming homogeneous temperature and plug flow velocity.

1.4.1.3 Journal Paper III

Since its first publication, various modifications to the Eddy Dissipation Concept (*EDC*), a combustion model for turbulent reactive flows, have been proposed in literature. This paper summarizes and discusses these modifications. In recent years, these modifications focus on Moderate or Intense Low-oxygen Dilution (*MILD*) combustion. Detailed chemistry is incorporated by solving a Perfectly Stirred Reactor (*PSR*) to steady-state, which is numerically expensive. Available literature uses the Plug Flow Reactor (*PFR*) approach instead of the PSR extensively to reduce the numerical effort. Previous literature has not thoroughly discussed the consequences of this simplification; therefore, they are discussed in detail by this paper, based on simple test problems and Sandia Flame D. The results showed that both approaches differ significantly for certain conditions in the test case. The flame simulations showed minor differences for the main species between the PSR and PFR approach. Differences of up to 10% arise for fast or intermediate species. The results suggest that both approaches are suitable for engineering applications.

1.4.1.4 Journal Paper IV

Modifications to the EDC for MILD combustion incorporate chemical time scales for the local adaption of the model constants. Various chemical time scale definitions have been proposed in literature. This work evaluates different chemical time scale definitions and compares them to analytic results from a simple test case using a single reaction. Subsequently, a complex mechanism is used to determine the chemical time scales for the same test case. Selected time scale definitions are then employed to calculate a MILD flame using the modified EDC model to evaluate their effect on the simulation results. The simple test cases reveal two distinct groups of time scale definitions: The first group is based on eigenvalues and represents the response time to system changes, while the second group consists of algebraic definitions that depict the time scale of the ongoing process. The flame simulations showed reasonable agreement with experimental results independent of the employed chemical time scale definition. However, a significant correlation between the chemical time scale and the complexity of the chemical mechanism was observed. Based on these results, a single surrogate reaction should be used for

the chemical time scale in CFD simulations to ensure the numerical efficiency and comparability of the results.

1.4.2 Reviewed Conference Paper Summary

1.4.2.1 Reviewed Conference Paper I

This paper investigates the thermo-chemical pulverized coal conversion in detail, based on simulation results. The process analysis concept is introduced by a simplified example and relies on the internal and external second Damköhler and Pyrolysis number. An alternative method proposed in this work uses the characteristic time scales for internal and external mass transfer and chemistry. Both approaches give comparable results. The analysis of the coal conversion process shows pore diffusion (internal mass transfer) limited conversion process in the vicinity of the tuyere, which eventually switches to boundary layer diffusion (external mass transfer) limited conversion towards the dense coke bed. The evaluation of different particle sizes showed that the residence time for smaller particles is lower than for larger particles and that larger particles turn to boundary layer-limited conversion earlier.

1.4.2.2 Reviewed Conference Paper II

This work investigates the influence of reaction mechanisms on the simulation results from gas-phase combustion at blast furnace conditions. An existing global reaction mechanism and its updated version are evaluated using experiments from literature and typical raceway conditions. The mechanism update is discussed in detail, including a review of published reaction parameters. The updated mechanism showed good agreement with experimental data. Two comprehensive mechanisms failed to predict reasonable results for certain conditions and, therefore, should not be used as a reference for these conditions. The results from the raceway test cases revealed significant differences in the characteristics of the original and updated global mechanism.

1.4.2.3 Reviewed Conference Paper III

The gas phase combustion regime in the raceway zone is discussed in this work based on a simplified test case. It introduces the classification concept for gas-phase combustion and is followed by the governing equations of the model. Gas phase combustion regimes depend on the characteristic turbulence and chemistry time scales. Since there is no uniquely-defined characteristic time scale, different definitions are introduced and later used to evaluate the

combustion regime in the raceway zone. The simulation results from the simplified test case indicate the existence of a chemical raceway border near the physical raceway border. The characterization of the combustion regime is sensitive to the chemical time scale definition. However, for all time scale definitions, chemical controlled gas phase combustion occurs in the vicinity of the tuyere and changes to mixing controlled combustion in the dense coke bed.

1.4.2.4 Reviewed Conference Paper IV

This publication evaluates the capabilities of the blast furnace model to predict the raceway size. The governing equations and the employed models are introduced and discussed, which are followed by the simulation of a two dimensional lab-scale raceway formation experiment from the literature. Subsequently, a real-scale raceway formation is simulated, and the equivalent raceway size is compared to a correlation from the literature. The equivalent raceway diameter and pressure drop were compared with the experimental results. The simulated raceway size is comparable to the measured one from the 2D test case. However, the agreement between simulation and experiment depends on the selected porosity iso-surface, which defines the raceway border. The pressure drop in the 2D raceway is overestimated by a factor of two in the simulations compared to the experimental results. These differences are probably caused by the employed drag model. The experimental trends from the pressure drop are preserved in the simulations. Compared to correlations from the literature, the simulated real-scale equivalent raceway diameters are under-predicted.

Chapter 2

Theory

2.1 Homogeneous Gas Phase Combustion

2.1.1 Laminar and Turbulent Combustion Theory

Homogeneous combustion refers to as the fast reaction of gaseous species releasing significant amounts of energy. This process can be classified according to several features, e.g., flow (laminar or turbulent), mixture (premixed or non-premixed), or ignition (spark or self-ignition). In terms of modeling, laminar premixed flames are the simplest flame configuration, because the flame propagation is only a function of the combustion rate in the finite combustion zone [121, 122]. Figure 2.1 schematically depicts the flame front in premixed flames, where the pre-heating zone is located between the reaction zone and the unburnt mixture.

Laminar non-premixed flames are described by the diffusion of reactants towards the combustion zone and the combustion rate. The combustion rate is a function of the reactant concentrations and temperature [121]. Figure 2.2 schematically depicts the flame front in non-premixed flames. The diffusion zone, where fuel and oxidizer mix, envelops the reaction zone on both sides.

Turbulent premixed and non-premixed flames are similar to their laminar counterparts, except that turbulent velocity fluctuations interact with chemistry. Hence, turbulent diffusion (or turbulent mixing) affects the mixing of gas phase species, e.g., reactants and products. The random velocity fluctuations can extinguish turbulent flames locally. Modeling these effects requires reasonable predictions of turbulent flows and models for the turbulence-chemistry interaction.

Common dimensionless or characteristic numbers are involved in turbulent combustion. They characterize the flow conditions as well as the interaction between flow and chemistry, i.e., the reaction zone. The Reynolds number (Re) and the turbulent Reynolds number (Re_t) describe
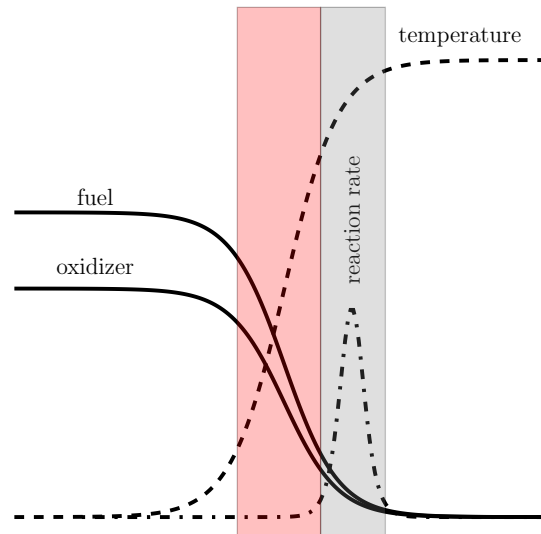
Fig. 2.1: Schematic flame front of a laminar premixed flame. Red zone is the preheat zone, gray is the reaction zone; adapted from [121–123].
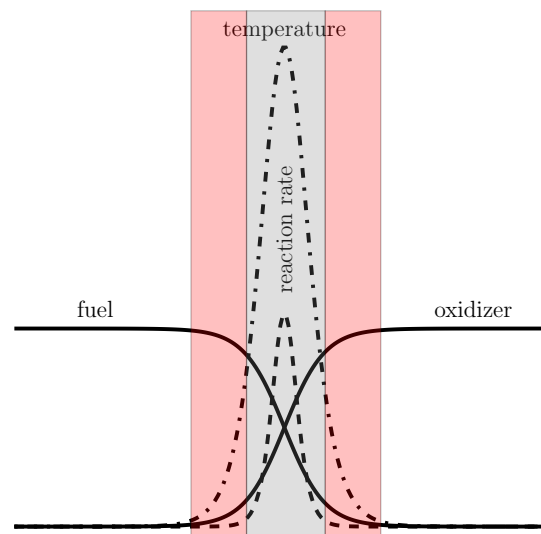
Fig. 2.2: Schematic flame front of a laminar non-premixed flame. Red zone is the diffusion zone; gray is the reaction zone; adapted from [121, 122, 124].

the intensity of the turbulence in turbulent flows [121, 122], where Re is a global measure for turbulence and Re_t is a local one. Both definitions are given below:

$$Re = \frac{\overline{u}L_c}{\nu} = \frac{\overline{u}L_c\rho}{\mu} \tag{2.1}$$

with:

$$\bar{u} = \text{mean velocity magnitude}$$
$$\nu = \text{kinematic viscosity}$$
$$L_c = \text{characteristic length}$$
$$\rho = \text{density}$$
$$\mu = \text{dynamic viscosity}$$

$$Re_t = \frac{u'l_t}{\nu} = \frac{\nu_t}{\nu} = \frac{k^2}{\epsilon\nu} \tag{2.2}$$

with:
$$u' = \text{turbulent velocity fluctuation magnitude}$$
$$l_t = \text{turbulence length scale}$$
$$\nu_t = \text{turbulent kinematic viscosity}$$
$$k = \text{turbulent kinetic energy}$$
$$\varepsilon = \text{turbulent dissipation rate}$$

The Re number compares inertial to viscous forces, while Re_t looks ate the relationship between local turbulent and kinematic viscosity. In combustion theory, the Damköhler number (Da) compares flow and chemical time scales, while the general definition of Da links the reaction rate and the convective mass transport rate [125, 126]. In the combustion field, Da is commonly referred to as the turbulent Damköhler number (Da_t), Da_t specifically defined as the ratio of the turbulent time scale (τ_t) and the chemical time scale (τ_c):

$$Da_t = \frac{\tau_t}{\tau_c} \tag{2.3}$$

The Kolmogorov scale Damköhler number (Da_η) is variation of the Da number, and is defined as the ratio of the Kolmogorov time scale (τ_η) and τ_c:

$$Da_\eta = \frac{\tau_\eta}{\tau_c} = \frac{1}{Ka} \tag{2.4}$$

with:
$$\tau_\eta = \text{Kolmogorov time scale}$$
$$Ka = \text{Karlovitz number}$$

The Karlovitz number (Ka) is the inverse of Da_η; both dimensionless numbers indicate if the smallest turbulence scales affect the reaction zone. In cases of low Da_η or high Ka values, turbulence thickens the flame front, while the reaction zone is thin and wrinkled for high Da_η or low Ka values [121, 122]. These dimensionless numbers can be expressed by various combinations of turbulence and reaction zone scales.

Because of the fundamental differences between premixed and non-premixed combustion, different classification schemes were proposed for each [121–124]. Both schemes define the combustion regime based on the ratio of the turbulent velocity fluctuation magnitude (u'), the characteristic combustion velocity, and the ratio of a characteristic turbulent length scale to a characteristic flame thickness. Combustion velocity and flame thickness are defined differently for premixed and non-premixed combustion.

Figure 2.3 shows a schematic premixed turbulent flame structure and the corresponding combustion regime map. Turbulence distorts and wrinkles the preheat and combustion zones and thickens them to the effective preheat zone thickness (δ_p) and reaction zone thickness (δ_r). The combined flame front is further thickened to the effective flame thickness (δ_f). The flamelet region (wrinkled and corrugated) is located at low-velocity ratios in the regime map, since the finest turbulence structures thicken the flame front at increasing velocity ratios.
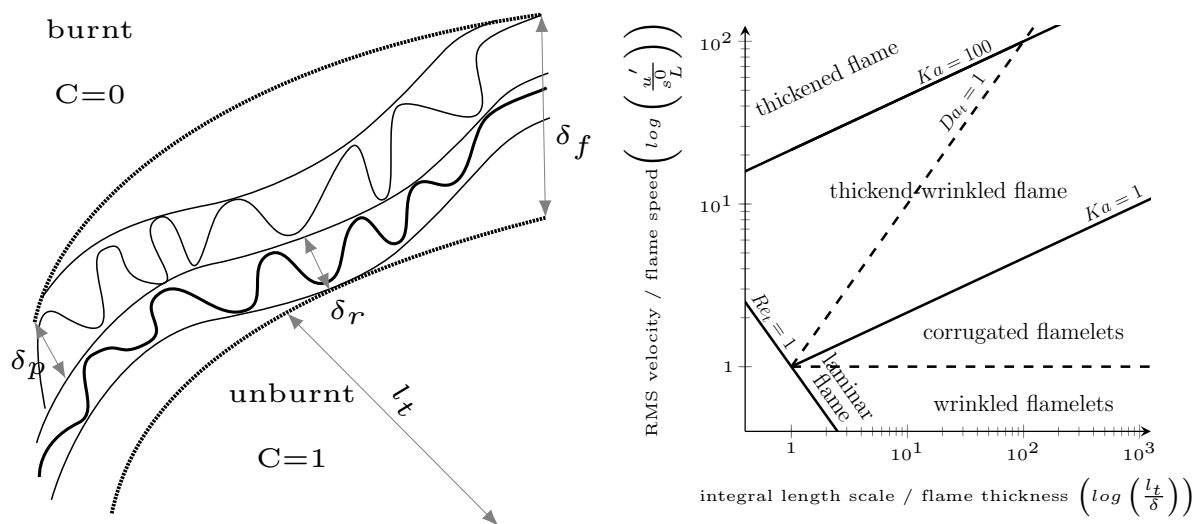
Fig. 2.3: Flame structure (left) and combustion regime diagram (right) for premixed combustion. Progress variable (C), turbulence length scale (l_t), effective flame thickness (δ_f), preheat zone thickness (δ_p), reaction zone thickness (δ_r), turbulent velocity fluctuation magnitude (u'), and laminar flame speed (s_L^0); adapted from [121–123].

Figure 2.4 shows a schematic flame structure and regime map for non-premixed combustion. Turbulence increases the effective mixing of reactants and products, since the smallest turbulence scale – the Kolmogorov length scale (η_k) – is of similar size as the flame structure. Like laminar non-premixed flames, a diffusion zone of size l_d surrounds the reaction zone. The actual effective flame thickness (δ_f) is equal to the reaction zone. Non-premixed turbulent flames show curvature and unsteady effects below a critical ratio of vortex length scale (l_r) and δ_f. Three distinct combustion regimes exist above this length scale threshold. The flamelet regime is located at

small ratios of the characteristic velocities. When the ratio exceeds a certain threshold (Da_{LFA}), unsteady effects occur in the flame structure. Quenching and local extinction occurs if Da_{Ext} is exceeded.
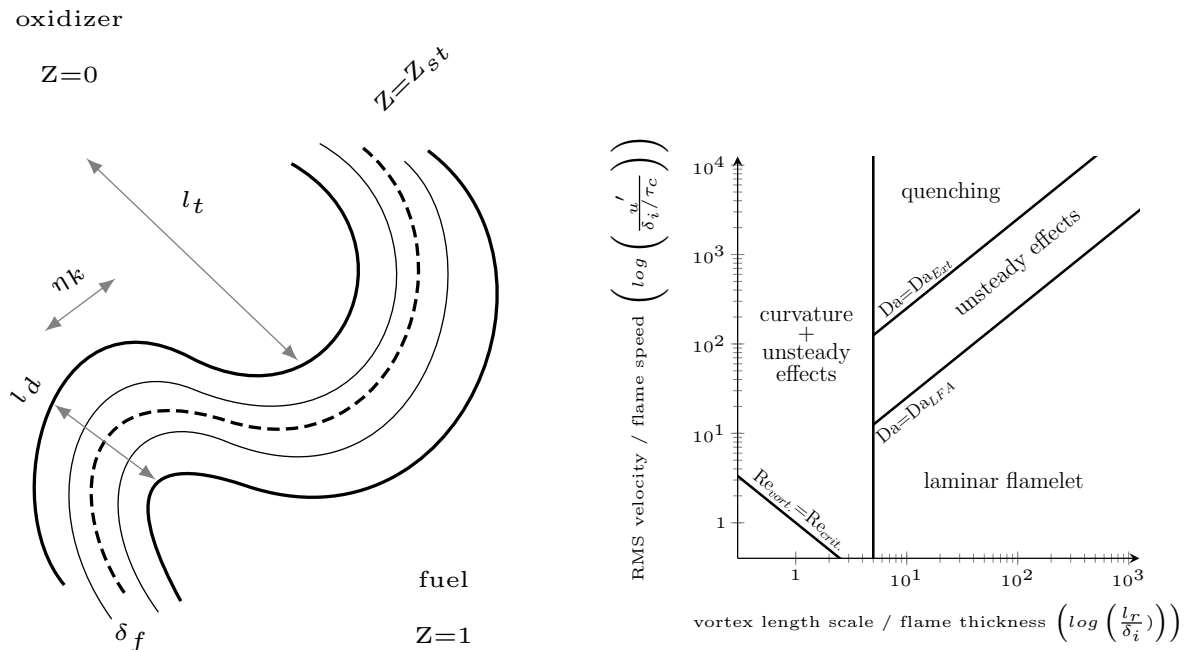
Fig. 2.4: Flame structure (left) and combustion regime diagram (right) for non-premixed combustion. Mixture fraction (Z), turbulence length scale (l_t), Kolmogorov length scale (η_k), diffusion zone thickness (l_d), effective flame thickness (δ_f), turbulent velocity fluctuation magnitude (u'), chemical time scale (τ_c), and vortex length scale (l_r); adapted from [121, 122, 124].

Available modeling approaches for turbulent-chemistry interaction are either based on geometrical analysis, turbulent mixing, or (one-point) statistical analysis [121, 122]. All three approaches attempt to express mean species consumption or production rates within turbulent flames. Geometrical models analyze the flame normal to the iso-surface of the progress variables, e.g., assuming dimensional laminar flames in the flamelet based models [127, 128]. Turbulent mixing models assume that chemistry is significantly faster than (turbulent) mixing. Thus, turbulent combustion is mixing-dominated. A well-known representative of this class is the Eddy Dissipation Concept (*EDC*) developed by Magnussen and Hjertager [129]. The statistical analyses uses Probability Density Functions (PDFs) to extract the mean values of scalar fields. If the progress variable or mixture fracture is the investigated scalar, the value and is subsequently linked to geometrical analysis [121, 122]. Veynante and Vervisch [122] showed that the different modeling approaches are connected to each other via the modeling of the mixing process.

Various turbulent combustion models based on these three approaches have been proposed in the literature. However, few can handle finite rate chemistry and the additional species and energy sources occurring in reactive multi-phase systems. Among others, certain types of flamelet-based models [130–135] and several mixing-based models, e.g. EDC [13, 129, 136–142] and the Partially-Stirred Reactor Model (*PaSR*) [143–148], are suitable models [113].

2.1.2 Flamelet Models

Flamelet-based models pre-process the detail chemistry and generate lookup tables based on characteristic reaction coordinates [121–123, 149, 150]. For efficiency reasons, multiple thermo-physical properties can be tabulated during the pre-processing step. The simplest reaction coordinates are the progress variable (C) and the mixture fraction (Z) for premixed and non-premixed combustion, respectively. The governing equations for premixed and non-premixed flamelets vary, since both flame types differ physically. Moreover, additional lookup parameters can be incorporated to account for different effects that occur during turbulent combustion.

2.1.2.1 Steady Laminar Flamelet Model

The Steady Laminar Flamelet Model (*SLFM*) is a common approach for modeling turbulent flames, where the models for premixed and non-premixed combustion differ slightly. The key assumption made by SLFM is of scale separation between chemistry and turbulence, which exists if the characteristic chemical time scale (τ_c) is significantly smaller than the Kolmogorov time scale (τ_η). In such cases, the flame consists of laminar flamelets [123], which can be pre-processed and mapped onto a lookup table based on suitable quantities or reaction coordinates.

Premixed Combustion   Premixed combustion uses a progress variable (C) as the mapping quantity for the lookup table. C must be defined so that a unique value exists for any point in the species composition space. Linear combinations of species mass fractions are typically used as progress variable [151]. The flamelet library is generated by solving the steady-state, unstretched one-dimensional premixed flame equations [127]:

$$\rho u \frac{\partial Y_i}{\partial x} = \frac{\partial}{\partial x}\left(\rho D_i \frac{\partial Y_i}{\partial x}\right) + \rho \dot{\omega}_i \tag{2.5}$$

$$\rho u \frac{\partial h}{\partial x} = \frac{\partial}{\partial x}\left(\rho \kappa_{th} \frac{\partial h}{\partial x}\right) + \rho \sum_{i=1}^{n} h_i \dot{\omega}_i \tag{2.6}$$

with:

Y_i = species mass fraction
D_i = species diffusivity
x_i = spatial coordinate(s)
$\dot{\omega}_i$ = species consumption/production rate
h = enthalpy
κ_{th} = thermal diffusivity
h_i = species enthalpy

The results are mapped to the progress variable at the end of the pre-processing to initialize the flamelet library.

An additional conservation equation must be solved during the flow calculations to track the evolution of the progress variable (C) [127]:

$$\frac{\partial(\rho C)}{\partial t} + \frac{\partial(\rho u_i C)}{\partial x_i} = \frac{\partial}{\partial x_i}\left(\rho \Gamma \frac{\partial C}{\partial x_i}\right) + \rho \dot{\omega}_C \tag{2.7}$$

with:

t = time
u_i = velocity vector
Γ = diffusivity
$\dot{\omega}_C$ = progress variable source term

Source terms for species, energy, and progress variable conservation equation are retrieved from the flamelet library as a function of C.

Non-Premixed Combustion In contrast to premixed combustion, the mapping quantity for non-premixed combustion is the mixture fraction (Z), since the flame front is located near the stoichiometric mixture fraction. Per definition Z is unity in the fuel stream and zero in the oxidizer stream. A common definition of Z for a system with two inlet streams is based on the atomic mass fraction of e.g. carbon [128]:

$$Z = \frac{Y_c - Y_{c,oxi}}{Y_{c,fuel} - Y_{c,oxi}} \tag{2.8}$$

with:

Z = mixture fraction
Y_{fuel} = fuel product mass fraction
Y_{oxi} = oxidizer product mass fraction

Coordinate-transformed equations can be derived from the one-dimensional SLFM species and enthalpy equations for non-premixed combustion [123]:

$$\rho \frac{\partial Y_i}{\partial t} - \frac{1}{2}\rho \dot{\chi} \frac{\partial^2 Y_i}{\partial Z^2} - \rho \dot{\omega}_i = 0 \tag{2.9}$$

$$\dot{\chi} = 2\Gamma \left(\frac{\partial Z}{\partial y} \right)^2 \tag{2.10}$$

$$\rho \frac{\partial T}{\partial t} - \frac{1}{2}\rho \dot{\chi} \left(\frac{\partial^2 T}{\partial Z^2} + \frac{1}{c_p} \frac{\partial c_p}{\partial Z} \frac{\partial T}{\partial Z} \right) + \frac{\rho}{c_p} \sum_{i=1}^{n} h_i \dot{\omega}_i = 0 \tag{2.11}$$

with:
$\dot{\chi}$ = scalar dissipation rate
T = temperature
c_p = (mixture) specific heat

The time derivative is disregarded for the SLFM, since laminar flamelets are assumed to be in a steady-state. Like the premixed approach, an additional transport equation for the conservation of Z must be solved to track its evolution:

$$\rho \frac{\partial Z}{\partial t} + \rho u_i \frac{\partial Z}{\partial x_i} = \frac{\partial}{\partial x_i} \left(\rho \Gamma \frac{\partial Z}{\partial x_i} \right) + \rho \dot{\omega}_Z \tag{2.12}$$

with:
$\dot{\omega}_Z$ = mixture fraction source term

A major disadvantage of the SLFM for non-premixed combustion is that the mapping between coordinate-transformed equations back to physical space is not unique [152].

2.1.3 Flamelet Progress Variable Approach

The Flamelet/Progress Variable Model ($FPVM$) developed by Pierce and Moin [152] introduces a progress variable (C) as a second mapping quantity to the mixture fraction (Z) for non-premixed combustion. This second mapping quantity ensures the correct lookup of the chemical state. Figure 2.5 illustrates the SLFM mapping problem and the improvements made by the FPVM. The unstable flamelet branch is included in the lookup tables by introducing the progress variable. The flamelet library is created by using equations (2.9) and (2.11), but the solutions are mapped to Z and C. The progress variable is extracted from the flamelets for the mapping.

A common shortcoming of the SLFM and the FPVM is that they ignore flame quenching or cooling effects due to heat losses to the surroundings [149].
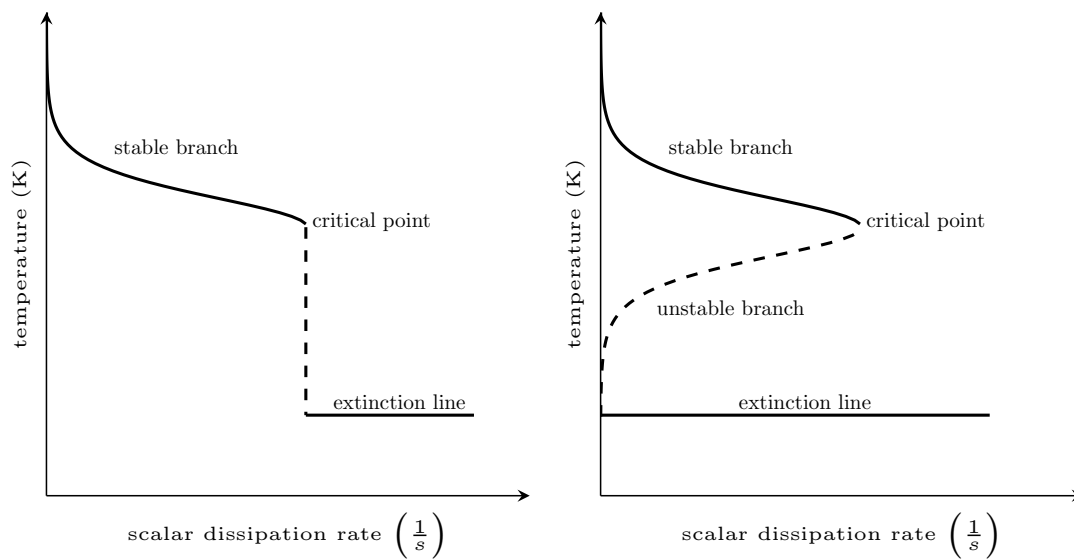
Fig. 2.5: Comparison Steady Laminar Flamelet Model (*SLFM*) (left) and Flamelet/Progress Variable Model (*FPVM*) (right) temperature lookup table; adapted from [152].

2.1.3.1 Flamelet Generated Manifold and Flame Prolongation of ILDM

Gicquel et al. [150] and van Oijen and de Goey [149] combine the flamelet approach and Intrinsic Low-Dimensional Manifolds (*ILDM*) [153] and proposed the Flame Prolongation of Intrinsic Low-Dimensional Manifolds (*FPI*) and the Flamelet Generated Manifold (*FGM*) models.

The FPI uses the one-dimensional ILDM for the high-temperature region and the one-dimensional laminar premixed flame for the low-temperature region. Differential diffusion effects are directly considered when generating the lookup tables adding additional reaction coordinates. These additional lookup parameters can be the element mass fraction of carbon, hydrogen, and/or oxygen.

The FGM, in contrast, directly creates manifolds from one-dimensional flame calculations, which reduces the number of progress variables to describe combustion more accurately. The enthalpy is added as a coordinate to the progress variable to account for cooling effects.

2.1.3.2 Multi-phase Flamelet Model

Among others, Rieth et al. [130, 131, 154], Watanabe and Yamamoto [132], Watanabe et al. [133], and Wen et al. [134, 135] propose flamelet-based models for pulverized coal combustion. These approaches are all based on the FPVM and define mixture fractions for moisture (m), volatiles (v), and char (c) in the gas phase as:

$$Z_i = \frac{m_i}{m_o + m_m + m_v + m_c} \tag{2.13}$$

with:

m_o = oxidizer mass
m_m = moisture mass
m_v = volatile mass
m_c = char mass

The sum over Z_i defines the mixture fraction (Z). To avoid multi-dimensional flamelet equations, two additional variables parameterize the flamelet tables, e.g., the ratios of Z_c to Z_v and Z_v to Z_m These ratios are denoted by $Z_{i,j}$ [132, 133]. Thus, the mixture fraction (Z), a progress variable (C), coordinates for the product ratios $Y_{i,j}$ (Equation 2.14), and the gas phase enthalpy (h_g) parameterize the flamelet library. Mapping h_g is necessary due to high heat transfer rates between coal and gas [130–135].

$$Z_{i,j} = \frac{Z_i}{Z_j} \tag{2.14}$$

with:

$Z_{i,j}$ = mixture fraction ratio

Separate conservation equations are solved for the lookup coordinates (except for $Z_{i,j}$):

$$\frac{\partial}{\partial t}\rho Z_j + \frac{\partial (\rho u_i Z_j)}{\partial x_i} = \frac{\partial}{\partial x_i}\left(\rho \Gamma \frac{\partial Z_j}{\partial x_i}\right) + \rho \dot{\omega}_j \tag{2.15}$$

$$\frac{\partial}{\partial t}\rho C + \frac{\partial (\rho u_i C)}{\partial x_i} = \frac{\partial}{\partial x_i}\left(\rho \Gamma \frac{\partial C}{\partial x_i}\right) + \rho \dot{\omega}_C \tag{2.16}$$

$$\frac{\partial}{\partial t}\rho h_g + \frac{\partial (\rho u_i h_g)}{\partial x_i} = \frac{\partial}{\partial x_i}\left(\rho \Gamma \frac{\partial h_g}{\partial x_i}\right) + \rho \dot{\omega}_h \tag{2.17}$$

with:

$\dot{\omega}_h$ = enthalpy source term

Current research activities focus on correctly capturing heat transfer and the ignition process in flamelet-based coal combustion models. Rieth et al. [130, 131] suggest using two lookup tables, where one is created from adiabatic non-premixed flamelets and the second is created from non-adiabatic non-premixed flamelets. If the enthalpy (h_p) undershoots the values of the adiabatic table, the non-adiabatic table is used for the lookup. Watanabe and Yamamoto [132] propose using the unsteady flamelet model for pulverized coal combustion to improve ignition

process predictions. Wen et al. [134, 135] propose a multi-regime flamelet model, since pulverized coal combustion features premixed, partially premixed, and non-premixed zones. A local flame index is calculated to determine the combustion regime and the premixed and non-premixed flamelets are weighted by this index to retrieve the solution inside the flame. The non-premixed flamelet table is used outside the flame.

Although flamelet-based coal combustion models might be more efficient than directly integrated chemistry models, the flamelet generation and lookup becomes inefficient if the number of fuel streams increases [134]. Increasing the number of product ratio coordinates for each fuel stream and its constituents, or solving multi-dimensional flamelet equations while keeping the product ratio coordinates for each stream, would allow for multiple solid fuel streams, e.g., coke, coal, and plastics [132–135].

2.1.4 Turbulent Mixing Models

Turbulent mixing controls the combustion process if the turbulent Damköhler number (Da_t) $\gg$ 1, since chemistry is significantly faster than the mixing [121, 122]. Educt species mix on a molecular scale in the finest turbulent structures, which affects finite-rate chemistry [122, 155, 156]. Turbulent mixing models rely on the proper prediction of the mixing process. Mixing models are commonly expressed by scalar dissipation rates [121, 122, 157]. Common turbulent combustion models based on the mixing approach are the EDC [129, 136–139, 158, 159] and the PaSR [143–148]. Both solve finite-rate chemistry for given initial conditions of species concentrations, temperature, and pressure. The independence of pre-calculated data enables them to handle reactive multi-phase systems.

2.1.4.1 Eddy Dissipation Concept

During the 1970s, Magnussen and Hjertager gradually developed the EDC [129, 136–138]. The EDC's core assumption is that reactions only occur in regions where reactants mix on a molecular scale. These regions are called (Reacting) Fine Structures (*FS*) and are believed to have vortex-sheet or tube-like shapes of Kolmogorov scale [137, 138, 160–162]. The fine structures exchange mass with the surrounding fluid via fine-scale turbulent fluid motion and molecular diffusion [147]. Figure 2.6 illustrates the FS based on the Tenneke's turbulence model [163].
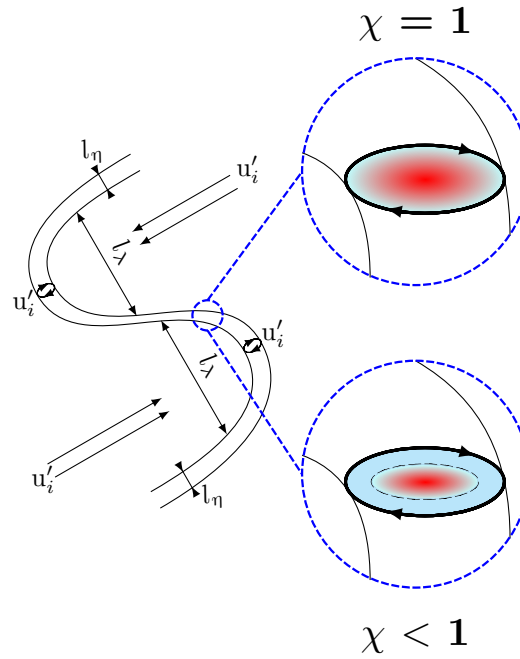
Fig. 2.6: Schematic illustration of the Fine Structures (*FS*) based on Tenneke's turbulence structure model; adapted from [163][**Journal Paper III**]. With the symbols velocity fluctuation vector (u_i'), Taylor length scale (l_λ), Kolmogorov length scale (l_η), and reacting fine structure share (χ).

Fine structure share (γ^*) and fine structure residence time (τ^*) were derived by a turbulent energy cascade, which has been proven to fit experimental data from turbulent combustion by Ertesvåg and Magnussen [158]:

$$\gamma^* = \gamma_L^3 = \left(\frac{3C_{D2}}{4C_{D1}^2}\right)^{3/4} \left(\frac{v\varepsilon}{k^2}\right)^{3/4} = C_\gamma^3 Re_T^{-3/4} \tag{2.18}$$

$$\gamma_L = \left(\frac{3C_{D2}}{4C_{D1}^2}\right)^{1/4} \left(\frac{v\varepsilon}{k^2}\right)^{1/4} = C_\gamma Re_T^{-1/4} \tag{2.19}$$

$$\tau^* = (\dot{m}^*)^{-1} = \left(\frac{C_{D2}}{3}\right)^{1/2} \left(\frac{v}{\varepsilon}\right)^{1/2} = C_\tau \left(\frac{v}{\varepsilon}\right)^{1/2} \tag{2.20}$$

with:

γ^* = fine structure share
γ_L = fine structure length scale
τ^* = fine structure residence time
C_{D1} = model constant (value = 0.135)
C_{D2} = model constant (value = 0.50)
C_γ = fine structure length scale constant
C_τ = fine structure residence time constant

The constants C_{D1} and C_{D2} originate from the energy cascade and were chosen to fit turbulent reactive flows [137, 158, 159].

In the original EDC development, Magnussen [137] proposed a fine structure species consumption/production rate (R_i^*) based on the mass transfer rate between FS and surroundings:

$$R_i^* = \frac{\rho^*}{\tau^*} \left(\frac{c_i^\circ}{\rho^\circ} - \frac{c_i^*}{\rho^*} \right) \qquad (2.21)$$

with:
R_i^* = fine structure species consumption/production rate
c_i^* = fine structure species concentration
ρ^* = fine structure density
c_i° = surrounding species concentration
ρ° = surrounding density

The superscript * denotes fine structure properties, while $^\circ$ and $^-$ subsequently denote surrounding and average properties. A simple relationship connects these quantities:

$$\overline{\Phi} = \Phi^\circ \left(1 - \gamma^* \chi \right) + \Phi^* \gamma^* \chi \qquad (2.22)$$

with:
χ = reacting fine structure share

According to Magnussen [137], the definition of the reacting fine structure share (χ) is:

$$\chi = \frac{Y_{\mathrm{pr}}/(1 + \Psi_{stoich})}{\gamma_\lambda \left(Y_{\mathrm{pr}}/(1 + \Psi_{stoich}) + Y_{\mathrm{fuel}} \right)} = \frac{1}{\gamma_\lambda} \chi' \qquad (2.23)$$

with:
Y_{pr} = product mass fraction
Ψ_{stoich} = stoichiometric fuel oxidizer ratio

Applying these relationships to the fine-structure mass transfer rate (2.21) yields an expression for the mean species consumption/production rate ($\overline{R}_i$):

$$\overline{R}_i = \frac{1}{\tau^*} \frac{\gamma^* \chi}{1 - \gamma^* \chi} \left(\frac{c_i^*}{\rho^*} - \frac{\overline{c}_i}{\overline{\rho}} \right) = \frac{1}{\tau^*} \frac{\gamma_L^2 \chi'}{1 - \gamma_L^2 \chi'} \left(\frac{c_i^*}{\rho^*} - \frac{\overline{c}_i}{\overline{\rho}} \right) \qquad (2.24)$$

with:
$\overline{c}_i$ = mean species concentration
$\overline{\rho}$ = mean density

Since its initial publication, several modifications and adaptions to the EDC have been proposed in the literature. For example, Ertesvåg [159], Lewandowski and Ertesvåg [162], Li et al. [164], and [**Journal Paper III**] discuss the evolution of the EDC over time in detail.

Magnussen [139] re-defined γ^* to follow the Tenneke's turbulence structure model [163] (tube-like) instead of Corrin's interpretation of the turbulent structure [165] (sheet-like):

$$\gamma^* = \gamma_L^2 = \left(\frac{3C_{D2}}{4C_{D1}^2}\right)^{2/4} \left(\frac{\nu\varepsilon}{k^2}\right)^{2/4} = C_\gamma^2 Re_{\mathrm{T}}^{-2/4} \tag{2.25}$$

In addition to the γ^* modifications, a new definition for χ has been proposed:

$$\chi = \frac{Y_{\mathrm{pr}}/(1 + \Psi_{stoich})}{(Y_{\mathrm{pr}}/(1 + \Psi_{stoich}) + min\left(Y_{\mathrm{oxi}}/\Psi_{stoich}, Y_{\mathrm{fuel}}\right))} \tag{2.26}$$

These changes result in an expression for $\overline{R}_i$ that differs by the factors χ and χ'.

$$\overline{R}_i = \frac{1}{\tau^*}\frac{\gamma^*\chi}{1 - \gamma^*\chi}\left(\frac{c_i^*}{\rho^*} - \frac{\overline{c}_i}{\overline{\rho}}\right) = \frac{1}{\tau^*}\frac{\gamma_L^2\chi}{1 - \gamma_L^2\chi}\left(\frac{c_i^*}{\rho^*} - \frac{\overline{c}_i}{\overline{\rho}}\right) \tag{2.27}$$

Gran and Magnussen [166] used a fixed value of unity for χ for simulations employing detailed chemistry. This assumption has been widely used in literature without challenging it, e.g., [12, 140, 164]. Two exceptions are Lewandowski and Ertesvåg [162], Lewandowski et al. [167], who showed that using the variable χ can improve the predicted temperature and concentration profiles in Moderate or Intense Low-oxygen Dilution (*MILD*) combustion.

Detailed chemistry is incorporated into the EDC by treating the FS as a Perfectly Stirred Reactor (*PSR*). The FS state is determined by advancing the PSR to steady-state and $\overline{R}_i$ is determined by the FS and mean composition space. Although the EDC theory enforces the PSR approach for the FS, the Plug Flow Reactor (*PFR*) approach is commonly used to reduce the numerical effort of the direct chemistry integration.

The PSR approach typically assumes an isobaric, adiabatic FS. The resulting conservation equations for the species, enthalpy, and pressure are given below:

$$\frac{dY_i^*}{dt} = \dot{\omega}_i^* + \frac{1}{\tau^*}\left(Y_i^\circ - Y_i^*\right) \tag{2.28}$$

$$\frac{dh}{dt} = 0 \tag{2.29}$$

$$\frac{dp}{dt} = 0 \tag{2.30}$$

with:

Y^* = fine structure species mass fraction
$\dot{\omega}_i^*$ = fine structure species consumption/production rate
Y° = surrounding species mass fraction
Y^* = fine structure species mass fraction
p = static pressure

The mixing term in the species conservation equations (Equation 2.28) couple the FS with the surroundings. The isobaric, adiabatic PFR neglects this mixing term for the species conservation equation, reducing the equation to:

$$\frac{dY_i}{dt} = \dot{\omega}_i^* \tag{2.31}$$

Lewandowski and Ertesvåg [162], Li et al. [164], and **Journal Paper III** investigated the effect of the fine structure treatment. While Lewandowski and Ertesvåg [162] and Li et al. [164] concluded that both give almost identical results, **Journal Paper III** showed that the FS state might significantly differ at certain γ^* and τ^* combinations.

Recent research efforts in the EDC field focus on applying model extension to MILD combustion conditions [168]. Regarding EDC, alternative definitions for the model constants have been proposed in literature [12, 13, 140–142, 159, 169], while Ertesvåg [159], Lewandowski and Ertesvåg [162], Lewandowski et al. [167] renew the notion of the reacting fine structure share (χ).

Model Constants Parente et al. [140], Bao [141], Evans et al. [142], and Bao et al. [169] proposed alternative definitions for the fine-structure scales. Since the smallest turbulent eddies thicken the reaction zone in MILD combustion, the turbulent flame speed can be interpreted as the characteristic fine structure velocity [121, 122, 140, 168]. This assumption allows for alternative definitions of the model constants C_γ and C_τ based on Re_t and Da_η. Parente et al. [140] propose the following expressions for the now local model constants:

$$C_\gamma = \left(\frac{3C_{D2}}{4C_{D1}^2}\right)^{\frac{1}{4}} \propto \sqrt{(Re_t + 1)\,Da_\eta} \qquad (2.32)$$

$$C_\tau = \left(\frac{C_{D2}}{3}\right)^{\frac{1}{2}} \propto \frac{1}{Da_\eta\sqrt{Re_t + 1}} \qquad (2.33)$$

Bao [141] and Bao et al. [169] adopt the concept by Parente et al. [140] and replace the turbulent flame speed with the ratio of the characteristic length and the chemical time scale, from which quantitative relationships for the model constants arise:

$$C_\gamma = \left(\frac{3C_{D2}}{4C_{D1}^2}\right)^{\frac{1}{4}} = \sqrt{\frac{3}{2}\,(Re_t + 1)}Da_\eta^{\frac{3}{4}} \qquad (2.34)$$

$$C_\tau = \left(\frac{C_{D2}}{3}\right)^{\frac{1}{2}} = \frac{1}{2}\frac{1}{Da_\eta\sqrt{Re_t + 1}} \qquad (2.35)$$

The calculation of Da_η is the demanding aspect of the model constants' local adaption, since there is no simple, well-established definition of the chemical time scale [170, 171]**Journal Paper IV**. Evans et al. [142] propose using Da_t instead of Da_η as well redefining the fine-scale Re_t to derive a more generalized form of the EDC for MILD combustion. The fine structure Reynolds number (Re^*) at Kolmogorov scale and the standard EDC were defined as 1 and 2.5, respectively, to ensure that the generalized form recovers the original EDC in highly-turbulent flows ($Re_t > 500$). In this case, the corresponding functional expressions for C_γ and C_τ are given by:

$$C_\gamma = \left(\frac{3C_{D2}}{4C_{D1}^2}\right)^{\frac{1}{4}} = \sqrt{\frac{2}{3}\,(Re_t + 1)\,Da_\eta} \qquad (2.36)$$

$$C_\tau = \left(\frac{C_{D2}}{3}\right)^{\frac{1}{2}} = \frac{1}{2}\frac{1}{Da_\eta\sqrt{Re_t + 1}} \qquad (2.37)$$

Farokhi and Birouk [13, 172] propose a different approach for the dynamic EDC constant adaption. They replace the turbulent energy cascade used in the EDC by a fractal modeling approach [173–175] to adopt the turbulence intermittency in the inertial region. As a result the definitions of γ^*, τ^*, and $\overline{R}_i$ change to:

$$\gamma^* = \xi^{3-D_c} \left(Re_t^{-3/4} \right)^{3-D_c} \tag{2.38}$$

$$\gamma_\lambda^2 \sim \gamma^{* \frac{2}{3} \left(\frac{D_c-2}{3-D_c} \right)} \tag{2.39}$$

$$\tau^* = 0.5 \frac{k}{\epsilon} \gamma^{* \frac{1+\frac{2}{3}-\frac{D_c}{3}}{3-D_c}} \tag{2.40}$$

$$\overline{R_i} = \frac{1}{\tau^*} \frac{\gamma^{* \frac{2}{3} \frac{D_c-2}{3-D_c}} \chi}{(1 - \gamma^* \chi)} \left(\frac{c_i^\circ}{\rho^\circ} - \frac{c_i^*}{\rho^*} \right) \tag{2.41}$$

with:

ξ = proportional constant
D_c = fractal dimension

The proportional constant (ξ) is set to 1.75 for low and 3.15 for high Re_t, while its value is interpolated between these extremes for cases including low- and high-turbulence regions [13, 176]. Functional expressions were derived for the newly introduced fractal dimension (D_c):

$$D_c = 1 + \frac{\log (N_\eta)}{\log \left(Re_t^{3/4} \right)} \tag{2.42}$$

$$N_\eta = \pi^{-1} Re_t^{3/2} \tag{2.43}$$

with:

N_η = number of locally generated dissipative scales

Farokhi and Birouk [13] conclude that D_c should be limited between 2 and 2.8 to ensure reasonable values for γ^* and τ^*.

Reacting Fine Structure Share χ Ertesvåg [159], Lewandowski and Ertesvåg [162] investigated the influence of χ on the EDC predictions under MILD combustion conditions, since the assumption of perfectly-mixed FS is no longer valid if the FS occupy a significant portion of the fluid. This effect is illustrated in Figure 2.6. The assumption that χ approaches unity only holds for stoichiometric conditions at elevated Re_t [159]. Lewandowski and Ertesvåg [162] show that a constant, global reduction of χ improves the results for the Delft Jet-in-Hot-Coflow flame [177]. Additionally, they prove that the local adaption of χ improves the predicted species and temperature profiles as well as the predicted lift-off height. However, they do not propose a method to determine χ for comprehensive chemistry. Recently, Lewandowski et al. [167] proposed a new generalized EDC for MILD combustion which combines the variable-reacting fine structure

share (for Re_t<28) and the local model constant adaption. The reduction of the reacting part of the FS at low Re_t compensates for the break-down of the turbulent energy cascade.

2.1.4.2 Partially Stirred Reactor Model

Golovitchev and et al. [143–145] propose the PaSR model for highly-turbulent gas phase combustion. The model assumes that at sufficiently high turbulence, the flame front will collapse and enclose regions of unburnt gases, which shrink due to combustion or combine with other enclosures (see Figure 2.7). The turbulence-chemistry interaction could be interpreted as a topological phenomenon, since the formation of these enclosures corresponds to fractalization of the reaction front [144, 145, 178]. Similar to the EDC, the PaSR divides the fluid into a reacting and a non-reacting region and defines a mean species consumption/production rate ($\overline{R}_i$) by introducing a combustion efficiency correction (κ):

$$\overline{R}_i = \kappa R_i = \frac{\tau_c}{\tau_c + \tau_{mix}} R_i \tag{2.44}$$

with:
R_i = species consumption / production rate
τ_{mix} = mixing time scale

Figure 2.7 and Figure 2.8 illustrate the processes in the PaSR concept. The derivation of κ uses three different pre-defined concentrations: The inlet species concentration ($c_{0,i}$), the mean reactor species concentration ($c_{m,i}$), and the species concentration in the reaction zone ($c_{r,i}$).

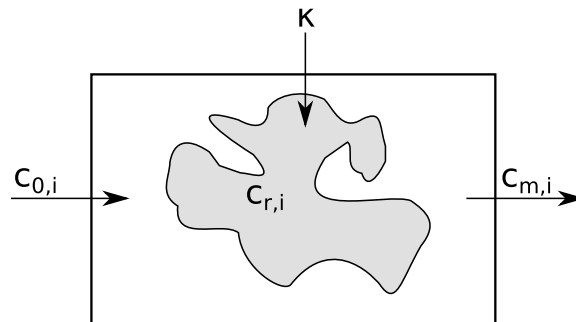**Fig. 2.7:** Flame front fractalization concept for the Partially-Stirred Reactor Model (*PaSR*); adapted from [144, 179]. The symbols denote inlet species concentration ($c_{0,i}$), mean reactor species concentration ($c_{m,i}$), species concentration in the reaction zone ($c_{r,i}$), and combustion efficiency correction (κ).

Using these definitions, the following equalities express the reaction rate:

$$\overline{R_i} = \frac{dc_i}{dt} = \frac{c_{0,i} - c_{m,i}}{\tau_{res}} = \frac{c_{r,i}}{\tau_c} = \frac{c_{m,i} - c_{r,i}}{\tau_{mix}} \tag{2.45}$$

with:

$\tau_{res} = $ residence time

The combustion efficiency correction (κ) is derived by first expressing the ratios $c_{m,i}/c_{0,i}$ and $c_{r,i}/c_{0,i}$ from Equation (2.45):

$$\frac{c_{m,i}}{c_{0,i}} = \frac{\tau_{mix} + \tau_c}{\tau_{res} + \tau_{mix} + \tau_c} \tag{2.46}$$

$$\frac{c_{r,i}}{c_{0,i}} = \frac{\tau_c}{\tau_{res} + \tau_{mix} + \tau_c} \tag{2.47}$$

Subsequently, $c_{r,i}/\tau_c$ is expressed in terms of $c_{m,i}$ to yield the following rate expression [143–145]:

$$\overline{R_i} = \frac{dc_i}{dt} = \frac{c_{m,i}}{\tau_{mix} + \tau_c} = \frac{\tau_c}{\tau_{mix} + \tau_c} \cdot \frac{c_{m,i}}{\tau_c} = \kappa \cdot R_i \tag{2.48}$$

Assuming that $c_{m,i}/\tau_c$ is a linearization of the Arrhenius source term gives the multiplicative reaction rate correction of R_i [143–145].

Figure 2.8 illustrates the PaSR model using the concentration profile of a consumed species. Chemical reactions reduce the species concentration from $c_{0,i}$ towards the equilibrium concentration ($c_{eq,i}$), which is zero for the consumed species. Mixing between the reacting and non-reacting fluid parts increases the species concentration towards the concentration of the non-reacting fluid ($c_{0,i}$). In addition, the depicted time scales (τ_{res}, τ_{mix}, τ_c) indicate the relationship between the involved processes.

The mixing time scale (τ_{mix}) is defined as a macro-mixing time based on the turbulent kinetic energy (k) and turbulent dissipation rate (ε):

$$\tau_{mix} = \sqrt{\frac{C_\mu}{Re_t}} \frac{k}{\epsilon} = C_{mix} \frac{k}{\epsilon} \tag{2.49}$$

with:

$C_{mix} = $ mixing time scale constant
$C_\mu \quad = $ turbulence model constant (value $= 0.135$)
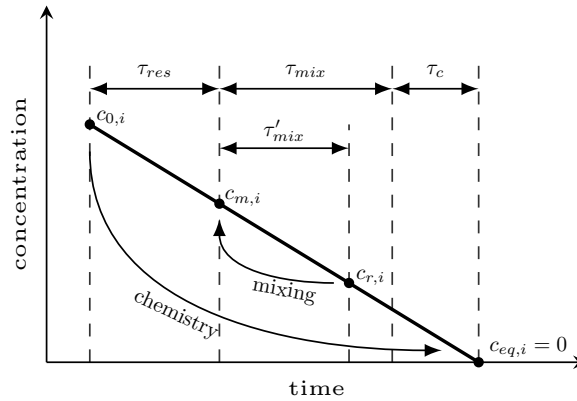
Fig. 2.8: Schematic Partially-Stirred Reactor Model (*PaSR*) concentration graph; adapted from [145]. The symbols denote inlet species concentration ($c_{0,i}$), mean reactor species concentration ($c_{m,i}$), species concentration in the reaction zone ($c_{r,i}$), equilibrium concentration ($c_{eq,i}$), residence time (τ_{res}), mixing time scale (τ_{mix}), and chemical time scale (τ_c).

The mixing time scale constant (C_{mix}) is an empirical constant typically defined as 0.01 for turbulent flows [144]. Golovitchev and Chomiak [145] propose a modified derivation, which yields a value of 0.025 for C_{mix}.

The chemical time scale (τ_c) can be specified according to various definitions, e.g., [170, 171]. However, Golovitchev et al. [143, 144] propose using the inverse from the diagonal of the species consumption/production rate ($\dot{\omega}_i$) rate Jacobian matrix:

$$\tau_c^{-1} = \left. \frac{\partial \dot{\omega}_i}{\partial c_j} \mathbf{I} \right|_{\frac{\partial \dot{\omega}_i}{\partial c_j} < 0} \tag{2.50}$$

In recent years, adaptions of the PaSR have been proposed in the literature. Ferrarotti et al. [157] propose a dynamic definition of τ_{mix} to improve the model predictions, while Sabelnikov et al. [146, 148] introduce an Extended Partially-Stirred Reactor Model (*EPaSR*) that accounts for mass transfer between the reacting regions and the surroundings and includes the PaSR as a limiting case.

Dynamic Mixing Time Scale τ_{mix} Ferrarotti et al. [157] proposed the incorporation of a dynamic mixing model to derive local mixing time scales (τ_{mix}). According to Raman and Pitsch [180], τ_{mix} is defined by the ratio of the variance ($\widetilde{\phi''^2}$) and the dissipation rate ($\widetilde{\epsilon}_\phi$) of the scalar ϕ:

$$\tau_{\mathrm{mix}} = \frac{\widetilde{\phi''^2}}{\widetilde{\epsilon_\phi}} \tag{2.51}$$

This approach requires solving two additional conservation equations for mixture fraction (Z) and scalar dissipation rate ($\dot{\chi}$) [157, 181]. The modified definition for τ_{mix} improves the predictions of the PaSR under MILD combustion conditions, since mixing rates are linked to turbulence [157].

Extended Partially-Stirred Reactor Model (EPaSR)   The Extended Partially-Stirred Reactor Model (*EPaSR*) [146–148] employs a multi-phase approach for the reacting fluid. Similar to the EDC, the EPaSR divides the fluid into Fine Structures (*FS*) and surroundings, which are in a dynamic equilibrium. The dynamic equilibrium is defined similarly to κ:

$$\gamma_{\mathrm{eq}}^* = \frac{\tau_{\mathrm{c}}}{\tau_{mix} + \tau_{\mathrm{c}}} \tag{2.52}$$

with:
$$\gamma_{equ}^* = \text{equilibrium fine structure volume fraction}$$

γ_{equ}^* is required to solve two additional conservation equations: the FS continuity equation and the FS species conservation equation [146–148]:

$$\frac{\partial}{\partial t}\left(\overline{\rho}\gamma^*\right) + \nabla \cdot \left(\overline{\rho}\gamma^*\mathbf{u}\right) = \dot{m} = -\frac{\overline{\rho}\left(\gamma^* - \gamma_{\mathrm{eq}}^*\right)}{\tau_{mix}} \tag{2.53}$$

$$\frac{\partial}{\partial t}\left(\overline{\rho}\gamma^* Y_i^*\right) + \nabla \cdot \left(\overline{\rho}\gamma^* Y_i^* \mathbf{u}\right) = -\nabla\left(\overline{\rho}\gamma^* D_i \nabla Y_i^*\right) + \gamma^* R_i + \overline{M}_i^* \tag{2.54}$$

with:
$$\begin{aligned}
\mathbf{u} &= \text{velocity vector} \\
\overline{Y}_i &= \text{mean species mass fraction} \\
\overline{M}_i^* &= \text{fine structure specie mass transfer term}
\end{aligned}$$

The last term on the right hand side (*RHS*) of Equation (2.54) ($\overline{M}_i^*$) is an additional mass transfer term representing the mass exchange between the FS and surroundings. The mass transfer contains a diffusion contribution ($\overline{\Omega}_i^*$) and a mass transfer contribution from the dynamic equilibrium ($\overline{\Theta}_i^*$):

$$\overline{M}_i^* = \overline{\Theta}_i^* + \overline{\Omega}_i^* = \frac{1}{2}(\dot{m} + |\dot{m}|)Y_i^\circ + \frac{1}{2}(\dot{m} - |\dot{m}|)Y_i^* - \frac{\gamma^* \overline{\rho}\left(Y_i^* - \overline{Y}_i\right)}{\tau_{mix}\left(1 - \gamma^*\right)} \tag{2.55}$$

with:
$\overline{\Theta}_i^* =$ dynamic equilibrium specie mass transfer term
$\overline{\Omega}_i^* =$ diffusion species mass transfer term

The PaSR model is retained if the left hand side (LHS) and the first RHS term diminish in Equation (2.54), since γ^* would be equal to γ^*_{equ} in this case.

2.2 Heterogeneous Gas-Solid Combustion

2.2.1 Heterogeneous Combustion Theory

Heterogeneous combustion refers to the thermo-chemical conversion of solid fuels, which can be classified by the rate-limiting reaction step (mass transfer, molecular diffusion, or chemistry) and the solid properties (dense or porous) [116, 182]. Mass transfer at the fluid-solid interface as well as mass diffusion play an important role in gas-solid reactions. A generalized heterogeneous reaction may include a subset or all of the following steps [116, 183]:

- Mass transfer of the reactant through the boundary layer from the bulk gas phase to the external solid surface

  - Pore diffusion of the gaseous reactant from the external surface towards the reaction site

  - Adsorption of the gaseous reactant at the reaction site

  - Chemical reaction between the adsorbed gaseous reaction and the solid reaction site

  - Desorption of the gaseous product from the reaction site

  - Pore diffusion of the gaseous product from the reaction site towards the external surface

- Mass transfer of the product through the boundary layer from the external solid surface to the bulk gas phase.

Figure 2.9 illustrates the nature of a general gas-solid reaction at the external and internal surface. The left side shows a surface reaction at the external surface, while the right side shows a reaction at the internal surface. Reactions at the internal surface rely on intra-particle and boundary layer mass and energy transport. In contrast, only the boundary layer effects influence reactions at the external surface. Mass and heat transport from the gas phase towards the reaction site can influence the apparent reactivity of solids [116, 117, 184, 185].

This dependence of the apparent reactivity classifies the kinetic conversion regimes for heterogeneous gas-solid reactions [117, 186]. Three different conversion regimes are identified based on three rate limiting processes [116–118, 187–189]:

- **Regime I:** Chemically-controlled conversion. The apparent conversion rate (k_{app}) is equal to the intrinsic conversion rate (k_{intr}), since mass transfer rates toward the reaction sites are orders of magnitudes higher than the chemical conversion rate.
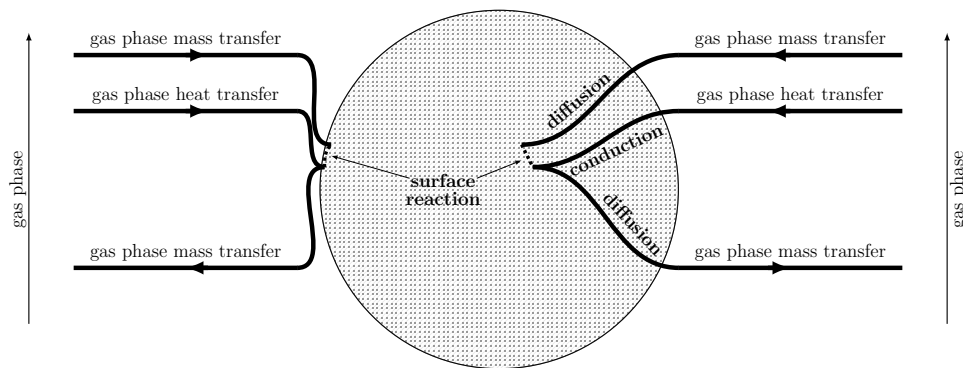
Fig. 2.9: Schematic reaction processes occurring in gas-solid reactions at the external surface (left) and the internal surface (right); adapted from [116].

- **Regime II:** Pore diffusion-controlled conversion. The depletion of reactants in the particle center limits the conversion process. The apparent activation energy ($E_{a,app}$) is approximately half of the intrinsic activation energy ($E_{a,int}$) and the reaction order (n) changes to approximately (n+1)/2.

- **Regime III:** Boundary layer diffusion-controlled conversion. Reactants are consumed at the particle surface, since the mass transfer rates through the boundary layer are significantly lower than the chemical conversion rates. The external particle surface and the boundary-layer diffusion controls the apparent conversion rate in this regime.

Figure 2.10 depicts the Arrhenius diagram for a typical gas-solid reaction to indicate the conversion regimes. Regime **I** prevails at low temperatures, while regime **II** occurs at intermediate temperatures. Regime **III** is located at high temperatures.

Figure 2.11 shows the schematic concentration profiles of the gaseous reactant in the solid particle and surrounding fluid phase. Regime **I** features uniform reactant species concentrations within the particle and the bulk gas phase. Increasing temperatures result in increasing chemical rates and the depletion of the gaseous reactant in the particle center. This is the transition between Regime **I** and **II**, also known as the transition regime A. Further depletion of the gaseous reactant in the particle center occurs in Regime **II**. In the transition between Regime **II** and **III** (transition regime B), reactant species deplete towards the external particle surface. Regime **III** starts when reactants are consumed directly at the outer particles surface by chemical rates.

Thiele [190], Wheeler [191], Damköhler [192], and Zeldovich [193] independently investigated the diffusion limitation of gas-solid reactions. The proposed Thiele modulus ($\phi_{Th,i}$) compares chemical and internal mass transfer (diffusion) rates to estimate if pore diffusion effects are relevant in the solid fuel conversion [182]:
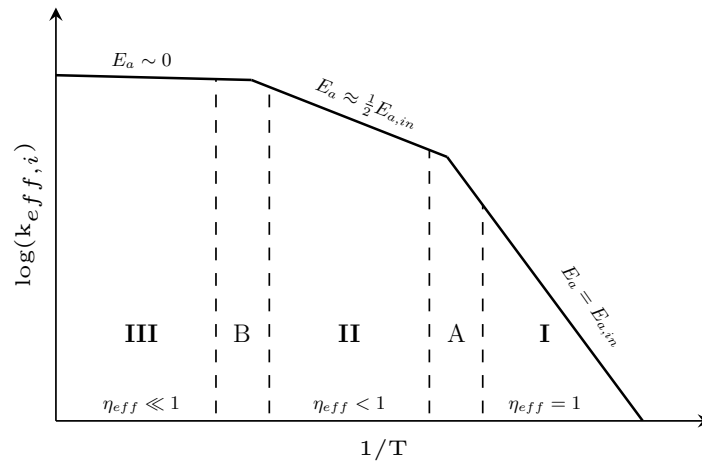
Fig. 2.10: Kinetic regimes in heterogeneous combustion; adapted from [117, 186]. **I**, **II**, and **III** refer to the chemistry, pore diffusion, and boundary-layer diffusion limited kinetic regime. A and B are the transition regions between **I**–**II** and **II**–**III**, with the following symbols: effective rate (k_{eff}), apparent activation energy ($E_{a,app}$), intrinsic activation energy ($E_{a,int}$), and effectiveness factor (η_{eff}).
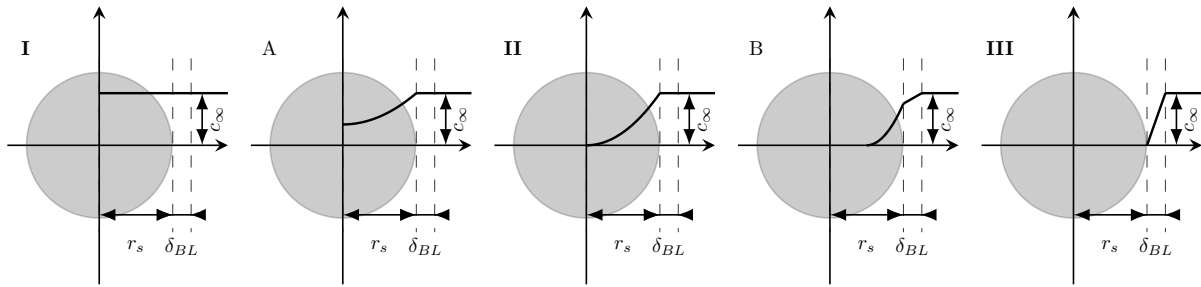
Fig. 2.11: Gaseous reactant concentration profiles of the heterogeneous combustion regimes; adapted from [117]. Regime **I**, **II**, and **III** refer to the chemistry, pore diffusion, and boundary-layer diffusion limited kinetic regime. A and B are the transition regions between **I**–**II** and **II**–**III**. Symbols denote the particle radius (r_s), the boundary layer thickness (δ_{BL}), and the bulk species concentration (c_∞).

$$\phi_{Th,i} = \sqrt{\frac{\tau_D}{\tau_c}} = L_c\sqrt{\frac{n+1}{2}\frac{k_{intr}c_s^{n-1}}{D}} = \frac{V_P}{A_P}\sqrt{\frac{n+1}{2}\frac{k_{intrinsic}c_s^{n-1}}{D}} \tag{2.56}$$

with:

D = mass diffusivity
τ_D = diffusion time scale
n = reaction order
c_s = surface species concentration

The Thiele modulus ($\phi_{Th,i}$) also characterizes the intra-particle educt species concentration profile. $\phi_{Th,i}$ above unity indicates that pore diffusion affects the solid conversion rates. An

effectiveness factor (η_{eff}) is defined according to the ratio between the effective conversion rate to the conversion rate at ambient conditions [116, 118, 194]:

$$\eta_{eff} = \frac{k_{eff}}{k_{intr,\infty}} = f\left(\phi_{Th,i}, L_c, ...\right) \tag{2.57}$$

with:
$\quad k_{eff}\ \ =$ effective rate
$\quad k_{int,\infty} =$ intrinsic rate at ambient conditions

Expressions for η_{eff} based on $\phi_{Th,i}$ can be derived analytically by solving the corresponding reaction-diffusion equations [190, 195–199] or experimentally [118]. The shape generalized form of the Thiele modulus (Equation 2.56) removes the influence of the particle shape on the effectiveness factor [182, 195, 198]. In case of exothermic reactions, η_{eff} can exceed unity, since temperatures above ambient levels might occur inside the particle and cause higher reaction rates [199–201]. This effect will be discussed later in detail.

Despite gas-solid reactions involve multiple subprocesses, solid fuel properties and reaction type can simplify the characteristics of the conversion process. This suggests a classification of heterogeneous combustion based on mechanistic considerations.

2.2.1.1 Mechanistic Classification of Gas-Solid Reactions

Fuel particles might be of porous or dense (non-porous) structure. Porous particles can react at the external and internal surface, which corresponds to the generic gas-solid reaction described above. The share of the reacting inner surface depends on $\phi_{Th,i}$. By contrast, dense particles lack a porous internal structure and, thus, the penetration of gaseous reactants towards the particle center is impossible. Consequently, conversion only takes place at the external surface.

Furthermore, two distinct reaction types might occur in heterogeneous combustion. The first is characterized by forming solid products, while the second forms no solid products [202]:

$$\mathrm{A_{(g)} + B_{(s)} \longrightarrow C_{(g)} + D_{(s)}}$$

$$\mathrm{A_{(g)} + B_{(s)} \longrightarrow C_{(g)}}$$
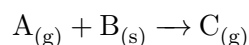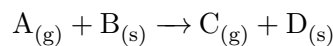
The first reaction type builds up a solid product layer that surrounds the unreacted solid. This layer represents an additional, increasing heat and mass transport resistance during the

conversion process. The second type results in either particle shrinkage for dense particles and/or significant density decrease for porous particles. Furthermore, pore size can enlarge due to the density decrease caused by the reactions at the pore surface [203, 204].

Figure 2.12 illustrates the mechanistic conversion of dense particles. The initial particle is surrounded by a boundary layer, which determines the mass transport from the bulk fluid phase towards the particle surface. If no solid products form, the particle size reduces by reactions at the external surface. This characteristic conversion is called the "**shrinking particle**" in literature [116, 189, 205–209]. Conversely, the reaction front recedes towards the particle center, while the product layer thickness increases if solid products form during the conversion process. In the literature, this characteristic is often referred to as the "**unreacted shrinking core**" [116, 189, 202, 205–207, 210–212]. The concentration profiles during the conversion of dense particles depend on the boundary layer of the shrinking particles. In addition to the boundary layer, the product layer properties affect the reactant concentration profiles in the unreacted shrinking core case.
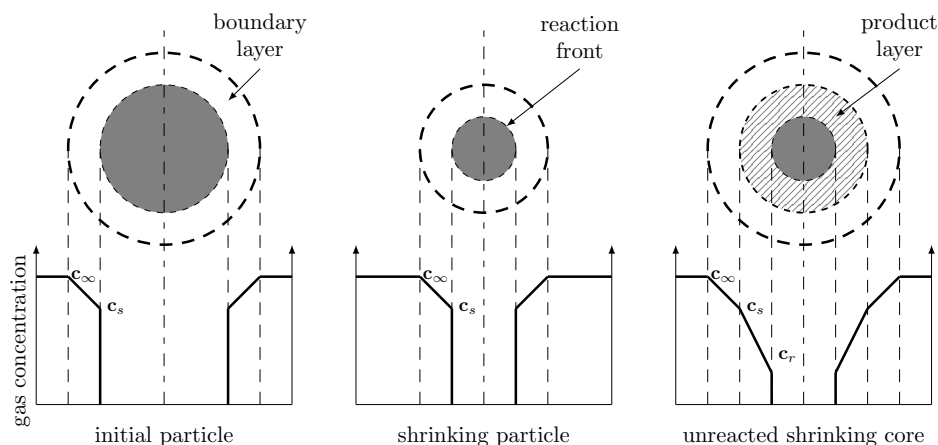
Fig. 2.12: Schematic conversion of dense solid fuel particles; adapted from [116, 189].

Figure 2.13 illustrates the mechanistic conversion of porous particles. Pores allow reactants to penetrate the particle and enable reactions at the inner surface. The mass transfer towards the external surface is determined by the boundary layer but additional pore diffusion effects influence the reactant transport towards the inner particle surface. For reactions without solid products, the total particle is subject to conversion. The actual extent of the inner surface reactivity depends on the Thiele modulus ($\phi_{Th,i}$). This characteristic of porous particle conversion is called the "**progressive core**" conversion in the literature [116, 189, 203, 204, 213–218]. Particle shrinkage might occur for the progressive core, since the external surface is subject to conversion
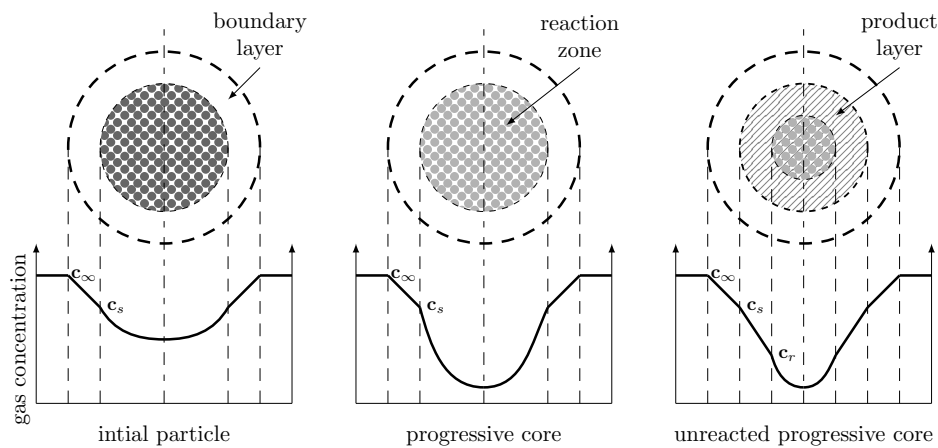
Fig. 2.13: Schematic conversion of porous solid fuel particles; adapted from [116, 189].

in any case. By contrast, the reaction zone contracts towards the center, while an increasing product layer emerges, if solid reaction products exist. This characteristics is referred to as the "**unreacted progressive core**" [116, 189, 203, 204, 213–220]. Particle shrinkage depends on the product layer properties of the unreacted progressive core conversion. The concentration profiles within porous particles depend on the boundary layer and pore diffusion rates as well as conversion rates at the inner surface. Pore diffusion through the product layer additionally affects the reactant concentration in case of the unreacted progressive core conversion.

The mechanistic classification simplifies assumptions used for developing heterogeneous combustion models. Multiple approaches to modeling heterogeneous reactions have been proposed in literature. These models are based on either apparent rate expressions, mechanistic assumptions, or theoretical considerations. The apparent rate expressions disregard species transport phenomena and use apparent Arrhenius parameters and dependence on gas phase reactants [184, 221, 222]. Mechanistic models consider mass transport effects and/or boundary layer effects to determine an effective conversion rate [116–118, 223, 224]. The models relying on theoretical considerations derive functional expressions for a progress variable to account for conversion effects [202–204, 214, 220, 225–227].

2.2.2 Coupling Homogeneous and Heterogeneous Combustion

Heterogeneous combustion involves two distinct phases: a solid phase (fuel) and a fluid phase (combustion gas). The interaction between these phases is critical for the heterogeneous conversion, since available reactants determine the solid reactivity [228–230]. Transporting gaseous products

towards the gas phase and their chemical conversion in the vicinity of the solid fuel affect the reactant availability for heterogeneous combustion. Figure 2.14 schematically shows the coupling between the fluid and solid phase in heterogeneous combustion.
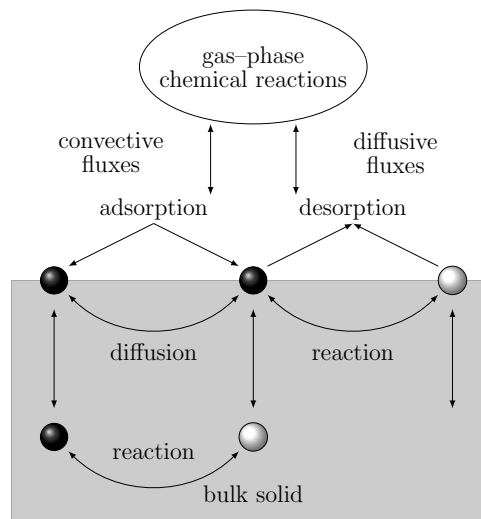
Fig. 2.14: Coupling between homogeneous and heterogeneous combustion; adapted from [183].

The reasonable description of the boundary layer and the particle pores are essential aspects of the coupling. Reactant concentrations in the boundary layer and pores might differ significantly from the bulk concentrations, which results in conflicting heterogeneous combustion behavior [228, 229, 231]. The reactants that reach the particle surface diffuse towards reaction sites either at the external surface or the internal surface. The gaseous products might shield the external surface from reactants or block pores from reactants. Products or other gas phase components might adsorb to active sites and block them from gaseous reactants.

2.2.3 Apparent Rate Models

The Apparent Rate Models (ARMs) are simple models that describe gas-solid reactions. The models disregard all influences except for temperature dependence and the distance to the chemical equilibrium. The distance to the equilibrium is accounted for by a partial pressure or concentration dependence of the reactants and/or products. Effective rate (k_{eff}) expressions for ARMs have the following formula:

$$k_{eff} = k\left(T\right) f\left(T, p, \mathbf{c}\right) \tag{2.58}$$

The temperature-dependent component is typically expressed by an Arrhenius expression [221, 222, 232]:

$$k\left(T\right) = AT^b exp\left(\frac{-E_a}{\mathcal{R}T}\right) \tag{2.59}$$

with:

A = frequency factor
b = temperature exponent
$E_{a,app}$ = apparent activation energy
$\mathcal{R}$ = ideal gas constant

The deviation from the equilibrium can be expressed by the reaction order (n), based on the species partial pressure (p_i) or the species concentration (c_i) [184, 221, 222]:

$$f\left(T, p, \mathbf{c}\right) = \prod \left(\frac{p_i}{\mathcal{R}T}\right)^{n_i} = \prod c_i^{n_i} \tag{2.60}$$

n is zero for species not relevant for the conversion rate.

Other functional relationships might be used for the distance to the equilibrium, e.g., Silcox et al. [233] propose an expression based on the equilibrium partial pressure:

$$f\left(T, p, \mathbf{c}\right) = \prod \left(\frac{p_{i,eq} - p_i}{\mathcal{R}T}\right) f_i = \prod \left(c_{i,eq} - c_i\right) f_i \tag{2.61}$$

In this model, f_i deviates from zero for species influencing the apparent rate.

Although the suitability of the Arrhenius approach to heterogeneous combustion has been questioned [234–236] because it has been derived for gas phase reactions [221, 232], no similar widespread expression of similar quality exists for the temperature dependence of heterogeneous gas-solid reactions.

2.2.4 Mechanistic Models

2.2.4.1 Thiele Based Models

The mechanistic Thiele Based Models (TBMs) provide comprehensive expressions for the effective rate (k_{eff}) of heterogeneous combustion. These expressions reproduce the characteristics depicted in Figure 2.10. A closed form for k_{eff} has been derived by combining characteristic rate-limiting steps into a single expression [116–118, 224]. The apparent conversion rate of Regime **I**, the

intrinsic rate, consists of two distinct rates: the conversion rate at the internal surface – the internal rate (k_{int}) – and the conversion rate at the external surface – the external rate (k_{ext}):

$$k_{eff}c_\infty^n = (k_{int} + k_{ext}) c_s^n = (A_{int}k(T) + A_s k(T)) c_s^n \tag{2.62}$$

with:

c_∞ = bulk species concentration
A_{int} = internal surface area
A_s = external surface area

The effectiveness factor corrects the internal rate to account for pore diffusion in the formal expression of k_{eff} for Regime **II**:

$$k_{eff}c_\infty^n = (\eta_{eff}k_{int} + k_{ext}) c_s^n \tag{2.63}$$

The mass transfer through the boundary layer is the dominating mechanism for Regime **III**. By assuming that the surface species concentration is close to zero in case of mass transfer limitation, c_s can be omitted from the approximation of k_{eff} [237]:

$$k_{eff}c_\infty^n = A_s h_{BL,m} (c_\infty - c_s) \cong A_s h_{BL,m} c_\infty \tag{2.64}$$

with:

$h_{BL,m}$ = convective mass transfer coefficient

Combining equations (2.62), (2.63), and (2.64) into a single equation leads to the following equality:

$$k_{eff}c_\infty^n = A_s h_{BL,m} (c_\infty - c_s) = (\eta_{eff}k_{int} + k_{ext}) c_s^n \tag{2.65}$$

Since reaction orders reduce to first order ($n = 1$) for Regime **III** temperatures [117, 118], expressing c_s from Equation (2.63) and (2.64) is possible. Substituting this expression into the left part of Equation (2.65) and employing the right side of Equation (2.64) provides a comprehensive closed form for k_{eff}:

$$k_{eff} = \frac{1}{\frac{1}{h_{BL,m} \cdot A_s \cdot c_\infty^{1-n}} + \frac{1}{\eta_{eff} \cdot k_{int} + k_{ext}}} \cdot c_\infty^n \tag{2.66}$$

The additional reaction order dependence of this conversion rate is obtained from the effectiveness factor calculation. Moreover, this general equation for k_{eff} is applicable for dense and porous solids. To account for product layer formation, reactant diffusion through the arising layer must be incorporated as an additional mass transfer resistance in Equation (2.66).

A mathematical definition for the effectiveness factor using the Thiele modulus ($\phi_{Th,i}$) and the reactant concentration gradient at the particle surface has been proposed in the literature [182, 238–240]:

$$\eta_{eff} = \frac{s+1}{\phi_{Th,i}^2} \left. \frac{d\mathcal{C}}{dX} \right|_{X=1} \tag{2.67}$$

with:
$\quad s \;=$ shape specific coefficient (0 = flat plate, 1 = cylinder, 2 = sphere)
$\quad \mathcal{C} \;=$ dimensionless species concentration
$\quad X =$ dimensionless distance

Analytically determining η_{eff} requires the solution of the dimensionless reaction-diffusion equation [190, 194, 195, 239, 241]:

$$\frac{d^2\mathcal{C}}{dX^2} + \frac{s}{X}\frac{d\mathcal{C}}{dX} = -\phi_{Th,i}^2 \mathcal{C} \cdot f\left(\mathcal{C}\right) \tag{2.68}$$

$$\mathcal{C} = 1|_{X=1} \,, \qquad \left. \frac{d\mathcal{C}}{dX} = 0 \right|_{X=0} \tag{2.69}$$

$\phi_{Th,i}$ incorporates the effect of gas-solid reactions of arbitrary reaction order. Thus, for isothermal particles and isochoric reactions of first order, the disturbance function $f\left(\mathcal{C}\right)$ is unity. This case enables analytic solutions to the reaction-diffusion equation for simple geometries. The shape-generalized Thiele modulus (Equation 2.56) yields effectiveness factors independent of the particle shape [182, 195, 198]. Figure 2.15 shows the correlation of η_{eff} versus $\phi_{Th,i}$ for various reaction orders. The effectiveness factor is proportional to the inverse of $\phi_{Th,i}$ for large values of the generalized Thiele modulus [182, 195, 198], which is indicated by the effectiveness factor of the zeroth order reaction for values of $\phi_{Th,i} > 1$.
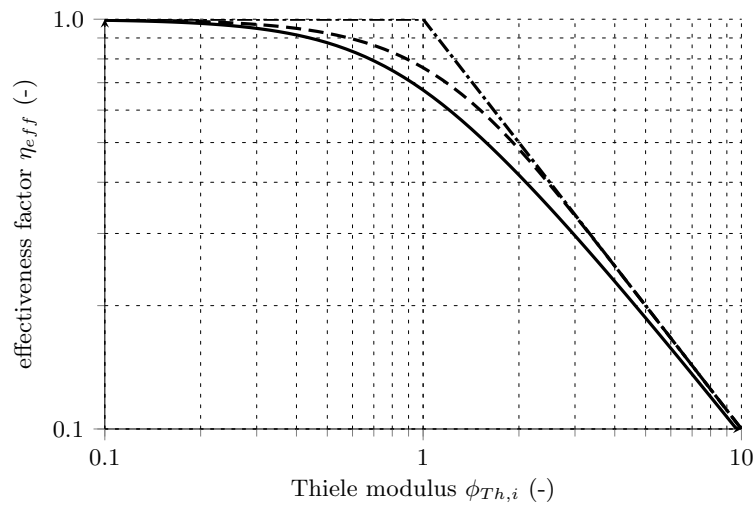
Fig. 2.15: Isothermal effectiveness factor (η_{eff}) versus the generalized Thiele modulus ($\phi_{Th,i}$) for a zeroth (—·—), first (— —), and second (——) order reaction; adapted from [182, 190, 196].

Heterogeneous combustion is a fast, exothermic process; thus, internal particle temperatures might exceed the ambient ones. In such a case, the internal conversion rates can exceed the rates at ambient conditions and yield effectiveness factors above unity [199, 200, 238–240]. By solving the coupled reaction-diffusion and energy equation, Damköhler [242] and Prater [243] derived a unique relationship between the reactant concentration and temperature inside solids:

$$\Delta T = T - T_\infty = -\frac{\Delta H_r D}{\lambda} \left(c_\infty - c\right) \tag{2.70}$$

with:

T_∞ = bulk temperature
ΔH_r = heat of reaction
λ = thermal conductivity
c = species concentration

By substituting this relationship into Equation (2.68), the disturbance function for non-isothermal conversion becomes [200]:

$$f\left(\mathcal{C}\right) = exp \left[\frac{\beta\gamma\left(1 - \mathcal{C}\right)}{1 + \beta\left(1 - \mathcal{C}\right)}\right] \tag{2.71}$$

with:

γ = reaction rate sensitivity to temperature
β = relative temperature variation

$$\gamma = \frac{E_a, int}{\mathcal{R}T_\infty}, \qquad \beta = \frac{c_\infty \Delta H_r D}{\lambda T_\infty}, \qquad \mathcal{C} = \frac{c}{c_\infty} \tag{2.72}$$

with:

$E_{a,int}$ = intrinsic activation energy

Numerical solutions to this equation have been published in literature using various combinations of γ and β [199, 200, 239–241, 244]. Figure 2.16 shows the effectiveness factor versus the Thiele modulus for non-isothermal conditions.
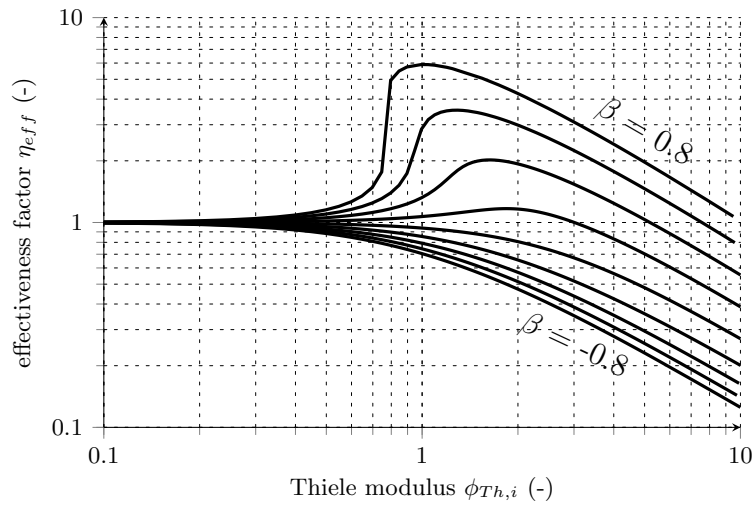
Fig. 2.16: Non-isothermal effectiveness factor (η_{eff}) versus the generalized Thiele modulus ($\phi_{Th,i}$) for a first-order reaction and a reaction rate sensitivity to temperature (γ) of 10 for relative temperature variations (β) of -0.8, -0.6, -0.4, -0.2, 0.0, 0.2, 0.4, 0.6, 0.8.

Besides temperature, other effects, e.g., volume change during the conversion process or reaction reversibility, affect the effectiveness factor [245–248]. A detailed discussion on this topic and the solution for the reaction-diffusion equation is given in [241].

2.2.4.2 Layer Models

The mechanistic Layer Models (LMs) provide a comprehensive approach to modeling the conversion of dense particles. A closed expression for k_{eff} that includes the buildup of a product layer for spherical particles has been proposed in literature [223]. This expression combines the characteristic rate limiting steps for Regime **I** (Equation 2.62) and Regime **III** (Equation 2.64). In case the reactant diffusion is the rate-limiting step, the species concentration at the reaction front (c_r) is close to zero, since the reactant is immediately consumed and, therefore, the effective reaction rate would take the following form [116, 182]:

$$k_{eff}c_\infty^n = (c_\infty - c_s) D \int_{r_s}^{r_r} A(r)dr \cong c_\infty D \int_{r_s}^{r_r} A(r)dr \tag{2.73}$$

with:

r_s = particle radius

r_r = radial position reaction front

The mass diffusivity (D) represents an effective diffusion coefficient, which depends on Knudsen and bulk diffusion as well as on solid porosity and tortuosity [116, 117]. Combining these three equations into a single expression yields the closed form of the LM [116, 182, 223]:

$$k_{eff} = \frac{1}{\frac{1}{h_{BL,m}A_s} + \frac{1}{D}\int_{r_s}^{r_r}\frac{dr}{A(r)} + \frac{1}{A_r k_{intr}}} \cdot c_\infty^n \tag{2.74}$$

with:

A_r = reaction front area

This model is suitable for the heterogeneous combustion of spherical particles featuring an infinitesimal thin reaction front. However, the model fails to reproduce progressive core characteristics. Unlike TBMs, an additional energy equation must be solved to obtain reaction front temperatures. This implies that fuel particles must be discretized by at least three grid points: surface, reaction front, and center [223].

The LM can solve other particle shapes by defining a radial coordinate for the location of the reaction front. Thunman et al. [249] propose such a transformation based on the definition of a control surface (Σ):

$$\Sigma dr = dV \tag{2.75}$$

Σ for spheres, infinite and finite cylinders is defined as [249]:

$$\Sigma_{\text{sphere}} = 4\pi r^2 \qquad \Sigma_{\text{infinite cylinder}} = 2\pi r \qquad \Sigma_{\text{finite cylinder}} = 2\pi \left(3r^2 + r\left(l - d\right)\right) \tag{2.76}$$

with:

r = radius

d = diameter

l = length

Figure 2.17 illustrates this coordinate transformation for the three geometries. The control surface definition and the radial coordinate redefine the particle center for all shapes except spheres. The symmetrical center of the infinite cylinder is a line at the rotation axis, while a plate perpendicular to the rotation axis defines the symmetry of a finite cylinder [249].
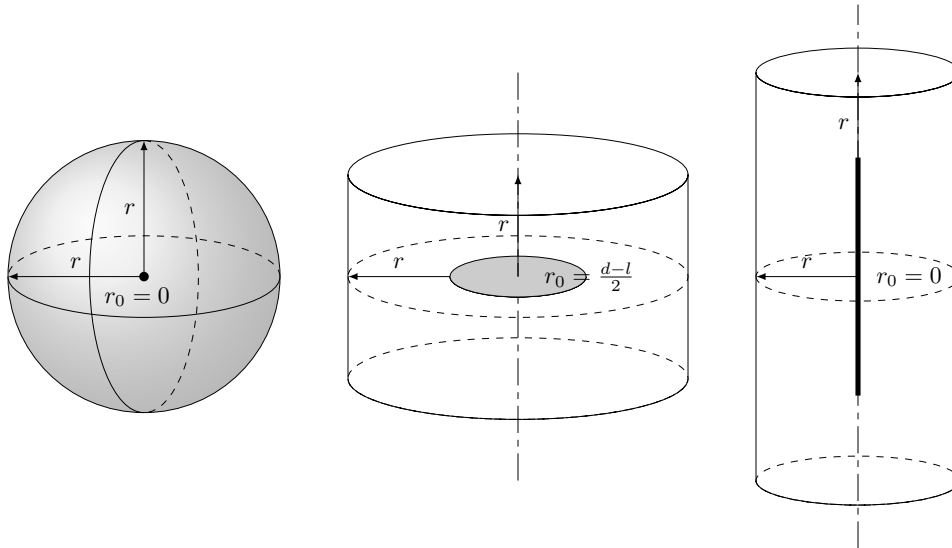
Fig. 2.17: Coordinate transformation for spheres, infinite and finite cylinders; adapted from [249].

2.2.5 Solid-State Kinetic Models

The heterogeneous combustion of solids is also described by the dimensionless conversion rate using the General Kinetic Equation [116, 225]:

$$\frac{d\alpha}{dt} = f\left(\alpha\right) k\left(T\right) h\left(p\right) \tag{2.77}$$

with:
$\quad\quad \alpha = $ conversion

Temperature $k(T)$, pressure $h(p)$, and conversion $f(\alpha)$ can affect the conversion rate. The Arrhenius equation (Equation 2.59) describes the temperature dependence, while the pressure dependence is described by relationships similar to Equation (2.60) and (2.61) or similar [250]. The conversion-dependent component incorporates other effects, e.g., nucleation, mass transport, and structural changes. [116, 225, 227].

The Solid-State Kinetic Models (SSKMs) have been developed to reproduce the decomposition of mainly (crystalline) solids [225, 227]. They provide functional relationships between these

conversion-dependent effects and the conversion rate, e.g., changes in solid crystal lattice or the formation of reactive nuclei [227]. The correlations are derived for certain, idealized solid-state conversion mechanisms, e.g. nucleation, geometrical changes, mass transport, and reaction order. An overview of the various models and a detailed discussion of their derivation is available in [225, 227]. The conversion dependence $f(\alpha)$ for three-dimensional diffusion (referred to as D3 model in literature) is given by Equation (2.78) for example.

$$f(\alpha) = \frac{3(1-\alpha)^{2/3}}{2\left(1-(1-\alpha)^{1/3}\right)}$$ (2.78)

Since the conversion-dependent functions were mathematically derived by solving idealized equations, the complex physical phenomena involved in the conversion process might be overlooked by these models. Therefore, using SSKMs requires a thorough knowledge of the physio-chemical processes during the reaction in order to predict reasonable conversion behavior. Szekely et al. [116] note that the Jander equation (Equation 2.78) for the diffusion-controlled conversion of spherical solids [225, 251] assumes that a flat product layer surrounds the particle. As a result, the model fails to predict reasonable results at elevated conversion.

The Random Pore Model (*RPM*) [203, 204, 218, 219, 252] has been demonstrated in literature about the thermo-chemical conversion of solid fuels using the SSKM approach. The RPM assumes that thermo-chemical conversion takes place at the surface of random pores pervading the solid structure. The specific inner surface first increases due to an enlargement of the pore size. After reaching a critical pore size, pores start to overlap and the specific inner surface decreases again. This overlapping results in a reduction of the conversion rate. The functional expression for the RPM is given by [203, 204]:

$$\frac{d\alpha}{dt} = (1-\alpha)\sqrt{1-\Psi\ln(1-\alpha)}$$ (2.79)

with:

$\Psi = $ pore structure parameter

The pore structure parameter (Ψ) is defined by the initial properties of the solid particle [203, 204]:

$$\Psi = \frac{4\pi L_0 \left(1 - \epsilon_0\right)}{A_0^2} \tag{2.80}$$

with:
L_0 = initial pore length
ϵ_0 = initial particle porosity
A_0 = initial pore surface

Moreover, mass transport effects can be incorporated by the effectiveness factor (η_{eff}) to reproduce the correct conversion characteristics [253]. In this case, the conversion rate modifies to:

$$\frac{d\alpha}{dt} = \eta_{eff}\left(T, p, \alpha\right) f\left(\alpha\right) k\left(T\right) h\left(p\right) \tag{2.81}$$

Unlike TBM and LM models, the shape, size, porosity, and composition of the particle must be considered in the functional expression instead of being directly modeled.

2.3 Computational Fluid Dynamics (CFD)

2.3.1 Finite Volume Method

Computation Fluid Dynamics (*CFD*) is a numerical method based upon the Finite Volume Method (*FVM*) that is used to solve the partial differential equations of fluid mechanics [10, 11]. In other words, the flow domain is divided into a finite number of tiny volumes to numerically solve the relevant conservation equations on discrete points in space. The size and number of volumes depend on the complexity and size of the flow domain as well as the expected gradients in the conserved quantities. The general differential conservation equation of a property ϕ solved in CFD consists of four different contributions [10, 11]:

$$\underbrace{\frac{\partial}{\partial t}(\rho\phi)}_{\text{unsteady term}} + \underbrace{\nabla \cdot (\rho\mathbf{u}\phi)}_{\text{convection term}} = -\underbrace{\nabla \cdot \left(\Gamma^{\phi}\nabla\phi\right)}_{\text{diffusion term}} + \underbrace{Q^{\phi}}_{\text{source term}} \tag{2.82}$$

with:

Γ^{ϕ} = diffusion coefficient

Table 2.1 gives the properties for the set of equations solved for single phase compressible flows in CFD. Besides the generic momentum source term, gravity and static pressure are explicitly shown in the source term of the momentum equation. The source terms of the energy and species conservation equation incorporate heat release and composition changes from chemical reactions. Furthermore, viscous heating must be accounted for in the generic energy source term for turbulent flows. The required source terms depend on the complexity of the flow problem. The stress tensor ($\boldsymbol{\tau}$) for compressible Newtonian fluids is a function of the strain rate and is given by [10, 11]:

$$\boldsymbol{\tau} = \underbrace{\mu\left[\nabla\boldsymbol{u} + (\nabla\boldsymbol{u})^{T}\right]}_{incompressible} + \underbrace{\mu_{vol}\left(\nabla \cdot \boldsymbol{u}\right)\boldsymbol{I}}_{compressible} \tag{2.83}$$

with:

μ_{vol} = dynamic volume viscosity
$\boldsymbol{I}$ = identity matrix

Tab. 2.1: Conservation equation properties [10, 11]. With the quantities density (ρ), velocity vector ($\mathbf{u}$), stress tensor ($\boldsymbol{\tau}$), static pressure (p), gravity vector ($\boldsymbol{g}$), (mixture) specific heat (c_p), thermal conductivity (λ), temperature (T), mass diffusivity (D), and the corresponding source terms (Q^ϕ).

equation	ϕ	$\Gamma^\phi \nabla \phi$	Q^ϕ
continuity	1	0	0
momentum	$\mathbf{u}$	$\boldsymbol{\tau}$	$-\nabla p + \rho \mathbf{g} + Q^{\mathbf{u}}$
energy	$c_p \rho T$	$\lambda \nabla T$	$Q^{c_p \rho T}$
species	ρY_i	ρD_i	Q^{Y_i}

The differential conservation equations must be integrated over the control volumes in the FVM. By using the convergence theorem, the differential equations simplify to algebraic equations [10, 11]:

$$
\int_V \left[\frac{\partial}{\partial t} (\rho \phi) + \nabla \cdot (\rho \mathbf{u} \phi) - \nabla \cdot \left(\Gamma^\phi \nabla \phi \right) - Q^\phi \right] dV =
$$
$$
= \int_V \left[\frac{\partial}{\partial t} (\rho \phi) - Q^\phi \right] dV + \oint_S \left[(\rho \boldsymbol{u} \phi) - \left(\Gamma^\phi \nabla \phi \right) \right] \cdot d\boldsymbol{S}
$$

(2.84)

with:
V = volume
S = surface
$\boldsymbol{S}$ = surface vector

The surface integrals for the convective and diffusive term can be expressed as surface fluxes in the discretized equations. Figure 2.18 illustrates this transformation using the hexahedral discretization of the cross-section of a rectangular duct. Summation over the surface fluxes (S_n, S_e, S_s, S_w) replaces the volume integral for the divergence terms.
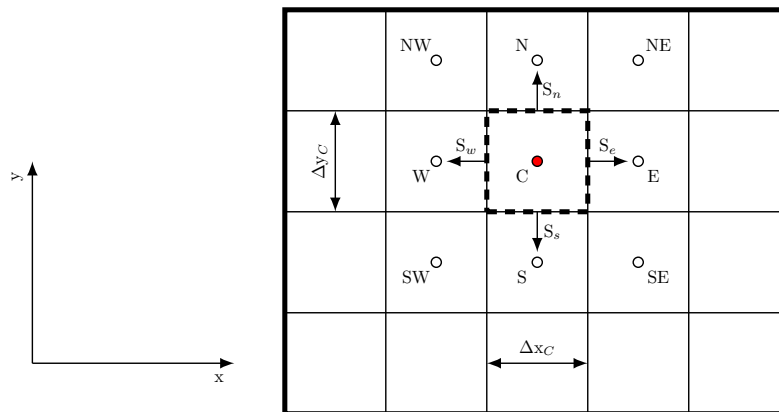

Fig. 2.18: Schematic discretization of a rectangular fluid domain with a hexahedral mesh. The surface fluxes are given by (S_n, S_e, S_s, S_w); adapted from [10].

The spatial and temporal terms are discretized by finite difference stencils on the computational grid. The complexity of the stencils depends on the desired accuracy of the discretization. Details about the discretization process are available in the relevant literature, e.g., [10, 11, 254].

Two distinct approaches exist to solve the coupled, discretized set of conservation equations: coupled or segregated. Coupled algorithms create a single block matrix, incorporating the conservation equations and solve for all properties simultaneously [255–257]. Segregated approaches divide coupled systems into sub-problems and solve each problem separately. Coupling the sub-problems is achieved by an iterative solution loop over the sub-problems [10, 11, 258, 259]. Segregated algorithms are employed for solving the momentum equation, since pressure-velocity coupling must be ensured for the solution [260]. The Semi-Implicit Method for Pressure Linked Equations (*SIMPLE*) algorithm [10, 254, 261–264] and the Pressure-Implicit Method with Splitting of Operators (*PISO*) algorithm [10, 11, 264–266] are the commonly-used algorithms for solving the momentum equation for steady-state or time-dependent problems. The Pressure-Implicit Method for Pressure Linked Equations (*PIMPLE*) algorithm [264] is a combination of the SIMPLE and PISO algorithm where an inner PISO loop is solved, followed by an outer SIMPLE loop that continues until the solution converges. The main advantage of the PIMPLE algorithm is that Courant-Friedrichs-Lewy numbers (CFL) above unity can be used for the time integration. The CFL criterion limits the time step size for a given spatial discretization in the temporal integration of the conservation equation [267, 268]. Generally, the CFL condition must be satisfied to ensure stable solutions:

$$CFL = \frac{|\boldsymbol{u}|\,\Delta t}{\Delta x} \leq 1 \tag{2.85}$$

The CFL criterion is evaluated for each finite volume of a domain; thus, choosing an intelligent spatial discretization can accelerate the time integration by avoiding unnecessary small time steps.

2.3.2 Turbulence

Temporal and spatial random motion characterizes turbulent flows [10, 11, 269]. The random motion at various length and time scales increases heat and mass transfer rates in fluids. This enhancement of the transport processes is called turbulent diffusion. Figure 2.19 illustrates the nature of turbulent flows. Resolving all temporal and spatial structures is called Direct

Numerical Simulation (*DNS*). Various turbulence modeling approaches have been developed to enable modeling industry-scale problems, since DNS is computationally too costly for this kind of application. Two general methods for modeling turbulent flows exist: Large Eddy Simulation (*LES*) and Reynolds-Average Navier-Stokes (*RANS*). LES resolves large and intermediate, energy containing eddies and models small-scale turbulence structures, while RANS solves a mean velocity field and models all turbulence structures.
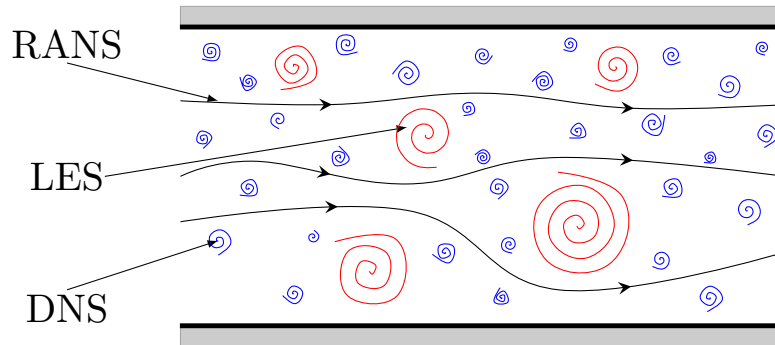
Fig. 2.19: Schematic of turbulence structures in turbulent pipe flows; adapted from [11].

2.3.2.1 Direct Numerical Simulation (*DNS*)

It is possible to describe the transient turbulence phenomenon by directly solving the momentum (Navier-Stokes) equations. This approach requires high spatial and temporal resolution in order to resolve all turbulent scales. The smallest turbulent scale is the Kolmogorov length scale (η_k) [270–272]. The grid size must resolve this scale, while maintaining the CFL condition for the time step size. The required number of grid points (N) to resolve Kolmogorov length scale (η_k) for DNS can be estimated by [273, 274]:

$$N^3 \approx 4.1 \left(\frac{L}{\eta_k} \right)^3 \approx 4.1 Re^3 \tag{2.86}$$

with:
$\qquad L = $ integral length scale

This correlation between the Reynolds number (Re) and computational gird indicates that the numerical effort scales non-linear with the peculiarity of the turbulence. Combined with the time step limitations needed to satisfy the CFL condition, the computational costs limit the applicability of DNS to academic problems.

2.3.2.2 Large Eddy Simulation (*LES*)

LES resolves the large-to-intermediate eddies and relies on sub-grid models for the small eddies in the inertial and viscous range of the energy spectrum [10, 11, 274]. The separation into resolved and unresolved scales is achieved by filtering the conservation equations. The filter width determines the cutoff eddy size. LES resolves the anisotropy and large portions ($\approx 80\%$) of the turbulent energy spectrum contained in the large scales, while modeling the numerically expensive small scales [274]. Different filtering techniques and sub-grid scale models exist for LES [11, 274]. The reduced computational effort required by LES compared to DNS allows its application at high *Re* numbers and, recently, also for more complex phenomena [11, 113, 133, 134, 147, 154, 180, 274, 275].

2.3.2.3 Reynolds-Average Navier-Stokes (*RANS*)

The RANS approach is the most common one used in modeling industrial applications. The governing conservation equations are filtered to obtain equations for the mean values. Filtering introduces additional terms into the conservation equations, which rely on suitable models [276]. Classical RANS for incompressible and density, or Favre-Average Navier-Stokes (*FANS*) for compressible flows [277], are used for this averaging [10]. The averaging procedure has been extensively discussed in the literature [10, 11, 269, 276, 277]. The RANS-averaged continuity, momentum, and scalar transport equation for incompressible flows are given by [10, 11, 269, 274]:

$$\frac{\partial \left(\rho \bar{u}_i \right)}{\partial x_i} = 0 \tag{2.87}$$

$$\frac{\partial \left(\rho \bar{u}_i \right)}{\partial t} + \frac{\partial}{\partial x_j} \left(\rho \bar{u}_i \bar{u}_j + \rho \overline{u'_i u'_j} \right) = -\frac{\partial \bar{p}}{\partial x_i} + \frac{\partial \bar{\tau}_{ij}}{\partial x_j} \tag{2.88}$$

$$\frac{\partial (\rho \bar{\phi})}{\partial t} + \frac{\partial}{\partial x_j} \left(\rho \bar{u}_j \bar{\phi} + \rho \overline{u'_j \phi'} \right) = \frac{\partial}{\partial x_j} \left(\Gamma \frac{\partial \bar{\phi}}{\partial x_j} \right) \tag{2.89}$$

with:
$\bar{u}_i$ = mean velocity vector
u'_i = velocity fluctuation vector
$\bar{p}$ = mean static pressure
$\bar{\tau}_{ij}$ = mean stress tensor

The mean viscous stress tensor is given by:

$$\bar{\tau}_{ij} = \mu \left(\frac{\partial \bar{u}_i}{\partial x_j} + \frac{\partial \bar{u}_j}{\partial x_i} \right) \tag{2.90}$$

The gradient-diffusion hypothesis is employed to close the scalar transport equation [163, 274]:

$$-\rho \overline{u'_j \phi'} = \Gamma_{\mathrm{t}} \frac{\partial \bar{\phi}}{\partial x_j} \tag{2.91}$$

with:

    Γ_t = turbulent diffusivity

The available closure models for the remaining terms of the momentum equation can be divided according to how the missing terms are deduced. The relevant modeling approaches for industrial application rely on eddy viscosity modeling or Reynolds stress modeling.

Eddy Viscosity Models   Eddy viscosity models apply the Boussinesq hypothesis as a closure for the Reynold stress term [10, 11, 269, 274]:

$$-\rho \overline{u'_i u'_j} = \mu_t \left\{ \nabla \bar{\mathbf{u}} + (\nabla \bar{\mathbf{u}})^{\mathrm{T}} \right\} - \frac{2}{3} \rho k \mathbf{I} \tag{2.92}$$

with:

    μ_t = dynamic turbulent viscosity
    $\bar{\boldsymbol{u}}$ = mean velocity vector

The turbulent kinetic energy (k) is defined as:

$$k = \frac{1}{2} \overline{u'_i u'_i} = \frac{1}{2} \left(\overline{u'_x u'_x} + \overline{u'_y u'_y} + \overline{u'_z u'_z} \right) \tag{2.93}$$

The eddy viscosity models rely on equations for the dynamic turbulent viscosity (μ_t) and the turbulent kinetic energy (k). The conservation equation of k is given by [274]:

$$\frac{\partial(\rho k)}{\partial t} + \frac{\partial(\rho \bar{u}_j k)}{\partial x_j} = \frac{\partial}{\partial x_j}\left(\mu \frac{\partial k}{\partial x_j}\right) - \underbrace{\frac{\partial}{\partial x_j}\left(\frac{\rho}{2}\overline{u_j' u_i' u_i'} + \overline{p' u_j'}\right)}_{\text{turbulent diffusive transport}} -$$

$$\underbrace{\rho\overline{u_i' u_j'}\frac{\partial \bar{u}_i}{\partial x_j}}_{\text{production rate}} - \underbrace{\mu\frac{\partial u_i'}{\partial x_k}\frac{\partial u_i'}{\partial x_k}}_{\text{dissipation rate}} \tag{2.94}$$

with:

$$p' = \text{pressure fluctuations}$$

The last three expressions in the RHS need to be modeled to solve the equation. Turbulent diffusion can be approximated by the gradient diffusion assumption:

$$D_k = -\left(\frac{\rho}{2}\overline{u_j' u_i' u_i'} + \overline{p' u_j'}\right) \approx \frac{\mu_t}{\sigma_k}\frac{\partial k}{\partial x_j} \tag{2.95}$$

with:

$$\sigma_k = \text{turbulence model constant (value = 1.0)}$$

Applying the Boussinesq eddy viscosity hypothesis to the production term in the RHS yields the following expression for the production of turbulent kinetic energy [11, 274]:

$$P_k = -\rho\overline{u_i' u_j'}\frac{\partial \bar{u}_i}{\partial x_j} \approx \mu_t\left(\frac{\partial \bar{u}_i}{\partial x_j} + \frac{\partial \bar{u}_j}{\partial x_i}\right)\frac{\partial \bar{u}_i}{\partial x_j} \tag{2.96}$$

A new quantity, the turbulent dissipation rate (ε), is introduced as the last term in the RHS. The corresponding conservation equation is similar to the equation for the turbulent kinetic energy given in Equation (2.94). The dynamic turbulent viscosity (μ_t) is then defined by:

$$\mu_t = \rho C_\mu \frac{k^2}{\varepsilon} \tag{2.97}$$

Rearranging and introducing a proportional constant to adapt the models to turbulent flow yields the conservation equations of k and ε of the standard k-ε model [10, 278]:

$$\frac{\partial}{\partial t}(\rho k) + \nabla \cdot (\rho \mathbf{\bar{u}} k) = \nabla \cdot \left[\left(\mu + \frac{\mu_t}{\sigma_k}\right)\nabla k\right] + \underbrace{P_k - \rho\varepsilon}_{S^k} \tag{2.98}$$

$$\frac{\partial}{\partial t}(\rho\varepsilon) + \nabla\cdot(\rho\overline{\mathbf{u}}\varepsilon) = \nabla\cdot\left[\left(\mu + \frac{\mu_t}{\sigma_\varepsilon}\right)\nabla\varepsilon\right] + \underbrace{C_{z1}\frac{\varepsilon}{k}P_k - C_{z2}\rho\frac{\varepsilon^2}{k}}_{S^\varepsilon} \tag{2.99}$$

with:

σ_ε = turbulence model constant (value = 1.3)
$C_{\varepsilon 1}$ = turbulence model constant (value = 1.44)
$C_{\varepsilon 2}$ = turbulence model constant (value = 1.92)

The model constants for the k-ε-model are summarized in Table 2.2.

Tab. 2.2: Standard k-ε-model constants [11, 278].

C_μ	$C_{\varepsilon 1}$	$C_{\varepsilon 2}$	σ_k	σ_ε
0.09	1.44	1.92	1.0	1.3

Various turbulence models that rely on the Boussinesq eddy viscosity hypothesis, with similar assumptions to the k-ε-model, have been proposed in the literature [10, 274].

Reynolds Stress Models   Reynolds stress models are also called second-order closure models because they solve additional conservation equations for the Reynolds stress (R_{ij}). Assuming isotropic stress, the number of additional transport equations decreases to six identical equations of the form [11, 274]:

$$\frac{\partial R_{ij}}{\partial t} + \frac{\partial(\overline{u}_k R_{ij})}{\partial x_k} = \frac{\partial}{\partial x_k}\left(\mu\frac{\partial R_{ij}}{\partial x_k}\right) - \left(R_{ik}\frac{\partial\overline{u}_j}{\partial x_k} + R_{jk}\frac{\partial\overline{u}_i}{\partial x_k}\right) + $$
$$\underbrace{2\mu\frac{\partial u_i'}{\partial x_k}\frac{\partial u_j'}{\partial x_k}}_{\text{dissipation tensor}} - \underbrace{\prod_{ij}}_{\text{pressure strain}} + \underbrace{\frac{\partial C_{ijk}}{\partial x_k}}_{\text{turbulent difussion}} \tag{2.100}$$

The last three terms in the RHS must be modeled. The dissipation tensor is given by:

$$2\mu\frac{\partial u_i'}{\partial x_k}\frac{\partial u_j'}{\partial x_k} = \rho\varepsilon_{ij} = \rho\frac{2}{3}\varepsilon\mathbf{I} \tag{2.101}$$

with:

ε_{ij} = turbulent dissipation rate tensor

which is a similar approach to the one used for the k-ε-model. The adaption of the turbulent dissipation rate in the closure implies that Reynolds stress models must also solve a transport equation similar to Equation (2.99). The pressure strain can be expressed by:

$$\prod_{ij} = p'\left(\frac{\partial u_i'}{\partial x_j} + \frac{\partial u_j'}{\partial x_i}\right) \tag{2.102}$$

where the pressure fluctuation (p') must be determined by solving the filtered Poisson equation for the pressure, where p' is decomposed into a fast, slow, and harmonic contribution [274]. The turbulent diffusion of the Reynolds stresses is modeled similar to the turbulent diffusion terms of the k-ε-model [11, 274]:

$$C_{ijk} = \rho\overline{u_i'u_j'u_k'} + \overline{p'u_i'}\delta_{jk} + \overline{p'u_j'}\delta_{ik} = \frac{\mu_\mathrm{t}}{\sigma_k}\frac{\partial R_{ij}}{\partial x_j} \tag{2.103}$$

The more sophisticated modeling of the Reynolds stresses is numerically more expensive than the eddy viscosity approaches, since it requires solving five additional equations. However, the higher-order approximation proved to be more accurate for modeling rotating flows, e.g., in cyclones [279–281].

2.4 Multi-Phase Flow

2.4.1 Multi-Phase Modeling Approaches

General multi-phase flows can be modeled using three different approaches: Euler-Euler (*E-E*), Euler-Lagrange (*E-L*), and the Computation Fluid Dynamics-Discrete Element Method (*CFD-DEM*) [282–286]. The E-E approach can model multiple fluid phases. Gas-solid systems can be modeled with the E-E approach by employing suitable property models for the solid phase rheology, e.g., the granular pressure model [114] and the Kinetic Theory of Granular Flow (*KTGF*) [111–113, 284, 286–288]. E-L and CFD-DEM resolve the particular solid phase and can resolve the solid-fluid and particle-particle interaction.

Figure 2.20 shows the occurring phase coupling regimes for gas-solid flows. At low solid phase fraction (α_s), the solid momentum acting on the carrier fluid phase is negligible, with the fluid flow field determining the solid movement. This approach is called one-way coupling. At a α_s between 10^{-6} and 10^{-3}, the solid movement rebounds on the fluid phase and the additional momentum source must be included for the fluid phase. This type of coupling is called two-way coupling, while three-way coupling occurs at solid phase fractions between 10^{-3} and 10^{-2}. The flow field changes due to a single particle's effect on other particles in this regime. Besides the particle-fluid interaction, particle-particle interactions become important above 10^{-2} solid phase fraction. Four-way coupling is required to describe this type of gas-solid flows. [283–285, 289]
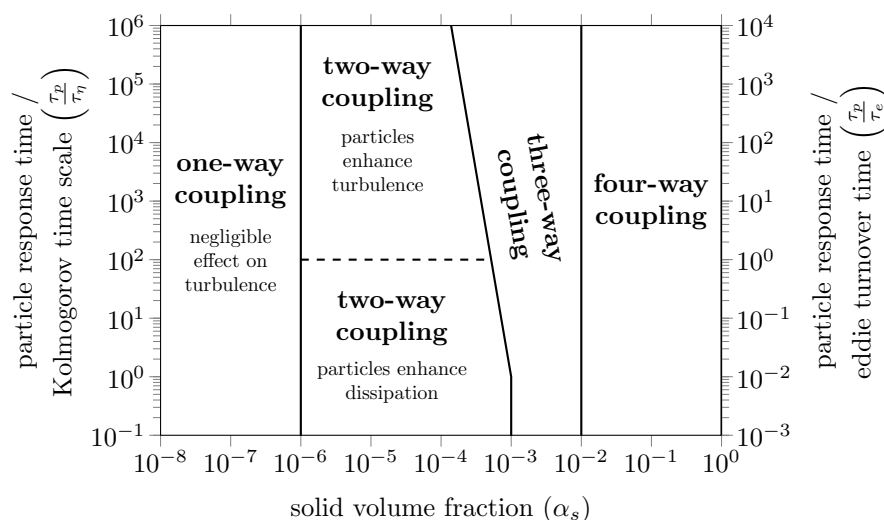

Fig. 2.20: Momentum-coupling regimes of gas-solid flow regimes; adapted from [283–285, 289].

The E-E, E-L, and CFD-DEM method offer different approaches for the required phase coupling. The rheological models for the solid phases determine the type of momentum coupling used in E-E models. Four-way coupling is the most commonly used type in E-E modeling. Turbulent interaction between fluid and solid phase can be included by suitable sub-grid models [290, 291]. E-L are capable of covering all four coupling regimes. Turbulent interaction of the Lagrangian particles and the carrier phase requires suitable models. Particle contact models, similar to the Discrete Element Method (*DEM*), are suitable for covering particle-particle interactions. CFD-DEM directly resolves the different regimes.

2.4.1.1 Euler-Euler Modeling

Phases are considered as inter-penetrating fluids in Euler-Euler (*E-E*) modeling. The transport equations are volume or conditionally averaged for the different phases to obtain the general Eulerian transport equation, which must be solved for the individual phases [282, 284, 286, 292–294]:

$$\underbrace{\frac{\partial \left(\alpha_\varphi \overline{\rho}_\varphi \overline{\phi}_\varphi \right)}{\partial t}}_{\text{unsteady term}} + \underbrace{\nabla \cdot \left(\alpha_\varphi \overline{\rho}_\varphi \overline{\mathbf{u}}_\varphi \overline{\phi}_\varphi \right)}_{\text{convection term}} = - \underbrace{\nabla \cdot \left(\alpha_\varphi \overline{\Gamma}_\varphi^\phi \nabla \overline{\phi}_\varphi \right)}_{\text{diffusion term}} + \underbrace{\alpha_\varphi \overline{Q}_\varphi^\phi}_{\text{source term}} + \underbrace{\Psi_\varphi^\phi}_{\text{exchange term}} \tag{2.104}$$

with:
$$\alpha_\varphi = \text{phase fraction}$$

Table 2.3 summarizes the quantities of the transport equation to obtain the continuity, momentum, energy, and species conservation equations. The mean Cauchy stress tensor ($\overline{\boldsymbol{\sigma}}_\varphi$) incorporates all normal and shear stresses that occur in fluid or solid Eulerian phases. The inter-phase coupling terms for the momentum, energy, and species equations rely on empirical or semi-empirical models.

Additional constraints provide the necessary closure conditions for the solution of E-E phase systems. The sum over all phase fractions (α_φ) must be unity:

$$\sum_i \alpha_\varphi = 1 \tag{2.105}$$

Tab. 2.3: Euler-Euler (*E-E*) averaged conservation equation properties [284, 286, 292, 294]. With the quantities mean velocity vector ($\overline{\boldsymbol{u}}$), mean Cauchy stress tensor ($\overline{\boldsymbol{\sigma}}_\varphi$), mean density ($\overline{\rho}$), gravity vector ($\boldsymbol{g}$), (mixture) specific heat (c_p), thermal conductivity (λ), mean temperature ($\overline{T}$), mean species mass fraction ($\overline{Y}_i$), species diffusivity (D_i), and the corresponding source terms ($\overline{Q}_\varphi^\phi$) and source terms ($\Psi_\varphi^\phi$).

equation	$\overline{\phi}_\varphi$	$\overline{\Gamma}_\varphi^\phi \nabla \overline{\phi}_\varphi$	$\overline{Q}_\varphi^\phi$	Ψ_φ^ϕ
continuity	1	0	0	Ψ_φ^ρ
momentum	$\overline{\mathbf{u}}_\varphi$	$\overline{\boldsymbol{\sigma}}_\varphi$	$\overline{\rho}_\varphi \mathbf{g}$	$\Psi_\varphi^{\mathbf{u}}$
energy	$c_{p,\varphi} \overline{\rho}_\varphi \overline{T}_\varphi$	$\lambda_\varphi \nabla \overline{T}_\varphi$	$\overline{Q}^{c_p \rho T}$	$\Psi_\varphi^{c_p \rho T}$
species	$\overline{\rho}_\varphi \overline{Y}_{j,\varphi}$	$\overline{\rho}_\varphi D_{j,\varphi} \nabla \overline{Y}_{j,\varphi}$	$\overline{Q}^{Y_\varphi}$	Ψ_φ^Y

Furthermore, the sum over all exchange terms for mass, momentum, energy, and species must be zero to obey conservation for the conserved quantities:

$$\sum_i \Psi_\varphi^\phi = 0 \tag{2.106}$$

Solving the coupled set of equations for multi-phase systems results in singularities if α_φ approaches zero [295]. Therefore, the continuity equation is used to modify the momentum equation to remove this singularity [293, 295–297]. The conservative form of the momentum equation is obtained by subtracting the phase continuity equation. Subsequently, expansion and transformation are done to obtain the non-conservative [295, 296], semi-conservative [296], and phase-intensive [293, 297] forms of the momentum equation. Although these equations are mathematically identical, the numerical integration of the modified momentum equations relies on approximations for the convective term. These approximations lead to solutions that deviate from the conservative form of the momentum equation [296, 297].

A modification of the phase continuity equation has been proposed in literature to ensure boundedness at the upper and lower limits of α_φ to increase mass conservativeness [293, 298, 299]. The modification defines a mixture velocity and a mean relative phase velocity vector ($\overline{\boldsymbol{u}}_r$). For the source-free incompressible case, the modified phase continuity equation yields:

$$\frac{\partial\left(\alpha_\varphi\right)}{\partial t} + \nabla \cdot \left(\alpha_\varphi \overline{\mathbf{u}}_\varphi\right)$$

$$= \frac{\partial\left(\alpha_\varphi\right)}{\partial t} + \nabla \cdot \left(\alpha_\varphi \overline{\mathbf{u}}\right) + \nabla \cdot \left(\alpha_\varphi \sum_{j \neq \varphi}\left(\alpha_j \left(\overline{\mathbf{u}}_\varphi - \overline{\mathbf{u}}_j\right)\right)\right) \quad (2.107)$$

$$= \frac{\partial\left(\alpha_\varphi\right)}{\partial t} + \nabla \cdot \left(\alpha_\varphi \overline{\mathbf{u}}\right) + \nabla \cdot \left(\alpha_\varphi \sum_{j \neq \varphi}\left(\alpha_j \overline{\mathbf{u}}_{r,j}\right)\right)$$

The non-linear (third) term of the bounded-phase continuity equation implicitly couples the different phases and requires special attention when solving the equation. Segregated and coupled approaches are used to solve the phase continuity equations [293, 300–302].

Multi-Fluid Models (MFMs) have an inherently non-conservative form and the equation type of the conserved quantities can deviate from being hyperbolic [288, 303–306]. Non-hyperbolic systems are characterized by complex eigenvalues. Non-linear coupling between the momentum equations has been identified as the source of the complex characteristics occurring in MFMs [288, 305]. Mathematical and numerical regularization has been used to enable solving ill-posed MFM systems [288, 303, 305, 306]. Regularizing the multi-phase system is believed to introduce non-physical effects and changes to the system's characteristics [303].

Mathematical regularization includes hyperbolization, which adds additional terms [307–312] or adopts modeling assumptions [111, 304, 313–318] to the equations, or parabolization, which adds additional diffusion terms to the equations [288, 304, 319, 320].

Numerical regularization is included in the MFMs solution algorithms. Suitable multi-phase algorithms have been developed that are based on the single phase flow SIMPLE and PISO algorithms [255, 256, 293, 296, 300, 305, 321–327]. Common multi-phase solution algorithms include the Partial Elimination Algorithm (*PEA*) [328, 329], Partially Implicit Treatment (*PIT*) [322, 326, 327], Implicit Multifield Method (*IMF*) [330], Simultaneous Solution of Non-Linearly Coupled Equations (*SINCE*) [331, 332], Advection Upstream Splitting Method (*AUSM*) [305, 333], Interphase Slip Algorithm (*IPSA*) [334, 335], and Interphase Slip Algorithm-Coupled (*IPSA-C*) [304, 322]. IPSA-C is a combination of the PIT and IPSA approaches.

2.4.1.2 Euler-Lagrange Modeling

In the E-L approach, the fluid phase is modeled as a Eulerian phase, but the solid phase is modeled as a Lagrangian phase. The Lagrangian equation describes the particle position and its motion [282, 284, 285, 289, 336, 337]:

$$m_p \frac{d\mathbf{u}_p}{dt} = \mathbf{f}_{pressure} + \mathbf{f}_{gravity} + \mathbf{f}_{drag} + \mathbf{f}_{fluid} + \mathbf{f}_{collision} \qquad (2.108)$$

with:
$$m_p = \text{particle mass}$$
$$\overline{\boldsymbol{u}}_p = \text{particle velocity vector}$$
$$\boldsymbol{f} \quad = \text{force vector}$$

$$\frac{d\mathbf{x}_p}{dt} = \mathbf{u}_p \qquad (2.109)$$

with:
$$\boldsymbol{x}_p = \text{particle position}$$

The source terms in the motion equation account for hydro-static and static pressure gradients ($\mathbf{f}_{pressure}$), gravity ($\mathbf{f}_{gravity}$), particle carrier momentum exchange ($\mathbf{f}_{drag}$), other fluid forces, e.g. virtual mass, Saffman or Magnus lift, or Basset force, ($\mathbf{f}_{fluid}$), and forces acting between individual particles ($\mathbf{f}_{collision}$) [284, 285]. The momentum exchange terms rely on suitable closure models.

The general conservation equation for particle properties (ϕ_p) is given by [285, 338]:

$$\frac{d}{dt}\left(\phi_p\right) = Q_{ext}^{\phi} + Q_{int}^{\phi} \qquad (2.110)$$

with:
$$Q_{ext}^{\phi} = \text{external Lagrangian source}$$
$$Q_{int}^{\phi} = \text{internal Lagrangian source}$$

Table 2.4 provides the internal and external source terms for the species and the energy equation. The sum over all species conservation equations resembles the mass conservation. Species equation source terms include convective transport from the carrier phase and a chemical source term. External source terms for the energy equation are the convective and radiative heat transfer, while internal source terms emerge from chemical conversion. The phase coupling relies on suitable closure models for the external source terms of the conservation equations.

Solving the conservation equations for every particle is computationally expensive. To overcome this limitation, particles are grouped into "parcels" and a single representative particle is solved for each parcel [113, 285, 339]. Particles and/or parcels are typically small compared to the computational cells in E-L modeling. The number of particles per parcel ($n_{p,i}$) depends on particle size and parcel mass. The local solid phase fraction is obtained by summing up the particle volumes of each parcel in a computational cell:

Tab. 2.4: Euler-Euler (*E-E*) averaged conservation equation properties [282, 284, 285, 338]. With the quantities denoting particle mass (m_p), species mass fraction (Y_i), convective species transfer ($\dot{S}_{conv,i}$) and chemical species ($\dot{S}_{chem,i}$) source term, (mixture) specific heat (c_p), temperature (T), external Lagrangian sources (Q_{ext}^ϕ), and internal Lagrangian sources (Q_{int}^ϕ).

equation	ϕ_p	Q_{ext}^ϕ	Q_{int}^ϕ
species	$m_p Y_i$	$Q_{conv,i}^{Y_i}$	$\dot{Q}_{chem,i}^{Y_i}$
energy	$c_p T_p$	$Q_{conv}^{c_p \rho T} + \dot{Q}_{rad}^{c_p \rho T}$	$\dot{Q}_{chem}$

$$\alpha_s = \frac{\sum_p \sum_i n_{p,i} V_{p,i}}{V_{cell}} \tag{2.111}$$

with:
$V_{p,i}$ = particle volume
V_{cell} = cell volume

Two-way coupled E-L models account for the momentum exchange term of the Lagrangian phase ($\mathbf{f}_{drag}$) for the fluid phase momentum equation, while one-way coupled models neglect the solid phase momentum in the fluid phase. The particle collision force ($\mathbf{f}_{collision}$) is disregarded in one- and two-way coupled models. Highly-dispersed gas-particle flows are commonly modeled using one- or two-way coupled E-L approaches.

Four-way coupled E-L models that resolve individual particles and particle-particle contacts ($\mathbf{f}_{collision}$) are similar to CFD-DEM. The Multiphase Particle-in-Cell (*MPPIC*) method applies the parcel approach to four-way coupled E-L models to reduce the numerical effort [339–344]. The MPPIC solves the solid phase using the Lagrangian method, but solid stresses to correct the solid motion are solved on a Eulerian grid. Employing suitable models for particle-particle interaction enables the efficient modeling of dense phase particle flows. Solid shear stress proved to be critical for reasonable results [344].

Segregated solution algorithms first solve the dispersed Lagrangian phase. In case of two- and four-way coupling, the solid phase fraction and coupling fields are mapped to the Eulerian gird before solving the continuous Eulerian phase [339].

2.4.1.3 CFD-DEM Coupling

CFD-DEM directly solves particle-particle interactions in the Lagrangian reference frame, while the fluid phase is solved on a Eulerian grid. The main difference from the previously discussed E-L models is that CFD-DEM resolves all particle-particle contacts [283, 285]. The fluid-particle

coupling originates from suitable correlations in case of unresolved CFD-DEM or is directly obtained from the fluid-particle interaction in case of resolved CFD-DEM [283]. The latter approach requires fine grids to reasonably resolve the forces acting upon the particles.

The hard sphere model, introduced by Campbell and Brennen [345], resolves particle-particle contacts in an event-driven manner, which allows for one interaction per particle and time step. This approach requires small time steps to resolve the individual contacts. The hard sphere model is typically used in dispersed gas-solid flows, since unreasonably small time steps must be employed in granular flows to resolve the multiple contacts each particle experiences in dense packing. [283, 285]

The soft sphere model represents a molecular dynamic approach to particle-particle collisions. The model resolves multiple contacts per time step by enabling an overlap between particles [346]. The overlap is then used to calculate the particle forces and the resulting velocity and position. Time step size must ensure that this overlap is small compared to the particle size. [283, 285]

The Discrete Element Method (*DEM*) side of the CFD-DEM solves a momentum and torque equation for each particle [283, 285, 347]:

$$m_p \frac{d\mathbf{u}_p}{dt} = \mathbf{f}_{fluid} + \sum_j \mathbf{f}_{collision,j} \tag{2.112}$$

$$I_p \frac{d\boldsymbol{\omega}_p}{dt} = \sum_j \left(\boldsymbol{M}_{pj}^t + \boldsymbol{M}_{pj}^r \right) \tag{2.113}$$

with:
$$
\begin{aligned}
I_p & = \text{moment of inertia} \\
\boldsymbol{\omega}_p & = \text{angular speed} \\
\boldsymbol{M}_{pj}^t & = \text{rotational torque} \\
\boldsymbol{M}_{pj}^r & = \text{rolling resistance torque}
\end{aligned}
$$

The torque represents particle rotation and consists of two contributions; the rolling resistance torque and the rotational torque. The former represents the resistance to rotation, while the latter is the rotation arising from particle collisions. Particle collisions and tangential and rolling resistance torque rely on suitable models, which have been extensively discussed in the literature [283, 285, 347].

The critical DEM time step ($\Delta t_{\text{DEM, crit}}$) is expressed as the inverse of the characteristic frequency of a corresponding mass-spring system [283, 348, 349]:

$$\Delta t_{\text{DEM, crit}} \approx 2\pi \sqrt{\frac{m_p}{k_{spring}}} \qquad (2.114)$$

with:
$$k_{spring} = \text{spring stiffness}$$

The actual time step must be a fraction of $\Delta t_{\text{DEM, crit}}$ to ensure that particle contacts are resolved by multiple time steps [283]. Typically, the time step required to obey the CFL criterion is larger than the time step required for the DEM site. For numerical efficiency, CFD-DEM coupling employs multiple DEM steps for one CFD step [350].

2.4.2 Multi-Phase Turbulence

Temporal and spatial random motion is also present in multi-phase flows. The same approaches as for single-phase flows are available to resolve this random motion: DNS, LES, and RANS. The fully-resolved DNS is currently limited to academic applications [351–354], while LES and RANS turbulence modeling are used for industrial applications. The turbulent interaction of dispersed phases with the continuous phase affects these random velocity fluctuations due to the momentum transfer caused by the dispersed phases' inertia [355–363]. This effect is called turbulence modulation. Conversely, the random fluid motion redistributes the dispersed phase towards regions of lower concentration via the turbulent dispersion force [357, 360, 364–368]. The turbulence modulation is incorporated into special multi-phase turbulence models, while the turbulent dispersion force requires an additional momentum transfer model.

Reynolds-Average Navier-Stokes ($RANS$) and/or Favre-Average Navier-Stokes ($FANS$) averaging of the multi-phase equations yields additional terms caused by the fluctuation of the phase fraction (α_φ). A generic filtered equation of a phase is given by [111, 286, 369, 370]:

$$
\begin{aligned}
\frac{\partial\left(\rho_\varphi \overline{\alpha}_\varphi \overline{\mathbf{u}}_{i,\varphi}\right)}{\partial t} &+ \nabla \cdot \left(\rho_\varphi \overline{\alpha}_\varphi \overline{\mathbf{u}}_{,i,\varphi} \overline{\mathbf{u}}_{j,\varphi}\right) \\
&+ \nabla \cdot \left(\rho_\varphi \overline{\alpha}_\varphi \overline{\mathbf{u}'_{i,\varphi} \mathbf{u}'_{j,\varphi}} + \rho_\varphi \overline{\mathbf{u}}_{i,\varphi} \overline{\alpha'_\varphi \mathbf{u}'_{j,\varphi}} + \rho_\varphi \overline{\mathbf{u}}_{j,\varphi} \overline{\alpha'_\varphi \mathbf{u}'_{i,\varphi}} + \rho_\varphi \overline{\alpha'_\varphi \mathbf{u}'_{i,\varphi} \mathbf{u}'_{j,\varphi}}\right) = \\
&- \nabla\left(\overline{\alpha}_\varphi \overline{p}\right) - \nabla\left(\overline{\alpha'_\varphi p'}\right) - \nabla \cdot \overline{\boldsymbol{\tau}}_\varphi + \Psi_{ij}^{\mathbf{u}}
\end{aligned}
\qquad (2.115)
$$

The terms including fluctuating variables require suitable modeling assumptions, which are usually similar to single phase turbulence, and have been extensively discussed in the liter-

ature [111, 286, 289, 369–372]. The momentum exchange term ($\Psi^{\mathbf{u}}_{ij}$) includes the mean and turbulent interaction between fluid and solid phase.

Momentum Exchange   Velocity differences and hydro-static and static pressure effects cause momentum exchange in multi-phase flows. Considering the drag force ($\boldsymbol{M_D}$), the turbulent dispersion force ($\boldsymbol{M}_{TD}$), the lift force ($\boldsymbol{M}_L$), and the virtual mass force ($\boldsymbol{M}_{VM}$), the momentum exchange term can be expressed as [288, 366, 367, 370, 373]:

$$\Psi^{\mathbf{u}}_{ij} = \boldsymbol{M}_D + \boldsymbol{M}_{TD} + \boldsymbol{M}_L + \boldsymbol{M}_{VM} \tag{2.116}$$

The lift force includes forces caused by static or hydro-static pressure differences, while the virtual mass force represents the force necessary to accelerate the continuous phase surrounding the dispersed phase [284, 365]. The drag force ($\boldsymbol{M_D}$) expresses the momentum exchange due to the mean relative velocity between the phases, whereas the turbulent dispersion force ($\boldsymbol{M}_{TD}$) represents the momentum exchange caused by random velocity fluctuations [352, 369, 370, 374, 375]. A common simplification for small particles is to disregard the turbulent dispersion force ($\boldsymbol{M}_{TD}$), but this approach neglects turbulent momentum exchange between the phases [282, 355, 376–379]. The turbulent dispersion force causes a diffusion-like transport of the dispersed phase from regions of high-dispersed phase fraction towards regions of low concentration [357, 365–368]. Squires and Eaton [380] showed that dispersed phases tend to cluster in certain regions, due to turbulent interactions between continuous and dispersed phases.

Multi-Phase k-ε Model   Elghobashi and Abou-Arab [381] proposed a turbulence model for gas-solid flows, which is similar to the k-ε turbulence model. The conservation equation for turbulent kinetic energy (k) (compare Equation 2.98) and turbulent dissipation rate (ε) (compare Equation 2.99) is solved for the fluid phase by incorporating source terms for the gas-phase turbulence modulation by dispersed solids:

$$\begin{aligned}
\frac{\partial}{\partial t} \left(\overline{\alpha}_g \rho_g k_g \right) + \nabla \cdot \left(\overline{\alpha}_g \rho_g \overline{\boldsymbol{u}}_g k_g \right) &= \nabla \cdot \left[\overline{\alpha}_g \left(\mu_g + \frac{\mu_{t,g}}{\sigma_k} \right) \nabla k_g \right] \\
&+ \overline{\alpha}_{\mathrm{g}} P_{k,g} - \overline{\alpha}_{\mathrm{g}} \rho_g \varepsilon_g + \Psi^{\overline{\mathbf{u}}}_{gs} \left(k_{sg} - 2k_g \right)
\end{aligned} \tag{2.117}$$

$$\frac{\partial}{\partial t} \left(\overline{\alpha}_g \rho_g \varepsilon_g \right) + \nabla \cdot \left(\overline{\alpha}_g \rho_g \overline{\mathbf{u}}_g \varepsilon_g \right) = \nabla \cdot \left[\overline{\alpha}_g \left(\mu_g + \frac{\mu_{t,g}}{\sigma_\varepsilon} \right) \nabla \varepsilon_g \right]$$
$$+ \overline{\alpha}_g \frac{\varepsilon_g}{k_g} \left(C_{1\varepsilon} P_{k,g} - C_{2\varepsilon} \rho_g \varepsilon_g \right) + C_{3\varepsilon} \frac{\varepsilon_g}{k_g} \Psi_{ij}^{\overline{\mathbf{u}}} \left(k_{sg} - 2k_g \right) \tag{2.118}$$

The dispersed phase turbulence modulation (k_{sg}) is defined as a function of the gas-phase turbulent kinetic energy and inter-phase momentum terms based on the virtual mass force coefficient (C_{VM}) [43, 286, 381]:

$$k_{sg} = 2k_g \left(\frac{(1 + C_{VM}) / \left(\frac{\rho_s}{\rho_g} + C_{VM} \right) + \eta_{sg}}{1 + \eta_{sg}} \right) \tag{2.119}$$

η_{sg} is the ratio of the Lagrangian integral time scale (τ_L) and the particle relaxation time scale (τ_p) [382]:

$$\eta_{sg} = \frac{\tau_L}{\tau_p} \tag{2.120}$$

The particle relaxation time is a function of the drag coefficient (C_D) and C_{VM}:

$$\tau_p = \frac{\alpha_s \rho_s}{C_D} \left(\frac{\rho_s}{\rho_g} + C_{VM} \right) \tag{2.121}$$

The Lagrangian integral time scale is defined as the ratio of the characteristic energetic eddy time scale (τ_{eddy}) and a factor for the turbulent gas-particle interaction (ζ) [286, 383]:

$$\tau_L = \frac{\tau_{eddy}}{\sqrt{1 + (1 - 1.35 \cos^2 \Theta) \zeta}} \tag{2.122}$$

with:
$\Theta = $ angle between the dispersed and the relative velocity

The three unknown parameters in Equation (2.122) are defined as follows [286, 383]:

$$\zeta = \frac{|\mathbf{u}_{sg}| \tau_t}{L_t} \tag{2.123}$$

$$\tau_{eddy} = \frac{2}{3} C_\mu \frac{k_g}{\varepsilon_g} \tag{2.124}$$

$$L_t = \sqrt{\frac{2}{3}} C_\mu \frac{k_g^{3/2}}{\varepsilon_g} \tag{2.125}$$

The multi-phase turbulence model reproduces the turbulence modulation due to the presence of solid particles but disregards the additional momentum transport caused by turbulent fluid motion [282, 355, 356, 371, 376–378].

Chapter 3

Raceway Model

3.1 Model Description

The Race Way Model (*RWM*) is implemented in the open-source Computation Fluid Dynamics (*CFD*) toolbox OpenFOAM® [120]. The basis of the model development is the Euler-Euler (*E-E*) *reactingEulerFoam* solver family from OpenFOAM® version 7 [384]. The following subsections introduce the different parts of the RWM. Although the model was developed for the blast furnace raceway zones, its generic implementation allows for simulating many kinds of reactive gas-solid flows.

3.1.1 Solution Algorithm

A segregated Pressure-Implicit Method for Pressure Linked Equations (*PIMPLE*) E-E multiphase solution algorithm solves the coupled system of equations [293, 300]. The employed phase continuity equation is based on relative velocities (Equation 2.107) and contains source terms for the inter-phase mass transfer and solid phase pressure. The equation is solved by a flux-corrected transport solver called the Multidimensional Universal Limited Explicit Solver (*MULES*) [385, 386], neglecting the solid pressure term. The solid pressure source term contribution is subsequently solved implicitly via first-order accurate operator splitting. This solution procedure ensures the boundedness of the phase fraction and the packing limit of the solid phase.

A special frozen phase fraction option has been implemented to enable simulating a fixed raceway shape. This option preserves the spatial phase fraction distribution by not solving the phase continuity equation. Coupling between the phases is ensured since the species, energy,

momentum, and shared pressure equation are solved. This option represents a pseudo-steady system state and its applicability is limited to Local Time Stepping (*LTS*) simulations.

The RWM is a Two-Fluid Model (*TFM*) that accounts for the hot blast or reducing gas within the blast furnace and the coke phase using the Kinetic Theory of Granular Flow (*KTGF*), which is the rheologic model for the coke phase [111, 287]. Inter-phase coupling terms are discretized using Partially Implicit Treatment (*PIT*) [293]. These coupling terms rely on suitable closure relations for heat, mass, and momentum.

The RWM incorporates additional Lagrangian phases, which represent Alternative Reducing Agents (ARAs) injected into the bast furnace's tuyeres. ARA are two-way coupled with the gas phase (carrier phase) by suitable models for mass, energy, and momentum. One-way momentum coupling is possible for the interaction between coke and ARA, and pseudo drag models exist for this kind of particle-particle [111, 387, 388]. Heat and mass transfer between ARA and the coke phase is currently neglected.

The Lagrangian phases employ a computational parcel approach, which combines single particles to reduce the computational effort. The conservation equations are solved for a representative particle of each parcel assuming uniform properties (see subsubsection 2.4.1.2). Heat, mass, and momentum exchange terms between the Lagrangian and carrier phase are obtained by transferring the particle-corrected sources of each computational parcel to a Eulerian field [113]. The parcel approach is numerically efficient, but neglects intra-particle gradients [223, 389] and clustering or group effects for thermo-chemical conversion [390–393].

3.1.2 Thermo-Chemical Conversion Modeling

3.1.2.1 Gas Phase

Thermo-chemical conversion processes in the hot blast are modeled by the Eddy Dissipation Concept (*EDC*) to account for turbulent mixing effects. As discussed in section 2.1 mixing-based combustion models like the EDC might be superior to flamelet-based models, since homogeneous combustion requires solving additional conservation equations for the mixture fraction of each contributing phase in flamelet based models. Furthermore, additional mapping coordinates to correctly lookup of the species and mass source terms, which leads to an inefficient lookup process.

Using optimized reaction mechanisms [394, 395] and speed-up techniques like In-Situ Adaptive Tabulation (*ISAT*) [396, 397] makes the EDC numerically efficient. The biggest advantage of the

mixing-based models is the current focus on their improvement to cope with Moderate or Intense Low-oxygen Dilution (*MILD*) combustion conditions (subsubsection 2.1.4.1). The combustion conditions within the raceway zone change from classical combustion to MILD combustion in the vicinity of the dense coke bed [**Reviewed Conference Paper III**], thus, adaptive combustion models improve the predictive capabilities of the RWM. However, the proposed modifications of the EDC rely on the chemical time scale (τ_c) which needs a proper, numerically efficient definition for CFD modeling [**Journal Paper IV**].

3.1.2.2 Coke Phase

A Thiele based model is used for the thermo-chemical coke phase conversion, and accounts for the coke conversion's pore and boundary layer diffusion limitations. As discussed in subsubsection 2.2.4.1, Thiele Based Models (TBMs) can model isothermal and non-isothermal conversion processes. The integrated modeling of mass transport effects by TBMs makes them more suited to modeling the thermo-chemical conversion of metallurgical coke than Apparent Rate Models (ARMs) and Solid-State Kinetic Models (SSKMs) (subsection 2.2.1). Combining TBM and SSKM models can be used to capture conversion-dependent influences from the instantaneous thermo-chemical conversion process [194].

The thermo-chemical conversion of metallurgical coke is assumed to be isothermal in the raceway zone, since temperatures are above 1300 °C and slow endothermic gasification reactions prevail in most of the raceway region [16, 104, 115]. Regions where fast, exothermic oxidation reactions occur would require non-isothermal effectiveness factors for the conversion model to account for higher conversion rates occurring for exothermic reactions (see subsubsection 2.2.4.1). These regions are limited to the oxygen-rich gas streaks in the vicinity of the tuyeres. However, only a fraction of the oxygen is consumed by coke, due to the additional injection of ARAs. An advantage of the isothermal TBM approach is its numerical efficiency compared to the non-isothermal one, since analytic expressions exist for isothermal effectiveness factors. Determining non-isothermal effectiveness factors relies on the solution of reaction-diffusion boundary value problems (see subsubsection 2.2.4.1), which are numerically expensive.

Implementing the TBM heterogeneous conversion model required the creation of a suitable phase interface and mass/species diffusion library in OpenFOAM® [**Reviewed Conference Paper IV**]. The implemented *multPhaseChemistryModel* is a generic framework that provides standardized interfaces for heterogeneous chemistry. The interface collects species and energy sources, and adds them as explicit source terms to the conservation equations. Similar to the

homogeneous chemistry model, a first-order accurate operator splitting is employed for the heterogeneous chemistry contribution to the reaction-diffusion equations for the species and the energy [398].

The implemented mass diffusion library includes Knudsen diffusion, bulk diffusion, and effective diffusion. The effective diffusion coefficient (D_{eff}) is a function of the bulk and Knudsen diffusion coefficient [116, 118]:

$$D_{eff} = \frac{1}{\frac{1}{D_{Kn}} + \frac{1}{D_{bulk}}}$$ (3.1)

with:
D_{Kn} = Knudsen diffusion coefficient
D_{bulk} = bulk diffusion coefficient

The bulk diffusion coefficient is calculated according to the Wilke mixing rule [399]:

$$D_{i,bluk} = \frac{(1 - x_i)}{\sum_{j \neq i} \frac{x_j}{D_{i,j}}}$$ (3.2)

with:
$D_{i,j}$ = binary diffusion coefficient
x = mole fraction

Binary diffusion coefficients are determined by employing the simplified Kinetic Theory of Gases (*KTG*) proposed by Hishida and Hayashi [400]. The Knudsen diffusion coefficient of a species correlates with the pore diameter (d_{pore}), the molar weight (W), and the temperature (T) [116, 118]:

$$D_{Kn} = \frac{d_{pore}}{3} \sqrt{\frac{8\mathcal{R}T}{\pi W}}$$ (3.3)

with:
$\mathcal{R}$ = ideal gas constant

The generic TBM approach relies on suitable correlations for the mass transfer coefficient and effectiveness factor, which can be found in literature for various particle shapes and particle beds.

3.1.2.3 Alternative Reducing Agent (*ARA*)

The thermo-chemical conversion of ARA needs to be numerically efficient, since chemistry must be solved for each Lagrangian parcel. The ARA conversion process, e.g. pulverized coal, consists

of three consecutive stages: drying, devolatilization, and oxidation and gasification [7, 184]. Absorbed water is removed from the solid during drying, while volatile compounds degas during devolatilization. The remaining carbon-rich solid matrix is subsequently oxidized by oxygen or gasified by carbon dioxide, hydrogen or water vapor.

Drying A thermal drying model assumes that moisture is evaporated by the incoming heat flux above the boiling point at constant particle temperature [184]. The drying rate is then given as the ratio of the total heat flux ($\dot{Q}_{tot}$) (convective and radiative) towards the particle and the enthalpy of vaporization (ΔH_{vap}):

$$\frac{dm_m}{dt} = \begin{cases} 0 & T < T_{boil} \\ \frac{\dot{Q}}{\Delta L_{vap}} & T \geq T_{boil} \end{cases} \tag{3.4}$$

with:
$$\begin{aligned} m_m &= \text{moisture mass} \\ t &= \text{time} \\ T_{boil} &= \text{boiling temperature} \end{aligned}$$

Thermally-controlled drying might be a reasonable approximation for pulverized coal conversion under high heating rates, as prevalent in the blast furnace raceway. The drying rates for larger solids might also be mass-transfer limited and, furthermore, can be affected by intra-particle temperature and concentration gradients.

Devolatilization Volatiles, typically small hydrocarbons and tars, degas during devolatilization. The volatiles emerge from the thermal cracking of higher hydrocarbons [185]. The devolatilization of pulverized coal is modeled by a competing rate model that considers two degradation pathways [119, 401, 402]:

$$\frac{dm_v}{dt} = \left[\zeta_1 \cdot A_1 \cdot \exp\left(\frac{-E_{a,1}}{\mathcal{R}T}\right) + \zeta_2 \cdot A_2 \cdot \exp\left(\frac{-E_{a,2}}{\mathcal{R}T}\right) \right] \tag{3.5}$$

with:
$$m_v = \text{volatile mass}$$

ζ_1 and ζ_2 represent the mass stoichiometric coefficients. ζ_1 is typically chosen to be the volatile content of the coal, while ζ_2 is determined by [403]:

$$\zeta_2 = 1.25\ \zeta_1^2 + 0.92\ \zeta_1 \tag{3.6}$$

The Arrhenius parameters for the two competing rate models must be determined from the experimental data for the corresponding coal and devolatilization conditions.

A prerequisite for this apparent rate devolatilization model is isothermal particles. Thus, non-isothermal devolatilization models are required for ARA other than pulverized coal. A shell-core model has been previously used for the devolatilization of large-sized (millimeter) plastic particles [16, 104, 115]. The shell-core model is a thermal model that assumes that devolatilization starts at a certain temperature. An isothermal particle is assumed during the pre-heating, while the particle temperature is kept constant assuming devolatilization only occurs at the surface during the degassing process. The devolatilization rate is given by:

$$\frac{dm_v}{dt} = \begin{cases} 0 & T < T_{dev} \\ \dfrac{\dot{Q}}{\Delta H_{dev}} & T \geq T_{dev} \end{cases} \tag{3.7}$$

with:
$\quad T_{dev} \quad$ = devolatilization temperature
$\quad \Delta H_{dev}$ = enthalpy of devolatilization

These kinds of surface devolatilization models tend to overestimate the heat flux towards the particle, since the surface temperature is kept constant at the devolatilization temperature. However, they are numerically more efficient compared to single-particle models, which resolve the intra-particle gradients (see subsubsection 2.2.4.2).

Oxidation and Gasification The oxidation and gasification of the residual char might be a mass transfer-limited process in certain regions of the raceway zone. However, employing a TBM model for each computational model is numerically too expensive. A simplified approach for the oxidation and gasification is obtained by assuming a first-order reaction with a fixed effectiveness factor (η_{eff}) and an approximation of the diffusion-limited conversion rate using the kinetic conversion rate (k_R) and the diffusion rate (Ω) [119, 404, 405]:

$$\frac{dm_C}{dt} = \eta_{eff} S_A \frac{\Omega \cdot k_R}{\Omega + k_R}\ p_i \tag{3.8}$$

with:

m_c = char mass
S_A = surface area
p_i = species partial pressure

The kinetic conversion rate is expressed by the Arrhenius rate expression, while the diffusion rate is approximated by [405]:

$$\Omega = \frac{\Omega_0}{d_P} \left(\frac{T_P + T_\infty}{2} \right)^{0.75} \tag{3.9}$$

with:
Ω_0 = reference diffusion coefficient
d_P = particle diameter
T_P = particle temperature
T_∞ = bulk temperature

This simplified conversion model is numerically efficient and can reproduce mass transport-limited particle combustion. Investigating pulverized coal oxidation revealed that the ratio between carbon monoxide and carbon dioxide is temperature dependent. This temperature dependence arises from gas phase reactions in the boundary layer, which are not captured by simplified models [228, 406]. Therefore, temperature-dependent stoichiometric coefficients (Ψ) are used for the global char oxidation reaction:

$$\Psi \, C_{(s)} + O_2 \rightarrow 2(\Psi - 1) \, CO + (2 - \Psi) \, CO_2$$
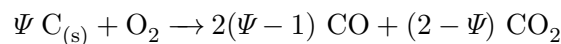
The temperature dependence of the stoichiometric coefficient is given by an Arrhenius-type expression [407]:

$$\frac{2 \, (\Psi - 1)}{2 - \Psi} = A_s \cdot \exp \left(-\frac{T_s}{T_P} \right) \tag{3.10}$$

3.2 Validation

This section summarizes and briefly discusses the problems used to validate the modeling framework. Thoroughly validating the individual sub-models is a prerequisite for reliable modeling results. A step-wise model validation was conducted, starting with heat-transfer problems, followed by homogeneous and heterogeneous combustion.

3.2.1 Heat Transfer

3.2.1.1 Low Temperature Heat Transfer

The experimental setup used by Dixon [408, 409] consists of a ceramic pebble bed in a pipe which is heated to 100 °C from the outside by steam. Cold air passes through the pipe cooling the particle bed. The emerging radial temperature profile is measured at the exit of the packing. Figure 3.1 illustrates the experimental setup.
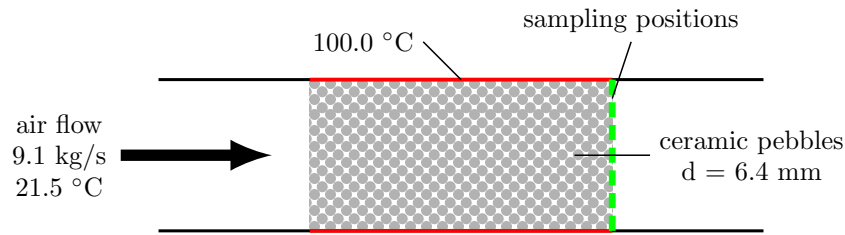

Fig. 3.1: Schematic illustration of the experimental setup of the Dixon test case; adapted from [408, 409].

The simulation domain consists of adiabatic inlet and outlet regions surrounding the pebble bed to ensure a proper flow profile in the heat transfer region. The momentum transfer is modeled by the Ergung [410, 411] model, while the heat transfer is modeled using the Nusselt correlation proposed by Gnielinski [412]. Turbulence is modeled by the standard Reynolds-Average Navier-Stokes (*RANS*) k-ε-model. The Zehner-Bauer-Schlünder Model (*ZBS*) [413, 414] is employed for the effective heat transfer in the Eulerian solid phase. The wall effect is considered in the porosity distribution of the packed bed by the expression of Giese [409, 415], assuming a bulk porosity of 0.40:

$$\epsilon(r) = \epsilon_\infty \cdot \left(1 + 1.36 \cdot \exp^{\left(-5 \cdot \frac{x_w}{d_P}\right)}\right) \tag{3.11}$$

with:
ϵ = porosity
ϵ_∞ = bulk porosity
x_w = wall distance

Figure 3.2 shows the central, axial temperature profile (a) and compares the simulated and measured radial temperature profiles (b). The predicted radial temperature profile is in reasonable agreement with the measured data, with some minor discrepancies near the center of the pipe. The radial temperature profile is sensitive to the heat flux from the pipe towards the fluid and solid phase. Neglecting the wall effect increases the central temperatures.
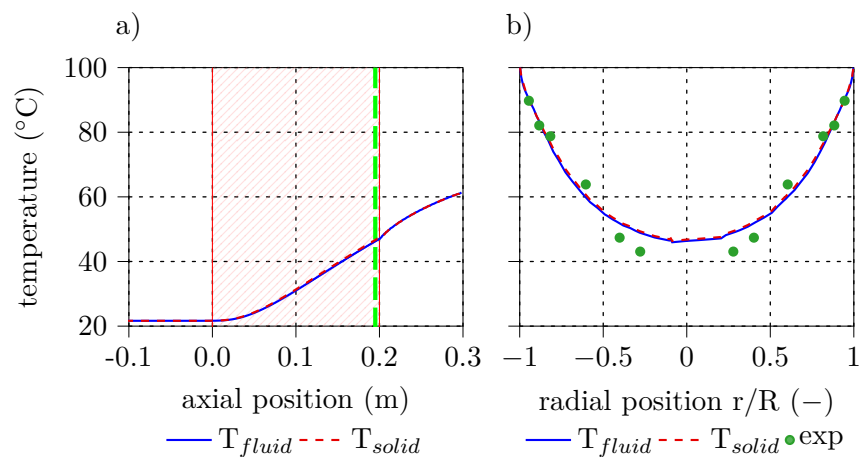
Fig. 3.2: Simulated axial temperature profile at the center line (a) and comparison between the measured [408, 409] and simulated radial temperature profile (b) for the Dixon test case. In a) the hatching indicates the pebble bed, while the dashed line indicates the sampling position from the radial temperature profile.

Figure 3.3 and Figure 3.4 depict the cross sectional and radial temperature and velocity contours from the Dixon case. The velocity contours indicate a homogeneous velocity profile through the majority of the packing. However, a significant share of the fluid passes the packing through the highly porous regions at the inner pipe surface due to the wall effect. The heat flux absorbed by the fluid next to the wall decreases the heat flux towards the pebble bed and decreases the central temperature of the pebble bed.
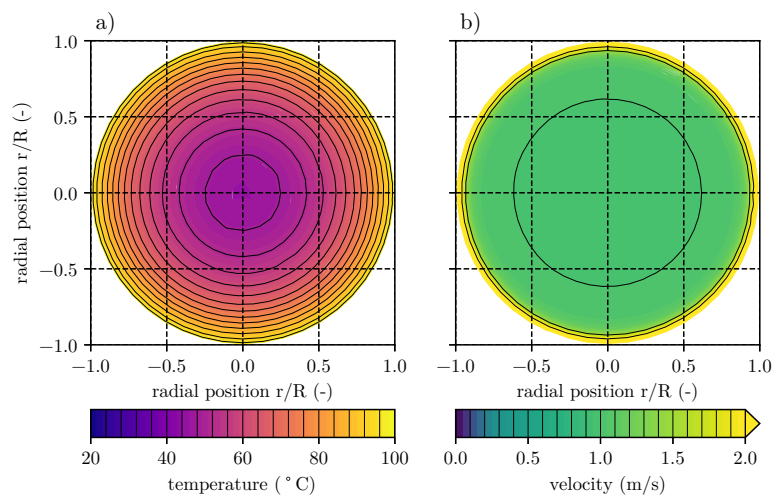
Fig. 3.3: Simulated cross-sectional temperature (a) and velocity (b) contours at the measurement plane of the Dixon test case.
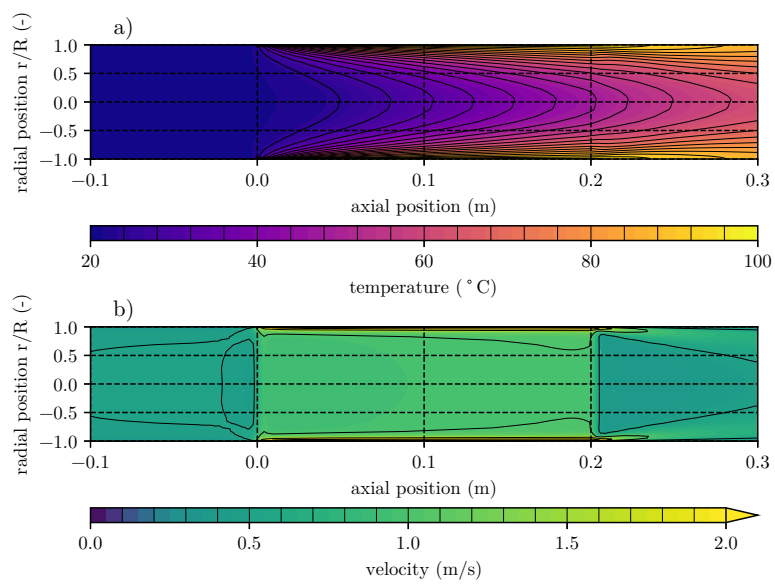
Fig. 3.4: Simulated radial temperature (a) and velocity (b) contours from the Dixon test case.

3.2.1.2 High Temperature Heat Transfer

The SANA experiment has been developed to investigate how nuclear power plants self-cool during failure events [416, 417]. Figure 3.5 shows a cut through the cylindrical experimental setup. The centrally-located heater is surrounded by a packed bed of graphite spheres filled with nitrogen or helium. Several insulation layers cover the upper and lower bed surface to provide adiabatic conditions in axial direction. A radial temperature profile emerges due to natural convection in the packed bed. Multiple experiments using different ceramic spheres, gases, and heating powers have been conducted with the SANA setup.
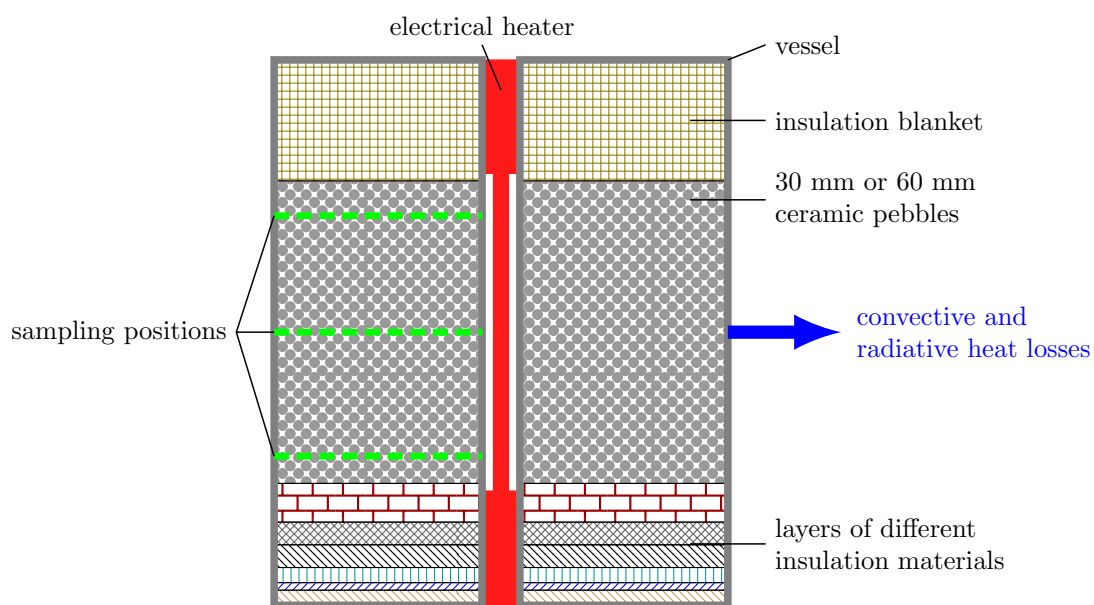
Fig. 3.5: Schematic illustration of the experimental setup from the SANA test case; adapted from [416, 417].

The rotational symmetric simulation domain consists of a region for each insulation layer and the pebble bed. The energy equation is solved for the insulation regions, since the regions are solids. An E-E phase system is solved for the pebble region. The individual regions are coupled by a loose coupling approach [418] employing mixed boundary conditions. Spatial variations in the bed porosity are incorporated by the expression proposed by Giese [409, 415] (Equation 3.11) using a bulk porosity of 0.41. Heat and momentum transfer between the fluid and the pebbles are modeled by the Nusselt correlation of Wakao and Kuaguei [419] and the Ergung [410, 411] model. Turbulent effects were considered by the standard k-ε-model. A constant heat loss of 8 W/m^2 and an ambient temperature of 300 K is assumed at the vessel surface, as recommended in literature [417]. Instead of modeling the heater region, temperature profiles were prescribed

at the central vessel surface. These temperature profiles were extracted from the measurement data for the corresponding cases [417]. LTS is used for the pebble region to obtain a steady-state solution, while the Semi-Implicit Method for Pressure Linked Equations (*SIMPLE*) approach is used in the solid regions.

Figure 3.6 compares the measured and simulated radial temperature profiles for multiple cases. The simulation results soundly agree with the measured temperatures. Similar dependencies between spatial variations in porosity and temperature profiles were observed for the Dixon validation case.
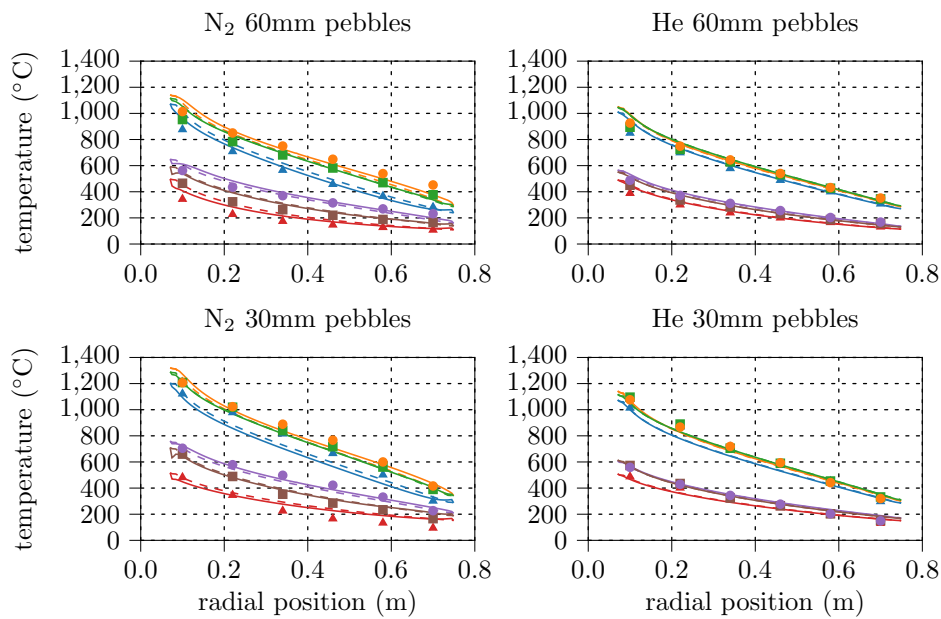
Fig. 3.6: Comparison between the measured [417] and the simulated radial temperature profiles from different SANA test conditions.

Figure 3.7 shows representative velocity and temperature contours for the SANA experiments. The buoyancy-driven flow in the vessel leads to hotspots in the upper central regions and coldspots in the lower outer regions. The high velocities next to the inner vessel wall enhance the heat removal rate from the heater towards the surroundings. The velocity field reveals that the fluid moves upwards in most vessel, except for a small region next to the outer surface where it cools down.
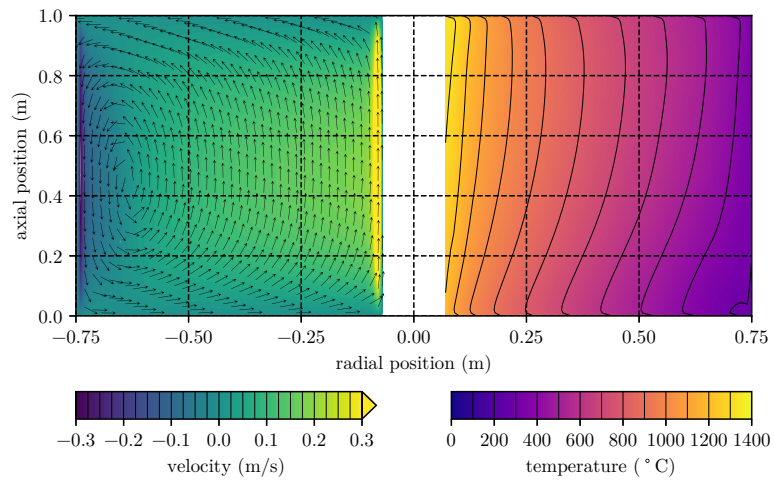
Fig. 3.7: Simulated velocity and temperature contours from the 30 kW N_2 SANA case with 30 mm graphite pebbles.

3.2.2 Combustion

3.2.2.1 Homogeneous Combustion

The homogeneous combustion model is validated with the Sandia Flame D [420–423] and Adelaide Jet in Hot Coflow (*AJHC*) flame [424].

Sandia Flame D   The flame is a piloted, under-stoichiometric premixed jet flame with a Reynolds number (*Re*) of 22,400 and a visible flame length of approx. 0.48 m. Figure 3.8 illustrates the piloted burner used in the experimental setup. The pilot flame is operated at approx. 6% of the total flame power.
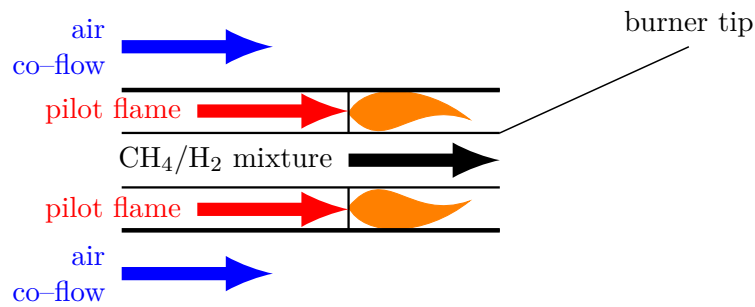

Fig. 3.8: Schematic illustration of the experimental setup of the Sandia Flame D test case [420–423].

The rotational symmetric modeling domain extends 0.5 m downstream the burner tip and 0.1 m upstream for the pilot and fuel stream. Table 3.1 summarizes the employed boundary conditions for the flame simulation.

Tab. 3.1: Sandia Flame D boundary conditions [421, 422].

species mass fraction	jet	pilot	co-flow
CH_4	0.156	-	-
CO	-	0.004	-
CO_2	-	0.110	-
H	-	$2.5 \cdot 10^{-5}$	-
H_2	-	$1.3 \cdot 10^{-4}$	-
H_2O	-	0.094	0.006
N_2	0.648	0.735	0.758
O_2	0.196	0.054	0.236
OH	-	0.003	-
T_{in} (K)	294	1880	291
u_{in} (m/s)	49.6	11.4	0.9

The EDC model version proposed by Magnussen [139] combined with the standard k-ε-turbulence model [10, 11, 278] was used in the simulations. The Plug Flow Reactor (*PFR*) Fine Structures (*FS*) closure was used for the EDC model. The $C_{\epsilon 2}$ constant was modified to 1.8 from 1.92 to account for the round-jet anomaly [425]. Radiation is modeled by the P1 radiation model [426, 427]. Gas phase radiation contribution is modeled by the Weighted Sum of Grey Gases Model (*WSGGM*) assuming grey mean absorption [428]. The specialized GRI3.0 methane combustion mechanism is used to describe the combustion chemistry [429]. An in-house developed steady-state solver based on the SIMPLE method was used for the Sandia Flame D simulations.

Figure 3.9 shows the comparison between experimental and simulated temperatures (a) and species concentrations (b). The simulation results agree well with the measured ones up to the peak temperature position. Downstream the peak temperature, the experimental and simulation temperatures start to deviate. These deviations might be caused by $C_{\epsilon 2}$ constant modification, since such modifications improve the prediction of the jet spreading rates, but tend to give poorer results further downstream [425].

Figure 3.10 shows temperature and velocity contours from Sandia Flame D. The reaction zone is located in the high-temperature regions. Comparing velocity and temperature contours indicates that the reaction zone occupies the mixing layer generated by the methane jet.
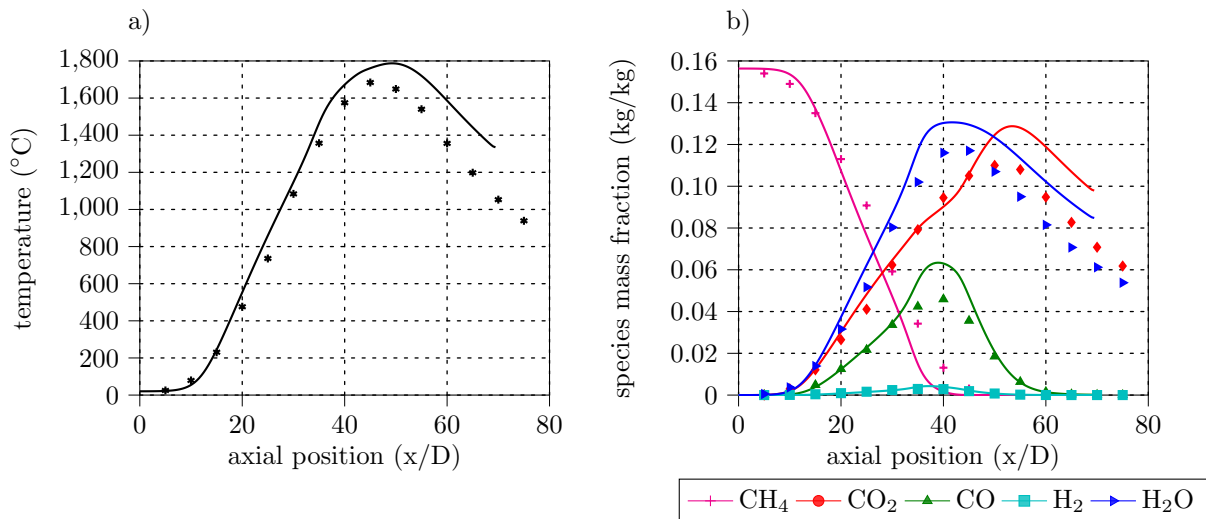

Fig. 3.9: Comparison of experimental(symbols) [421] and simulated (lines) temperature (a) and species concentration (b) center line profiles along the axial direction of Sandia Flame D.
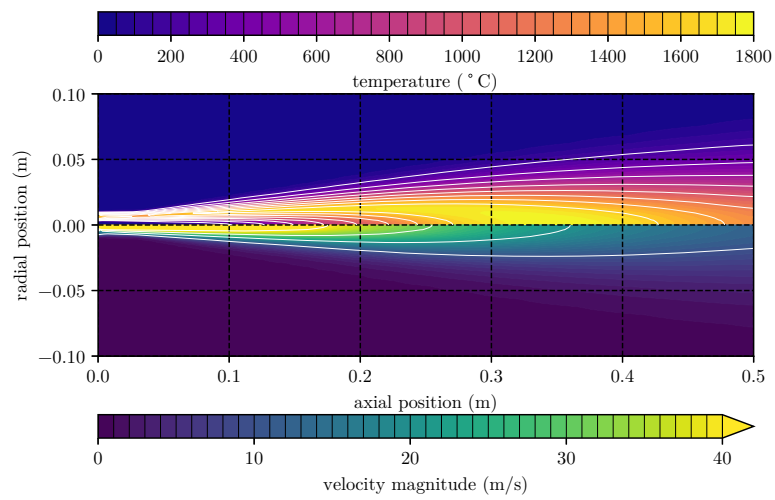
Fig. 3.10: Temperature (positive radial position) and velocity (negative radial position) contours of Sandia Flame D.

Adelaide Jet in Hot Coflow (*AJHC*)   The Adelaide Jet in Hot Coflow flame series consists of three MILD flames, each operated at a *Re* of 10,000 but at different oxygen concentrations [424]. Oxygen mass fractions of 3%, 6%, and 9% are employed for the HM1, HM2, and HM3 flames. The MILD combustion characteristics of the AJHC flames are obtained from a second burner located upstream from the burner tip. Figure 3.11 illustrates the burner setup schematically.
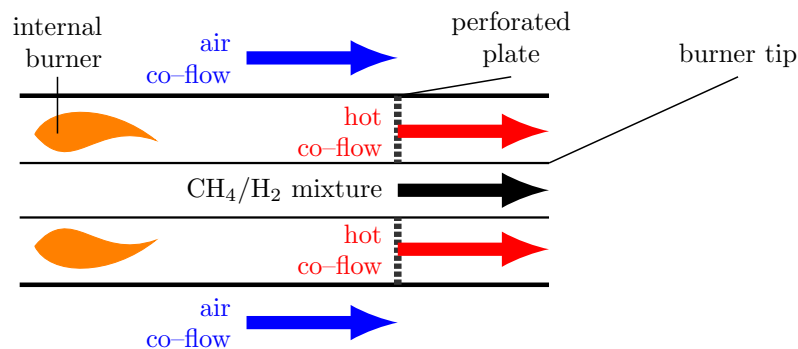

Fig. 3.11: Schematic illustration of the experimental setup of the Adelaide Jet in Hot Coflow (*AJHC*) test case [424].

A rotational symmetric domain has been used for the simulation of the AJHC HM1 flame. The simulation domain extends 0.55 m downstream the burner tip. The upstream part is neglected. Table 3.2 summarizes the employed boundary conditions for the HM1 simulation.

Tab. 3.2: Adelaide Jet in Hot Coflow (*AJHC*) HM1 flame boundary conditions [424].

species mass fraction	jet	hot co-flow	co-flow
CH_4	0.875	-	-
CO_2	-	0.055	-
H	-	0.125	-
H_2	-	0.065	-
H_2O	-	0.094	0.006
N_2	-	0.850	0.770
O_2	-	0.03	0.230
T_{in} (K)	294	1300	294
u_{in} (m/s)	58.74	3.2	3.3

The simulations were performed with the variable constant EDC version proposed by Bao [141] using the PFR FS closure. The local constant adaption relies on chemical time scales, which were determined by the method proposed by Golovitchev et al. [143, 144]. The standard k-ε-turbulence model [10, 11, 278] and the P1 radiation model [426, 427] were used in the simulations. Gas phase radiation effects were considered by the WSGGM [428]. The GRI3.0 methane combustion mechanism was used in the simulations [429]. Differential diffusion effects were incorporated

by Fick's first law using bulk diffusion coefficients determined by the Wilke mixing rule [399] using binary diffusion coefficients determined by a simplified KTG approach [400]. An in-house developed, steady-state solver based on the SIMPLE method was used for the AJHC HM1 simulations.

Figure 3.12 compares measured and simulated temperature and species concentration profiles. The simulation results show good agreement with the measured ones in axial flame direction. Figure 3.13 shows the temperature and velocity contours. The flame structure differs significantly from that of the Sandia Flame D (see Figure 3.10).
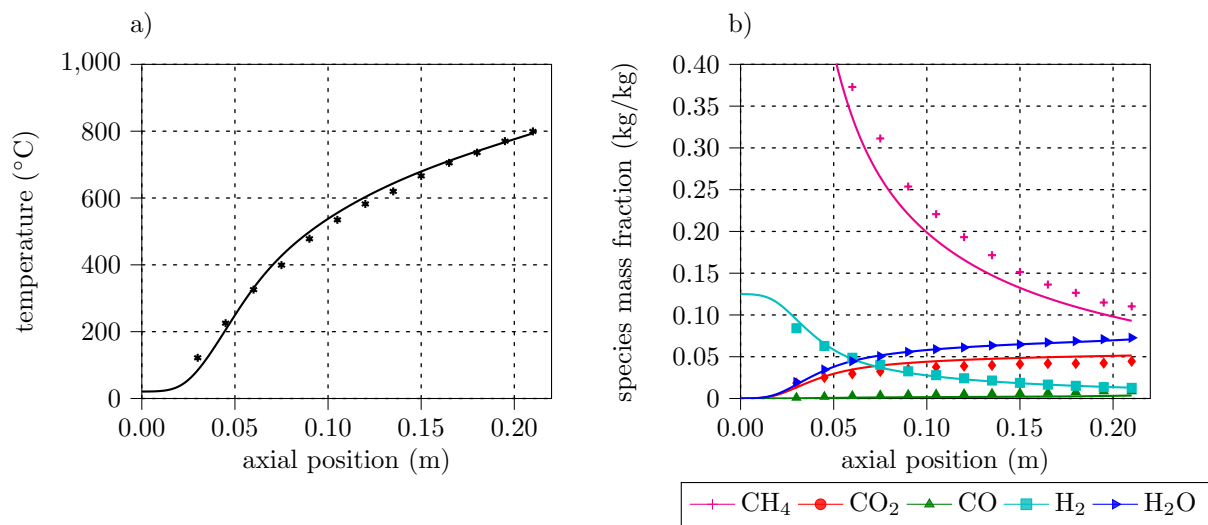

Fig. 3.12: Comparison of experimental(symbols) [424] and simulated (lines) temperature (a) and species concentration (b) center line profiles along the axial direction of the HM1 flame.
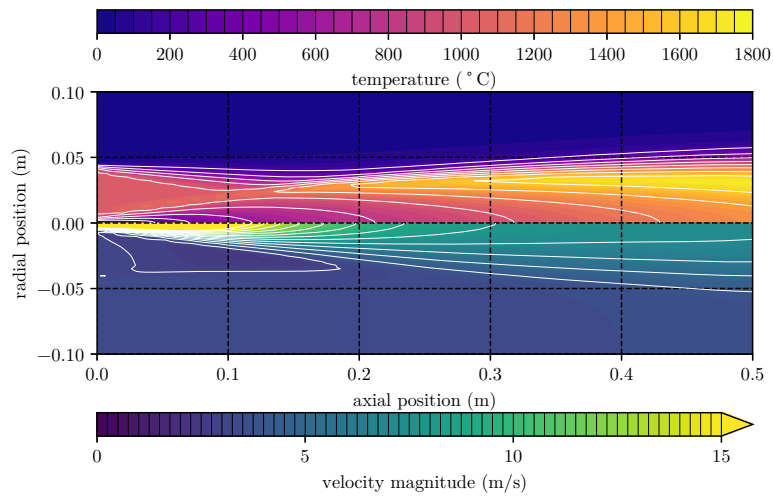
Fig. 3.13: Temperature (positive radial position) and velocity (negative radial position) contours of the HM1 flame.

3.2.2.2 Heterogeneous Combustion

The continuous gasification experiment conducted by Van de Steene et al. [430] is used to validate
the implemented heterogeneous combustion model. Figure 3.14 illustrates the experimental setup.
Pre-devolatilized biomass is continuously fed from above, while wetted propane combustion gas
flows through the char bed in co-current mode. The char bed is quasi-stationary and stagnates
from the gas stream view point. The average char and combustion gas mass flows are 28 g/min
and 275 g/min. Measuring points for temperature, pressure, and species concentrations exist
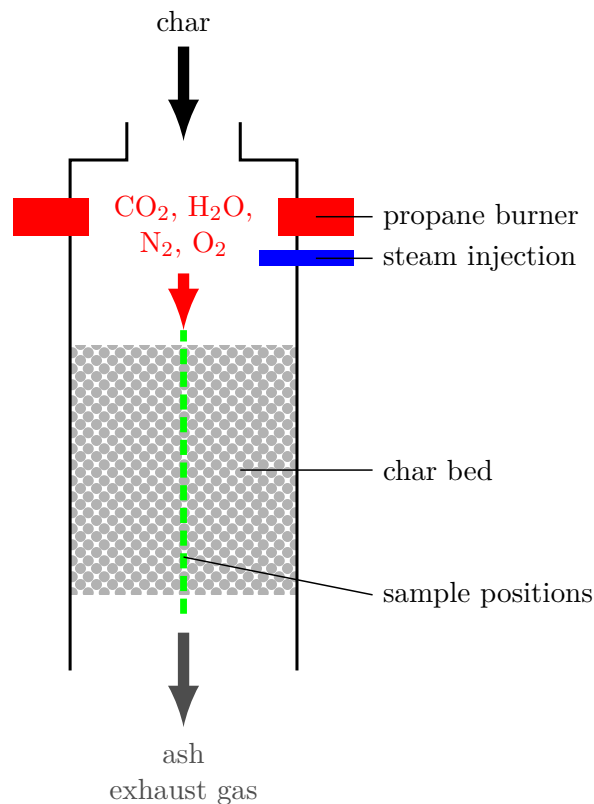along the pebble bed.

Fig. 3.14: Schematic illustration of the experimental setup of the van de Steene test case;
adapted from [430].

The cylindrical gasifier is simplified to a one-dimensional case, since the reactor can be assumed
to be adiabatic and perfectly mixed in radial position. Pre-evaluation confirmed the validity of
this approach. The char bed is assumed to be stagnant in the steady-state simulations, due its
low velocity compared to the gas phase. Table 3.3 summarizes the remaining inlet and other
boundary conditions.

Tab. 3.3: Boundary conditions of the van de Steene case [430].

inlet species mass fraction (kg/kg)	
CO_2	0.130
H_2O	0.201
N_2	0.638
O_2	0.031
inlet gas mass flow (kg/h)	16.49
inlet gas velocity (m/s)	0.68
inlet gas temperature (°C)	1020
char bed height (m)	0.65

Table 3.4 shows the properties of the biomass char gasified in the experiments. The ash as well as nitrogen and sulfur are neglected, and constant particle size is assumed for the simulation.

Tab. 3.4: Char properties of the van de Steene case [430].

proximate analyses	
ash	0.014
volatile matter	0.049
fixed carbon	0.937
ultimate analysis	
C	0.898
H	0.022
O	0.061
N	0.001
S	< 0.001
density (kg/m^3)	900
particle diameter (m)	0.005
particle porosity (-)	0.41
particle tortuosity (-)	3.70

Table 3.5 shows the chemical mechanism used in the van de Steene test case. Heterogeneous reactions consider the oxidation and gasification (with carbon dioxide, water vapor, and hydrogen) of the biomass char. Gaseous reactions are the homogeneous Boudouard equation (included as two irreversible reactions) and the water-gas shift reaction. This global mechanism can efficiently predict the relevant features of the reactive two-phase system.

The TBM heterogeneous combustion model requires correlations for the mass transfer between gas and solid, and an expression for the effectiveness factor (η_{eff}). The Sherwood correlation suggested by Petrovic and Thodos [435] is used for the van de Steene case:

Tab. 3.5: Chemical mechanism used for the van de Steene case case [102, 115].

gas phase reactions	Units: kmol/ m³/K	
reaction	A	T_a
$CO_2{}^1 \longrightarrow CO^0 + 0.5\,O_2{}^0$	$5 \cdot 10^8$	20446 [431]
$CO^1 + 0.5\,O_2{}^{0.25} \longrightarrow CO_2{}^0 + 0\,H_2O^0$	$7.08 \cdot 10^{10}$	20446 [431]
$CO^1 + H_2O^1 \rightleftharpoons CO_2{}^1 + 0.5\,H_2{}^1$	$2.75 \cdot 10^9$	10064 [432]
gas-solid reactions	Units: mol/kg/m³/K	
reaction	A	T_a
$CH_{0.292}O_{0.051}{}^0 + 1.0475\,O_2{}^{0.59} \longrightarrow CO_2{}^0 + 0.146\,H_2O^0$	$4.8 \cdot 10^9$	16731 [237]
$CH_{0.292}O_{0.051}{}^0 + CO_2{}^{0.13} \longrightarrow 2\,CO^0 + 0.051\,H_2O^0 + 0.095\,H_2{}^0$	$2.7 \cdot 10^5$	18520 [237]
$CH_{0.292}O_{0.051}{}^0 + 0.949\,H_2O^1 \longrightarrow CO^0 + 1.095\,H_2{}^0 + 0.095\,H_2{}^0$	3.42	15600 [433]
$CH_{0.292}O_{0.051}{}^0 + 1.905\,H_2{}^1 \longrightarrow CH_4{}^0 + 0.051\,H_2O^0$	$3.42 \cdot 10^{-3}$	15600 [434]

$$Sh = \frac{0.375}{\epsilon} Re^{0.641} \cdot Sc^{1/3} \tag{3.12}$$

with:
  Sh = Sherwood number
  Sc = Schmidt number

The expression derived from Liu and Niksa [436] is used for η_{eff}:

$$\eta_{eff} = \frac{1}{\phi_{Th,i}} \cdot \left(\frac{1}{\tanh(\phi_{Th,i})} - \frac{1}{\phi_{Th,i}} \right) \tag{3.13}$$

with:
  $\phi_{Th,i}$ = Thiele modulus

Inter-phase heat transfer is modeled with the expression proposed by Wakao and Kuaguei [419], while the momentum transfer is modeled via the Ergun expression with modified constants [410, 411]. The inertial and viscous constants were set to 1.8 and 176, respectively. An LTS solution algorithm is used to advance to a steady-state solution. Chemistry source terms are linearized around mass fractions of 0 and 1 to accelerate steady-state convergence [437].

Figure 3.15 compares the measured and simulated species concentration (a), temperature (b), and relative pressure (c) profiles. Species concentrations show reasonable agreement between simulation and experiments. The simulation does not capture the experimentally-observed water

vapor consumption above and in the first half of the char bed, since continuous char feeding is neglected. The hydrogen content is under-predicted in the upper half of the bed, while it is over-predicted in the lower half. Carbon monoxide is over-predicted throughout the particle bed, while the carbon dioxide is well predicted for most of the bed. Predicted temperatures are below the measured ones above the char bed. Intense oxygen consumption results in a steep temperature increase directly at the surface of the particle bed. Simulated temperatures decrease downwards in the particle bed and under-predict the experimental ones in the lower half of the bed. The relative pressure drop is predicted in line with the measured one.
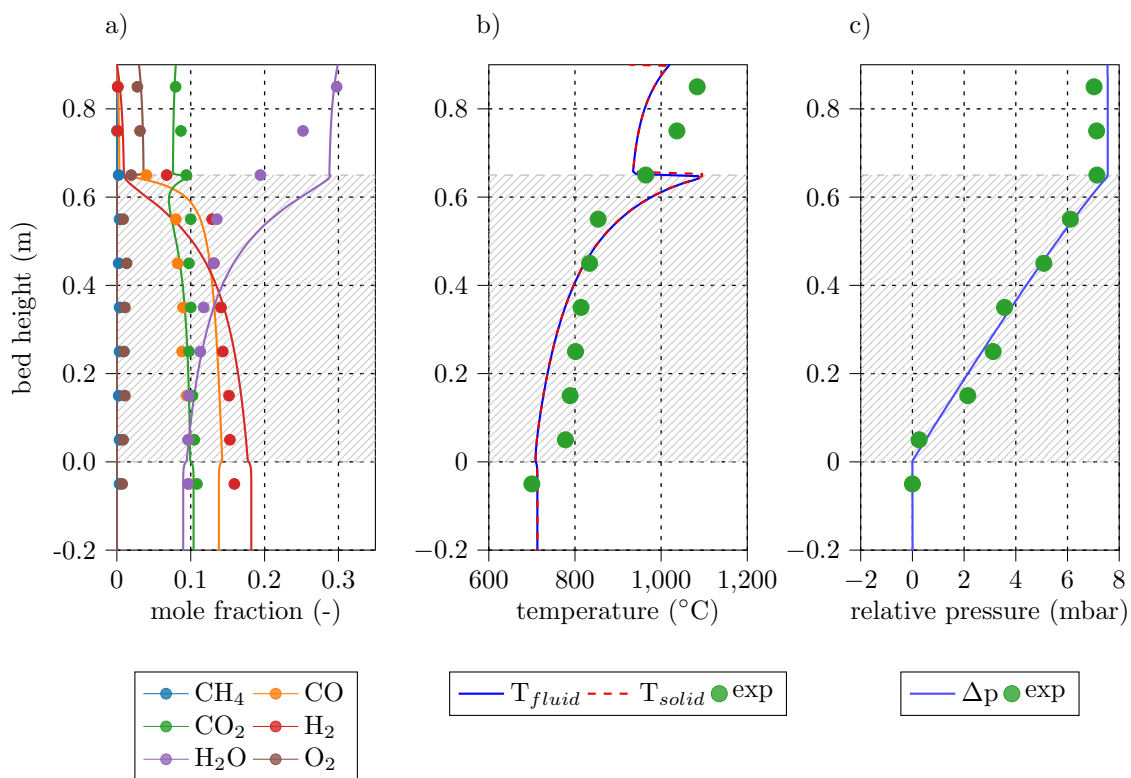

Fig. 3.15: Comparison of the experimental [430] and simulated species concentrations (a), temperature (b), and relative pressure (c) profiles from the van de Steene case. The hatching indicates the position of the char bed. Symbols indicate experimental results, while lines indicate simulated results.

Chapter 4

Summary and Discussion

4.1 Identification of Conversion Rates Under Blast Furnace Conditions

The quality of the raceway modeling results relies on suitable kinetic parameters determined under similar conditions as they exist in the raceway zone of blast furnaces. A review of existing equipment revealed that test rigs which are suitable to determine solid Alternative Reducing Agent (*ARA*) conversion rates are sparse [438][**Journal Paper I**]. A mechanistic evaluation of the thermo-chemical conversion process indicates that the conversion temperature, heating rates, pressure, and particle size are the major influence parameters. The existing coal test rigs were evaluated with regard to the reference blast furnace conditions from Table 1.1. The evaluation neglects particle diameters, since they can be readily adapted for any test rig. Heating rates and/or pressure limitations for existing equipment limits the applicability of blast furnace conditions in most cases, while temperatures up to 1,500 or 1,700 °C are feasible in most test rigs. However, none of the investigated test rigs seems to achieve the necessary particle heating rates at elevated pressures.

Sandia's Pressurized Entrained Flow Reactor (*PEFR*) [**Journal Paper II**] is one of the few reactors capable of roughly providing blast furnace conditions, permitting experimental temperatures and pressures of up to 1,400 °C and 20 atm are possible. A Computation Fluid Dynamics (*CFD*) analysis of the Pressurized Entrained Flow Reactor (*PEFR*) revealed particle heating rates of up to $8 \cdot 10^4$ K/s [**Journal Paper II**]. Analyzing the temperature velocity distributions indicated substantial homogeneities in the vicinity of the injection point. Gas phase temperature deviations in the reaction zone from the set point temperature are significant. Additional deviations of the particle residence time in the simulation and the residence time,

assuming plug flow, introduce an error of approximately 10% in extracted kinetic parameters at ambient pressure. Similar errors/uncertainties might exist in kinetic parameters derived by other experimental setups, since most evaluation methods assume homogeneous velocity, temperature, and species distributions. However, this needs to be verified for each individual test rig.

These results suggest that detailed knowledge of the reaction zone is required to extract reliable kinetic parameters. The spatial temperature, velocity, and species distributions might be obtained by a comprehensive experimental setup or spatially-resolved modeling. Simone et al. [439] proposed a method to extract global kinetic parameters by combining experimental data and CFD, taking advantage of the predicted spatial temperature, velocity, and species distributions. Sophisticated diffusion-limited conversion models are required to derive comprehensive and reliable kinetic parameters based on intrinsic conversion rates [188, 190], since pulverized coal conversion under blast furnace condition is partially pore-diffusion limited (Regime **II**) [**Reviewed Conference Paper I**]. Recently, Mularski et al. [119] summarized commonly used models for the thermo-chemical conversion of carbon-rich solids.

Mitchell [440], Hurt and Mitchell [441], Murphy and Shaddix [442] proposed techniques to derive solid particle conversion rates based on the temperature difference between the particle surface and the surrounding fluid. This approach is insensitive to the particle history, since the conversion rate is determined by solving a local heat balance. The particle's diameter, velocity, and temperature, as well as the ambient fluid temperatures, need to be measured to close the heat balance. CFD modeling could be used to extract particle velocities and ambient temperatures to close the instantaneous energy balance.

The following issues must be considered to derive reliable kinetic parameters from experiments under raceway conditions:

- Pressure, conversion temperature, and heating rates need to be as close as possible to the actual conversion conditions in the raceway [**Journal Paper I**]. The conversion conditions may vary significantly over the flight time: Hot blast temperatures are around 1,200 °C, while they might exceed 2,000 °C in the raceway cavity. Furthermore, the blast particle slip velocity significantly decreases after leaving the lance [**Reviewed Conference Paper I**].

- The heating rate at elevated pressures is the critical feature for reproducing raceway conditions in test rigs [**Journal Paper I**]. Taking into account the published test rig parameters presented in the literature indicates that a flame sheet is required at the ARA injection point to obtain heating rates similar to the raceway zone.

- The extraction of reliable kinetic parameters for blast furnace conditions requires sophisticated approaches, which incorporate the spatial distributions of the temperature, velocity, and species [**Journal Paper II**]. CFD-aided approaches are convenient since they provide an efficient way understand complex flow, heat, and mass transfer phenomena that occur in lab-scale equipment. Moreover, CFD enables determining spatially-resolved velocity, temperature, and species concentration profiles within the test rig.

- An efficient and reasonable method for extracting kinetic parameters could employ the Euler-Lagrange (*E-L*) approach, where two-way coupled ARA tracer particles, which are tracked through the test rig, undergo thermo-chemical conversion. One way to extract kinetic parameters is to employ an optimization procedure that adopts selected Arrhenius parameters to minimize the difference between the simulated and experimental particle conversion. Intrinsic reaction parameters can be determined by employing diffusion-limited particle conversion models for the optimization procedure. Statistical methods can be employed for the kinetic parameter extraction when using the Euler-Lagrange (*E-L*) approach, since an arbitrary number of computational particles can be used in the evaluation [442, 443].

- Another way to derive kinetic parameters could use transient boundary conditions extracted from the E-L simulations for detailed single particle conversion simulations. The detailed simulations enable thoroughly studying the thermo-chemical conversion process for representing ARA particles. Intra-particle temperature gradients and effectiveness factors can be derived from the detailed simulations. Furthermore, reliable kinetic parameters can be determined by fitting diffusion limited models from the detailed simulations.

4.2 Modeling Framework

A modeling framework for the simulation of industrial-scale, multi-phase reactive flows has been developed, with a special focus on ironmaking processes. The Euler-Euler (*E-E*) Multi-Fluid Model (*MFM*) model is capable of incorporating an arbitrary number of continuous phases. Dilute discrete phases can be used for modeling the thermo-chemical conversion of ARAs in the raceway zone. The current implementation allows for two-way coupling between one Eulerian phase and multiple Lagrangian phases. One-way coupling between multiple Eulerian and Lagrangian phases is possible with suitable models.

Homogeneous reactions are modeled by the Eddy Dissipation Concept (*EDC*), which is a turbulent mixing-based combustion model. The EDC can model gas phase reactions for a broad range of turbulent Damköhler numbers (Da_t) [140, 162, 167]. Unlike flamelet-based combustion models, the EDC does not require chemistry pre-processing. This is beneficial for multi-phase systems, since the pre-processing for the flamelet models is numerically expensive and, furthermore, multi-phase combustion requires multiple, additional reaction coordinates for each phase, which makes the lookup computationally expensive [132–135].

A generic multi-phase modeling framework was implemented in OpenFOAM®, which enables multi-phase chemistry in the *reactingEulerFoam* solver family. Thiele Based Models (TBMs) are used to model the thermo-chemical conversion in the metallurgical coke phase. Isothermal effectiveness factor (η_{eff}) expressions are currently used in these models. Single or representative particle models could increase the accuracy of the coke conversion modeling, but numerically efficient methods are required to ensure reasonable simulation effort.

The thermo-chemical conversion models for the discrete Lagrangian phases that represent ARA use a simplified TBM assuming constant η_{eff} values and typically neglect group combustion effects. These group effects play an important role in the combustion of pulverized solids, since particles cluster in turbulent structures and deplete gaseous oxidizing or gasifing agents locally [391–393].

The advancement and improvement of the current model should focus on the following issues:

- Turbulence-chemistry interaction for Moderate or Intense Low-oxygen Dilution (*MILD*) homogeneous and heterogeneous (pulverized fuels) combustion conditions, which are similar to the prevailing conditions in the raceway zone [444, 445]. Establishing a combustion model suitable for a broad range of Da_t is essential from a modeling perspective [**Reviewed Conference Paper III**]. A critical component of current approaches, e.g. the EDC, is an efficient, well defined chemical time scale and the thorough characterization of the combustion conditions [167][**Journal Paper IV**]. Another aspect is that the influence of the dense coke bed on the gas phase chemistry remains unclear for MILD conditions, since previous and current research focuses on jet flames.

- It is necessary to thoroughly investigate the consequences of the assumption that metallurgical coke conversion is isothermal in the raceway zone and bosh. Isothermal conversion might be a reasonable assumption in most of the furnace, due to the slow coke velocities. However, the intense oxidation and gasification occurring in the raceway zone and the

adjacent region of the coke bed might induce significant intra-particle temperature gradients. Exothermic effects can increase the effectiveness factor by several orders of magnitudes, while endothermic reactions reduce the solid reactivity [200]. If these opposed effects are dominant, assuming isothermal conversion would result in the under-estimation of coke oxidation rates and, would thus, over-predict the ARA replacement ratio.

- The dynamic prediction of the raceway size and shape is essential for correctly predicting the ARA conversion. Current Two-Fluid Model (*TFM*) or MFM use the Kinetic Theory of Granular Flow (*KTGF*) to model the rheology of the particulate phases [111]. The KTGF intrinsically relies on particle velocity fluctuations, which limits their applicability for slowly-moving packed beds. Special models have been developed for dense flows to overcome this issue [287, 344, 446]. Nevertheless, using the KTGF for dense packed beds is questionable. Therefore, other, suitable modeling approaches should be used for the dense part of the packing. Discrete approaches would be the first choice, but exceed current computing capacity. Blended modeling approaches using the KTGF for the raceway zone and suitable continuum approaches for packed beds could solve this issue [112, 344, 446].

- The pulverized ARA conversion model currently neglects particle-particle interaction for mass, energy, and momentum. A first step towards more realistic thermo-chemical conversion behavior is to implement a group combustion model, which accounts for the preferential clustering of small particles in turbulent structures and the resulting conversion rate reduction due to the depletion of gas phase reactants in particle clusters [392, 393]. Similar considerations are required for the energy exchange, since thermal radiation is dominant in the raceway zone, thus, shielding effects might occur in particle clusters [390].

Chapter 5

Conclusion and Outlook

5.1 Identification of Conversion Rates Under Blast Furnace Conditions

As noted in chapter 4, reproducing raceway conditions requires specially designed experimental equipment. If such a lab-scale reactor is available, extracting reliable kinetic parameters poses an additional challenge. Experimental data is limited to distinct measurement locations or final gas and solid properties. Kinetic parameters can be obtained by optimizing them to fit either the overall burnout [443] or the instantaneous energy balance based on the temperature difference between the particle and the fluid [440, 442]. The latter approach is not vulnerable to history effects but requires measuring the particle size, velocity, and temperature. Computation Fluid Dynamics (*CFD*) can be used to improve knowledge about the velocity, temperature, and species distributions within the lab-equipment and to improve the quality of the obtained kinetic parameters.

Additional insights can be obtained by extracting the detailed particle conversion conditions from the Euler-Lagrange (*E-L*) simulations and use them as boundary conditions for detailed single particle simulations. These simulations allow for an in-depth analysis of the thermo-chemical conversion processes and help to understand the complexity of the involved heat and mass transfer effects of the experiment. Figure 5.1 shows snapshots of the single particle heat-up within the Sandia Pressurized Entrained Flow Reactor (*PEFR*). Transient boundary conditions were extracted from the E-L simulations presented in [**Journal Paper II**]. The intra-particle temperature distribution indicates thermally thick behavior of the 97.5 μm coal particle for the assumed constant coal properties. By replacing the inert particle from the current simulation

with a single particle model, the single particle combustion behavior within the PEFR can be studied in detail.
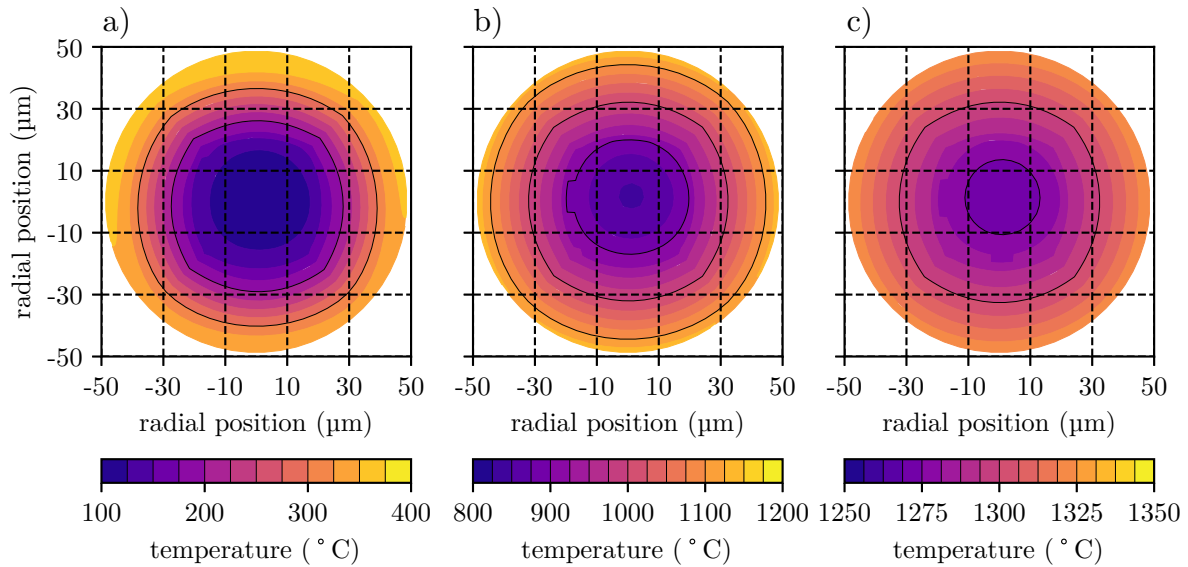

Fig. 5.1: Radial coal particle temperature snapshots for a representative coal particle in the Pressurized Entrained Flow Reactor (*PEFR*) after residence times of 0.01 (a), 0.1 (b), 0.2 (c) seconds.

5.2 Modeling Framework

The suggested model improvements discussed in chapter 4 summarize the discrepancies between the model implementation and the underlying physical phenomena. However, since the overall aim is to establish a digital twin of the blast furnace, additional functionality must be added to the current modeling framework. A critical step toward the full-scale raceway modeling is the sophisticated three-phase (solid, liquid, gas) coupling for mass, energy, and momentum [447, 448]. This coupling also relies on numerically efficient approaches for the additional heterogeneous reactions occurring within the additional liquid and solid phases.

The detailed single particle modeling approach discussed in the previous section can also be applied to the thorough investigation into the thermo-chemical conversion of Alternative Reducing Agent (*ARA*) in the raceway zone. Furthermore, individual or representative metallurgical coke particles can be modeled with the same approach to improve the understanding of their thermo-chemical conversion throughout the whole blast furnace.

References

[1] B. J. Brown, M. E. Hanson, D. M. Liverman, and R. W. Merideth. Global sustainability: Toward definition. *Environmental Management*, 11(6):713–719, 1987. ISSN 1432-1009. doi: 10.1007/BF01867238. URL `https://doi.org/10.1007/BF01867238`.

[2] T. Kuhlman and J. Farrington. What is sustainability? *Sustainability*, 2(11):3436–3448, 2010. doi: 10.3390/su2113436. URL `https://doi.org/10.3390/su2113436`.

[3] P. Scaife, J. Nunn, A. Cottrell, and L. Wibberley. Towards sustainable steelmaking - An LCA perspective. *ISIJ International*, 42(Suppl):S5–S9, 2002. doi: 10.2355/isijinternational.42.Suppl_S5. URL `https://doi.org/10.2355/isijinternational.42.Suppl_S5`.

[4] J. P. Birat. Sustainable steelmaking paradigms for growth and development in the early 21st century. *Revue de Métallurgie*, 98(1):19–40, 2001. doi: 10.1051/metal:2001155. URL `https://doi.org/10.1051/metal:2001155`.

[5] R. J. Fruehan. Research on sustainable steelmaking. *Metallurgical and Materials Transactions B*, 40(2):123–133, 2009. ISSN 1543-1916. doi: 10.1007/s11663-008-9223-x. URL `https://doi.org/10.1007/s11663-008-9223-x`.

[6] T. Ariyama, M. Sato, T. Nouchi, and K. Takahashi. Evolution of blast furnace process toward reductant flexibility and carbon dioxide mitigation in steel works. *ISIJ International*, 56(10):1681–1696, 2016. doi: 10.2355/isijinternational.ISIJINT-2016-210. URL `https://doi.org/10.2355/isijinternational.ISIJINT-2016-210`.

[7] H. Suopajärvi, K. Umeki, E. Mousa, A. Hedayati, H. Romar, A. Kemppainen, C. Wang, A. Phounglamcheik, S. Tuomikoski, N. Norberg, A. Andefors, M. Öhman, U. Lassi, and T. Fabritius. Use of biomass in integrated steelmaking – Status quo, future needs and comparison to other low-CO_2 steel production technologies. *Applied Energy*, 213: 384–407, 2018. ISSN 0306-2619. doi: 10.1016/j.apenergy.2018.01.060. URL `https://www.sciencedirect.com/science/article/pii/S0306261918300709`.

[8] E. Mousa. Modern blast furnace ironmaking technology: Potentials to meet the demand of high hot metal production and lower energy consumption. *Metallurgical and Materials Engineering*, 25(2):69–104, 2019. doi: 10.30544/414. URL `https://doi.org/10.30544/414`.

[9] A. K. Runchal. The future of CFD and the CFD of the future. *Computational Thermal Sciences: An International Journal*, 4(6):517–524, 2012. ISSN 1940-2503. doi: 10.1615/ComputThermalScien.2012006511. URL `https://doi.org/10.1615/ComputThermalScien.2012006511`.

[10] F. Moukalled, L. Mangani, and M. Darwish. *The Finite Volume Method in Computational Fluid Dynamics - An Advanced Introduction with OpenFOAM® and Matlab*. Springer, Berlin, Heidelberg, 1st ed. 2015 edition, 2015. ISBN 978-3-319-16874-6.

[11] J. H. Ferziger, M. Perić, and R. L. Street. *Computational Methods for Fluid Dynamics*. Springer, Berlin, Heidelberg, 4th edition edition, 2019. ISBN 978-3-319-99693-6.

[12] M. Farokhi and M. Birouk. Modeling of the gas-phase combustion of a grate-firing biomass furnace using an extended approach of Eddy Dissipation Concept. *Fuel*, 227:412–423, 2018. ISSN 0016-2361. doi: 10.1016/j.fuel.2018.04.102. URL https://www.sciencedirect.com/science/article/pii/S0016236118307361.

[13] M. Farokhi and M. Birouk. A new EDC approach for modeling turbulence/chemistry interaction of the gas-phase of biomass combustion. *Fuel*, 220:420–436, 2018. ISSN 0016-2361. doi: 10.1016/j.fuel.2018.01.125. URL https://www.sciencedirect.com/science/article/pii/S0016236118301200.

[14] Y. Zhuo and Y. Shen. Three-dimensional transient modelling of coal and coke co-combustion in the dynamic raceway of ironmaking blast furnaces. *Applied Energy*, 261:114456, 2020. ISSN 0306-2619. doi: 10.1016/j.apenergy.2019.114456. URL https://www.sciencedirect.com/science/article/pii/S0306261919321440.

[15] T. Okosun, A. K. Silaen, G. Tang, B. Wu, and C. Q. Zhou. *CFD Analysis of Blast Furnace Operating Condition Impacts on Operational Efficiency*, chapter 10, pages 75–82. John Wiley & Sons, Ltd, 2016. ISBN 9781119274681. doi: 10.1002/9781119274681.ch10. URL https://onlinelibrary.wiley.com/doi/abs/10.1002/9781119274681.ch10.

[16] M. Harasek, C. Maier, C. Jordan, M. Bösenhofer, and C. Feilmayr. Investigation of alternative reducing agent conversion in the raceway cavity of blast furnaces by numerical simulation. In *AISTech - Iron and Steel Technology Conference Proceedings*, pages 353–365, 2016.

[17] J. G. Marvin. Perspective on computational fluid dynamics validation. *AIAA Journal*, 33 (10):1778–1787, 1995. doi: 10.2514/3.12727. URL https://doi.org/10.2514/3.12727.

[18] W. L. Oberkampf and T. G. Trucano. Verification and validation in computational fluid dynamics. *Progress in Aerospace Sciences*, 38(3):209–272, 2002. ISSN 0376-0421. doi: 10.1016/S0376-0421(02)00005-2. URL https://www.sciencedirect.com/science/article/pii/S0376042102000052.

[19] W. L. Oberkampf and B. L. Smith. Assessment criteria for computational fluid dynamics model validation experiments. *Journal of Verification, Validation and Uncertainty Quantification*, 2(3):031002, 10 2017. ISSN 2377-2158. doi: 10.1115/1.4037887. URL https://doi.org/10.1115/1.4037887.

[20] R. Safavi Nick, A. Tilliander, L. T. I. Jonsson, and P. G. Jönsson. A mathematical model of the solid flow behavior in a real dimension blast furnace: Effects of the solid volume fraction on the velocity profile. *steel research international*, 84(10):999–1010, 2013. doi: 10.1002/srin.201200283. URL https://onlinelibrary.wiley.com/doi/abs/10.1002/srin.201200283.

[21] X. Dong, A. Yu, J. I. Yagi, and P. Zulli. Modelling of multiphase flow in a blast furnace: Recent developments and future work. *ISIJ International*, 47(11):1553–1570, 2007. doi: 10.2355/isijinternational.47.1553. URL https://doi.org/10.2355/isijinternational.47.1553.

[22] S. Kuang, Z. Li, and A. Yu. Review on modeling and simulation of blast furnace. *steel research international*, 89(1):1700071, 2018. doi: 10.1002/srin.201700071. URL `https://onlinelibrary.wiley.com/doi/abs/10.1002/srin.201700071`.

[23] S. Ueda, S. Natsui, H. Nogami, J. I. Yagi, and T. Ariyama. Recent progress and future perspective on mathematical modeling of blast furnace. *ISIJ International*, 50(7): 914–923, 2010. doi: 10.2355/isijinternational.50.914. URL `https://doi.org/10.2355/isijinternational.50.914`.

[24] P. B. Abhale, N. N. Viswanathan, and H. Saxén. Numerical modelling of blast furnace – Evolution and recent trends. *Mineral Processing and Extractive Metallurgy*, 0(0):1–18, 2020. doi: 10.1080/25726641.2020.1733357. URL `https://doi.org/10.1080/25726641.2020.1733357`.

[25] S. J. Zhang, A. B. Yu, P. Zulli, B. Wright, and U. Tüzün. Modelling of the solids flow in a blast furnace. *ISIJ International*, 38(12):1311–1319, 1998. doi: 10.2355/isijinternational.38.1311. URL `https://doi.org/10.2355/isijinternational.38.1311`.

[26] S. Zhang, A. Yu, P. Zulli, B. Wright, and P. Austin. Numerical simulation of solids flow in a blast furnace. *Applied Mathematical Modelling*, 26(2):141–154, 2002. ISSN 0307-904X. doi: 10.1016/S0307-904X(01)00052-X. URL `https://www.sciencedirect.com/science/article/pii/S0307904X0100052X`.

[27] P. Zhou, H. lan Li, P. yu Shi, and C. Q. Zhou. Simulation of the transfer process in the blast furnace shaft with layered burden. *Applied Thermal Engineering*, 95:296–302, 2016. ISSN 1359-4311. doi: 10.1016/j.applthermaleng.2015.11.004. URL `https://www.sciencedirect.com/science/article/pii/S135943111501234X`.

[28] R. Remus, M. A. Aguado-Monsonet, S. Roudier, and L. D. Sanc. Best available techniques (BAT) reference document for iron and steel production. *European Commission Joint Research Centre Institute for Prospective Technological Studies (Report EUR 25521 EN). Luxembourg: Publications Office of the European Union*, Industrial Emissions Directive 2010/75/EU:339–347, 2013. ISSN 1831-9424. doi: 10.2791/97469. URL `https://doi.org/10.2791/97469`.

[29] European Commission. On the review of the list of critical raw materials for the EU and the implementation of the Raw Materials Initiative. Communication from the commission to the European Parliament, the Council, the European Economic and Social Committee and the Committee of the Regions COM(2014) 297, European Commission, 2014. URL `https://eur-lex.europa.eu/legal-content/EN/TXT/PDF/?uri=CELEX:52014DC0297&from=EN`.

[30] European Commission. On the 2017 list of Critical Raw Materials for the EU. Communication from the commission to the European Parliament, the Council, the European Economic and Social Committee and the Committee of the Regions COM(2017) 490, European Commission, 2017. URL `https://ec.europa.eu/transparency/regdoc/rep/1/2017/EN/COM-2017-490-F1-EN-MAIN-PART-1.PDF`.

[31] H. Ahmed. New trends in the application of carbon-bearing materials in blast furnace iron-making. *Minerals*, 8(12):561, 2018. doi: 10.3390/min8120561. URL `https://doi.org/10.3390/min8120561`.

[32] K. Takahashi, T. Nouchi, M. Sato, and T. Ariyama. Perspective on progressive development of oxygen blast furnace for energy saving. *ISIJ International*, 55(9):1866–1875, 2015. doi: 10.2355/isijinternational.ISIJINT-2015-196. URL `https://doi.org/10.2355/isijinternational.ISIJINT-2015-196`.

[33] T. Deno. *Advanced pulverized coal injection technology and blast furnace operation*, chapter Upper Limit of PCR. Elsevier Science Ltd, Oxford, UK, 2000. ISBN 9780080436517. URL `https://www.elsevier.com/books/advanced-pulverized-coal-injection-technology-and-blast-furnace-operation/ishii/978-0-08-043651-7`.

[34] G. Fick, O. Mirgaux, P. Neau, and F. Patisson. Using biomass for pig iron production: A technical, environmental and economical assessment. *Waste and Biomass Valorization*, 5 (1):43–55, 2014. ISSN 1877-265X. doi: 10.1007/s12649-013-9223-1. URL `https://doi.org/10.1007/s12649-013-9223-1`.

[35] A. M. A. Campos, K. Novack, and P. S. Assis. Selection of materials for blast furnace injection using quality indicators. *REM - International Engineering Journal*, 72:119–123, 03 2019. ISSN 2448-167X. doi: 10.1590/0370-44672018720025. URL `https://www.scielo.br/scielo.php?script=sci_arttext&pid=S2448-167X2019000100119&nrm=iso`.

[36] A. Babich, D. Senk, and S. Born. Interaction between co-injected substances with pulverized coal into the blast furnace. *ISIJ International*, 54(12):2704–2712, 2014. doi: 10.2355/isijinternational.54.2704. URL `https://doi.org/10.2355/isijinternational.54.2704`.

[37] S.-W. Du, W.-H. Chen, and J. A. Lucas. Pretreatment of biomass by torrefaction and carbonization for coal blend used in pulverized coal injection. *Bioresource Technology*, 161:333–339, 2014. ISSN 0960-8524. doi: 10.1016/j.biortech.2014.03.090. URL `https://www.sciencedirect.com/science/article/pii/S0960852414003952`.

[38] C.-M. Wiklund, H. Saxén, and M. Helle. Optimal resource allocation in steel making using torrefied biomass as auxiliary reductant. In A. Y. Oral, Z. B. Bahsi, and M. Ozer, editors, *International Congress on Energy Efficiency and Energy Related Materials (ENEFM2013)*, pages 33–41, Cham, 2014. Springer International Publishing. ISBN 978-3-319-05521-3. URL `https://link.springer.com/chapter/10.1007/978-3-319-05521-3_5`.

[39] C. F. Bruzual and J. A. Mathews. Economic assessment of charcoal injection in the ironmaking process (bio-PCI): Methodology and data. *Universidad, Ciencia y Tecnología*, 18:31–53, 03 2014. ISSN 1316-4821. URL `https://ve.scielo.org/scielo.php?script=sci_arttext&pid=S1316-48212014000100004&nrm=iso`.

[40] I. Naruse and T. Inada. *Advanced pulverized coal injection technology and blast furnace operation*, chapter Characteristics of pulverized coal combustion. Elsevier Science Ltd, Oxford, UK, 2000. ISBN 9780080436517. URL `https://www.elsevier.com/books/advanced-pulverized-coal-injection-technology-and-blast-furnace-operation/ishii/978-0-08-043651-7`.

[41] T. Kamijou and M. Shimizu. *Advanced pulverized coal injection technology and blast furnace operation*, chapter PC Combustion in blast furnace. Elsevier Science Ltd, Oxford, UK, 2000. ISBN 9780080436517. URL `https://www.elsevier.com/books/advanced-pulverized-coal-injection-technology-and-blast-furnace-operation/ishii/978-0-08-043651-7`.

[42] J. I. Yagi. Mathematical modeling of the flow of four fluids in a packed bed. *ISIJ International*, 33(6):619–639, 1993. doi: 10.2355/isijinternational.33.619. URL `https://doi.org/10.2355/isijinternational.33.619`.

[43] S. S. Mondal, S. K. Som, and S. K. Dash. Numerical predictions on the influences of the air blast velocity, initial bed porosity and bed height on the shape and size of raceway zone in a blast furnace. *Journal of Physics D: Applied Physics*, 38(8):1301–1307, apr 2005. doi: 10.1088/0022-3727/38/8/030. URL `https://doi.org/10.1088%2F0022-3727%2F38%2F8%2F030`.

[44] Z. Zhou, H. Zhu, A. Yu, B. Wright, and P. Zulli. Discrete particle simulation of gas–solid flow in a blast furnace. *Computers & Chemical Engineering*, 32(8):1760–1772, 2008. ISSN 0098-1354. doi: 10.1016/j.compchemeng.2007.08.018. URL `https://www.sciencedirect.com/science/article/pii/S0098135407002281`.

[45] X. F. Dong, A. B. Yu, J. M. Burgess, D. Pinson, S. Chew, and P. Zulli. Modelling of multiphase flow in ironmaking blast furnace. *Industrial & Engineering Chemistry Research*, 48(1):214–226, 2009. doi: 10.1021/ie800147v. URL `https://doi.org/10.1021/ie800147v`.

[46] H. P. Zhu, Z. Y. Zhou, A. B. Yu, and P. Zulli. Stress fields of solid flow in a model blast furnace. *Granular Matter*, 11(5):269–280, 2009. ISSN 1434-7636. doi: 10.1007/s10035-008-0123-1. URL `https://doi.org/10.1007/s10035-008-0123-1`.

[47] S. Natsui, S. Ueda, H. Nogami, J. Kano, R. Inoue, and T. Ariyama. Analysis on non-uniform gas flow in blast furnace based on DEM-CFD combined model. *steel research international*, 82(8):964–971, 2011. doi: 10.1002/srin.201000292. URL `https://onlinelibrary.wiley.com/doi/abs/10.1002/srin.201000292`.

[48] S. Natsui, S. Ueda, H. Nogami, J. Kano, R. Inoue, and T. Ariyama. Penetration effect of injected gas at shaft gas injection in blast furnace analyzed by hybrid model of DEM-CFD. *ISIJ International*, 51(9):1410–1417, 2011. doi: 10.2355/isijinternational.51.1410. URL `https://doi.org/10.2355/isijinternational.51.1410`.

[49] Z. Zhou, H. Zhu, B. Wright, A. Yu, and P. Zulli. Gas–solid flow in an ironmaking blast furnace - II: Discrete particle simulation. *Powder Technology*, 208(1):72–85, 2011. ISSN 0032-5910. doi: 10.1016/j.powtec.2010.12.005. URL `https://www.sciencedirect.com/science/article/pii/S0032591010006364`.

[50] J. Hilton and P. Cleary. Raceway formation in laterally gas-driven particle beds. *Chemical Engineering Science*, 80:306–316, 2012. ISSN 0009-2509. doi: 10.1016/j.ces.2012.06.044. URL `https://www.sciencedirect.com/science/article/pii/S0009250912004009`.

[51] D. Rangarajan, T. Shiozawa, Y. Shen, J. S. Curtis, and A. Yu. Influence of operating parameters on raceway properties in a model blast furnace using a two-fluid model. *Industrial & Engineering Chemistry Research*, 53(13):4983–4990, 2014. doi: 10.1021/ie301936r. URL `https://doi.org/10.1021/ie301936r`.

[52] Z. Miao, Z. Zhou, A. Yu, and Y. Shen. CFD-DEM simulation of raceway formation in an ironmaking blast furnace. *Powder Technology*, 314:542–549, 2017. ISSN 0032-5910. doi: 10.1016/j.powtec.2016.11.039. URL `https://www.sciencedirect.com/science/article/pii/S0032591016308312`.

[53] Y. Sun, R. Chen, Z. Zhang, G. Wu, H. Zhang, L. Li, Y. Liu, X. Li, and Y. Huang. Numerical simulation of the raceway zone in melter gasifier of COREX process. *Processes*, 7(12):867, 2019. doi: 10.3390/pr7120867. URL `https://doi.org/10.3390/pr7120867`.

[54] G. Wei, H. Zhang, X. An, and D. E. Numerical investigation on the mutual interaction between heat transfer and non-spherical particle dynamics in the blast furnace raceway. *International Journal of Heat and Mass Transfer*, 153:119577, 2020. ISSN 0017-9310. doi: 10.1016/j.ijheatmasstransfer.2020.119577. URL `https://www.sciencedirect.com/science/article/pii/S0017931019349890`.

[55] X. Peng, J. Wang, C. Li, H. Zuo, X. She, G. Wang, and Q. Xue. Numerical study of raceway shape and size in a model blast furnace. In *TMS 2020 149th Annual Meeting & Exhibition Supplemental Proceedings*, pages 1071–1081, Cham, 2020. Springer International Publishing. ISBN 978-3-030-36296-6. doi: 10.1007/978-3-030-36296-6_100. URL `https://doi.org/10.1007/978-3-030-36296-6_100`.

[56] T. Kon, S. Natsui, S. Matsuhashi, S. Ueda, R. Inoue, and T. Ariyama. Influence of cohesive zone thickness on gas flow in blast furnace analyzed by DEM-CFD model considering low coke operation. *steel research international*, 84(11):1146–1156, 2013. doi: 10.1002/srin.201300025. URL `https://onlinelibrary.wiley.com/doi/abs/10.1002/srin.201300025`.

[57] G. L. Qing, L. Ma, X. S. Zhang, J. L. Zhou, and M. Kuwabara. Numerical investigation of gas flow through blast furnace shaft with designed layered structure of ore and coke burdens. *Ironmaking & Steelmaking*, 37(7):546–552, 2010. doi: 10.1179/030192310X12706364542867. URL `https://doi.org/10.1179/030192310X12706364542867`.

[58] Q.-F. Hou, M. Samman, J. Li, and A.-B. Yu. Modeling the gas-solid flow in the reduction shaft of COREX. *ISIJ International*, 54(8):1772–1780, 2014. doi: 10.2355/isijinternational.54.1772. URL `https://doi.org/10.2355/isijinternational.54.1772`.

[59] Xu, Kuan and Bai, Ming-hua. DEM simulation of particle descending velocity distribution in the reduction shaft furnace. *Metall. Res. Technol.*, 113(6):603, 2016. doi: 10.1051/metal/2016035. URL `https://doi.org/10.1051/metal/2016035`.

[60] A. T. Adema, Y. Yang, and R. Boom. Discrete element method-computational fluid dynamic simulation of the materials flow in an iron-making blast furnace. *ISIJ International*, 50(7):954–961, 2010. doi: 10.2355/isijinternational.50.954. URL `https://doi.org/10.2355/isijinternational.50.954`.

[61] Z. Dong, Q. Xue, H. Zuo, X. She, J. Li, and J. Wang. Gas-solid flow and shaft injected gas penetration in an oxygen blast furnace analyzed using a three-dimensional DEM-CFD coupling mathematical model. *ISIJ International*, 56(9):1588–1597, 2016. doi: 10.2355/isijinternational.ISIJINT-2016-217. URL `https://doi.org/10.2355/isijinternational.ISIJINT-2016-217`.

[62] S. Natsui, S. Ueda, H. Nogami, J. Kano, R. Inoue, and T. Ariyama. Dynamic analysis of gas and solid flows in blast furnace with shaft gas injection by hybrid model of DEM-CFD. *ISIJ International*, 51(1):51–58, 2011. doi: 10.2355/isijinternational.51.51. URL `https://doi.org/10.2355/isijinternational.51.51`.

[63] E. Rabadan Santana, G. Pozzetti, and B. Peters. Application of a dual-grid multiscale CFD-DEM coupling method to model the raceway dynamics in packed bed reactors. *Chemical Engineering Science*, 205:46–57, 2019. ISSN 0009-2509. doi: 10.1016/j.ces.2019.04.025. URL https://www.sciencedirect.com/science/article/pii/S0009250919303902.

[64] J. Xu, S. Yu, N. Wang, M. Chen, and Y. Shen. Characterization of high-turbulence zone in slowly moving bed slagging coal gasifier by a 3D mathematical model. *Powder Technology*, 314:524–531, 2017. ISSN 0032-5910. doi: 10.1016/j.powtec.2016.10.022. URL https://www.sciencedirect.com/science/article/pii/S0032591016307069.

[65] *Prediction of Raceways in a Blast Furnace*, volume Energy Conversion and Resources of *ASME International Mechanical Engineering Congress and Exposition*, 11 2006. doi: 10.1115/IMECE2006-15573. URL https://doi.org/10.1115/IMECE2006-15573.

[66] Y.-Q. Feng, D. Pinson, A.-B. Yu, S. J. Chew, and P. Zulli. Numerical study of gas-solid flow in the raceway of a blast furnace. *steel research international*, 74(9):523–530, 2003. doi: 10.1002/srin.200300229. URL https://onlinelibrary.wiley.com/doi/abs/10.1002/srin.200300229.

[67] F. Holzleithner. *A detailed, three-dimensional model for the slowly moving coal bed inside a Melter-Gasifier*. PhD thesis, Institute of Energy Systems and Thermodynamics, Technische Universität Wien, 2013.

[68] M. Vångö, S. Pirker, and T. Lichtenegger. Unresolved CFD–DEM modeling of multiphase flow in densely packed particle beds. *Applied Mathematical Modelling*, 56:501–516, 2018. ISSN 0307-904X. doi: 10.1016/j.apm.2017.12.008. URL https://www.sciencedirect.com/science/article/pii/S0307904X17307370.

[69] M. Vangö. *CFD-DEM modeling of multi-phase fluid-granular systems and its application to blast furnace tapping*. PhD thesis, Department of Particulate Flow Modelling, Johannes Keppler University Linz, 2019.

[70] P. R. Austin, H. Nogami, and J. I. Yagi. A mathematical model for blast furnace reaction analysis based on the four fluid model. *ISIJ International*, 37(8):748–755, 1997. doi: 10.2355/isijinternational.37.748. URL https://doi.org/10.2355/isijinternational.37.748.

[71] P. R. Austin, H. Nogami, and J. I. Yagi. A mathematical model of four phase motion and heat transfer in the blast furnace. *ISIJ International*, 37(5):458–467, 1997. doi: 10.2355/isijinternational.37.458. URL https://doi.org/10.2355/isijinternational.37.458.

[72] S. A. Zaïmi, T. Akiyama, J.-B. Guillot, and J. I. Yagi. Sophisticated multi-phase multi-flow modeling of the blast furnace. *ISIJ International*, 40(4):322–331, 2000. doi: 10.2355/isijinternational.40.322. URL https://doi.org/10.2355/isijinternational.40.322.

[73] J. A. de Castro, H. Nogami, and J. I. Yagi. Transient mathematical model of blast furnace based on multi-fluid concept, with application to high PCI operation. *ISIJ International*, 40(7):637–646, 2000. doi: 10.2355/isijinternational.40.637. URL https://doi.org/10.2355/isijinternational.40.637.

[74] J. A. de Castro, H. Nogami, and J. I. Yagi. Numerical investigation of simultaneous injection of pulverized coal and natural gas with oxygen enrichment to the blast furnace. *ISIJ International*, 42(11):1203–1211, 2002. doi: 10.2355/isijinternational.42.1203. URL https://doi.org/10.2355/isijinternational.42.1203.

[75] H. Nogami, M. Chu, and J. I. Yagi. Numerical analysis on blast furnace performance with novel feed material by multi-dimensional simulator based on multi-fluid theory. *Applied Mathematical Modelling*, 30(11):1212–1228, 2006. ISSN 0307-904X. doi: 10.1016/j.apm.2006.03.013. URL https://www.sciencedirect.com/science/article/pii/S0307904X06000229.

[76] M. Gu, G. Chen, M. Zhang, D. Huang, P. Chaubal, and C. Q. Zhou. Three-dimensional simulation of the pulverized coal combustion inside blast furnace tuyere. *Applied Mathematical Modelling*, 34(11):3536–3546, 2010. ISSN 0307-904X. doi: 10.1016/j.apm.2010.03.004. URL https://www.sciencedirect.com/science/article/pii/S0307904X10001046.

[77] Y. Shen, A. Yu, P. Austin, and P. Zulli. Modelling in-furnace phenomena of pulverized coal injection in ironmaking blast furnace: Effect of coke bed porosities. *Minerals Engineering*, 33:54–65, 2012. ISSN 0892-6875. doi: 10.1016/j.mineng.2011.10.014. URL https://www.sciencedirect.com/science/article/pii/S0892687511003815.

[78] H. Nogami, Y. Kashiwaya, and D. Yamada. Simulation of blast furnace operation with intensive hydrogen injection. *ISIJ International*, 52(8):1523–1527, 2012. doi: 10.2355/isijinternational.52.1523. URL https://doi.org/10.2355/isijinternational.52.1523.

[79] S. Kuang, Z. Li, D. Yan, Y. Qi, and A. Yu. Numerical study of hot charge operation in ironmaking blast furnace. *Minerals Engineering*, 63:45–56, 2014. ISSN 0892-6875. doi: 10.1016/j.mineng.2013.11.002. URL https://www.sciencedirect.com/science/article/pii/S0892687513003610.

[80] D. Fu, Y. Chen, Y. Zhao, J. D'Alessio, K. J. Ferron, and C. Q. Zhou. CFD modeling of multiphase reacting flow in blast furnace shaft with layered burden. *Applied Thermal Engineering*, 66(1):298–308, 2014. ISSN 1359-4311. doi: 10.1016/j.applthermaleng.2014.01.065. URL https://www.sciencedirect.com/science/article/pii/S1359431114000714.

[81] Y. Shen, B. Guo, S. Chew, P. Austin, and A. Yu. Three-dimensional modeling of flow and thermochemical behavior in a blast furnace. *Metallurgical and Materials Transactions B*, 46(1):432–448, 2015. ISSN 1543-1916. doi: 10.1007/s11663-014-0204-y. URL https://doi.org/10.1007/s11663-014-0204-y.

[82] J. A. de Castro, C. Takano, and J. I. Yagi. A theoretical study using the multiphase numerical simulation technique for effective use of H_2 as blast furnaces fuel. *Journal of Materials Research and Technology*, 6(3):258–270, 2017. ISSN 2238-7854. doi: 10.1016/j.jmrt.2017.05.007. URL https://www.sciencedirect.com/science/article/pii/S2238785417300820.

[83] D. Wu, P. Zhou, H. Yan, P. Shi, and C. Q. Zhou. Numerical investigation of the effects of size segregation on pulverized coal combustion in a blast furnace. *Powder Technology*, 342:41–53, 2019. ISSN 0032-5910. doi: 10.1016/j.powtec.2018.09.067. URL https://www.sciencedirect.com/science/article/pii/S0032591018307952.

[84] D. Wu, P. Zhou, and C. Q. Zhou. Evaluation of pulverized coal utilization in a blast furnace by numerical simulation and grey relational analysis. *Applied Energy*, 250:1686–1695, 2019. ISSN 0306-2619. doi: 10.1016/j.apenergy.2019.05.051. URL https://www.sciencedirect.com/science/article/pii/S0306261919309043.

[85] C. Zhou, G. Tang, J. Wang, D. Fu, T. Okosun, A. Silaen, and B. Wu. Comprehensive numerical modeling of the blast furnace ironmaking process. *JOM - The Journal of The*

Minerals, Metals & Materials Society (TMS), 68(5):1353–1362, 2016. ISSN 1543-1851. doi: 10.1007/s11837-016-1891-4. URL `https://doi.org/10.1007/s11837-016-1891-4`.

[86] Y. Shen, B. Guo, A. Yu, S. Chew, and P. Austin. Modelling ironmaking blast furnace: Solid flow and thermochemical behaviours. *AIP Conference Proceedings*, 1542(1):1274–1277, 2013. doi: 10.1063/1.4812171. URL `https://aip.scitation.org/doi/abs/10.1063/1.4812171`.

[87] D. Fu, G. Tang, Y. Zhao, J. D'Alessio, and C. Q. Zhou. Modeling of iron ore reactions in blast furnace. *International Journal of Heat and Mass Transfer*, 103:77–86, 2016. ISSN 0017-9310. doi: 10.1016/j.ijheatmasstransfer.2016.06.060. URL `https://www.sciencedirect.com/science/article/pii/S0017931016305932`.

[88] B. Peters, M. Baniasadi, and M. Baniasadi. The extended discrete element method (XDEM): An advanced approach to model blast furnace. In V. Shatokha, editor, *Iron Ores and Iron Oxide Materials*, chapter 7. IntechOpen, Rijeka, 2018. doi: 10.5772/intechopen.75436. URL `https://doi.org/10.5772/intechopen.75436`.

[89] H. Hamadeh, O. Mirgaux, and F. Patisson. Detailed modeling of the direct reduction of iron ore in a shaft furnace. *Materials*, 11(10):1865, 2018. doi: 10.3390/ma11101865. URL `https://doi.org/10.3390/ma11101865`.

[90] J. A. A. d. Castro, E. P. Rocha, E. M. d. Oliveira, M. F. Campos, and A. S. Francisco. Mathematical modeling of the shaft furnace process for producing DRI based on the multiphase theory. *REM - International Engineering Journal*, 71:81–87, 03 2018. ISSN 2448-167X. doi: 10.1590/0370-44672015710199. URL `https://www.scielo.br/scielo.php?script=sci_arttext&pid=S2448-167X2018000100081&nrm=iso`.

[91] M. Baniasadi, M. Baniasadi, G. Pozzetti, and B. Peters. A numerical study on the softening process of iron ore particles in the cohesive zone of an experimental blast furnace using a coupled CFD-DEM method. *CoRR*, abs/1806.08114, 2018. URL `https://arxiv.org/abs/1806.08114`.

[92] A. Vuokila, O. Mattila, R. L. Keiski, and E. Muurinen. CFD study on the heavy oil lance positioning in the blast furnace tuyere to improve combustion. *ISIJ International*, 57(11):1911–1920, 2017. doi: 10.2355/isijinternational.ISIJINT-2017-213. URL `https://doi.org/10.2355/isijinternational.ISIJINT-2017-213`.

[93] A. Vuokila, M. Riihimäki, and E. Muurinen. CFD-modeling of heavy oil injection into blast furnace – Atomization and mixing in raceway-tuyere area. *Steel Research International*, 85 (11):1544–1551, 2014. doi: 10.1002/srin.201300316. URL `https://onlinelibrary.wiley.com/doi/abs/10.1002/srin.201300316`.

[94] D. Safronov, A. Richter, and B. Meyer. Numerical predictions of the shape and size of the raceway zone in a blast furnace. In J. E. Olsen and S. T. Johansen, editors, *SINTEF Proceedings*, Oslo, NO, 2017. SINTEF Academic Press. ISBN 9788253615448. URL `https://hdl.handle.net/11250/2480072`.

[95] J. Cui, Q. Hou, and Y. Shen. CFD-DEM study of coke combustion in the raceway cavity of an ironmaking blast furnace. *Powder Technology*, 362:539–549, 2020. ISSN 0032-5910. doi: 10.1016/j.powtec.2019.12.012. URL `https://www.sciencedirect.com/science/article/pii/S003259101931112X`.

[96] Y. Liu, J. Curtis, and Y. Shen. Computational fluid dynamics study of re-blowin operation in an ironmaking blast furnace. *Powder Technology*, 361:145–159, 2020. ISSN 0032-5910. doi: 10.1016/j.powtec.2019.09.061. URL https://www.sciencedirect.com/science/article/pii/S0032591019307879.

[97] P. Hellberg, T. L. I. Jonsson, and P. G. Jönsson. Mathematical modelling of the injection of coke oven gas into a blast furnace tuyere. *Scandinavian Journal of Metallurgy*, 34(5): 269–275, 2005. doi: 10.1111/j.1600-0692.2005.00744.x. URL https://onlinelibrary.wiley.com/doi/abs/10.1111/j.1600-0692.2005.00744.x.

[98] P. Hellberg, T. L. I. Jonsson, and P. G. Jönsson. A mathematical model of a blast furnace injection tuyere. *steel research international*, 76(11):755–763, 2005. doi: 10.1002/srin.200506093. URL https://onlinelibrary.wiley.com/doi/abs/10.1002/srin.200506093.

[99] S.-W. Du and W.-H. Chen. Numerical prediction and practical improvement of pulverized coal combustion in blast furnace. *International Communications in Heat and Mass Transfer*, 33(3):327–334, 2006. ISSN 0735-1933. doi: 10.1016/j.icheatmasstransfer.2005.10.015. URL https://www.sciencedirect.com/science/article/pii/S0735193305001995.

[100] S.-W. Du, W.-H. Chen, and J. Lucas. Performances of pulverized coal injection in blowpipe and tuyere at various operational conditions. *Energy Conversion and Management*, 48(7):2069–2076, 2007. ISSN 0196-8904. doi: 10.1016/j.enconman.2007.01.013. URL https://www.sciencedirect.com/science/article/pii/S0196890407000404.

[101] S.-W. Du, C.-P. Yeh, W.-H. Chen, C.-H. Tsai, and J. A. Lucas. Burning characteristics of pulverized coal within blast furnace raceway at various injection operations and ways of oxygen enrichment. *Fuel*, 143:98–106, 2015. ISSN 0016-2361. doi: 10.1016/j.fuel.2014.11.038. URL https://www.sciencedirect.com/science/article/pii/S0016236114011429.

[102] C. Maier, C. Jordan, M. Harasek, C. Feilmayr, and C. Thaler. Implementation and validation of a three-dimensional multiphase-CFD-model for blast furnace processes. *Chemical Engineering Transactions*, 29:925–930, 2012. doi: 10.3303/CET1229155. URL https://doi.org/10.3303/CET1229155.

[103] C. Maier, C. Jordan, M. Knepper, A. Babich, D. Senk, C. Feilmayr, C. Thaler, and M. Harasek. Numerical and experimental study of alternative reductant injection into the raceway of the blast furnace. *BHM Berg- und Hüttenmännische Monatshefte*, 158 (11):453–454, 2013. ISSN 1613-7531. doi: 10.1007/s00501-013-0191-3. URL https://doi.org/10.1007/s00501-013-0191-3.

[104] C. Maier, C. Jordan, M. Harasek, C. Feilmayr, and C. Thaler. Investigation of alternative reducing agent injection into the raceway of blast furnaces using CFD. *Chemical Engineering Transactions*, 35:1345–1350, 2013. doi: 10.3303/CET1335224. URL https://doi.org/10.3303/CET1335224.

[105] C. Jordan, M. Harasek, C. Maier, F. Winter, G. Aichinger, C. Feilmayr, and S. Schuster. CFD simulation of heat transfer and high temperature conversion of plastic particles after injection into blast furnace raceway. In *Proceedings of CHT-08 ICHMT International Symposium on Advances in Computational Heat Transfer*. Begel House Inc., Begel House Inc., 2008. ISBN 9781567002539. doi: 10.1615/ICHMT.2008.CHT.1060. URL https://doi.org/10.1615/ICHMT.2008.CHT.1060.

[106] Q. Hou, D. E, S. Kuang, Z. Li, and A. Yu. DEM-based virtual experimental blast furnace: A quasi-steady state model. *Powder Technology*, 314:557–566, 2017. ISSN 0032-5910. doi: 10.1016/j.powtec.2016.12.017. URL https://www.sciencedirect.com/science/article/pii/S0032591016308853.

[107] J. Liao, A. Yu, and Y. Shen. Modelling the injection of upgraded brown coals in an ironmaking blast furnace. *Powder Technology*, 314:550–556, 2017. ISSN 0032-5910. doi: 10.1016/j.powtec.2016.11.005. URL https://www.sciencedirect.com/science/article/pii/S0032591016307744.

[108] H. Zhang, Z. Zhou, A. Yu, S.-Y. Kim, and S.-K. Jung. Discrete particle simulation of solid flow in a melter-gasifier in smelting reduction process. *Powder Technology*, 314: 641–648, 2017. ISSN 0032-5910. doi: 10.1016/j.powtec.2016.10.041. URL https://www.sciencedirect.com/science/article/pii/S0032591016307227.

[109] J. A. de Castro, A. J. da Silva, Y. Sasaki, and J. I. Yagi. A six-phases 3-D model to study simultaneous injection of high rates of pulverized coal and charcoal into the blast furnace with oxygen enrichment. *ISIJ International*, 51(5):748–758, 2011. doi: 10.2355/isijinternational.51.748. URL https://doi.org/10.2355/isijinternational.51.748.

[110] L. Jiao, S. Kuang, A. Yu, Y. Li, X. Mao, and H. Xu. Three-dimensional modeling of an ironmaking blast furnace with a layered cohesive zone. *Metallurgical and Materials Transactions B*, 51(1):258–275, 2020. ISSN 1543-1916. doi: 10.1007/s11663-019-01745-3. URL https://doi.org/10.1007/s11663-019-01745-3.

[111] D. Gidaspow. *Multiphase Flow and Fluidization - Continuum and Kinetic Theory Descriptions*. Academic Press, Amsterdam, Boston, 1994. ISBN 978-0-122-82470-8.

[112] J. Wang. Continuum theory for dense gas-solid flow: A state-of-the-art review. *Chemical Engineering Science*, 215:115428, 2020. ISSN 0009-2509. doi: 10.1016/j.ces.2019.115428. URL https://www.sciencedirect.com/science/article/pii/S0009250919309182.

[113] W. Zhong, A. Yu, G. Zhou, J. Xie, and H. Zhang. CFD simulation of dense particulate reaction system: Approaches, recent advances and applications. *Chemical Engineering Science*, 140:16 – 43, 2016. ISSN 0009-2509. doi: 10.1016/j.ces.2015.09.035. URL https://www.sciencedirect.com/science/article/pii/S0009250915006661.

[114] C. Orr. *Particulate technology*. Macmillan New York, 1966.

[115] C. Maier. *Numerical Modeling of the Blast Furnace Process - Injection of Auxiliary Reducing Agents Into the Raceway*. PhD thesis, Institute of Chemical, Environmental and Bioscience Engineering, Technische Universität Wien, 2015.

[116] J. Szekely, J. W. Evans, and H. Y. Sohn. *Gas–solid reactions*. Academic Press, Cambridge, MA, USA, 1976. ISBN 0126808503.

[117] P. Walker, F. Rusinko, and L. Austin. Gas reactions of carbon. In D. Eley, P. Selwood, and P. B. Weisz, editors, *Advances in catalysis*, volume 11 of *Advances in Catalysis*, pages 133–221. Academic Press, 1959. doi: 10.1016/S0360-0564(08)60418-6. URL https://www.sciencedirect.com/science/article/pii/S0360056408604186.

[118] C. N. Satterfield. *Mass Transfer in Heterogeneous Catalysis*. The MIT Press, 1969. ISBN 9780262190626.

[119] J. Mularski, H. Pawlak-Kruczek, and N. Modlinski. A review of recent studies of the CFD modelling of coal gasification in entrained flow gasifiers, covering devolatilization, gas-phase reactions, surface reactions, models and kinetics. *Fuel*, 271:117620, 2020. ISSN 0016-2361. doi: 10.1016/j.fuel.2020.117620. URL `https://www.sciencedirect.com/science/article/pii/S0016236120306153`.

[120] H. G. Weller, G. Tabor, H. Jasak, and C. Fureby. A tensorial approach to computational continuum mechanics using object-oriented techniques. *Computers in Physics*, 12(6):620–631, 1998. doi: 10.1063/1.168744. URL `https://aip.scitation.org/doi/abs/10.1063/1.168744`.

[121] T. Poinsot and D. Thierry. *Theoretical and numerical combustion, 3ʳᵈ ed.* T. Poinsot, Institut de Mécanique des Fluides de Toulouse, 31400 Toulouse Cedex, 2012. ISBN 9782746639904.

[122] D. Veynante and L. Vervisch. Turbulent combustion modeling. *Progress in Energy and Combustion Science*, 28(3):193–266, 2002. ISSN 0360-1285. doi: 10.1016/S0360-1285(01)00017-X. URL `https://www.sciencedirect.com/science/article/pii/S036012850100017X`.

[123] N. Peters. Laminar flamelet concepts in turbulent combustion. *Symposium (International) on Combustion*, 21(1):1231–1250, 1988. ISSN 0082-0784. doi: 10.1016/S0082-0784(88)80355-2. URL `https://www.sciencedirect.com/science/article/pii/S0082078488803552`.

[124] B. Cuenot and T. Poinsot. Effects of curvature and unsteadiness in diffusion flames. implications for turbulent diffusion combustion. *Symposium (International) on Combustion*, 25(1):1383–1390, 1994. ISSN 0082-0784. doi: 10.1016/S0082-0784(06)80781-2. URL `https://www.sciencedirect.com/science/article/pii/S0082078406807812`.

[125] H. D. Baehr and K. Stephan. *Heat and Mass Transfer*. Springer, 2011. ISBN 9783642200205.

[126] T. L. Bergman, F. P. Incropera, D. P. DeWitt, and A. S. Lavine. *Fundamentals of heat and mass transfer*. John Wiley & Sons, 2011. ISBN 9781119353881.

[127] V. Mittal and H. Pitsch. A flamelet model for premixed combustion under variable pressure conditions. *Proceedings of the Combustion Institute*, 34(2):2995 – 3003, 2013. ISSN 1540-7489. doi: 10.1016/j.proci.2012.07.069. URL `https://www.sciencedirect.com/science/article/pii/S1540748912003616`.

[128] Y. Sivathanu and G. Faeth. Generalized state relationships for scalar properties in nonpremixed hydrocarbon/air flames. *Combustion and Flame*, 82(2):211–230, 1990. ISSN 0010-2180. doi: 10.1016/0010-2180(90)90099-D. URL `https://www.sciencedirect.com/science/article/pii/001021809090099D`.

[129] B. F. Magnussen and B. H. Hjertager. On mathematical modeling of turbulent combustion with special emphasis on soot formation and combustion. *Symposium (International) on Combustion*, 16(1):719–729, 1977. ISSN 0082-0784. doi: 10.1016/S0082-0784(77)80366-4. URL `https://www.sciencedirect.com/science/article/pii/S0082078477803664`.

[130] M. Rieth, A. M. Kempf, O. T. Stein, A. Kronenburg, C. Hasse, and M. Vascellari. Evaluation of a flamelet/progress variable approach for pulverized coal combustion in a turbulent mixing layer. *Proceedings of the Combustion Institute*, 2018. ISSN 1540-7489. doi: 10.1016/j.proci.2018.05.150. URL `https://www.sciencedirect.com/science/article/pii/S1540748918301561`.

[131] M. Rieth, A. Kempf, A. Kronenburg, and O. Stein. Carrier-phase DNS of pulverized coal particle ignition and volatile burning in a turbulent mixing layer. *Fuel*, 212:364–374, 2018. ISSN 0016-2361. doi: 10.1016/j.fuel.2017.09.096. URL `https://www.sciencedirect.com/science/article/pii/S0016236117312048`.

[132] J. Watanabe and K. Yamamoto. Flamelet model for pulverized coal combustion. *Proceedings of the Combustion Institute*, 35(2):2315–2322, 2015. ISSN 1540-7489. doi: 10.1016/j.proci.2014.07.065. URL `https://www.sciencedirect.com/science/article/pii/S1540748914003757`.

[133] J. Watanabe, T. Okazaki, K. Yamamoto, K. Kuramashi, and A. Baba. Large-Eddy Simulation of pulverized coal combustion using flamelet model. *Proceedings of the Combustion Institute*, 36(2):2155–2163, 2017. ISSN 1540-7489. doi: 10.1016/j.proci.2016.06.031. URL `https://www.sciencedirect.com/science/article/pii/S154074891630089X`.

[134] X. Wen, K. Luo, Y. Luo, H. I. Kassem, H. Jin, and J. Fan. Large Eddy Simulation of a semi-industrial scale coal furnace using non-adiabatic three-stream flamelet/progress variable model. *Applied Energy*, 183:1086–1097, 2016. ISSN 0306-2619. doi: 10.1016/j.apenergy.2016.09.034. URL `https://www.sciencedirect.com/science/article/pii/S0306261916313368`.

[135] X. Wen, Y. Luo, K. Luo, H. Jin, and J. Fan. LES of pulverized coal combustion with a multi-regime flamelet model. *Fuel*, 188:661–671, 2017. ISSN 0016-2361. doi: 10.1016/j.fuel.2016.10.070. URL `https://www.sciencedirect.com/science/article/pii/S0016236116310328`.

[136] B. F. Magnussen, B. H. Hjertager, J. Olsen, and D. Bhaduri. Effects of turbulent structure and local concentrations on soot formation and combustion in C_2H_2 diffusion flames. *Symposium (International) on Combustion*, 17(1):1383–1393, 1979. ISSN 0082-0784. doi: 10.1016/S0082-0784(79)80130-7. URL `https://www.sciencedirect.com/science/article/pii/S0082078479801307`.

[137] B. F. Magnussen. On the structure of turbulence and a generalized Eddy Dissipation Concept for chemical reaction in turbulent flow. In *19th Aerospace Sciences Meeting*, St. Louis, MO, USA, 1981. American Institute of Aeronautics and Astronautics (AIAA). doi: 10.2514/6.1981-42. URL `https://doi.org/10.2514/6.1981-42`.

[138] B. F. Magnussen. Modeling of NO_X and soot formation by the Eddy Dissipation Concept. In *First Topic Oriented Technical Meeting*, Amsterdam, The Netherland, 1989. International Flame Research Foundation. URL `https://folk.ntnu.no/ivarse/edc/EDC1989.pdf`.

[139] B. F. Magnussen. The Eddy Dissipation Concept—A bridge between science and technology. In *ECCOMAS Thematic Conference on Computational Combustion*, Lisbon, Portugal, 2005. European Community on Computational Methods in Applied Sciences (ECCOMAS). URL `http://folk.ntnu.no/ivarse/edc/BFM_ECOMAS2005_Lisboa.pdf`.

[140] A. Parente, M. R. Malik, F. Contino, A. Cuoci, and B. B. Dally. Extension of the Eddy Dissipation Concept for turbulence/chemistry interactions to MILD combustion. *Fuel*, 163:98–111, 2016. ISSN 00162361. doi: 10.1016/j.fuel.2015.09.020. URL `https://doi.org/10.1016/j.fuel.2015.09.020`.

[141] H. Bao. Development and validation of a new Eddy Dissipation Concept (EDC) model for MILD combustion. Master's thesis, Delft University of Technology, 2017.

[142] M. Evans, C. Petre, P. Medwell, and A. Parente. Generalisation of the Eddy-Dissipation Concept for jet flames with low turbulence and low damköhler number. *Proceedings of the Combustion Institute*, 37(4):4497–4505, 2019. ISSN 1540-7489. doi: 10.1016/j.proci.2018.06.017. URL `https://www.sciencedirect.com/science/article/pii/S1540748918302001`.

[143] V. I. Golovitchev, N. Nordin, and J. Chomiak. Neat dimethyl ether: Is it really diesel fuel of promise? In *SAE Technical Paper*. SAE International, 1998. doi: 10.4271/982537. URL `https://doi.org/10.4271/982537`.

[144] V. I. Golovitchev, N. Nordin, R. Jarnicki, and J. Chomiak. 3-D diesel spray simulations using a new detailed chemistry turbulent combustion model. In *CEC/SAE Spring Fuels & Lubricants Meeting & Exposition*. SAE International, 2000. doi: 10.4271/2000-01-1891. URL `https://doi.org/10.4271/2000-01-1891`.

[145] V. Golovitchev and J. Chomiak. Numerical modeling of high temperature air flameless combustion. In *Proceedings of the 4th International Symposium on High Temperature Air Combustion and Gasification (HiTACG)*, pages 27–30, 2001.

[146] V. Sabelnikov and C. Fureby. Extended LES-PaSR model for simulation of turbulent combustion. In *EUCASS Proceedings Series - Advances in AeroSpace Sciences*, volume 4, pages 539–568, 2013. doi: 10.1051/eucass/201304539. URL `10.1051/eucass/201304539`.

[147] V. Sabelnikov and C. Fureby. LES combustion modeling for high Re flames using a multi-phase analogy. *Combustion and Flame*, 160(1):83–96, 2013. ISSN 0010-2180. doi: 10.1016/j.combustflame.2012.09.008. URL `https://www.sciencedirect.com/science/article/pii/S0010218012002696`.

[148] N. Petrova, V. Sabelnikov, and N. Bertier. Numerical simulation of a backward-facing step combustor using Reynolds-Averaged Navier-Stokes / extended partially stirred reactor model. In *EUCASS Book Series - Advances in AeroSpace Sciences*, volume 11, pages 625–656, 2019. doi: 10.1051/eucass/201911625. URL `https://doi.org/10.1051/eucass/201911625`.

[149] J. van Oijen and L. de Goey. Modelling of premixed laminar flames using Flamelet-Generated Manifolds. *Combustion Science and Technology*, 161(1):113–137, 2000. doi: 10.1080/00102200008935814. URL `https://doi.org/10.1080/00102200008935814`.

[150] O. Gicquel, N. Darabiha, and D. Thévenin. Liminar premixed hydrogen/air counterflow flame simulations using flame prolongation of ILDM with differential diffusion. *Proceedings of the Combustion Institute*, 28(2):1901–1908, 2000. ISSN 1540-7489. doi: 10.1016/S0082-0784(00)80594-9. URL `https://www.sciencedirect.com/science/article/pii/S0082078400805949`.

[151] Y.-S. Niu, L. Vervisch, and P. Dinh Tao. An optimization-based approach to detailed chemistry tabulation: Automated progress variable definition. *Combustion and Flame*, 160: 776–785, 04 2013. doi: 10.1016/j.combustflame.2012.11.015. URL `https://doi.org/10.1016/j.combustflame.2012.11.015`.

[152] C. D. Pierce and P. Moin. Progress-variable approach for Large-Eddy Simulation of non-premixed turbulent combustion. *Journal of Fluid Mechanics*, 504:73–97, 2004. doi: 10.1017/S0022112004008213. URL `https://doi.org/10.1017/S0022112004008213`.

[153] U. Maas and S. Pope. Simplifying chemical kinetics: Intrinsic low-dimensional manifolds in composition space. *Combustion and Flame*, 88(3):239–264, 1992. ISSN 0010-2180. doi: 10.1016/0010-2180(92)90034-M. URL `https://www.sciencedirect.com/science/article/pii/001021809290034M`.

[154] M. Rieth, A. Clements, M. Rabaçal, F. Proch, O. Stein, and A. Kempf. Flamelet LES modeling of coal combustion with detailed devolatilization by directly coupled CPD. *Proceedings of the Combustion Institute*, 36(2):2181–2189, 2017. ISSN 1540-7489. doi: 10.1016/j.proci.2016.06.077. URL `https://www.sciencedirect.com/science/article/pii/S1540748916301353`.

[155] K. Bray. The challenge of turbulent combustion. *Symposium (International) on Combustion*, 26(1):1–26, 1996. ISSN 0082-0784. doi: 10.1016/S0082-0784(96)80195-0. URL `https://www.sciencedirect.com/science/article/pii/S0082078496801950`.

[156] W. Hawthorne, D. Weddell, and H. Hottel. Mixing and combustion in turbulent gas jets. *Symposium on Combustion and Flame, and Explosion Phenomena*, 3(1):266–288, 1948. ISSN 1062-2896. doi: 10.1016/S1062-2896(49)80035-3. URL `https://www.sciencedirect.com/science/article/pii/S1062289649800353`.

[157] M. Ferrarotti, Z. Li, and A. Parente. On the role of mixing models in the simulation of MILD combustion using finite-rate chemistry combustion models. *Proceedings of the Combustion Institute*, 37(4):4531–4538, 2019. ISSN 1540-7489. doi: 10.1016/j.proci.2018.07.043. URL `https://www.sciencedirect.com/science/article/pii/S1540748918304619`.

[158] I. S. Ertesvåg and B. F. Magnussen. The Eddy Dissipation turbulence energy cascade model. *Combustion Science and Technology*, 159(1):213–235, 2007. ISSN 0010-2202. doi: 10.1080/00102200008935784. URL `https://doi.org/10.1080/00102200008935784`.

[159] I. S. Ertesvåg. Analysis of some recently proposed modifications to the Eddy Dissipation Concept (EDC). *Combustion Science and Technology*, 0(0):1–29, 2019. doi: 10.1080/00102202.2019.1611565. URL `https://doi.org/10.1080/00102202.2019.1611565`.

[160] A. Y.-S. Kuo and S. Corrsin. Experiments on internal intermittency and fine-structure distribution functions in fully turbulent fluid. *Journal of Fluid Mechanics*, 50(2):285–319, 1971. doi: 10.1017/S0022112071002581. URL `https://doi.org/10.1017/S0022112071002581`.

[161] A. Y.-S. Kuo and S. Corrsin. Experiment on the geometry of the fine-structure regions in fully turbulent fluid. *Journal of Fluid Mechanics*, 56(3):447–479, 1972. doi: 10.1017/S0022112072002459. URL `https://doi.org/10.1017/S0022112072002459`.

[162] M. T. Lewandowski and I. S. Ertesvåg. Analysis of the Eddy Dissipation Concept formulation for MILD combustion modelling. *Fuel*, 224:687–700, 2018. ISSN 0016-2361. doi: 10.1016/j.fuel.2018.03.110. URL `https://doi.org/10.1016/j.fuel.2018.03.110`.

[163] H. Tennekes. Simple model for the small-scale structure of turbulence. *The Physics of Fluids*, 11(3):669–671, 1968. doi: 10.1063/1.1691966. URL `https://doi.org/10.1063/1.1691966`.

[164] Z. Li, A. Cuoci, A. Sadiki, and A. Parente. Comprehensive numerical study of the Adelaide Jet in Hot-Coflow burner by means of RANS and detailed chemistry. *Energy*, 139:555–570, 2017. ISSN 0360-5442. doi: 10.1016/j.energy.2017.07.132. URL `https://www.sciencedirect.com/science/article/pii/S0360544217313142`.

[165] S. Corrsin. Turbulent flow. *American Scientist*, 49(3):300–325, 1961. ISSN 00030996. URL `https://www.jstor.org/stable/27827853`.

[166] I. R. Gran and B. F. Magnussen. A numerical study of a bluff-body stabilized diffusion flame. Part 2. Influence of combustion modeling and finite-rate chemistry. *Combustion Science and Technology*, 119(1-6):191–217, 1996. ISSN 0010-2202. doi: 10.1080/00102209608951999. URL `https://doi.org/10.1080/00102209608951999`.

[167] M. T. Lewandowski, A. Parente, and J. Pozorski. Generalised Eddy Dissipation Concept for MILD combustion regime at low local Reynolds and damköhler numbers. Part 1: Model framework development. *Fuel*, page 117743, 2020. ISSN 0016-2361. doi: 10.1016/j.fuel.2020.117743. URL `https://www.sciencedirect.com/science/article/pii/S0016236120307389`.

[168] A. Cavaliere and M. de Joannon. MILD combustion. *Progress in Energy and Combustion Science*, 30(4):329–366, 2004. ISSN 0360-1285. doi: 10.1016/j.pecs.2004.02.003. URL `https://www.sciencedirect.com/science/article/pii/S0360128504000127`.

[169] H. Bao, X. Huang, and D. Roekaerts. Validation of standard and extended Eddy Dissipation Concept Model for the Delft Jet-in Hot Coflow (DJHC) flame. *Combura 2016*, 2016.

[170] U. Prüfert, F. Hunger, and C. Hasse. The analysis of chemical time scales in a partial oxidation flame. *Combustion and Flame*, 161(2):416–426, 2014. ISSN 0010-2180. doi: 10.1016/j.combustflame.2013.09.001. URL `https://www.sciencedirect.com/science/article/pii/S0010218013003313`.

[171] B. J. Isaac, A. Parente, C. Galletti, J. N. Thornock, P. J. Smith, and L. Tognotti. A novel methodology for chemical time scale evaluation with detailed chemical reaction kinetics. *Energy & Fuels*, 27(4):2255–2265, 2013. doi: 10.1021/ef301961x. URL `https://doi.org/10.1021/ef301961x`.

[172] M. Farokhi and M. Birouk. Assessment of fractal/wrinkling theories for describing turbulent reacting fine structures under MILD combustion regimes. *Combustion Science and Technology*, 0(0):1–28, 2020. doi: 10.1080/00102202.2020.1715963. URL `https://doi.org/10.1080/00102202.2020.1715963`.

[173] Ömer L. Gülder. Contribution of small scale turbulence to burning velocity of flamelets in the thin reaction zone regime. *Proceedings of the Combustion Institute*, 31(1):1369 – 1375, 2007. ISSN 1540-7489. doi: 10.1016/j.proci.2006.07.189. URL `https://www.sciencedirect.com/science/article/pii/S1540748906002008`.

[174] E. Giacomazzi, C. Bruno, and B. Favini. Fractal modelling of turbulent combustion. *Combustion Theory and Modelling*, 4(4):391–412, 2000. doi: 10.1088/1364-7830/4/4/302. URL `https://doi.org/10.1088/1364-7830/4/4/302`.

[175] E. Giacomazzi, C. Bruno, and B. Favini. Fractal modelling of turbulent mixing. *Combustion Theory and Modelling*, 3(4):637–655, 1999. doi: 10.1088/1364-7830/3/4/303. URL `https://doi.org/10.1088/1364-7830/3/4/303`.

[176] A. Shiehnejadhesar, R. Mehrabian, R. Scharler, G. M. Goldin, and I. Obernberger. Development of a gas phase combustion model suitable for low and high turbulence conditions. *Fuel*, 126:177–187, 2014. ISSN 0016-2361. doi: 10.1016/j.fuel.2014.02.040. URL `https://www.sciencedirect.com/science/article/pii/S0016236114001793`.

[177] E. Oldenhof, M. Tummers, E. van Veen, and D. Roekaerts. Role of entrainment in the stabilisation of Jet-In-Hot-Coflow flames. *Combustion and Flame*, 158(8):1553–1563, 2011. ISSN 0010-2180. doi: 10.1016/j.combustflame.2010.12.018. URL `https://www.sciencedirect.com/science/article/pii/S001021801000372X`.

[178] B. Denet. A lagrangian method to simulate turbulent flames with reconnections. *Combustion Science and Technology*, 123(1-6):247–260, 1997. doi: 10.1080/00102209708935630. URL `https://doi.org/10.1080/00102209708935630`.

[179] L. A. Vulis. *Thermal regimes of combustion*. McGraw-Hill, New York, NW, USA, 1961.

[180] V. Raman and H. Pitsch. A consistent LES/filtered-density function formulation for the simulation of turbulent flames with detailed chemistry. *Proceedings of the Combustion Institute*, 31(2):1711–1719, 2007. ISSN 1540-7489. doi: 10.1016/j.proci.2006.07.152. URL `https://www.sciencedirect.com/science/article/pii/S154074890600160X`.

[181] J. P. H. Sanders and I. Gökalp. Scalar dissipation rate modelling in variable density turbulent axisymmetric jets and diffusion flames. *Physics of Fluids*, 10(4):938–948, 1998. doi: 10.1063/1.869616. URL `https://doi.org/10.1063/1.869616`.

[182] G. F. Froment, K. B. Bischoff, and J. D. Wilde. *Chemical Reactor Analysis and Design*, volume 3. Wiley New York, 2010. ISBN 0470565411.

[183] R. J. Kee, M. E. Coltrin, P. Glarborg, and H. Zhu. *Heterogeneous Chemistry*, chapter 16, pages 549–587. John Wiley & Sons, Ltd, 2017. ISBN 9781119186304. doi: 10.1002/9781119186304.ch16. URL `https://onlinelibrary.wiley.com/doi/abs/10.1002/9781119186304.ch16`.

[184] D. T. Pratt, L. Smoot, and D. Pratt. *Pulverized coal combustion and gasification*. Springer Science & Business Media, New York, USA, 1979. ISBN 9781475716962. doi: 10.1007/978-1-4757-1696-2. URL `https://doi.org/10.1007/978-1-4757-1696-2`.

[185] L. D. Smoot and P. J. Smith. *Coal combustion and gasification*. Springer Science & Business Media, New York, USA, 1985. ISBN 9781475797213. doi: 10.1007/978-1-4757-9721-3. URL `https://doi.org/10.1007/978-1-4757-9721-3`.

[186] M. Rossberg and E. Wicke. Transportvorgänge und Oberflächenreaktionen bei der Verbrennung graphitischen Kohlenstoffs. *Chemie Ingenieur Technik*, 28(3):181–189, 1956. doi: 10.1002/cite.330280309. URL `https://onlinelibrary.wiley.com/doi/abs/10.1002/cite.330280309`.

[187] P. Weisz and C. Prater. Interpretation of measurements in experimental catalysis. volume 6 of *Advances in Catalysis*, pages 143–196. Academic Press, 1954. doi: 10.1016/S0360-0564(08)60390-9. URL `https://www.sciencedirect.com/science/article/pii/S0360056408603909`.

[188] P. B. Weisz and R. B. Goodwin. Combustion of carbonaceous deposits within porous catalyst particles: II. Intrinsic burning rate. *Journal of Catalysis*, 6(2):227–236, 1966. ISSN 0021-9517. doi: 10.1016/0021-9517(66)90053-4. URL `https://www.sciencedirect.com/science/article/pii/0021951766900534`.

[189] N. M. Laurendeau. Heterogeneous kinetics of coal char gasification and combustion. *Progress in Energy and Combustion Science*, 4(4):221–270, 1978. ISSN 0360-1285. doi: 10.1016/

0360-1285(78)90008-4. URL https://www.sciencedirect.com/science/article/pii/0360128578900084.

[190] E. W. Thiele. Relation between catalytic activity and size of particle. *Industrial & Engineering Chemistry*, 31(7):916–920, 1939. doi: 10.1021/ie50355a027. URL https://doi.org/10.1021/ie50355a027.

[191] A. Wheeler. Reaction rates and selectivity in catalyst pores. volume 3 of *Advances in Catalysis*, pages 249–327. Academic Press, 1951. doi: 10.1016/S0360-0564(08)60109-1. URL https://www.sciencedirect.com/science/article/pii/S0360056408601091.

[192] G. Damköhler. Einflüsse der Strömung, Diffusion und des Wärmeüberganges auf die Leistung von Reaktionsöfen.: I. Allgemeine Gesichtspunkte für die Übertragung eines chemischen Prozesses aus dem Kleinen ins Große. *Zeitschrift für Elektrochemie und angewandte physikalische Chemie*, 42(12):846–862, 1936. doi: 10.1002/bbpc.19360421203. URL https://onlinelibrary.wiley.com/doi/abs/10.1002/bbpc.19360421203.

[193] Y. Zeldovich. On the theory of the reaction on a porous or powder catalyst. *Acta Physiochimica URSS*, 10:584–592, 1939.

[194] A. Gómez-Barea, P. Ollero, and B. Leckner. Mass transport effects during measurements of gas–solid reaction kinetics in a fluidised bed. *Chemical Engineering Science*, 62(5):1477–1493, 2007. ISSN 0009-2509. doi: 10.1016/j.ces.2006.10.018. URL https://www.sciencedirect.com/science/article/pii/S000925090600666X.

[195] R. Aris. On shape factors for irregular particles — I: The steady state problem. Diffusion and reaction. *Chemical Engineering Science*, 6(6):262–268, 1957. ISSN 0009-2509. doi: 10.1016/0009-2509(57)85028-3. URL https://www.sciencedirect.com/science/article/pii/0009250957850283.

[196] K. B. Bischoff. Effectiveness factors for general reaction rate forms. *AIChE Journal*, 11(2):351–355, 1965. doi: 10.1002/aic.690110229. URL https://aiche.onlinelibrary.wiley.com/doi/abs/10.1002/aic.690110229.

[197] H. Sohn, R. Merrill, and E. Petersen. Effectiveness factor for surface diffusion and reaction on catalyst surface. *Chemical Engineering Science*, 25(3):399–406, 1970. ISSN 0009-2509. doi: 10.1016/0009-2509(70)80038-0. URL https://www.sciencedirect.com/science/article/pii/0009250970800380.

[198] R. Datta and S. W.-K. Leung. Shape generalized isothermal effectiveness factor for first-order kinetics. *Chemical Engineering Communications*, 39(1–6):155–173, 1985. doi: 10.1080/00986448508911668. URL https://doi.org/10.1080/00986448508911668.

[199] V. Ananthaswamy and L. Rajendran. Analytical solution of non-isothermal diffusion-reaction processes and effectiveness factors. *ISRN Physical Chemistry*, 2013:1–14, 2013. doi: 10.1155/2013/487240. URL https://doi.org/10.1155/2013/487240.

[200] P. Weisz and J. Hicks. The behaviour of porous catalyst particles in view of internal mass and heat diffusion effects. *Chemical Engineering Science*, 50(24):3951–3958, 1995. ISSN 0009-2509. doi: 10.1016/0009-2509(96)81827-6. URL https://www.sciencedirect.com/science/article/pii/0009250996818276.

[201] S. Kimura, J. I. Nakagawa, S. Tone, and T. Otake. Non-isothermal behavior of gas-solid reactions based on the volume reaction model. *Journal of Chemical Engineering of Japan*, 15(2):115–121, 1982. doi: 10.1252/jcej.15.115. URL `https://doi.org/10.1252/jcej.15.115`.

[202] C. Y. Wen. Noncatalytic heterogeneous solid-fluid reaction models. *Industrial & Engineering Chemistry*, 60(9):34–54, 1968. doi: 10.1021/ie50705a007. URL `https://doi.org/10.1021/ie50705a007`.

[203] S. K. Bhatia and D. D. Perlmutter. A random pore model for fluid-solid reactions: I. Isothermal, kinetic control. *AIChE Journal*, 26(3):379–386, 1980. doi: 10.1002/aic.690260308. URL `https://aiche.onlinelibrary.wiley.com/doi/abs/10.1002/aic.690260308`.

[204] S. K. Bhatia and D. D. Perlmutter. A random pore model for fluid-solid reactions: II. Diffusion and transport effects. *AIChE Journal*, 27(2):247–254, 1981. doi: 10.1002/aic.690270211. URL `https://aiche.onlinelibrary.wiley.com/doi/abs/10.1002/aic.690270211`.

[205] V. Safari, G. Arzpeyma, F. Rashchi, and N. Mostoufi. A shrinking particle—shrinking core model for leaching of a zinc ore containing silica. *International Journal of Mineral Processing*, 93(1):79–83, 2009. ISSN 0301-7516. doi: 10.1016/j.minpro.2009.06.003. URL `https://www.sciencedirect.com/science/article/pii/S0301751609001422`.

[206] P. Pednekar, D. Bhattacharyya, J. S. Kasule, R. Turton, and R. Rengaswamy. Development of a hybrid shrinking-core shrinking-particle model for entrained-flow gasifiers. *AIChE Journal*, 62(3):659–669, 2016. doi: 10.1002/aic.15055. URL `https://aiche.onlinelibrary.wiley.com/doi/abs/10.1002/aic.15055`.

[207] T. Salmi, H. Grénman, J. Wärnå, and D. Y. Murzin. Revisiting shrinking particle and product layer models for fluid–solid reactions – From ideal surfaces to real surfaces. *Chemical Engineering and Processing: Process Intensification*, 50(10):1076–1084, 2011. ISSN 0255-2701. doi: 10.1016/j.cep.2011.05.015. URL `https://www.sciencedirect.com/science/article/pii/S0255270111001255`.

[208] C. Núñez, M. Cruells, and L. García-Soto. A general shrinking-particle model for the chemical dissolution of all types of cylinders and discs. *Hydrometallurgy*, 36(3):285–294, 1994. ISSN 0304-386X. doi: 10.1016/0304-386X(94)90027-2. URL `https://www.sciencedirect.com/science/article/pii/0304386X94900272`.

[209] C. Núñez, J. Viñals, A. Roca, and L. García-Soto. A general shrinking-particle model for the chemical dissolution of crystalline forms. *Hydrometallurgy*, 36(1):1–17, 1994. ISSN 0304-386X. doi: 10.1016/0304-386X(94)90038-8. URL `https://www.sciencedirect.com/science/article/pii/0304386X94900388`.

[210] S. Homma, S. Ogata, J. Koga, and S. Matsumoto. Gas–solid reaction model for a shrinking spherical particle with unreacted shrinking core. *Chemical Engineering Science*, 60(18):4971–4980, 2005. ISSN 0009-2509. doi: 10.1016/j.ces.2005.03.057. URL `https://www.sciencedirect.com/science/article/pii/S0009250905002757`.

[211] P. R. Jena, S. De, and J. K. Basu. A generalized shrinking core model applied to batch adsorption. *Chemical Engineering Journal*, 95(1):143–154, 2003. ISSN 1385-8947. doi: 10.1016/S1385-8947(03)00097-4. URL `https://www.sciencedirect.com/science/article/pii/S1385894703000974`.

[212] X. Liu, F. Song, and Z. Wen. A novel dimensionless form of unreacted shrinking core model for solid conversion during chemical looping combustion. *Fuel*, 129:231–237, 2014. ISSN 0016-2361. doi: 10.1016/j.fuel.2014.04.006. URL https://www.sciencedirect.com/science/article/pii/S0016236114003275.

[213] P. B. Weisz and R. Goodwin. Combustion of carbonaceous deposits within porous catalyst particles I. Diffusion-controlled kinetics. *Journal of Catalysis*, 2(5):397–404, 1963. ISSN 0021-9517. doi: 10.1016/0021-9517(63)90104-0. URL https://www.sciencedirect.com/science/article/pii/0021951763901040.

[214] J. Szekely and J. Evans. A structural model for gas—solid reactions with a moving boundary. *Chemical Engineering Science*, 25(6):1091–1107, 1970. ISSN 0009-2509. doi: 10.1016/0009-2509(70)85053-9. URL https://www.sciencedirect.com/science/article/pii/0009250970850539.

[215] P. Kaushal, T. Proell, and H. Hofbauer. Application of a detailed mathematical model to the gasifier unit of the dual fluidized bed gasification plant. *Biomass and Bioenergy*, 35(7):2491–2498, 2011. ISSN 0961-9534. doi: 10.1016/j.biombioe.2011.01.025. URL https://www.sciencedirect.com/science/article/pii/S0961953411000262.

[216] D. Kunii and O. Levenspiel. *Fluidization Engineering*. Butterworth-Heinemann, Stoneham, MA, USA, 2nd edition, 1969. ISBN 978-0-080-50664-7.

[217] P. Kaushal and J. Abedi. A simplified model for biomass pyrolysis in a fluidized bed reactor. *Journal of Industrial and Engineering Chemistry*, 16(5):748–755, 2010. ISSN 1226-086X. doi: 10.1016/j.jiec.2010.07.008. URL https://www.sciencedirect.com/science/article/pii/S1226086X10002029.

[218] R. C. Everson, H. W. Neomagus, and R. Kaitano. The random pore model with intraparticle diffusion for the description of combustion of char particles derived from mineral- and inertinite rich coal. *Fuel*, 90(7):2347–2352, 2011. ISSN 0016-2361. doi: 10.1016/j.fuel.2011.03.012. URL https://www.sciencedirect.com/science/article/pii/S0016236111001402.

[219] J. Cai, S. Wang, and C. Kuang. A modified random pore model for carbonation reaction of CaO-based limestone with CO_2 in different calcination-carbonation cycles. *Energy Procedia*, 105:1924–1931, 2017. ISSN 1876-6102. doi: 10.1016/j.egypro.2017.03.561. URL https://www.sciencedirect.com/science/article/pii/S1876610217306136.

[220] M. H. Sedghkerdar and N. Mahinpey. A modified grain model in studying the CO_2 capture process with a calcium-based sorbent: A semianalytical approach. *Industrial & Engineering Chemistry Research*, 54(3):869–877, 2015. doi: 10.1021/ie503989n. URL https://doi.org/10.1021/ie503989n.

[221] K. J. Laidler. Chemical kinetics and the origins of physical chemistry. *Archive for History of Exact Sciences*, 32(1):43–75, 1985. ISSN 00039519, 14320657. URL https://www.jstor.org/stable/41133743.

[222] K. J. Laidler. A glossary of terms used in chemical kinetics, including reaction dynamics (IUPAC recommendations 1996). *Pure and Applied Chemistry*, 68(1):149–192, 1996. ISSN 13653075. doi: 10.1351/pac199668010149. URL https://www.degruyter.com/view/j/pac.1996.68.issue-1/pac199668010149/pac199668010149.xml.

[223] R. Mehrabian, S. Zahirovic, R. Scharler, I. Obernberger, S. Kleditzsch, S. Wirtz, V. Scherer, H. Lu, and L. L. Baxter. A CFD model for thermal conversion of thermally thick biomass particles. *Fuel Processing Technology*, 95:96–108, 2012. ISSN 0378-3820. doi: 10.1016/j.fuproc.2011.11.021. URL https://www.sciencedirect.com/science/article/pii/S0378382011004085.

[224] K. Hedden. Die Bedeutung der Reaktionsgeschwindigkeit für die Abgaszusammensetzung bei Vergasungsprozessen. *Chemie Ingenieur Technik*, 30(3):125–132, 1958. doi: 10.1002/cite.330300304. URL https://onlinelibrary.wiley.com/doi/abs/10.1002/cite.330300304.

[225] A. Khawam and D. R. Flanagan. Solid-state kinetic models: Basics and mathematical fundamentals. *The Journal of Physical Chemistry B*, 110(35):17315–17328, 2006. doi: 10.1021/jp062746a. URL https://doi.org/10.1021/jp062746a.

[226] J. Szekely and J. Evans. A structural model for gas-solid reactions with a moving boundary-II: The effect of grain size, porosity and temperature on the reaction of porous pellets. *Chemical Engineering Science*, 26(11):1901–1913, 1971. ISSN 0009-2509. doi: 10.1016/0009-2509(71)86033-5. URL https://www.sciencedirect.com/science/article/pii/0009250971860335.

[227] W. E. Garner, editor. *Chemistry of solid state*. Butterworths Scientific Publications, London, 1955.

[228] M. Geier, C. Shaddix, K. Davis, and H.-S. Shim. On the use of single-film models to describe the oxy-fuel combustion of pulverized coal char. *Applied Energy*, 93:675–679, 2012. ISSN 0306-2619. doi: 10.1016/j.apenergy.2011.12.097. URL https://www.sciencedirect.com/science/article/pii/S0306261912000025.

[229] E. S. Hecht, C. R. Shaddix, M. Geier, A. Molina, and B. S. Haynes. Effect of CO_2 and steam gasification reactions on the oxy-combustion of pulverized coal char. *Combustion and Flame*, 159(11):3437–3447, 2012. ISSN 0010-2180. doi: 10.1016/j.combustflame.2012.06.009. URL https://www.sciencedirect.com/science/article/pii/S0010218012001897.

[230] E. S. Hecht, C. R. Shaddix, and J. S. Lighty. Analysis of the errors associated with typical pulverized coal char combustion modeling assumptions for oxy-fuel combustion. *Combustion and Flame*, 160(8):1499–1509, 2013. ISSN 0010-2180. doi: 10.1016/j.combustflame.2013.02.015. URL https://www.sciencedirect.com/science/article/pii/S0010218013000655.

[231] E. S. Hecht, C. R. Shaddix, A. Molina, and B. S. Haynes. Effect of CO_2 gasification reaction on oxy-combustion of pulverized coal char. *Proceedings of the Combustion Institute*, 33 (2):1699–1706, 2011. ISSN 1540-7489. doi: 10.1016/j.proci.2010.07.087. URL https://www.sciencedirect.com/science/article/pii/S1540748910003718.

[232] S. Arrhenius. Über die Reaktionsgeschwindigkeit bei der Inversion von Rohrzucker durch Säuren. *Zeitschrift für physikalische Chemie*, 4(1):226–248, 1889. doi: 10.1515/zpch-1889-0416. URL https://doi.org/10.1515/zpch-1889-0416.

[233] G. D. Silcox, J. C. Kramlich, and D. W. Pershing. A mathematical model for the flash calcination of dispersed calcium carbonate and calcium hydroxide particles. *Industrial & Engineering Chemistry Research*, 28(2):155–160, 1989. doi: 10.1021/ie00086a005. URL https://doi.org/10.1021/ie00086a005.

[234] C. Bamford and C. Tipper. Chapter 3 - Theory of solid state reaction kinetics. In C. Bamford and C. Tipper, editors, *Reactions in the Solid State*, volume 22 of *Comprehensive Chemical Kinetics*, pages 41–113. Elsevier, 1980. doi: 10.1016/S0069-8040(08)70384-4. URL `https://www.sciencedirect.com/science/article/pii/S0069804008703844`.

[235] P. Michèle, F. Loïc, and S. Michel. From the drawbacks of the Arrhenius-f(α) rate equation towards a more general formalism and new models for the kinetic analysis of solid–gas reactions. *Thermochimica Acta*, 525(1):93–102, 2011. ISSN 0040-6031. doi: 10.1016/j.tca.2011.07.026. URL `https://www.sciencedirect.com/science/article/pii/S0040603111004163`.

[236] A. K. Galwey. Solid state reaction kinetics, mechanisms and catalysis: A retrospective rational review. *Reaction Kinetics, Mechanisms and Catalysis*, 114(1):1–29, 2015. ISSN 1878-5204. doi: 10.1007/s11144-014-0770-7. URL `https://doi.org/10.1007/s11144-014-0770-7`.

[237] S. Rumpel. *Die autotherme Wirbelschichtpyrolyse zur Erzeugung heizwertreicher Stützbrennstoffe*. PhD thesis, Faculty of Chemical and Process Engineering, Karlsruhe Institute of Technology, 2000.

[238] J. G. Jouven and R. Airs. A method of representing the nonisothermal effectiveness factor for fixed bed calculations. *AIChE Journal*, 18(2):402–408, 1972. doi: 10.1002/aic.690180224. URL `https://aiche.onlinelibrary.wiley.com/doi/abs/10.1002/aic.690180224`.

[239] D. H. Kim and J. Lee. A robust iterative method of computing effectiveness factors in porous catalysts. *Chemical Engineering Science*, 59(11):2253–2263, 2004. ISSN 0009-2509. doi: 10.1016/j.ces.2004.01.056. URL `https://www.sciencedirect.com/science/article/pii/S0009250904001393`.

[240] J. Lee and D. H. Kim. Effectiveness factor approximations for multiple steady states in porous catalysts. *Chemical Engineering Science*, 62(8):2179–2186, 2007. ISSN 0009-2509. doi: 10.1016/j.ces.2007.01.021. URL `https://www.sciencedirect.com/science/article/pii/S0009250907000723`.

[241] R. Aris. *The Mathematical Theory of Diffusion and Reaction in Permeable Catalysts. Volume 1: The Theory of the Steady State. Volume 2: Questions of Uniqueness Stability and transient Behavior. 2 Volume Set.* Oxford University Press, 1975. ISBN 0195198298.

[242] G. Damköhler. Übertemperatur in Kontaktkörnern. *Zeitschrift für Physikalische Chemie*, 193(1):16–28, 1943. doi: 10.1515/zpch-1943-19303. URL `https://doi.org/10.1515/zpch-1943-19303`.

[243] C. D. Prater. The temperature produced by heat of reaction in the interior of porous particles. *Chemical Engineering Science*, 8(3):284–286, 1958. ISSN 0009-2509. doi: 10.1016/0009-2509(58)85035-6. URL `https://www.sciencedirect.com/science/article/pii/0009250958850356`.

[244] R. L. Wong, G. L. Hubbard, and V. E. Denny. Effects of temperature and pressure gradients on catalyst pellet effectiveness factors — I. *Chemical Engineering Science*, 31(7):541–548, 1976. ISSN 0009-2509. doi: 10.1016/0009-2509(76)80017-6. URL `https://www.sciencedirect.com/science/article/pii/0009250976800176`.

[245] V. W. Weekman and R. L. Gorring. Influence of volume change on gas-phase reactions in porous catalysts. *Journal of Catalysis*, 4(2):260–270, 1965. ISSN 0021-9517. doi: 10.1016/0021-9517(65)90017-5. URL https://www.sciencedirect.com/science/article/pii/0021951765900175.

[246] V. W. Weekman. Combined effect of volume change and internal heat and mass transfer on gas-phase reactions in porous catalysts. *Journal of Catalysis*, 5(1):44–54, 1966. ISSN 0021-9517. doi: 10.1016/S0021-9517(66)80124-0. URL https://www.sciencedirect.com/science/article/pii/S0021951766801240.

[247] H. S. P. Kao and C. N. Satterfield. Effectiveness factors for reversible reactions. *Industrial & Engineering Chemistry Fundamentals*, 7(4):664–667, 1968. doi: 10.1021/i160028a025. URL https://doi.org/10.1021/i160028a025.

[248] A. H. Aguirre, M. A. M. Cabrera, E. M. Zarate, V. M. Rivera, H. Puebla, and E. H. Martinez. Non-isothermal effectiveness factor for catalytic particles with non-Fickian diffusion. *International Journal of Chemical Reactor Engineering*, 15(5):12, 2017. doi: 10.1515/ijcre-2017-0024. URL https://doi.org/10.1515/ijcre-2017-0024.

[249] H. Thunman, B. Leckner, F. Niklasson, and F. Johnsson. Combustion of wood particles—a particle model for Eulerian calculations. *Combustion and Flame*, 129(1):30–46, 2002. ISSN 0010-2180. doi: 10.1016/S0010-2180(01)00371-6. URL https://www.sciencedirect.com/science/article/pii/S0010218001003716.

[250] M. Deutsch, F. Birkelbach, C. Knoll, M. Harasek, A. Werner, and F. Winter. An extension of the NPK method to include the pressure dependency of solid state reactions. *Thermochimica Acta*, 654:168–178, 2017. ISSN 0040-6031. doi: 10.1016/j.tca.2017.05.019. URL https://www.sciencedirect.com/science/article/pii/S0040603117301405.

[251] W. Jander. Reaktionen im festen Zustande bei höheren Temperaturen. Reaktionsgeschwindigkeiten endotherm verlaufender Umsetzungen. *Zeitschrift für anorganische und allgemeine Chemie*, 163(1):1–30, 1927. doi: 10.1002/zaac.19271630102. URL https://onlinelibrary.wiley.com/doi/abs/10.1002/zaac.19271630102.

[252] R. M. Paul and J. E. Morral. A 3D random pore model for the oxidation of graphite with open porosity. *Journal of Nuclear Materials*, 499:344–352, 2018. ISSN 0022-3115. doi: 10.1016/j.jnucmat.2017.11.056. URL https://www.sciencedirect.com/science/article/pii/S0022311517312849.

[253] A. Gómez-Barea, B. Leckner, D. Santana, and P. Ollero. Gas–solid conversion in fluidised bed reactors. *Chemical Engineering Journal*, 141(1):151–168, 2008. ISSN 1385-8947. doi: 10.1016/j.cej.2007.12.014. URL https://www.sciencedirect.com/science/article/pii/S1385894707008017.

[254] S. V. Patankar. *Numerical Heat Transfer and Fluid Flow*. Hemisphere Publishing Corporation, Washington, New York, London, 1980. ISBN 0-07-048740-5.

[255] S. Vasquez. A phase coupled method for solving multiphase problems on unstructured mesh. In *ASME 200 Fluids Engineering Division Summer Meeting*, 2000.

[256] M. Darwish, A. A. Aziz, and F. Moukalled. A coupled pressure-based finite-volume solver for incompressible two-phase flow. *Numerical Heat Transfer, Part B: Fundamentals*, 67(1):47–74, 2015. doi: 10.1080/10407790.2014.949500. URL https://doi.org/10.1080/10407790.2014.949500.

[257] M. Darwish, I. Sraj, and F. Moukalled. A coupled finite volume solver for the solution of incompressible flows on unstructured grids. *Journal of Computational Physics*, 228 (1):180–201, 2009. ISSN 0021-9991. doi: 10.1016/j.jcp.2008.08.027. URL `https://www.sciencedirect.com/science/article/pii/S0021999108004725`.

[258] F. H. Harlow and J. E. Welch. Numerical calculation of time-dependent viscous incompressible flow of fluid with free surface. *The Physics of Fluids*, 8(12):2182–2189, 1965. doi: 10.1063/1.1761178. URL `https://aip.scitation.org/doi/abs/10.1063/1.1761178`.

[259] A. J. Chorin. Numerical solution of the Navier-Stokes equations. *Mathematics of Computation*, 22(104):745–762, 1968. doi: 10.1090/S0025-5718-1968-0242392-2. URL `https://doi.org/10.1090/S0025-5718-1968-0242392-2`.

[260] J. Kim and P. Moin. Application of a fractional-step method to incompressible navier-stokes equations. *Journal of Computational Physics*, 59(2):308–323, 1985. ISSN 0021-9991. doi: 10.1016/0021-9991(85)90148-2. URL `https://www.sciencedirect.com/science/article/pii/0021999185901482`.

[261] S. Patankar and D. Spalding. A calculation procedure for heat, mass and momentum transfer in three-dimensional parabolic flows. *International Journal of Heat and Mass Transfer*, 15(10):1787–1806, 1972. ISSN 0017-9310. doi: 10.1016/0017-9310(72)90054-3. URL `https://www.sciencedirect.com/science/article/pii/0017931072900543`.

[262] L. S. Caretto, A. D. Gosman, S. V. Patankar, and D. B. Spalding. Two calculation procedures for steady, three-dimensional flows with recirculation. In H. Cabannes and R. Temam, editors, *Proceedings of the Third International Conference on Numerical Methods in Fluid Mechanics*, pages 60–68, Berlin, Heidelberg, 1973. Springer Berlin Heidelberg. ISBN 978-3-540-38392-5. URL `https://link.springer.com/chapter/10.1007/BFb0112677`.

[263] S. V. Patankar. A calculation procedure for two-dimensional elliptic situations. *Numerical Heat Transfer*, 4(4):409–425, 1981. doi: 10.1080/01495728108961801. URL `https://doi.org/10.1080/01495728108961801`.

[264] I. E. Barton. Comparison of SIMPLE- and PISO-type algorithms for transient flows. *International Journal for Numerical Methods in Fluids*, 26(4): 459–483, 1998. doi: 10.1002/(SICI)1097-0363(19980228)26:4<459::AID-FLD645> 3.0.CO;2-U. URL `https://onlinelibrary.wiley.com/doi/abs/10.1002/%28SICI%291097-0363%2819980228%2926%3A4%3C459%3A%3AAID-FLD645%3E3.0.CO%3B2-U`.

[265] R. Issa. Solution of the implicitly discretised fluid flow equations by operator-splitting. *Journal of Computational Physics*, 62(1):40–65, 1986. ISSN 0021-9991. doi: 10.1016/0021-9991(86)90099-9. URL `https://www.sciencedirect.com/science/article/pii/0021999186900999`.

[266] R. Issa, B. Ahmadi-Befrui, K. Beshay, and A. Gosman. Solution of the implicitly discretised reacting flow equations by operator-splitting. *Journal of Computational Physics*, 93(2): 388–410, 1991. ISSN 0021-9991. doi: 10.1016/0021-9991(91)90191-M. URL `https://www.sciencedirect.com/science/article/pii/002199919190191M`.

[267] R. Courant, K. Friedrichs, and H. Lewy. Über die partiellen Differenzengleichungen der mathematischen Physik. *Mathematische Annalen*, 100(1):32–74, 1928. ISSN 1432-1807. doi: 10.1007/BF01448839. URL `https://doi.org/10.1007/BF01448839`.

[268] R. Courant, K. Friedrichs, and H. Lewy. On the partial difference equations of mathematical physics. *IBM Journal of Research and Development*, 11(2):215–234, 1967. ISSN 0018-8646. doi: 10.1147/rd.112.0215. URL `https://doi.org/10.1147/rd.112.0215`.

[269] A. Dewan. *Tackling turbulent flows in engineering.* Springer, Berlin Heidelberg, 2011. ISBN 978-3-642-14766-1.

[270] A. N. Kolmogorov. A refinement of previous hypotheses concerning the local structure of turbulence in a viscous incompressible fluid at high Reynolds number. *Journal of Fluid Mechanics*, 13(1):82–85, 1962. doi: 10.1017/S0022112062000518. URL `https://doi.org/10.1017/S0022112062000518`.

[271] A. N. Kolmogorov. Dissipation of energy in the locally isotropic turbulence. *Proceedings: Mathematical and Physical Sciences*, 434(1890):15–17, 1991. ISSN 09628444. doi: 10.1098/rspa.1991.0076. URL `https://doi.org/10.1098/rspa.1991.0076`.

[272] A. N. Kolmogorov. The local structure of turbulence in incompressible viscous fluid for very large Reynolds numbers. *Proceedings: Mathematical and Physical Sciences*, 434(1890): 9–13, 1991. ISSN 09628444. doi: 10.1098/rspa.1991.0075. URL `https://www.jstor.org/stable/51980`.

[273] P. Moin and K. Mahesh. DIRECT NUMERICAL SIMULATION: A tool in turbulence research. *Annual Review of Fluid Mechanics*, 30(1):539–578, 1998. doi: 10.1146/annurev.fluid.30.1.539. URL `https://doi.org/10.1146/annurev.fluid.30.1.539`.

[274] S. B. Pope. *Turbulent Flows.* Cambridge University Press, 2000. doi: 10.1017/CBO9780511840531. URL `https://doi.org/10.1017/CBO9780511840531`.

[275] M. Rieth, F. Proch, M. Rabaçal, B. Franchetti, F. C. Marincola, and A. Kempf. Flamelet LES of a semi-industrial pulverized coal furnace. *Combustion and Flame*, 173:39–56, 2016. ISSN 0010-2180. doi: 10.1016/j.combustflame.2016.07.013. URL `https://www.sciencedirect.com/science/article/pii/S0010218016301730`.

[276] O. Reynolds. On the dynamical theory of incompressible viscous fluids and the determination of the criterion. *Philosophical Transactions of the Royal Society of London. A*, 186:123–164, 1895. ISSN 02643820. URL `https://www.jstor.org/stable/90643`.

[277] A. Favre. Turbulence: Space-time statistical properties and behavior in supersonic flows. *The Physics of Fluids*, 26(10):2851–2863, 1983. doi: 10.1063/1.864049. URL `https://aip.scitation.org/doi/abs/10.1063/1.864049`.

[278] W. Jones and B. Launder. The prediction of laminarization with a two-equation model of turbulence. *International Journal of Heat and Mass Transfer*, 15(2):301 – 314, 1972. ISSN 0017-9310. doi: 10.1016/0017-9310(72)90076-2. URL `https://www.sciencedirect.com/science/article/pii/0017931072900762`.

[279] C. Cambon, L. Jacquin, and J. L. Lubrano. Toward a new Reynolds stress model for rotating turbulent flows. *Physics of Fluids A: Fluid Dynamics*, 4(4):812–824, 1992. doi: 10.1063/1.858298. URL `https://doi.org/10.1063/1.858298`.

[280] W. Chen and F. Song. Reynolds-stress modelling of turbulent rotating flows. *Acta Mechanica Sinica*, 13(4):323–330, 1997. ISSN 1614-3116. doi: 10.1007/BF02487191. URL `https://doi.org/10.1007/BF02487191`.

[281] S. P. Yuan and R. M. C. So. Turbulent rotating flow calculations: An assessment of two-equation anisotropic and Reynolds stress models. *Proceedings of the Institution of Mechanical Engineers, Part G: Journal of Aerospace Engineering*, 212(3):193–212, 1998. doi: 10.1243/0954410981532270. URL `https://doi.org/10.1243/0954410981532270`.

[282] L. Zhou. *Theory and modeling of dispersed multiphase turbulent reacting flows.* Butterworth-Heinemann, Oxford, 2018. ISBN 978-0-12-813465-8.

[283] H. R. Norouzi, R. Zarghami, R. Sotudeh-Gharebagh, and N. Mostoufi. *Coupled CFD-DEM modeling: Formulation, implementation and application to multiphase flows.* John Wiley & Sons, Chichester, West Sussex, United Kingdom, 2016. ISBN 9781119005131.

[284] H. A. Jakobsen. *Chemical Reactor Modeling - Multiphase reactive Flows.* Springer-Verlag, Berlin Heidelberg, 2008. ISBN 9783540251972.

[285] J. D. Schwarzkopf, M. Sommerfeld, C. T. Crowe, and Y. Tsuji. *Multiphase flows with droplets and particles.* CRC press, 2011. ISBN 9780429106392. doi: 10.1201/b11103. URL `https://doi.org/10.1201/b11103`.

[286] R. Borghi and F. Anselmet. *Turbulent multiphase flows with heat and mass transfer.* ISTE Wiley, London, U.K. Hoboken, N.J, 2014. ISBN 9781848216174.

[287] A. Passalacqua and L. Marmo. A critical comparison of frictional stress models applied to the simulation of bubbling fluidized beds. *Chemical Engineering Science*, 64(12):2795–2806, 2009. ISSN 0009-2509. doi: 10.1016/j.ces.2009.03.005. URL `https://www.sciencedirect.com/science/article/pii/S0009250909001699`.

[288] D. A. Drew and S. L. Passman. *Applied Mathematical Sciences – Theory of Multicomponent Fluids.* Springer New York, Berlin-Heidelberg, Series Volume 135 edition, 1998. ISBN 9780387983806.

[289] S. Elghobashi. On predicting particle-laden turbulent flows. *Applied Scientific Research*, 52(4):309–329, 1994. ISSN 1573-1987. doi: 10.1007/BF00936835. URL `https://doi.org/10.1007/BF00936835`.

[290] S. Schneiderbauer and M. Saeedipour. Approximate deconvolution model for the simulation of turbulent gas-solid flows: An a priori analysis. *Physics of Fluids*, 30(2):023301, 2018. doi: 10.1063/1.5017004. URL `https://doi.org/10.1063/1.5017004`.

[291] S. Schneiderbauer and M. Saeedipour. Numerical simulation of turbulent gas–solid flow using an approximate deconvolution model. *International Journal of Multiphase Flow*, 114:287 – 302, 2019. ISSN 0301-9322. doi: 10.1016/j.ijmultiphaseflow.2019.03.017. URL `https://www.sciencedirect.com/science/article/pii/S0301932218307419`.

[292] D. A. Drew and L. A. Segel. Averaged equations for two-phase flows. *Studies in Applied Mathematics*, 50(3):205–231, 1971. doi: 10.1002/sapm1971503205. URL `https://onlinelibrary.wiley.com/doi/abs/10.1002/sapm1971503205`.

[293] H. Weller. Derivation, modelling and solution of the conditionally averaged two-phase flow equations. Technical report, Nabla Ltd, No Technical Report TR/HGW, 02 2005.

[294] M. Ishii and T. Hibiki. *Thermo-fluid Dynamics of Two-Phase Flow.* Springer Science & Business Media, Berlin Heidelberg, 1st ed. 2005 edition, 2007. ISBN 9780387283210.

[295] P. J. Oliveira and R. I. Issa. Numerical aspects of an algorithm for the eulerian simulation of two-phase flows. *International Journal for Numerical Methods in Fluids*, 43(10–11): 1177–1198, 2003. doi: 10.1002/fld.508. URL `https://onlinelibrary.wiley.com/doi/abs/10.1002/fld.508`.

[296] I. Park, H. Cho, H. Yoon, and J. Jeong. Numerical effects of the semi-conservative form of momentum equations for multi-dimensional two-phase flows. *Nuclear Engineering and Design*, 239(11):2365–2371, 2009. ISSN 0029-5493. doi: 10.1016/j.nucengdes.2009.06.011. URL `https://www.sciencedirect.com/science/article/pii/S0029549309003021`.

[297] C. M. Venier, S. M. Damian, and N. M. Nigro. Numerical aspects of Eulerian gas–particles flow formulations. *Computers & Fluids*, 133:151–169, 2016. ISSN 0045-7930. doi: 10.1016/j.compfluid.2016.05.003. URL `https://www.sciencedirect.com/science/article/pii/S0045793016301438`.

[298] K. Kissling, J. Springer, H. Jasak, S. Schutz, K. Urban, and M. Piesche. A coupled pressure based solution algorithm based on the volume-of-fluid approach for two or more immiscible fluids. In *Proceedings of the V European Conference on Computational Fluid Dynamics ECCOMAS CFD 2010*, 2010.

[299] L. Silva and P. Lage. Development and implementation of a polydispersed multiphase flow model in OpenFOAM. *Computers & Chemical Engineering*, 35(12):2653–2666, 2011. ISSN 0098-1354. doi: 10.1016/j.compchemeng.2011.04.011. URL `https://www.sciencedirect.com/science/article/pii/S0098135411001451`.

[300] A. Passalacqua and R. Fox. Implementation of an iterative solution procedure for multi-fluid gas–particle flow models on unstructured grids. *Powder Technology*, 213(1):174–187, 2011. ISSN 0032-5910. doi: 10.1016/j.powtec.2011.07.030. URL `https://www.sciencedirect.com/science/article/pii/S0032591011003652`.

[301] R. Keser, V. Vukčević, M. Battistoni, H. Im, and H. Jasak. Implicitly coupled phase fraction equations for the Eulerian multi-fluid model. *Computers & Fluids*, 192:104277, 2019. ISSN 0045-7930. doi: 10.1016/j.compfluid.2019.104277. URL `https://www.sciencedirect.com/science/article/pii/S0045793019302403`.

[302] G. G. Ferreira, P. L. Lage, L. F. L. Silva, and H. Jasak. Implementation of an implicit pressure–velocity coupling for the Eulerian multi-fluid model. *Computers & Fluids*, 181: 188–207, 2019. ISSN 0045-7930. doi: 10.1016/j.compfluid.2019.01.018. URL `https://www.sciencedirect.com/science/article/pii/S0045793019300143`.

[303] H. Pokharna, M. Mori, and V. H. Ransom. Regularization of two-phase flow models: A comparison of numerical and differential approaches. *Journal of Computational Physics*, 134(2):282–295, 1997. ISSN 0021-9991. doi: 10.1006/jcph.1997.5695. URL `https://www.sciencedirect.com/science/article/pii/S0021999197956953`.

[304] T. Dinh, R. Nourgaliev, and T. Theofanous. Understanding the ill-posed two-fluid model. In *Proceedings of the 10th International Topical Meeting on Nuclear Reactor Thermal-Hydraulics (NURETH'03)*, 2003.

[305] C.-H. Chang and M.-S. Liou. Simulation of multifluid multiphase flows with AUSM+-up scheme. In C. Groth and D. W. Zingg, editors, *Computational Fluid Dynamics 2004*, pages 613–618, Berlin, Heidelberg, 2006. Springer Berlin Heidelberg. ISBN 978-3-540-31801-9.

[306] N. Panicker, A. Passalacqua, and R. Fox. On the hyperbolicity of the two-fluid model for gas–liquid bubbly flows. *Applied Mathematical Modelling*, 57:432–447, 2018. ISSN 0307-904X. doi: 10.1016/j.apm.2018.01.011. URL https://www.sciencedirect.com/science/article/pii/S0307904X18300234.

[307] R. Lahey, L. Cheng, D. Drew, and J. Flaherty. The effect of virtual mass on the numerical stability of accelerating two-phase flows. *International Journal of Multiphase Flow*, 6 (4):281–294, 1980. ISSN 0301-9322. doi: 10.1016/0301-9322(80)90021-X. URL https://www.sciencedirect.com/science/article/pii/030193228090021X.

[308] D. A. Drew and R. T. Lahey. Application of general constitutive principles to the derivation of multidimensional two-phase flow equations. *International Journal of Multiphase Flow*, 5(4):243–264, 1979. ISSN 0301-9322. doi: 10.1016/0301-9322(79)90024-7. URL https://www.sciencedirect.com/science/article/pii/0301932279900247.

[309] I. Toumi and A. Kumbaro. An approximate linearized Riemann solver for a two-fluid model. *Journal of Computational Physics*, 124(2):286–300, 1996. ISSN 0021-9991. doi: 10.1006/jcph.1996.0060. URL https://www.sciencedirect.com/science/article/pii/S0021999196900601.

[310] L. Sainsaulieu. Finite volume approximation of two phase-fluid flows based on an approximate Roe-type Riemann solver. *Journal of Computational Physics*, 121(1):1–28, 1995. ISSN 0021-9991. doi: 10.1006/jcph.1995.1176. URL https://www.sciencedirect.com/science/article/pii/S002199918571176X.

[311] J. H. Song and M. Ishii. The well-posedness of incompressible one-dimensional two-fluid model. *International Journal of Heat and Mass Transfer*, 43(12):2221–2231, 2000. ISSN 0017-9310. doi: 10.1016/S0017-9310(99)00287-2. URL https://www.sciencedirect.com/science/article/pii/S0017931099002872.

[312] S.-J. L. Moon-Sun Chung, Keun-Shik Chang. Wave propagation in two-phase flow based on a new hyperbolic two-fluid model. *Numerical Heat Transfer, Part A: Applications*, 38 (2):169–191, 2000. doi: 10.1080/10407780050135397. URL https://doi.org/10.1080/10407780050135397.

[313] V. Ransom and D. Hicks. Hyperbolic two-pressure models for two-phase flow. *Journal of Computational Physics*, 53(1):124–151, 1984. ISSN 0021-9991. doi: 10.1016/0021-9991(84)90056-1. URL https://www.sciencedirect.com/science/article/pii/0021999184900561.

[314] J. D. Ramshaw and J. A. Trapp. Characteristics, stability, and short-wavelength phenomena in two-phase flow equation systems. *Nuclear Science and Engineering*, 66(1):93–102, 1978. doi: 10.13182/NSE78-A15191. URL https://doi.org/10.13182/NSE78-A15191.

[315] S.-J. Lee, K.-S. Chang, and S.-J. Kim. Surface tension effect in the two-fluids equation system. *International Journal of Heat and Mass Transfer*, 41(18):2821–2826, 1998. ISSN 0017-9310. doi: 10.1016/S0017-9310(98)00043-X. URL https://www.sciencedirect.com/science/article/pii/S001793109800043X.

[316] R. Saurel and R. Abgrall. A multiphase Godunov method for compressible multifluid and multiphase flows. *Journal of Computational Physics*, 150(2):425–467, 1999. ISSN 0021-9991. doi: 10.1006/jcph.1999.6187. URL https://www.sciencedirect.com/science/article/pii/S0021999199961879.

[317] M. Baer and J. Nunziato. A two-phase mixture theory for the deflagration-to-detonation transition (DDT) in reactive granular materials. *International Journal of Multiphase Flow*, 12(6):861–889, 1986. ISSN 0301-9322. doi: 10.1016/0301-9322(86)90033-9. URL `https://www.sciencedirect.com/science/article/pii/0301932286900339`.

[318] J. B. Bdzil, R. Menikoff, S. F. Son, A. K. Kapila, and D. S. Stewart. Two-phase modeling of deflagration-to-detonation transition in granular materials: A critical examination of modeling issues. *Physics of Fluids*, 11(2):378–402, 1999. doi: 10.1063/1.869887. URL `https://doi.org/10.1063/1.869887`.

[319] H.-O. Kreiss and J. Yström. Parabolic problems which are ill-posed in the zero dissipation limit. *Mathematical and Computer Modelling*, 35(11):1271–1295, 2002. ISSN 0895-7177. doi: 10.1016/S0895-7177(02)00085-7. URL `https://www.sciencedirect.com/science/article/pii/S0895717702000857`.

[320] B. L. Keyfitz, M. Sever, and F. Zhang. Viscous singular shock structure for a nonhyperbolic two-fluid model. *Nonlinearity*, 17(5):1731–1747, jul 2004. doi: 10.1088/0951-7715/17/5/010. URL `https://doi.org/10.1088%2F0951-7715%2F17%2F5%2F010`.

[321] P. J. Oliveira and R. I. Issa. On the numerical treatment of interphase forces in two-phase flow. In *Proceedings ASME Fluids Engineering Division Meeting*, pages 131–131, Lake Tahoe, USA, 1994. ASME.

[322] H. Karema and S. Lo. Efficiency of interphase coupling algorithms in fluidized bed conditions. *Computers & Fluids*, 28(3):323–360, 1999. ISSN 0045-7930. doi: 10.1016/S0045-7930(98)00028-0. URL `https://www.sciencedirect.com/science/article/pii/S0045793098000280`.

[323] B. S. M. Darwish, F. Moukalled. A unified formulation of the segregated class of algorithms for multifluid flow at all speeds. *Numerical Heat Transfer, Part B: Fundamentals*, 40 (2):99–137, 2001. doi: 10.1080/104077901750475887. URL `https://doi.org/10.1080/104077901750475887`.

[324] R. Nourgaliev, N. Dinh, and T. Theofanous. A characteristics-based approach to the numerical solution of the two-fluid model. In *Proceedings of the ASME/JSME Joint Fluids Engineering Conference*, volume 2, pages 1–20, 01 2003. doi: 10.1115/FEDSM2003-45551. URL `https://doi.org/10.1115/FEDSM2003-45551`.

[325] F. Moukalled, M. Darwish, and B. Sekar. A pressure-based algorithm for multi-phase flow at all speeds. *Journal of Computational Physics*, 190(2):550–571, 2003. ISSN 0021-9991. doi: 10.1016/S0021-9991(03)00297-3. URL `https://www.sciencedirect.com/science/article/pii/S0021999103002973`.

[326] H. Stewart. Fractional step methods for thermohydraulic calculation. *Journal of Computational Physics*, 40(1):77–90, 1981. ISSN 0021-9991. doi: 10.1016/0021-9991(81)90200-X. URL `https://www.sciencedirect.com/science/article/pii/002199918190200X`.

[327] D. Liles and W. Reed. A semi-implicit method for two-phase fluid dynamics. *Journal of Computational Physics*, 26(3):390–407, 1978. ISSN 0021-9991. doi: 10.1016/0021-9991(78)90077-3. URL `https://www.sciencedirect.com/science/article/pii/0021999178900773`.

[328] D. B. Spalding. Numerical computation of multi-phase fluid flow and heat transfer. In *Recent Advances in Numerical Methods in Fluids*, pages 139–168, 1980.

[329] R. F. Kunz, B. W. Siebert, W. Cope, N. F. Foster, S. P. Antal, and S. M. Ettorre. A coupled phasic exchange algorithm for three-dimensional multi-field analysis of heated flows with mass transfer. *Computers & Fluids*, 27(7):741–768, 1998. ISSN 0045-7930. doi: 10.1016/S0045-7930(97)00064-9. URL http://www.sciencedirect.com/science/article/pii/S0045793097000649.

[330] F. H. Harlow and A. A. Amsden. Numerical calculation of multiphase fluid flow. *Journal of Computational Physics*, 17(1):19–52, 1975. ISSN 0021-9991. doi: 10.1016/0021-9991(75)90061-3. URL https://www.sciencedirect.com/science/article/pii/0021999175900613.

[331] S. Lo. Mathematical basis of a multi-phase flow model. Technical report, United Kingdom Atomic Energy Authority, Computational Fluid Dynamics Section, Report AERE R 13432, 1989.

[332] S. Lo. Multiphase flow model in the Harwell-FLOW3D computer code. Technical report, AEA Industrial Technology, AEA-InTech-0062, 1990.

[333] M.-S. Liou. A further development of the AUSM+ scheme towards robust and accurate solutions for all speeds. In *16th AIAA Computational Fluid Dynamics Conference*, pages 1–18, 2012. doi: 10.2514/6.2003-4116. URL https://arc.aiaa.org/doi/abs/10.2514/6.2003-4116.

[334] D. B. Spalding. The calculation of free-convection phenomena in gas-liquid mixtures. In *Heat Transfer and Turbulent Buoyant Convection Studies and Applications for Natural Environment, Buildings and Engineering Systems*, pages 569–586, 1976.

[335] D. Spalding. Developments in the IPSA procedure for numerical computation of multiphase-flow phenomena with interphase slip, unequal temperatures, etc. *Numerical Methodologies in Heat Transfer*, pages 421–436, 1983.

[336] M. R. Maxey and J. J. Riley. Equation of motion for a small rigid sphere in a nonuniform flow. *The Physics of Fluids*, 26(4):883–889, 1983. doi: 10.1063/1.864230. URL https://aip.scitation.org/doi/abs/10.1063/1.864230.

[337] B. Hoomans, J. Kuipers, W. Briels, and W. van Swaaij. Discrete particle simulation of bubble and slug formation in a two-dimensional gas-fluidised bed: A hard-sphere approach. *Chemical Engineering Science*, 51(1):99–118, 1996. ISSN 0009-2509. doi: 10.1016/0009-2509(95)00271-5. URL https://www.sciencedirect.com/science/article/pii/0009250995002715.

[338] W. P. Adamczyk. Application of the numerical techniques for modelling fluidization process within industrial scale boilers. *Archives of Computational Methods in Engineering*, 24(4):669–702, Nov 2017. ISSN 1886-1784. doi: 10.1007/s11831-016-9186-z. URL https://doi.org/10.1007/s11831-016-9186-z.

[339] M. Andrews and P. O'Rourke. The multiphase particle-in-cell (MP-PIC) method for dense particulate flows. *International Journal of Multiphase Flow*, 22(2):379–402, 1996. ISSN 0301-9322. doi: 10.1016/0301-9322(95)00072-0. URL https://www.sciencedirect.com/science/article/pii/0301932295000720.

[340] D. Snider. An incompressible three-dimensional multiphase particle-in-cell model for dense particle flows. *Journal of Computational Physics*, 170(2):523–549, 2001. ISSN 0021-9991. doi: 10.1006/jcph.2001.6747. URL https://www.sciencedirect.com/science/article/pii/S0021999101967476.

[341] P. J. O'Rourke, P. P. Zhao, and D. Snider. A model for collisional exchange in gas/liquid/solid fluidized beds. *Chemical Engineering Science*, 64(8):1784–1797, 2009. ISSN 0009-2509. doi: 10.1016/j.ces.2008.12.014. URL https://www.sciencedirect.com/science/article/pii/S0009250908006829.

[342] P. J. O'Rourke and D. M. Snider. An improved collision damping time for MP-PIC calculations of dense particle flows with applications to polydisperse sedimenting beds and colliding particle jets. *Chemical Engineering Science*, 65(22):6014–6028, 2010. ISSN 0009-2509. doi: 10.1016/j.ces.2010.08.032. URL https://www.sciencedirect.com/science/article/pii/S0009250910005075.

[343] P. J. O'Rourke and D. M. Snider. Inclusion of collisional return-to-isotropy in the MP-PIC method. *Chemical Engineering Science*, 80:39–54, 2012. ISSN 0009-2509. doi: 10.1016/j.ces.2012.05.047. URL https://www.sciencedirect.com/science/article/pii/S0009250912003284.

[344] V. Verma and J. T. Padding. A novel approach to MP-PIC: Continuum particle model for dense particle flows in fluidized beds. *Chemical Engineering Science: X*, 6:100053, 2020. ISSN 2590-1400. doi: 10.1016/j.cesx.2019.100053. URL https://www.sciencedirect.com/science/article/pii/S2590140019300607.

[345] C. S. Campbell and C. E. Brennen. Computer simulation of granular shear flows. *Journal of Fluid Mechanics*, 151:167–188, 1985. doi: 10.1017/S002211208500091X. URL https://doi.org/10.1017/S002211208500091X.

[346] A. Stevens and C. Hrenya. Comparison of soft-sphere models to measurements of collision properties during normal impacts. *Powder Technology*, 154(2):99–109, 2005. ISSN 0032-5910. doi: 10.1016/j.powtec.2005.04.033. URL https://www.sciencedirect.com/science/article/pii/S0032591005001658.

[347] S. Luding. *Collisions & Contacts between Two Particles*, pages 285–304. Springer Netherlands, Dordrecht, 1998. ISBN 978-94-017-2653-5. doi: 10.1007/978-94-017-2653-5_20. URL https://doi.org/10.1007/978-94-017-2653-5_20.

[348] Y. Li, Y. Xu, and C. Thornton. A comparison of discrete element simulations and experiments for 'sandpiles' composed of spherical particles. *Powder Technology*, 160 (3):219–228, 2005. ISSN 0032-5910. doi: 10.1016/j.powtec.2005.09.002. URL https://www.sciencedirect.com/science/article/pii/S0032591005004079.

[349] O. Catherine and B. J. D. Selecting a suitable time step for discrete element simulations that use the central difference time integration scheme. *Engineering Computations*, 21 (2/3/4):278–303, Jan 2004. ISSN 0264-4401. doi: 10.1108/02644400410519794. URL https://doi.org/10.1108/02644400410519794.

[350] L. Fries, S. Antonyuk, S. Heinrich, and S. Palzer. DEM–CFD modeling of a fluidized bed spray granulator. *Chemical Engineering Science*, 66(11):2340–2355, 2011. ISSN 0009-2509. doi: 10.1016/j.ces.2011.02.038. URL https://www.sciencedirect.com/science/article/pii/S0009250911001333.

[351] P. Bagchi and S. Balachandar. Effect of turbulence on the drag and lift of a particle. *Physics of Fluids*, 15(11):3496–3513, 2003. doi: 10.1063/1.1616031. URL `https://doi.org/10.1063/1.1616031`.

[352] S. Balachandar and J. K. Eaton. Turbulent dispersed multiphase flow. *Annual Review of Fluid Mechanics*, 42(1):111–133, 2010. doi: 10.1146/annurev.fluid.010908.165243. URL `https://doi.org/10.1146/annurev.fluid.010908.165243`.

[353] T. M. Burton and J. K. Eaton. Fully resolved simulations of particle-turbulence interaction. *Journal of Fluid Mechanics*, 545:67–111, 2005. doi: 10.1017/S0022112005006889. URL `https://doi.org/10.1017/S0022112005006889`.

[354] J. K. Eaton. Two-way coupled turbulence simulations of gas-particle flows using point-particle tracking. *International Journal of Multiphase Flow*, 35(9):792–800, 2009. ISSN 0301-9322. doi: 10.1016/j.ijmultiphaseflow.2009.02.009. URL `https://www.sciencedirect.com/science/article/pii/S0301932209000330`.

[355] K. Luo, J. Fan, and K. Cen. Modulations on turbulent characteristics by dispersed particles in gas-solid jets. *Proceedings of the Royal Society A: Mathematical, Physical and Engineering Sciences*, 461(2062):3279–3295, 2005. doi: 10.1098/rspa.2005.1517. URL `https://royalsocietypublishing.org/doi/abs/10.1098/rspa.2005.1517`.

[356] A. A. Taweel and J. Landau. Turbulence modulation in two-phase jets. *International Journal of Multiphase Flow*, 3(4):341–351, 1977. ISSN 0301-9322. doi: 10.1016/0301-9322(77)90014-3. URL `https://www.sciencedirect.com/science/article/pii/0301932277900143`.

[357] Y. Zhang and J. M. Reese. Gas turbulence modulation in a two-fluid model for gas–solid flows. *AIChE Journal*, 49(12):3048–3065, 2003. doi: 10.1002/aic.690491207. URL `https://aiche.onlinelibrary.wiley.com/doi/abs/10.1002/aic.690491207`.

[358] C. T. Crowe. On models for turbulence modulation in fluid–particle flows. *International Journal of Multiphase Flow*, 26(5):719–727, 2000. ISSN 0301-9322. doi: 10.1016/S0301-9322(99)00050-6. URL `https://www.sciencedirect.com/science/article/pii/S0301932299000506`.

[359] M. Y. Louge, E. Mastorakos, and J. T. Jenkins. The role of particle collisions in pneumatic transport. *Journal of Fluid Mechanics*, 231:345–359, 1991. doi: 10.1017/S0022112091003427. URL `https://doi.org/10.1017/S0022112091003427`.

[360] S. Lee and F. Durst. On the motion of particles in turbulent duct flows. *International Journal of Multiphase Flow*, 8(2):125–146, 1982. ISSN 0301-9322. doi: 10.1016/0301-9322(82)90013-1. URL `https://www.sciencedirect.com/science/article/pii/0301932282900131`.

[361] Y. Tsuji, Y. Morikawa, and H. Shiomi. LDV measurements of an air-solid two-phase flow in a vertical pipe. *Journal of Fluid Mechanics*, 139:417–434, 1984. doi: 10.1017/S0022112084000422. URL `https://doi.org/10.1017/S0022112084000422`.

[362] E. J. Bolio and J. L. Sinclair. Gas turbulence modulation in the pneumatic conveying of massive particles in vertical tubes. *International Journal of Multiphase Flow*, 21(6):985–1001, 1995. ISSN 0301-9322. doi: 10.1016/0301-9322(95)00004-H. URL `https://www.sciencedirect.com/science/article/pii/030193229500004H`.

[363] R. Gore and C. Crowe. Effect of particle size on modulating turbulent intensity. *International Journal of Multiphase Flow*, 15(2):279–285, 1989. ISSN 0301-9322. doi: 10.1016/0301-9322(89)90076-1. URL https://www.sciencedirect.com/science/article/pii/0301932289900761.

[364] R. Mei and R. J. Adrian. Effect of Reynolds number on isotropic turbulent dispersion. *Journal of Fluids Engineering*, 117(3):402–409, 09 1995. ISSN 0098-2202. doi: 10.1115/1.2817276. URL https://doi.org/10.1115/1.2817276.

[365] D. A. Drew. A turbulent dispersion model for particles or bubbles. *Journal of Engineering Mathematics*, 41(2):259–274, Nov 2001. ISSN 1573-2703. doi: 10.1023/A:1011901711594. URL https://doi.org/10.1023/A:1011901711594.

[366] M. A. L. de Bertodano. Two fluid model for two-phase turbulent jets. *Nuclear Engineering and Design*, 179(1):65–74, 1998. ISSN 0029-5493. doi: 10.1016/S0029-5493(97)00244-6. URL https://www.sciencedirect.com/science/article/pii/S0029549397002446.

[367] M. Lopez de Bertodano, F. J. Moraga, D. A. Drew, and J. Lahey, R. T. The modeling of lift and dispersion forces in two-fluid model simulations of a bubbly jet. *Journal of Fluids Engineering*, 126(4):573–577, 09 2004. ISSN 0098-2202. doi: 10.1115/1.1777231. URL https://doi.org/10.1115/1.1777231.

[368] M. W. Reeks. On the continuum equations for dispersed particles in nonuniform flows. *Physics of Fluids A: Fluid Dynamics*, 4(6):1290–1303, 1992. doi: 10.1063/1.858247. URL https://doi.org/10.1063/1.858247.

[369] C. M. Hrenya and J. L. Sinclair. Effects of particle-phase turbulence in gas-solid flows. *AIChE Journal*, 43(4):853–869, 1997. doi: 10.1002/aic.690430402. URL https://aiche.onlinelibrary.wiley.com/doi/abs/10.1002/aic.690430402.

[370] T. J. O'Brien. A multiphase turbulence theory for gas–solid flows: I. Continuity and momentum equations with Favre-averaging. *Powder Technology*, 265:83–87, 2014. ISSN 0032-5910. doi: 10.1016/j.powtec.2014.01.030. URL https://www.sciencedirect.com/science/article/pii/S0032591014000394.

[371] K. Mohanarangam and J. Y. Tu. Two-fluid model for particle-turbulence interaction in a backward-facing step. *AIChE Journal*, 53(9):2254–2264, 2007. doi: 10.1002/aic.11248. URL https://aiche.onlinelibrary.wiley.com/doi/abs/10.1002/aic.11248.

[372] L. I. Zaichik, V. M. Alipchenkov, and E. G. Sinaiski. *Particles in Turbulent Flows*. John Wiley & Sons, Ltd, 2009. ISBN 9783527626250. doi: 10.1002/9783527626250. URL https://onlinelibrary.wiley.com/doi/abs/10.1002/9783527626250.

[373] F. Moraga, A. Larreteguy, D. Drew, and R. Lahey. Assessment of turbulent dispersion models for bubbly flows in the low Stokes number limit. *International Journal of Multiphase Flow*, 29(4):655–673, 2003. ISSN 0301-9322. doi: 10.1016/S0301-9322(03)00018-1. URL https://www.sciencedirect.com/science/article/pii/S0301932203000181.

[374] D. Besnard and F. Harlow. Turbulence in multiphase flow. *International Journal of Multiphase Flow*, 14(6):679–699, 1988. ISSN 0301-9322. doi: 10.1016/0301-9322(88)90068-7. URL https://www.sciencedirect.com/science/article/pii/0301932288900687.

[375] J. N. Chung and T. R. Troutt. Simulation of particle dispersion in an axisymmetric jet. *Journal of Fluid Mechanics*, 186:199–222, 1988. doi: 10.1017/S0022112088000102. URL `https://doi.org/10.1017/S0022112088000102`.

[376] A. Brucato, F. Grisafi, and G. Montante. Particle drag coefficients in turbulent fluids. *Chemical Engineering Science*, 53(18):3295–3314, 1998. ISSN 0009-2509. doi: 10.1016/S0009-2509(98)00114-6. URL `https://www.sciencedirect.com/science/article/pii/S0009250998001146`.

[377] A. A. Mostafa, H. C. Mongia, V. G. McDonell, and G. S. Samuelsen. Evolution of particle-laden jet flows - A theoretical and experimental study. *AIAA Journal*, 27(2):167–183, 1989. doi: 10.2514/3.10079. URL `https://doi.org/10.2514/3.10079`.

[378] N. Caraman, J. Borée, and O. Simonin. Effect of collisions on the dispersed phase fluctuation in a dilute tube flow: Experimental and theoretical analysis. *Physics of Fluids*, 15(12):3602–3612, 2003. doi: 10.1063/1.1619136. URL `https://doi.org/10.1063/1.1619136`.

[379] A. D. Burns, T. Frank, I. Hamill, J.-M. Shi, et al. The Favre averaged drag model for turbulent dispersion in Eulerian multi-phase flows. In *5th international conference on multiphase flow, ICMF*, volume 4, pages 1–17. ICMF, 2004.

[380] K. D. Squires and J. K. Eaton. Preferential concentration of particles by turbulence. *Physics of Fluids A: Fluid Dynamics*, 3(5):1169–1178, 1991. doi: 10.1063/1.858045. URL `https://doi.org/10.1063/1.858045`.

[381] S. E. Elghobashi and T. W. Abou-Arab. A two-equation turbulence model for two-phase flows. *The Physics of Fluids*, 26(4):931–938, 1983. doi: 10.1063/1.864243. URL `https://aip.scitation.org/doi/abs/10.1063/1.864243`.

[382] C. Simonin and P. Viollet. Predictions of an oxygen droplet pulverization in a compressible subsonic coflowing hydrogen flow. *Numerical Methods for Multiphase Flows*, 91(2):65–82, 1990.

[383] G. T. Csanady. Turbulent diffusion of heavy particles in the atmosphere. *Journal of the Atmospheric Sciences*, 20(3):201–208, 1963. doi: 10.1175/1520-0469(1963)020<0201:TDOHPI>2.0.CO;2. URL `https://doi.org/10.1175/1520-0469(1963)020<0201:TDOHPI>2.0.CO;2`.

[384] C. J. Greenshields. *OpenFOAM User's Guide*. OpenFOAM Foundation Ltd., United Kingdom, version 7 edition, 2019. URL `https://openfoam.org`.

[385] S. M. Damián and N. M. Nigro. An extended mixture model for the simultaneous treatment of small-scale and large-scale interfaces. *International Journal for Numerical Methods in Fluids*, 75(8):547–574, 2014. doi: 10.1002/fld.3906. URL `https://onlinelibrary.wiley.com/doi/abs/10.1002/fld.3906`.

[386] S. S. Deshpande, L. Anumolu, and M. F. Trujillo. Evaluating the performance of the two-phase flow solver interFoam. *Computational Science & Discovery*, 5(1):014016, 2012. doi: 10.1088/1749-4699/5/1/014016. URL `https://doi.org/10.1088%2F1749-4699%2F5%2F1%2F014016`.

[387] D. Gera, M. Syamlal, and T. J. O'Brien. Hydrodynamics of particle segregation in fluidized beds. *International Journal of Multiphase Flow*, 30(4):419–428, 2004. ISSN 0301-9322. doi: 10.1016/j.ijmultiphaseflow.2004.01.003. URL `https://www.sciencedirect.com/science/article/pii/S0301932204000175`.

[388] M. Syamlal. The particle-particle drag term in a multiparticle model of fluidization. Report DOE/MC/21353-2373, National Technical Information Service, Springfield, VA, USA, 1987. URL `https://www.osti.gov/servlets/purl/6355923`.

[389] T. Chen, X. Ku, J. Lin, and H. Ström. Pyrolysis simulation of thermally thick biomass particles based on a multistep kinetic scheme. *Energy & Fuels*, 34(2):1940–1957, 2020. doi: 10.1021/acs.energyfuels.9b04174. URL `https://doi.org/10.1021/acs.energyfuels.9b04174`.

[390] N. E. L. Haugen and R. E. Mitchell. Modeling radiation in particle clouds: On the importance of inter-particle radiation for pulverized solid fuel combustion. *Heat and Mass Transfer*, 51(7):991–999, 2015. ISSN 1432-1181. doi: 10.1007/s00231-014-1472-4. URL `https://doi.org/10.1007/s00231-014-1472-4`.

[391] N. E. L. Haugen, J. Krüger, D. Mitra, and T. Løvås. The effect of turbulence on mass transfer rates of small inertial particles with surface reactions. *Journal of Fluid Mechanics*, 836:932–951, 2018. doi: 10.1017/jfm.2017.820. URL `https://doi.org/10.1017/jfm.2017.820`.

[392] J. Krüger, N. E. Haugen, D. Mitra, and T. Løvås. The effect of turbulent clustering on particle reactivity. *Proceedings of the Combustion Institute*, 36(2):2333–2340, 2017. ISSN 1540-7489. doi: 10.1016/j.proci.2016.06.187. URL `https://www.sciencedirect.com/science/article/pii/S1540748916302498`.

[393] J. Krüger, N. E. L. Haugen, and T. Løvås. Correlation effects between turbulence and the conversion rate of pulverized char particles. *Combustion and Flame*, 185:160–172, 2017. ISSN 0010-2180. doi: 10.1016/j.combustflame.2017.07.008. URL `https://www.sciencedirect.com/science/article/pii/S0010218017302535`.

[394] H. J. Curran. Developing detailed chemical kinetic mechanisms for fuel combustion. *Proceedings of the Combustion Institute*, 37(1):57–81, 2019. ISSN 1540-7489. doi: 10.1016/j.proci.2018.06.054. URL `https://www.sciencedirect.com/science/article/pii/S1540748918302372`.

[395] C. K. Law, C. J. Sung, H. Wang, and T. F. Lu. Development of comprehensive detailed and reduced reaction mechanisms for combustion modeling. *AIAA Journal*, 41(9):1629–1646, 2003. doi: 10.2514/2.7289. URL `https://doi.org/10.2514/2.7289`.

[396] S. Pope. Computationally efficient implementation of combustion chemistry using in-situ adaptive tabulation. *Combustion Theory and Modelling*, 1(1):41–63, 1997. doi: 10.1080/713665229. URL `https://doi.org/10.1080/713665229`.

[397] M. A. Singer, S. B. Pope, and H. N. Najm. Modeling unsteady reacting flow with operator splitting and ISAT. *Combustion and Flame*, 147(1):150–162, 2006. ISSN 0010-2180. doi: 10.1016/j.combustflame.2006.06.007. URL `https://www.sciencedirect.com/science/article/pii/S0010218006001556`.

[398] D. Zhou and S. Yang. *A robust reacting flow solver with detailed transport, chemistry, and steady-state preserving splitting schemes based on OpenFOAM and Cantera*, page 9. American Institute of Aeronautics and Astronautics (AIAA), 2020. doi: 10.2514/6.2020-2139. URL `https://arc.aiaa.org/doi/abs/10.2514/6.2020-2139`.

[399] D. F. Fairbanks and C. R. Wilke. Diffusion coefficients in multicomponent gas mixtures. *Industrial & Engineering Chemistry*, 42(3):471–475, 1950. doi: 10.1021/ie50483a022. URL `https://doi.org/10.1021/ie50483a022`.

[400] M. Hishida and A. Hayashi. *Numerical Simulation of Pulsed Jet Plume Combustion*, pages 343–361. American Institute of Aeronautics and Astronautics (AIAA), 1991. doi: 10.2514/5.9781600866258.0343.0361. URL `https://arc.aiaa.org/doi/abs/10.2514/5.9781600866258.0343.0361`.

[401] H. Kobayashi, J. Howard, and A. Sarofim. Coal devolatilization at high temperatures. *Symposium (International) on Combustion*, 16(1):411–425, 1977. ISSN 0082-0784. doi: 10.1016/S0082-0784(77)80341-X. URL `https://www.sciencedirect.com/science/article/pii/S008207847780341X`.

[402] S. K. Ubhayakar, D. B. Stickler, C. W. Von Rosenberg, and R. E. Gannon. Rapid devolatilization of pulverized coal in hot combustion gases. *Symposium (International) on Combustion*, 16(1):427–436, 1977. ISSN 0082-0784. doi: 10.1016/S0082-0784(77)80342-1. URL `https://www.sciencedirect.com/science/article/pii/S0082078477803421`.

[403] Y. Shen, B. Guo, A. Yu, D. Maldonado, P. Austin, and P. Zulli. Three-dimensional modelling of coal combustion in blast furnace. *ISIJ International*, 48(6):777–786, 2008. doi: 10.2355/isijinternational.48.777. URL `https://doi.org/10.2355/isijinternational.48.777`.

[404] M. M. Baum and P. J. Street. Predicting the combustion behaviour of coal particles. *Combustion Science and Technology*, 3(5):231–243, 1971. doi: 10.1080/00102207108952290. URL `https://doi.org/10.1080/00102207108952290`.

[405] M. Field. Rate of combustion of size-graded fractions of char from a low-rank coal between 1 200 k and 2 000 k. *Combustion and Flame*, 13(3):237–252, 1969. ISSN 0010-2180. doi: 10.1016/0010-2180(69)90002-9. URL `https://www.sciencedirect.com/science/article/pii/0010218069900029`.

[406] J. Yu, M. C. Zhang, and J. Zhang. An improved model for char combustion in blast furnace pulverized coal injection. *steel research international*, 80(10):717–726, 2009. doi: 10.2374/SRI08SP132. URL `https://onlinelibrary.wiley.com/doi/abs/10.2374/SRI08SP132`.

[407] J. R. Arthur. Reactions between carbon and oxygen. *Trans. Faraday Soc.*, 47:164–178, 1951. doi: 10.1039/TF9514700164. URL `https://dx.doi.org/10.1039/TF9514700164`.

[408] A. G. Dixon. Wall and particle–shape effects on heat transfer in packed beds. *Chemical Engineering Communications*, 71(1):217–237, 1988. doi: 10.1080/00986448808940426. URL `https://doi.org/10.1080/00986448808940426`.

[409] E. Tsotsas. *M7 Heat and Mass Transfer in Packed Beds with Fluid Flow*, pages 1327–1342. Springer, Berlin, Heidelberg, 2010. ISBN 978-3-540-77877-6. doi: 10.1007/978-3-540-77877-6_100. URL `https://doi.org/10.1007/978-3-540-77877-6_100`.

[410] S. Ergun and A. A. Orning. Fluid flow through randomly packed columns and fluidized beds. *Industrial & Engineering Chemistry*, 41(6):1179–1184, 1949. doi: 10.1021/ie50474a011. URL https://doi.org/10.1021/ie50474a011.

[411] H. Enwald, E. Peirano, and A.-E. Almstedt. Eulerian two-phase flow theory applied to fluidization. *International Journal of Multiphase Flow*, 22:21–66, 1996. ISSN 0301-9322. doi: 10.1016/S0301-9322(96)90004-X. URL https://www.sciencedirect.com/science/article/pii/S030193229690004X.

[412] V. Gnielinski. Wärme- und Stoffübertragung in Festbetten. *Chemie Ingenieur Technik*, 52(3):228–236, 1980. doi: 10.1002/cite.330520306. URL https://onlinelibrary.wiley.com/doi/abs/10.1002/cite.330520306.

[413] P. Zehner and E. U. Schlünder. Wärmeleitfähigkeit von Schüttungen bei mäßigen Temperaturen. *Chemie Ingenieur Technik*, 42(14):933–941, 1970. doi: 10.1002/cite.330421408. URL https://onlinelibrary.wiley.com/doi/abs/10.1002/cite.330421408.

[414] M. Neubronner, T. Bodmer, C. Hübner, P. B. Kempa, E. Tsotsas, A. Eschner, G. Kasparek, F. Ochs, H. Müller-Steinhagen, H. Werner, and M. H. Spitzner. *D6 Properties of Solids and Solid Materials*, pages 551–614. Springer, Berlin, Heidelberg, 2010. ISBN 978-3-540-77877-6. doi: 10.1007/978-3-540-77877-6_26. URL https://doi.org/10.1007/978-3-540-77877-6_26.

[415] M. Giese. *Strömung in porösen Medien unter Berücksichtigung effektiver Viskositäten*. PhD thesis, Technical University of Munich, 1998.

[416] H. Nießen and B. Stöcker. SANA-1 code-to-experiment summary description of benchmark. In *Proc. of 3rd IAEA Research Coordination Meeting on «Heat Transport and Afterheat Removal for Gas-cooled Reactors under Accident Conditions»/IAEA.- Vienna, Austria: IAEA*, 1995.

[417] H. Niessen and S. Ball. Heat transport and afterheat removal for gas cooled reactors under accident conditions. Report IAEA-TECDOC-1163, International Atomic Energy Agency, Vienna,Austria, 2000. URL https://www-pub.iaea.org/MTCD/Publications/PDF/te_1163_prn.pdf.

[418] P. M. Ferrer, D. Causon, L. Qian, C. Mingham, and Z. Ma. A multi-region coupling scheme for compressible and incompressible flow solvers for two-phase flow in a numerical wave tank. *Computers & Fluids*, 125:116–129, 2016. ISSN 0045-7930. doi: 10.1016/j.compfluid.2015.11.005. URL https://www.sciencedirect.com/science/article/pii/S004579301500376X.

[419] N. Wakao and S. Kuaguei. *Heat and mass transfer in packed beds*. Gordon and Breach Science Publishers, New York, 1982. ISBN 9780677058603.

[420] R. Barlow and J. Frank. Effects of turbulence on species mass fractions in methane/air jet flames. *Symposium (International) on Combustion*, 27(1):1087–1095, 1998. ISSN 0082-0784. doi: 10.1016/S0082-0784(98)80510-9. URL https://www.sciencedirect.com/science/article/pii/S0082078498805109.

[421] R. S. Barlow, A. N. Karpetis, J. H. Frank, and J.-Y. Chen. Scalar profiles and NO formation in laminar opposed-flow partially premixed methane/air flames. *Combustion and Flame*, 127(3):2102–2118, 2001. ISSN 00102180. doi: 10.1016/S0010-2180(01)00313-3. URL https://doi.org/10.1016/S0010-2180(01)00313-3.

[422] C. Schneider, A. Dreizler, J. Janicka, and E. P. Hassel. Flow field measurements of stable and locally extinguishing hydrocarbon-fuelled jet flames. *Combustion and Flame*, 135(1-2):185–190, 2003. ISSN 00102180. doi: 10.1016/S0010-2180(03)00150-0. URL `https://doi.org/10.1016/S0010-2180(03)00150-0`.

[423] R. Barlow, J. Frank, A. Karpetis, and J. Chen. Piloted methane/air jet flames: Transport effects and aspects of scalar structure. *Combustion and Flame*, 143(4):433–449, 2005. ISSN 00102180. doi: 10.1016/j.combustflame.2005.08.017. URL `https://doi.org/10.1016/j.combustflame.2005.08.017`.

[424] B. Dally, A. Karpetis, and R. Barlow. Structure of turbulent non-premixed jet flames in a diluted hot coflow. *Proceedings of the Combustion Institute*, 29(1):1147–1154, 2002. ISSN 1540-7489. doi: 10.1016/S1540-7489(02)80145-6. URL `https://www.sciencedirect.com/science/article/pii/S1540748902801456`.

[425] S. B. Pope. An explanation of the turbulent round-jet/plane-jet anomaly. *AIAA Journal*, 16(3):279–281, 1978. doi: 10.2514/3.7521. URL `https://doi.org/10.2514/3.7521`.

[426] M. F. Modest and S. Lei. The simplified spherical harmonics method for radiative heat transfer. *Journal of Physics: Conference Series*, 369:012019, 2012. doi: 10.1088/1742-6596/369/1/012019. URL `https://doi.org/10.1088%2F1742-6596%2F369%2F1%2F012019`.

[427] M. F. Modest and D. C. Haworth. *Radiative Heat Transfer in Turbulent Combustion Systems.* Springer International Publishing, Cham, Switzerland, 2016. ISBN 978-3-319-27289-4. doi: 10.1007/978-3-319-27291-7. URL `https://doi.org/10.1007%2F978-3-319-27291-7`.

[428] W. L. Grosshandler. RADCAL: A narrow-band model for radiation - Calculations in a combustion environment. Technical Note 1402, National Institute of Standards and Technology (NIST), Gaithersburg, MD, 1993.

[429] G. P. Smith, D. M. Golden, M. Frenklach, N. W. Moriarty, B. Eiteneer, M. Goldenberg, C. T. Bowman, R. K. Hanson, S. Song, W. C. Gardiner Jr., V. V. Lissianski, and Z. Qin. GRI-Mech 3.0. `https://www.me.berkeley.edu/gri_mech/`, 2018.

[430] L. Van de Steene, J. Tagutchou, F. Mermoud, E. Martin, and S. Salvador. A new experimental continuous fixed bed reactor to characterise wood char gasification. *Fuel*, 89(11):3320–3329, 2010. ISSN 0016-2361. doi: 10.1016/j.fuel.2010.03.035. URL `https://www.sciencedirect.com/science/article/pii/S0016236110001407`.

[431] C. K. Westbrook and F. L. Dryer. Simplified reaction mechanisms for the oxidation of hydrocarbon fuels in flames. *Combustion Science and Technology*, 27(1-2):31–43, 1981. ISSN 0010-2202. doi: 10.1080/00102208108946970. URL `https://doi.org/10.1080/00102208108946970`.

[432] W. Jones and R. Lindstedt. Global reaction schemes for hydrocarbon combustion. *Combustion and Flame*, 78:233–249, 1988. doi: 10.1016/0010-2180(88)90021-1. URL `https://doi.org/10.1016/0010-2180(88)90021-1`.

[433] M. L. Hobbs, P. T. Radulovic, and L. D. Smoot. Modeling fixed-bed coal gasifiers. *AIChE Journal*, 38(5):681–702, 1992. doi: 10.1002/aic.690380506. URL `https://aiche.onlinelibrary.wiley.com/doi/abs/10.1002/aic.690380506`.

[434] H. Tepper. *Zur Vergasung von Rest-und Abfallholz in Wirbelschichtreaktoren für dezentrale Energieversorgungsanlagen.* PhD thesis, Faculty of Process and Systems Engineering, Otto-von-Guericke-Universität Magdeburg, Universitätsbibliothek, 2005.

[435] L. J. Petrovic and G. Thodos. Mass transfer in flow of gases through packed beds. low Reynolds number region. *Industrial & Engineering Chemistry Fundamentals*, 7(2):274–280, 1968. doi: 10.1021/i160026a016. URL `https://doi.org/10.1021/i160026a016`.

[436] G.-S. Liu and S. Niksa. Coal conversion submodels for design applications at elevated pressures. Part II. Cshar gasification. *Progress in Energy and Combustion Science*, 30 (6):679–717, 2004. ISSN 0360-1285. doi: 10.1016/j.pecs.2004.08.001. URL `https://www.sciencedirect.com/science/article/pii/S0360128504000498`.

[437] A. Inc. *ANSYS CFX-Solver Theory Guide.* ANSYS, Inc., Canonsburg, PA, USA, release 14.0 edition, November 2011.

[438] M. Bösenhofer, C. Jordan, M. Harasek, C. Feilmayr, F. Hauzenberger, A. Walk, and S. Tjaden. Pulverized coal injection (PCI) test facilities and methods - Overview and recommendations. In *AISTech - Iron and Steel Technology Conference Proceedings*, pages 287–295, 2018. ISBN 978-193511772-8.

[439] M. Simone, E. Biagini, C. Galletti, and L. Tognotti. Evaluation of global biomass devolatilization kinetics in a drop tube reactor with CFD aided experiments. *Fuel*, 88 (10):1818–1827, 2009. ISSN 0016-2361. doi: 10.1016/j.fuel.2009.04.032. URL `https://www.sciencedirect.com/science/article/pii/S0016236109002087`.

[440] R. E. Mitchell. Experimentally determined overall burning rates of coal chars. *Combustion Science and Technology*, 53(2-3):165–186, 1987. doi: 10.1080/00102208708947025. URL `https://doi.org/10.1080/00102208708947025`.

[441] R. Hurt and R. Mitchell. On the combustion kinetics of heterogeneous char particle populations. *Symposium (International) on Combustion*, 24(1):1233–1241, 1992. ISSN 0082-0784. doi: 10.1016/S0082-0784(06)80145-1. URL `https://www.sciencedirect.com/science/article/pii/S0082078406801451`.

[442] J. J. Murphy and C. R. Shaddix. Combustion kinetics of coal chars in oxygen-enriched environments. *Combustion and Flame*, 144(4):710–729, 2006. ISSN 0010-2180. doi: 10.1016/j.combustflame.2005.08.039. URL `https://www.sciencedirect.com/science/article/pii/S0010218005002658`.

[443] D. Chen, Z. Zhang, Z. Li, Z. Lv, and N. Cai. Optimizing in-situ char gasification kinetics in reduction zone of pulverized coal air-staged combustion. *Combustion and Flame*, 194: 52–71, 2018. ISSN 0010-2180. doi: 10.1016/j.combustflame.2018.04.015. URL `https://www.sciencedirect.com/science/article/pii/S0010218018301676`.

[444] Y. Kuang, B. He, W. Tong, C. Wang, and Z. Ying. Effects of oxygen concentration and inlet velocity on pulverized coal MILD combustion. *Energy*, 198:117376, 2020. ISSN 0360-5442. doi: 10.1016/j.energy.2020.117376. URL `https://www.sciencedirect.com/science/article/pii/S0360544220304837`.

[445] Z. Zhang, B. Lu, Z. Zhao, L. Zhang, Y. Chen, S. Li, C. Luo, and C. Zheng. CFD modeling on char surface reaction behavior of pulverized coal MILD-oxy combustion: Effects of oxygen and steam. *Fuel Processing Technology*, 204:106405, 2020. ISSN 0378-3820.

doi: 10.1016/j.fuproc.2020.106405. URL https://www.sciencedirect.com/science/article/pii/S0378382020300564.

[446] S. Vun, J. Naser, and P. Witt. Extension of the kinetic theory of granular flow to include dense quasi-static stresses. *Powder Technology*, 204(1):11–20, 2010. ISSN 0032-5910. doi: 10.1016/j.powtec.2010.07.001. URL https://www.sciencedirect.com/science/article/pii/S0032591010003384.

[447] P. R. Gunjal, M. N. Kashid, V. V. Ranade, and R. V. Chaudhari. Hydrodynamics of trickle-bed reactors: Experiments and CFD modeling. *Industrial & Engineering Chemistry Research*, 44(16):6278–6294, 2005. doi: 10.1021/ie0491037. URL https://doi.org/10.1021/ie0491037.

[448] Y. Wang, J. Chen, and F. Larachi. Modelling and simulation of trickle-bed reactors using computational fluid dynamics: A state-of-the-art review. *The Canadian Journal of Chemical Engineering*, 91(1):136–180, 2013. doi: 10.1002/cjce.20702. URL https://onlinelibrary.wiley.com/doi/abs/10.1002/cjce.20702.

Appended Publications

Journal Paper I

M. Bösenhofer, EM. Wartha, C. Jordan, C. Feilmayr, H. Stocker, F. Hauzenberger, J. Rieger, S. Tjaden, A. Walk, M. Harasek (2020), Suitability of pulverised coal testing facilities for blast furnace applications, Ironmaking & Steelmaking, 47(5), pp. 574-585, DOI: 10.1080/03019233.2019.1565152.

Journal Paper II

M. Bösenhofer, E. Hecht, CR. Shaddix, B. König, J. Rieger, M. Harasek (2020), Computational fluid dynamics analysis of char conversion in Sandia's pressurized entrained flow reactor, Review of Scientific Instruments, 91, 074103, DOI: 10.1063/5.0005733.

Journal Paper III

M. Bösenhofer, EM. Wartha, C. Jordan, M. Harasek (2018), The Eddy Dissipation Concept—Analysis of Different Fine Structure Treatments for Classical Combustion, Energies, 11, 1902, DOI: 10.3390/en11071902.

Journal Paper IV

EM. Wartha, M. Bösenhofer, M. Harasek (2020), Characteristic Chemical Time Scales for Reactive Flow Modeling, Combustion Science and Technology, 2020, in press, DOI: 10.1080/00102202.2020.1760257.

Reviewed Conference Paper I

M. Bösenhofer, EM. Wartha, C. Jordan, F. Hauzenberger, C. Feilmayr, H. Stoker, J. Rieger, B. König, M. Harasek (2020), Multi-Phase Reactive Systems – Analysis of Involved Time Scales, AISTech - Iron and Steel Technology Conference Proceedings, 9 pages, DOI: 10.1063/5.0005733.

Reviewed Conference Paper II

M. Bösenhofer, M. Harasek, C. Jordan, C. Feilmayr, F. Hauzenberger (2017), The Relevance of Reaction Mechanisms in the CFD Modelling of Blast Furnaces, AISTech - Iron and Steel Technology Conference Proceedings, pp. 539–553, ISBN: 978-193511764-3.

Reviewed Conference Paper III

M. Bösenhofer, EM. Wartha, C. Jordan, M. Harasek, C. Feilmayr, F. Hauzenberger (2018), Characterization of Gas Phase Reaction Regime in the Raceway Zone, AISTech - Iron and Steel Technology Conference Proceedings, pp. 441–454, ISBN: 978-193511772-8.

Reviewed Conference Paper IV

M. Bösenhofer, EM. Wartha, C. Jordan, M. Harasek, C. Feilmayr, F. Hauzenberger, B. König (2019), A Raceway Model Based on Open-Source Software, AISTech - Iron and Steel Technology Conference Proceedings, pp. 2641–2651, DOI: 10.33313/377/272.

List of Figures

List of Tables

List of Symbols

Symbol	Unit	Description
A	$[\frac{\text{kg}}{\text{m}^2\text{sPa}^{-\text{n}}}]$	frequency factor
A_0	$[\frac{\text{m}^2}{\text{m}^3}]$	initial pore surface
A_{int}	$[\text{m}^2]$	internal surface area
A_r	$[\text{m}^2]$	reaction front area
A_s	$[\text{m}^2]$	external surface area
$\mathcal{C}$	$[-]$	dimensionless species concentration
C	$[-]$	progress variable
C_{D1}	$[-]$	model constant (value = 0.135)
C_{D2}	$[-]$	model constant (value = 0.50)
CFL	$[-]$	Courant-Friedrichs-Lewy number
C_D	$[-]$	drag coefficient
C_{VM}	$[-]$	virtual mass force coefficient
$C_{\varepsilon 1}$	$[-]$	turbulence model constant (value = 1.44)
$C_{\varepsilon 2}$	$[-]$	turbulence model constant (value = 1.92)
C_γ	$[-]$	fine structure length scale constant
C_{mix}	$[-]$	mixing time scale constant
C_μ	$[-]$	turbulence model constant (value = 0.135)
C_τ	$[-]$	fine structure residence time constant
D	$[\frac{\text{m}^2}{\text{s}}]$	mass diffusivity
D_{Kn}	$[\frac{\text{m}^2}{\text{s}}]$	Knudsen diffusion coefficient
Da	$[-]$	Damköhler number
Da_η	$[-]$	Kolmogorov scale Damköhler number
Da_t	$[-]$	turbulent Damköhler number
D_{bulk}	$[\frac{\text{m}^2}{\text{s}}]$	bulk diffusion coefficient

Symbol	Unit	Description
D_c	$[-]$	fractal dimension
D_{eff}	$[\frac{\text{m}^2}{\text{s}}]$	effective diffusion coefficient
D_i	$[\frac{\text{m}^2}{\text{s}}]$	species diffusivity
$D_{i,j}$	$[\frac{\text{m}^2}{\text{s}}]$	binary diffusion coefficient
$E_{a,app}$	$[\frac{\text{kJ}}{\text{mol}}]$	apparent activation energy
$E_{a,int}$	$[\frac{\text{kJ}}{\text{mol}}]$	intrinsic activation energy
$\boldsymbol{I}$	$[-]$	identity matrix
I_p	$[\frac{\text{kg}}{\text{m}^2}]$	moment of inertia
Ka	$[-]$	Karlovitz number
L	$[\text{m}]$	integral length scale
L_0	$[\frac{\text{m}}{\text{m}^3}]$	initial pore length
L_c	$[\text{m}]$	characteristic length
$\overline{M}_i^*$	$[\frac{\text{kg}}{\text{m}^3\text{s}}]$	fine structure specie mass transfer term
$\boldsymbol{M_D}$	$[\frac{\text{N}}{\text{m}^3}]$	drag force
$\boldsymbol{M}_L$	$[\frac{\text{N}}{\text{m}^3}]$	lift force
$\boldsymbol{M}_{TD}$	$[\frac{\text{N}}{\text{m}^3}]$	turbulent dispersion force
$\boldsymbol{M}_{VM}$	$[\frac{\text{N}}{\text{m}^3}]$	virtual mass force
$\boldsymbol{M}_{pj}^r$	$[\text{Nm}]$	rolling resistance torque
$\boldsymbol{M}_{pj}^t$	$[\text{Nm}]$	rotational torque
N	$[-]$	number of grid points
N_η	$[-]$	number of locally generated dissipative scales
Q_{ext}^ϕ	[suitable units]	external Lagrangian source
Q_{int}^ϕ	[suitable units]	internal Lagrangian source
Q^ϕ	[suitable units]	source term
$\overline{Q}_\varphi^\phi$	[suitable units]	source term
$\dot{Q}_{tot}$	$[\text{W}]$	total heat flux
R_i^*	$[\frac{\text{kg}}{\text{m}^3\text{s}}]$	fine structure species consumption/production rate
$\overline{R}_i$	$[\frac{\text{kg}}{\text{m}^3\text{s}}]$	mean species consumption/production rate
Re	$[-]$	Reynolds number
Re^*	$[-]$	fine structure Reynolds number
Re_t	$[-]$	turbulent Reynolds number

Symbol	Unit	Description
R_i	$[\frac{\text{kg}}{\text{m}^3\text{s}}]$	species consumption / production rate
R_{ij}	[Pas]	Reynolds stress
S	$[\text{m}^2]$	surface
S_A	$[\text{m}^2]$	surface area
$\boldsymbol{S}$	$[\text{m}^2]$	surface vector
Sc	$[-]$	Schmidt number
Sh	$[-]$	Sherwood number
T	[K]	temperature
$\overline{T}$	[K]	mean temperature
T_P	[K]	particle temperature
T_{boil}	[K]	boiling temperature
T_{dev}	[K]	devolatilization temperature
T_∞	[K]	bulk temperature
V	$[\text{m}^3]$	volume
V_{cell}	$[\text{m}^3]$	cell volume
$V_{p,i}$	$[\text{m}^3]$	particle volume
W	$[\frac{\text{kg}}{\text{kmol}}]$	molar weight
X	$[-]$	dimensionless distance
Y^*	$[\frac{\text{kg}}{\text{kg}}]$	fine structure species mass fraction
$\overline{Y}_i$	$[\frac{\text{kg}}{\text{kg}}]$	mean species mass fraction
Y°	$[\frac{\text{kg}}{\text{kg}}]$	surrounding species mass fraction
Y_{fuel}	$[\frac{\text{kg}}{\text{kg}}]$	fuel product mass fraction
Y_i	$[-]$	species mass fraction
Y_{oxi}	$[\frac{\text{kg}}{\text{kg}}]$	oxidizer product mass fraction
Y_{pr}	$[\frac{\text{kg}}{\text{kg}}]$	product mass fraction
Z	$[-]$	mixture fraction
$Z_{i,j}$	$[-]$	mixture fraction ratio
b	$[-]$	temperature exponent
c	$[\frac{\text{(k)mol}}{\text{m}^3}]$	species concentration
$c_{0,i}$	$[\frac{\text{(k)mol}}{\text{m}^3}]$	inlet species concentration
$\bar{c}_i$	$[\frac{\text{(k)mol}}{\text{m}^3}]$	mean species concentration

Symbol	Unit	Description
c_i°	$[\frac{\text{(k)mol}}{\text{m}^3}]$	surrounding species concentration
c_i	$[\frac{\text{(k)mol}}{\text{m}^3}]$	species concentration
c_∞	$[\frac{\text{(k)mol}}{\text{m}^3}]$	bulk species concentration
$c_{m,i}$	$[\frac{\text{(k)mol}}{\text{m}^3}]$	mean reactor species concentration
c_p	$[\frac{\text{J}}{\text{kgK}}]$	(mixture) specific heat
c_r	$[\frac{\text{(k)mol}}{\text{m}^3}]$	species concentration at the reaction front
$c_{r,i}$	$[\frac{\text{(k)mol}}{\text{m}^3}]$	species concentration in the reaction zone
c_s	$[\frac{\text{(k)mol}}{\text{m}^3}]$	surface species concentration
c_i^*	$[\frac{\text{(k)mol}}{\text{m}^3}]$	fine structure species concentration
d	$[\text{m}]$	diameter
d_P	$[\text{m}]$	particle diameter
d_{pore}	$[\text{m}]$	pore diameter
$\boldsymbol{f}$	$[\text{N}]$	force vector
$\boldsymbol{g}$	$[\frac{\text{m}}{\text{s}^2}]$	gravity vector
h	$[\frac{\text{J}}{\text{kg}}]$	enthalpy
$h_{BL,m}$	$[\frac{\text{m}^2}{\text{s}}]$	convective mass transfer coefficient
h_i	$[\text{J}]$	species enthalpy
k	$[\frac{\text{m}^2}{\text{s}^2}]$	turbulent kinetic energy
k_R	$[\frac{\text{kg}}{\text{m}^2\text{s}}]$	kinetic conversion rate
k_{app}	$[\frac{\text{kg}}{\text{m}^3\text{s}}]$	apparent conversion rate
k_{eff}	$[\frac{\text{kg}}{\text{m}^3\text{s}}]$	effective rate
k_{ext}	$[\frac{\text{kg}}{\text{m}^3\text{s}}]$	external rate
k_{int}	$[\frac{\text{kg}}{\text{m}^3\text{s}}]$	internal rate
$k_{int,\infty}$	$[\frac{\text{kg}}{\text{m}^3\text{s}}]$	intrinsic rate at ambient conditions
k_{intr}	$[\frac{\text{kg}}{\text{m}^3\text{s}}]$	intrinsic conversion rate
k_{sg}	$[\frac{\text{m}^2}{\text{m}^2}]$	dispersed phase turbulence modulation
k_{spring}	$[\frac{\text{N}}{\text{m}}]$	spring stiffness
l	$[\text{m}]$	length
l_d	$[\text{m}]$	diffusion zone thickness
l_η	$[\text{m}]$	Kolmogorov length scale
l_λ	$[\text{m}]$	Taylor length scale

Symbol	Unit	Description
l_r	[m]	vortex length scale
l_t	[m]	turbulence length scale
m_c	[kg]	char mass
m_m	[kg]	moisture mass
m_o	[kg]	oxidizer mass
m_p	[kg]	particle mass
m_v	[kg]	volatile mass
n	[−]	reaction order
$n_{p,i}$	[−]	number of particles per parcel
p	[Pa]	static pressure
$\bar{p}$	[Pa]	mean static pressure
p_i	[Pa]	species partial pressure
p'	[Pa]	pressure fluctuations
r	[m]	radius
r_r	[m]	radial position reaction front
r_s	[m]	particle radius
s	[−]	shape specific coefficient (0 = flat plate, 1 = cylinder, 2 = sphere)
s_L^0	$[\frac{\text{m}}{\text{s}}]$	laminar flame speed
t	[s]	time
$\mathbf{u}$	$[\frac{\text{m}}{\text{s}}]$	velocity vector
$\overline{\boldsymbol{u}}$	$[\frac{\text{m}}{\text{s}}]$	mean velocity vector
$\overline{\boldsymbol{u}}_p$	$[\frac{\text{m}}{\text{s}}]$	particle velocity vector
$\overline{\boldsymbol{u}}_r$	$[\frac{\text{m}}{\text{s}}]$	mean relative phase velocity vector
u_i	$[\frac{\text{m}}{\text{s}}]$	velocity vector
$\bar{u}_i$	$[\frac{\text{m}}{\text{s}}]$	mean velocity vector
u'_i	$[\frac{\text{m}}{\text{s}}]$	velocity fluctuation vector
$\overline{u}$	$[\frac{\text{m}}{\text{s}}]$	mean velocity magnitude
u'	$[\frac{\text{m}}{\text{s}}]$	turbulent velocity fluctuation magnitude
x	$[\frac{\text{kmol}}{\text{kmol}}]$	mole fraction
$\boldsymbol{x}_p$	[m]	particle position
x_i	[m]	spatial coordinate(s)

Symbol	Unit	Description
x_w	[m]	wall distance
ΔH_{dev}	$[\frac{\text{J}}{\text{kg}}]$	enthalpy of devolatilization
ΔH_r	$[\frac{\text{kJ}}{\text{(k)mol}}]$	heat of reaction
ΔH_{vap}	$[\frac{\text{J}}{\text{kg}}]$	enthalpy of vaporization
$\Delta t_{\text{DEM, crit}}$	[s]	critical Discrete Element Method (*DEM*) time step
Γ	$[\frac{\text{m}^2}{\text{s}}]$	diffusivity
Γ^ϕ	$[\frac{\text{m}^2}{\text{s}}]$	diffusion coefficient
Γ_t	$[\frac{\text{m}^2}{\text{s}}]$	turbulent diffusivity
Ω	$[\frac{\text{m}}{\text{s}}]$	diffusion rate
Ω_0	$[\frac{\text{m}^2}{\text{K}^{0.75}\text{s}}]$	reference diffusion coefficient
$\overline{\Omega}_i^*$	$[\frac{\text{kg}}{\text{m}^3\text{s}}]$	diffusion species mass transfer term
Ψ	$[-]$	pore structure parameter
Ψ_φ^ϕ	[suitable units]	source term
Ψ_{stoich}	$[-]$	stoichiometric fuel oxidizer ratio
$\mathcal{R}$	$[\frac{\text{J}}{\text{molK}}]$	ideal gas constant
Σ	$[\text{m}^2]$	control surface
Θ	$[-]$	angle between the dispersed and the relative velocity
$\overline{\Theta}_i^*$	$[\frac{\text{kg}}{\text{m}^3\text{s}}]$	dynamic equilibrium specie mass transfer term
α	$[-]$	conversion
α_φ	$[\frac{\text{m}^3}{\text{m}^3}]$	phase fraction
β	$[-]$	relative temperature variation
χ	$[-]$	reacting fine structure share
$\dot{\chi}$	$[\frac{1}{\text{s}}]$	scalar dissipation rate
δ_{BL}	[m]	boundary layer thickness
δ_f	[m]	effective flame thickness
δ_p	[m]	preheat zone thickness
δ_r	[m]	reaction zone thickness
ϵ	$[-]$	porosity
ϵ_0	$[-]$	initial particle porosity
ϵ_∞	$[-]$	bulk porosity
$\widetilde{\epsilon}_\phi$	$[\frac{\text{m}^2}{\text{s}^3}]$	dissipation rate

Symbol	Unit	Description
ε	$[\frac{\text{m}^2}{\text{s}^3}]$	turbulent dissipation rate
ε_{ij}	$[\frac{\text{m}^2}{\text{s}^3}]$	turbulent dissipation rate tensor
η_{eff}	$[-]$	effectiveness factor
η_k	$[\text{m}]$	Kolmogorov length scale
γ	$[-]$	reaction rate sensitivity to temperature
γ^*	$[-]$	fine structure share
γ^*_{equ}	$[-]$	equilibrium fine structure volume fraction
γ_L	$[-]$	fine structure length scale
κ	$[-]$	combustion efficiency correction
κ_{th}	$[\frac{\text{m}^2}{\text{s}}]$	thermal diffusivity
λ	$[\frac{\text{W}}{\text{mK}}]$	thermal conductivity
μ	$[\text{Pas}]$	dynamic viscosity
μ_t	$[\text{Pas}]$	dynamic turbulent viscosity
μ_{vol}	$[\text{Pas}]$	dynamic volume viscosity
ν	$[\frac{\text{m}^2}{\text{s}}]$	kinematic viscosity
ν_t	$[\frac{\text{m}^2}{\text{s}}]$	turbulent kinematic viscosity
$\dot{\omega}_i^*$	$[\frac{1}{\text{s}}]$	fine structure species consumption/production rate
$\dot{\omega}_C$	$[\frac{1}{\text{s}}]$	progress variable source term
$\dot{\omega}_Z$	$[\frac{1}{\text{s}}]$	mixture fraction source term
$\boldsymbol{\omega}_p$	$[\frac{1}{\text{s}}]$	angular speed
$\dot{\omega}_h$	$[\frac{\text{J}}{\text{m}^3\text{s}}]$	enthalpy source term
$\dot{\omega}_i$	$[\frac{\text{kg}}{\text{m}^3\text{s}}]$	species consumption/production rate
$\phi_{Th,i}$	$[-]$	Thiele modulus
$\widetilde{\phi''^2}$	$[\frac{\text{m}^2}{\text{s}^2}]$	variance
ρ	$[\frac{\text{kg}}{\text{m}^3}]$	density
ρ^*	$[\frac{\text{kg}}{\text{m}^3}]$	fine structure density
$\overline{\rho}$	$[\frac{\text{kg}}{\text{m}^3}]$	mean density
ρ°	$[\frac{\text{kg}}{\text{m}^3}]$	surrounding density
$\overline{\boldsymbol{\sigma}}_\varphi$	$[\frac{\text{m}^3}{\text{m}^3}]$	mean Cauchy stress tensor
σ_ε	$[-]$	turbulence model constant (value = 1.3)
σ_k	$[-]$	turbulence model constant (value = 1.0)

Symbol	Unit	Description
τ^*	[s]	fine structure residence time
τ_D	[s]	diffusion time scale
τ_L	[s]	Lagrangian integral time scale
$\bar{\tau}_{ij}$	[Pa]	mean stress tensor
$\boldsymbol{\tau}$	[Pa]	stress tensor
τ_c	[s]	chemical time scale
τ_η	[s]	Kolmogorov time scale
τ_{mix}	[s]	mixing time scale
τ_p	[s]	particle relaxation time scale
τ_{res}	[s]	residence time
τ_{eddy}	[s]	characteristic energetic eddy time scale
τ_t	[s]	turbulent time scale
ξ	[−]	proportional constant

List of Acronyms

AJHC Adelaide Jet in Hot Coflow

ARA Alternative Reducing Agent

ARM Apparent Rate Model

AUSM Advection Upstream Splitting Method

CFD Computation Fluid Dynamics

CFD-**DEM** Computation Fluid Dynamics-Discrete Element Method

DEM Discrete Element Method

DNS Direct Numerical Simulation

EDC Eddy Dissipation Concept

E-E Euler-Euler

E-L Euler-Lagrange

EPaSR Extended Partially-Stirred Reactor Model

EU European Union

FANS Favre-Average Navier-Stokes

FGM Flamelet Generated Manifold

FPI Flame Prolongation of Intrinsic Low-Dimensional Manifolds

FPVM Flamelet/Progress Variable Model

FS Fine Structures

FVM Finite Volume Method

ILDM Intrinsic Low-Dimensional Manifolds

IMF Implicit Multifield Method

IPSA Interphase Slip Algorithm

IPSA-**C** Interphase Slip Algorithm-Coupled

ISAT In-Situ Adaptive Tabulation

KTG Kinetic Theory of Gases

KTGF Kinetic Theory of Granular Flow

LES Large Eddy Simulation

LHS left hand side

LM Layer Model

LTS Local Time Stepping

MFM Multi-Fluid Model

MILD Moderate or Intense Low-oxygen Dilution

MPPIC Multiphase Particle-in-Cell

MULES Multidimensional Universal Limited Explicit Solver

PaSR Partially-Stirred Reactor Model

PCI Pulverized Coal Injection

PDF Probability Density Function

PEA Partial Elimination Algorithm

PEFR Pressurized Entrained Flow Reactor

PFR Plug Flow Reactor

PIMPLE Pressure-Implicit Method for Pressure Linked Equations

PISO Pressure-Implicit Method with Splitting of Operators

PIT Partially Implicit Treatment

PSR Perfectly Stirred Reactor

RANS Reynolds-Average Navier-Stokes

RHS right hand side

RPM Random Pore Model

RWM Race Way Model

SIMPLE Semi-Implicit Method for Pressure Linked Equations

SINCE Simultaneous Solution of Non-Linearly Coupled Equations

SLFM Steady Laminar Flamelet Model

SSKM Solid-State Kinetic Model

TBM Thiele Based Model

TFM Two-Fluid Model

WSGGM Weighted Sum of Grey Gases Model

ZBS Zehner-Bauer-Schlünder Model

Markus Bösenhofer

Date of birth:
13th September 1988

Place of birth:
Güssing, Austria

Current address:
Am Wiesengrund 6
7543 Limbach

Languages
German
(native tongue)
English
(very good)
French
(basic)
Spain
(basic)

Computer skills
ANSYS Fluent (basic)
AutoCAD (basic)
C/C++ (advanced)
Catia V5 (basic)
MATLAB (advanced)
octave (advanced)
OpenFOAM
(advanced)
python (advanced)
web design (HTML,
MySQL, PHP, CSS)

Education

07/2014 - present	**Doctoral program "Chemical Engineering"** Technische Universität Wien *Working title: On the modeling of multi-phase reactive flows*
09/2011 - 04/2014	**Master course "Energy- and Environmental Management"** University of Applied Sciences Burgenland *Master thesis title: Validation and Optimization of a Torrefaction Model for Thermally Thick Biomass Particles*
09/2008 - 07/2011	**Bachelor course "Energy- and Environmental Management"** University of Applied Sciences Burgenland *Bachelor thesis title: How serious are oil & gas companies and utilities on Renewable Power?*

Work Experience

01/2016 - present	**K1-MET GmbH, Area 4 - Simulation and Analyses** Linz, Austria *Researcher (part time)*
01/2016 - present	**Research Group Computational Fluid Dynamics (CFD), Institute of Chemical, Environmental and Bioscience Engineering, Technische Universität Wien** Vienna, Austria *Project assistant (part time)*
10/2018 - 02/2019	**Combustion Research Facility (CRF), Reacting Flow Research Division, Sandia National Laboratories** Livermore, CA, USA *Incoming researcher*
02/2014 - 12/2016	**Research Group Reaction Engineering and Combustion, Institute of Chemical, Environmental and Bioscience Engineering, Technische Universität Wien** Vienna, Austria *Project assistant (part time)*
09/2013	**Competence area "Modelling and Simulation", Bioenergy2020+ (now Bioenergy and Sustainable Technologies GmbH)** Graz, Austria *Researcher*
11/2012 - 08/2013	**Competence area "Modelling and Simulation", Bioenergy2020+ (now Bioenergy and Sustainable Technologies GmbH)** Graz, Austria *MSc degree candidate*
08/2012 - 12/2014	**Department Technology Services, T-Mobile Austria** Vienna, Austria *employee (part time)*
06/2011 - 08/2012	**MG Energy+** Vienna, Austria *Analyst (part time)*
03/2011 - 06/2011	**Department "Development & Construction Renewables", Business Unit "Power Generation", OMV Power International GmbH** Vienna, Austria *Intern*

Project Contributions

07/2019 - present	**K1-MET - P1.4 Reaktivität alternativer Reduktionsmittel:** Development of a test rig and test procedure for the evaluation of alternative reducing agents.
07/2019 - present	**K1-MET - P4.3 WP1 CFD-DEM Chemical Coupling:** Development of a detailed and a simplified single particle model for metallurgical applications.
07/2019 - present	**K1-MET - P4.3 WP3 Enhancement and Optimizing of the Raceway Model:** Optimization and extension of a reactive multi-phase modeling framework for the blast furnace raceway zone.
01/2016 - 06/2019	**K1-MET - P4.2 WP1 Raceway Simulation (CFD):** Development of a numerical model for the simulation of multi-phase reactive flows, e.g. the blast furnace raceway zone.
01/2016 - 06/2019	**K1-MET - P1.2 Reducing Agents:** Evaluation of possible alternative reducing agents for the blast furnace process.
02/2014 - 12/2015	**IEA TCP Fluidized Bed Conversion (FBC). Working period 2013-2016:** The Implementing Agreement gives a worldwide overview of the state of the art of fluidized bed technology for its application in the area of energy technology.

Teaching Experience

03/2020 - present	**Chemical Engineering Calculations:** Teaching of calculation procedures to solve mixing problems.
05/2018 - 07/2018	**moreCFD:** Teaching current capabilities of CFD in chemical engineering applications.
04/2017 - 07/2017	**Computational Fluid Dynamics (CFD) of Separation Processes Exercise:** Supervision of final projects of of students.
07/2016	**Chemical Engineering Summer School:** Teaching of Unit operations of chemical engineering for incoming students.
10/2014 - 12/2015	**Energy and Fuel Technology Laboratory Exercise:** Teaching of combustion fundamentals of flames and solid fuel conversion.

Journal Publications

Bösenhofer, M., Hecht, E., Shaddix, CR., König, B., Rieger, J., Harasek, M. (2020): **"Computational fluid dynamics analysis of char conversion in Sandia's pressurized entrained flow reactor"**, Review of Scientific Instruments, 91, pp. 074103, DOI: 10.1080/00102202.2020.1760257.

Wartha, E.-M., Bösenhofer, M., Harasek, M. (2020): **"Characteristic Chemical Time Scales for Reactive Flow Modeling"**, Combustion Science and Technology, in press, DOI: 10.1080/00102202.2020.1760257.

Bösenhofer, M., Wartha, E.-M., Jordan, C., Feilmayr, C., Stocker, H., Hauzenberger, F., Rieger, J., Tjaden, S., Walk, A., Harasek, M. (2020): **"Suitability of pulverised coal testing facilities for blast furnace applications"**, Ironmaking and Steelmaking, 47(5), pp. 574-585, DOI: 10.1080/03019233.2019.1565152.

Bösenhofer, M., Wartha, E.-M., Jordan, C., Harasek, M. (2018): **"The eddy dissipation concept-analysis of different fine structure treatments for classical combustion"**, Energies 11(7), pp. 1902, DOI: 10.3390/en11071902.

Conference Publications

Bösenhofer, M., Wartha, E.M., Jordan, C., Harasek, M., Feilmayr, C., Hauzenberger, F., König, B. (2019): **"A raceway model based on open-source software"**, AISTech - Iron and Steel Technology Conference Proceedings, pp. 2641-2651, DOI: 10.33313/377/272.

Bösenhofer, M., Antunes Paiva, I.I., Tjaden, S., Jordan, C., Harasek, M., Rieger, J., Feilmayr, C., Hauzenberger, F. (2019): **"Pulverized coal feeding vessels - Characterization and optimization"**, AISTech - Iron and Steel Technology Conference Proceedings, pp. 407-416, DOI: 10.33313/377/042.

Bösenhofer, M., Wartha, E.-M., Jordan, C., Harasek, M., Feilmayr, C., Hauzenberger, F. (2018): **"Characterization of gas phase reaction regime in the raceway zone"**, AISTech - Iron and Steel Technology Conference Proceedings, pp. 441-454, ISBN: 978-193511772-8.

Bösenhofer, M., Jordan, C., Harasek, M., Feilmayr, C., Hauzenberger, F., Walk, A., Tjaden, S. (2018): **"Pulverized coal injection (PCI) test facilities and methods - Overview and recommendations"**, AISTech - Iron and Steel Technology Conference Proceedings, pp. 287-295, ISBN: 978-193511772-8.

Wartha, E.-M., Bösenhofer, M., Harasek, M. (2018): **"Computational Improvements for the Eddy Dissipation Concept by Operator Splitting and Tabulation"**, Computer Aided Chemical Engineering 43, pp. 1687-1692, DOI: 10.1016/B978-0-444-64235-6.50294-1.

Bösenhofer, M., Harasek, M., Jordan, C., Feilmayr, C., Hauzenberger, F. (2017): **"The relevance of reaction mechanisms in the CFD modeling of blast furnaces"**, AISTech - Iron and Steel Technology Conference Proceedings, pp. 539-553, ISBN: 978-193511764-3.

Harasek, M., Maier, C., Jordan, C., Bösenhofer, M., Feilmayr, C. (2016): **"Investigation of alternative reducing agent conversion in the raceway cavity of blast furnaces by numerical simulation"**, AISTech - Iron and Steel Technology Conference Proceedings, pp. 353-365, ISBN: 978-193511755-1.